Airborne In-Situ Observations of Atmospheric Composition: Instrument Characterization, Regional Fluxes, and Tropospheric Transport

Dissertation
zur Erlangung des akademischen Grades

„Doktor der Naturwissenschaften“

am Fachbereich Physik, Mathematik und Informatik
der Johannes Gutenberg-Universität
in Mainz

Linda Martina Ort

geb. am 09.03.1995 in Erlenbach am Main

Mainz, 5 März 2026

Betreuer

Prof. Dr. Peter Hoor
Institut für Physik der Atmosphäre, Johannes Gutenberg-Universität, Mainz

Prof. Dr. Johannes Lelieveld
Atmosphären Chemie, Max-Planck-Institut für Chemie, Mainz

Tag der mündlichen Prüfung:

12. Mai 2026

Formal Declaration

I hereby declare that I wrote this dissertation without any unauthorized external assistance and acknowledged all sources within the text. This document and work is my own and has been carried out in accordance with good scientific practice standards as stated by the Johannes Gutenberg University and the Paul Crutzen Graduate School Center.

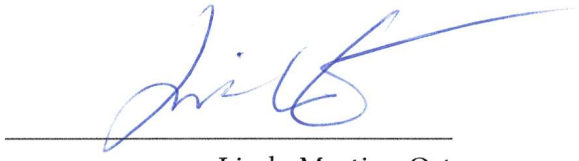

Linda Martina Ort
Mainz, 5 March 2026

Declaration of Independence

I further declare that I have written this paper independently and have not used any sources or aids other than those specified (including AI-based applications or tools). All literal or paraphrased quotations and citations are identified and referenced. I have documented the AI tools used in the Appendix "Use of AI Tools". By submitting this work, I assume responsibility for the entire product submitted. I am therefore also responsible for any AI-generated content that I have included in my work. I have checked the accuracy of the (AI-generated) statements and content to the best of my knowledge and belief. I am aware that any violation of the above points will have consequences under examination law.

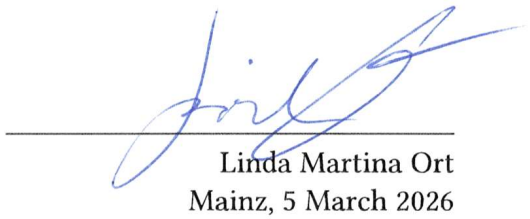

Linda Martina Ort
Mainz, 5 March 2026

"The important thing is not to stop questioning.
Curiosity has its own reason for existing."

– Albert Einstein

Acknowledgements

Abstract

Airborne in-situ observations provide a unique perspective on atmospheric composition by combining high-precision trace gas measurements with three-dimensional sampling of the troposphere. They are crucial to evaluate atmospheric models, calibrate satellites, and to investigate chemical interactions in the atmosphere. This dissertation presents an integrated investigation of the atmospheric composition using airborne measurements, focusing on instrument characterization, regional surface flux estimation, and transport and chemistry in the troposphere.

The first part of this work addresses the development of a new quantum cascade laser infrared absorption spectrometer, the Airborne Tropospheric Tracer In-situ Laser Absorption spectrometer (ATTILA), designed to meet the demanding requirements of airborne measurements. ATTILA is a dual multipass cell system, able to observe on two spectral ranges simultaneously. In this study, the instrumental setup and construction is described. Moreover, in-flight diagnostics, and inter-comparisons are used to quantify the instruments performance, stability, and uncertainty contributions. On the basis of a dedicated test flight, continuous measurements of calibration gas revealed insights of challenges and limitations for airborne in situ measurements, which were used to improve instrumental performance on research campaigns.

In the second part, airborne observations of methane (CH_4), conducted with ATTILA over the Amazon region in the scope of the Chemistry of the Atmosphere Field Experiment (CAFE Brazil) campaign, are used to constrain regional surface fluxes through Bayesian inverse modeling. To spatially identify the areas of influence of the measurements, high-resolution transport simulations from the STILT (Stochastic Time-Inverted Lagrangian Transport) model are used. The solution to the inverse problem involves the utilization of prior information on CH_4 emissions, derived from WetCHARTs – a bottom-up approach estimating wetland emissions. Spatial correlations are then implemented to ensure the dependency between similar and neighboring land-cover types. The results indicate that measurements have a substantial impact on regional CH_4 emissions, particularly in the vicinity of large riverbeds, reservoirs, and extensive river deltas. The inversion shows that CH_4 emissions in these regions are underestimated by up to a factor of four.

The final part of this dissertation uses global airborne observations from twelve different aircraft missions to investigate tropospheric transport and chemical processes influencing trace gas distributions. In the tropics, photochemical processes can reduce carbon monoxide (CO) and produce ozone (O_3), which then can be transported over the Hadley cells into the subtropics. Here, strong stratosphere-troposphere exchange processes can dilute stratospheric air masses into the troposphere, resulting in similar mixing ratios of O_3 and CO, which originate from the tropics. To distinguish between those two different mechanisms, a comparison and a sensitivity study with the global three-dimensional ECHAM5/MESSy Atmospheric Chemistry (EMAC) model are performed, revealing a strong annual relative reduction in the O_3 – CO ratio in the upper troposphere of the tropics and subtropics attributable to lightning-induced emissions.

Altogether, this work demonstrates the critical role of airborne in-situ observations in advancing our understanding of atmospheric composition, improving emission estimates, and evaluating transport and chemistry in the troposphere. The results underscore the value of integrated measurement-model approaches for studying regional to global-scale atmospheric processes.

Zusammenfassung

Luftgestützte In-situ-Beobachtungen bieten eine einzigartige Perspektive auf die Zusammensetzung der Atmosphäre, indem sie hochpräzise Spurengasmessungen mit dreidimensionalen Probenahmen aus der Troposphäre kombinieren. Sie sind von entscheidender Bedeutung für die Evaluierung von Atmosphärenmodellen, die Kalibrierung von Satelliten und für die Untersuchung chemischen Wechselwirkungen in der Atmosphäre. Diese Dissertation präsentiert eine integrierte Untersuchung der Zusammensetzung der Atmosphäre anhand von luftgestützten Messungen, wobei der Schwerpunkt auf der Charakterisierung von Instrumenten, der Schätzung regionaler Bodenemissionen, sowie der Interaktion von Transport und Chemie in der Troposphäre liegt.

Der erste Teil dieser Arbeit befasst sich mit der Entwicklung eines neuen Infrarot-Absorptionsspektrometers mit Quantenkaskadenlaser, dem "Airborne Tropospheric Tracer In-situ Laser Absorption Spectrometer" (ATTILA), welches für die hohen Anforderungen von fluggetragenden Messungen konstruiert wurde. ATTILA ist ein duales Multireflextionszellensystem, welches zwei Spektralbereiche gleichzeitig beobachten kann. In dieser Studie werden der Aufbau und die Konstruktion des Instruments beschrieben. Darüber hinaus werden Flugdiagnosen und Vergleichsmessungen verwendet, um die Leistung, Stabilität und Fehlerfaktoren des Instruments zu quantifizieren. Auf der Grundlage eines speziellen Testflugs lieferten kontinuierliche Messungen von Kalibriergas Einblicke in die Herausforderungen und Limitierungen von fluggetragenden Messungen, die zur Verbesserung der Instrumentenleistung bei Forschungskampagnen genutzt wurden.

Im zweiten Teil werden Messungen von Methan (CH_4) verwendet, die mit ATTILA über dem Amazonasgebiet im Rahmen der Kampagne "Chemistry of the Atmosphere Field Experiment" (CAFE Brazil) beobachtet wurden. Es wurden regionale Bodenemissionen durch Bayesian Inversion Modellierung abgeschätzt. Dafür werden hochauflösende Transportsimulationen aus dem STILT-Modell (Stochastic Time-Inverted Lagrangian Transport) verwendet, um die Einflussbereiche der Messungen räumlich zu identifizieren. Die Lösung des inversen Problems umfasst die Nutzung von Vorabinformationen zu CH_4-Emissionen, die aus WetCHARTs abgeleitet wurden – einem Bottom-up-Ansatz zur Schätzung von Emissionen aus

Feuchtgebieten. Anschließend werden räumliche Korrelationen implementiert, um die Abhängigkeit zwischen den gleichen, benachbarten Landbedeckungstypen sicherzustellen. Die Ergebnisse zeigen, dass die Messungen regionale Bodenemissionen erheblich verbessern, insbesondere in der Nähe von großen Flussbetten, Stauseen und großen Flussdeltas. Die Inversion zeigt zudem, dass in diesen Regionen CH_4-Emissionen bis zu einem Faktor von vier unterschätzt werden.

Der letzte Teil dieser Dissertation nutzt globale fluggetragende Messungen aus zwölf verschiedenen Flugzeugmissionen, um den Transport in der Troposphäre und chemische Prozesse zu untersuchen, die die Verteilung von Spurengasen beeinflussen. Kohlenmonoxid (CO) und Ozon (O_3) können in den Tropen photochemisch reduziert bzw. erzeugt werden, um dann über die Hadley Zellen in die Subtropen transportiert zu werden. Hier können starke Stratosphären-Troposphären-Vermischungen stratosphärische Luftmassen in die Troposphäre mischen und zu ähnlichen Mischungsverhältnissen von O_3 und CO führen, wie aus den Tropen kommend. Um zwischen diesen beiden verschiedenen Mechanismen zu unterscheiden, werden ein Vergleich und eine Sensitivitätsstudie mit dem globalen dreidimensionalen ECHAM5/MESSy Atmospheric Chemistry (EMAC)-Modell durchgeführt. Diese zeigen eine starke relative Verringerung des O_3 – CO-Verhältnisses im jährlichen Mittel in der oberen Troposphäre der Tropen und Subtropen, welche nur auf Blitzemissionen zurückzuführen sind.

Insgesamt zeigt diese Arbeit die entscheidende Rolle von In-situ-Beobachtungen von Flugzeugen für ein verbessertes Verständnis der Zusammensetzung der Atmosphäre, die Verbesserung von Emissionsinventaren und die Rolle von Transport und Chemie in der Troposphäre. Die Ergebnisse unterstreichen den Wert integrierter Mess-Modell-Ansätze, hilfreich für die Untersuchung regionaler bis globaler atmosphärischer Prozesse.

Contents

1 Motivation

In recent decades, the field of atmospheric trace and greenhouse gas detection has undergone significant development due to advances in measurement techniques, data acquisition, and atmospheric chemistry-coupled dynamical models. Despite this progress, several fundamental challenges remain unresolved, particularly in remote regions (e. g., the tropics), where data collection is limited. Remote-sensed data derived from satellites or surface stations are subject to the challenges posed by the dense lower atmosphere, where clouds often interfere in the visible, infrared to thermal-infrared range through reflection or absorption of sunlight or thermal cloud emissions. Therefore, those techniques often cannot look beneath or above a cloud, resulting in a loss of important information about vertical distribution, surface, or upper tropospheric emissions. Particularly in the tropics, where pronounced convection frequently occurs, data is limited, resulting in higher uncertainties in emission inventories and climate modeling.
This research is using airborne in situ measurements, which can provide detailed information, bridging the gap between surface and satellite observations. Combined with model and analytical approaches, this thesis investigates the intersection between emission sources, transport pathways in the troposphere and lower stratosphere, by considering atmospheric chemical interactions. Together, the results aim to better understand how these processes interact within the troposphere and what role they play in the distribution of trace- and greenhouse gases.

2 Introduction

2.1 The Earth's Atmosphere

The Earth's atmosphere is separated into several gaseous spheres surrounding the globe, distinguishable by their different physical properties and chemical composition. These individual layers are separated by regions of strong changes in the vertical temperature gradient, also referred to as "pauses", as illustrated in Figure 2.1 for a "standardized" atmosphere (Andrews, 2010).

The top of the atmosphere is defined by the exosphere, the outermost region at altitudes > 500 km, where gas molecules with sufficient energy may escape the Earth's gravitational field. In the exosphere, most satellites are positioned on an orbit around the Earth. Below the exosphere lays the thermosphere, separated by the thermopause (Abdu et al., 2011). In the thermosphere, short wavelength radiation gets absorbed by nitrogen (N_2) and oxygen (O_2) leading to high temperatures and rapid vertical mixing. The mesopause at approximately 90 km leads to the mesosphere, where temperature decreases with altitude, exceeding the coldest temperatures of our atmosphere at the mesopause (Andrews et al., 1987). Extending from the upper mesosphere through the thermosphere into the lower exosphere, the ionosphere comprises several layers defined by significant ion production driven primarily by solar ultraviolet and X-ray radiation (not shown in Fig. 2.1) (Abdu et al., 2011).
At approximately 50 km lies the stratopause, followed by the stratosphere which is the second lowest layer of the atmosphere. The stratosphere contains most of the atmospheric ozone (O_3), which protects life on Earth from harmful ultraviolet (UV) radiation (Andrews et al., 1987). Absorption of UV radiation by ozone leads to radiative heating, causing temperatures to increase with altitude within the stratosphere. The resulting stable stratification suppresses convective mixing and limits vertical transport, so gases are redistributed primarily by slow large-scale circulation and weak eddy diffusion, contributing to their relatively long residence times (Brewer, 1949; Dobson, 1956; Wallace and Hobbs, 2006).
The lowest layer of the atmosphere is the troposphere, where weather occurs. The tropopause separates the troposphere from the stratosphere and defines a local temperature minimum in the vertical profile (cold-point tropopause). A variety of

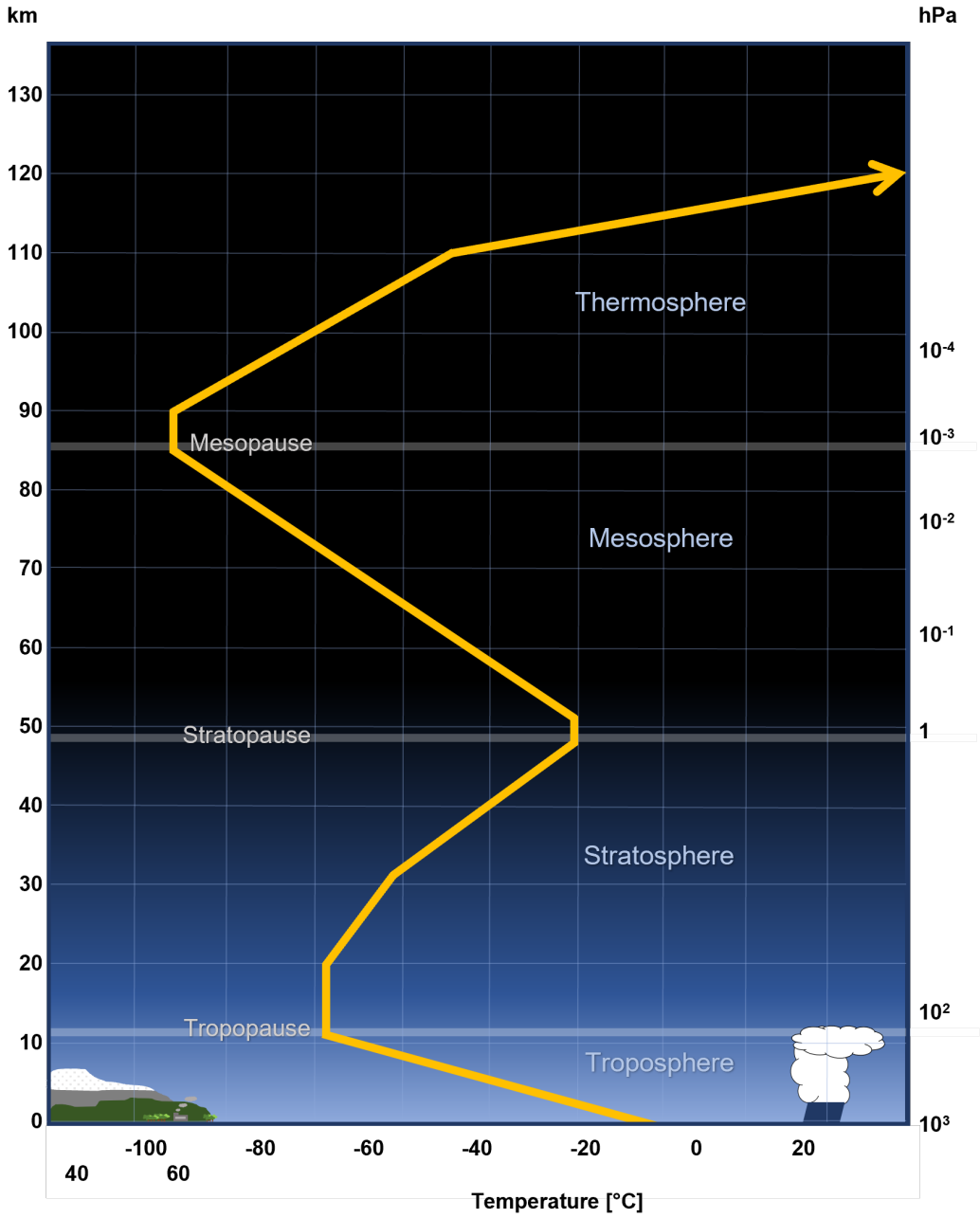

Figure 2.1: Average temperature profile for the lower layers of the atmosphere with the typical altitude scale on the left and pressure scale on the right side. This figure was self-constructed on the basis of Oceanic and Administration, 2024 and Seinfeld and Pandis, 2016.

different tropopause definitions exist, for example, the thermal (lapse-rate), dynamical (potential vorticity surface), or chemical (tracer gradients) tropopause. The thermal tropopause, or also known as lapse-rate tropopause, defines the lowest layer at which the temperature lapse-rate decreases to $2\,\mathrm{K\,km^{-1}}$, hence, defines static stability changing from a convective troposphere to a stable stratosphere (Holton et al., 1995). The dynamical tropopause is based on potential vorticity (PV). Potential vorticity is a dynamically conserved quantity that combines the effects of rotation and stratification, linking vorticity to the vertical stability of the atmosphere. The dynamical tropopause was often defined to be represented by a particular PV surface, ranging from 1.5 to 5 potential vorticity units ($1\,\mathrm{PVU} = 10^{-6}\,\mathrm{K\,m^2\,kg^{-1}\,s^{-1}}$) (Hoskins et al., 1985; Hoerling et al., 1991; Holton et al., 1995). More recent literature defines the dynamical tropopause over strong changing isentropic PV gradients (Kunz et al., 2011). However, the dynamical tropopause is particularly useful for studying large-scale circulation and stratosphere–troposphere exchange. Chemical tropopauses are defined by the fast changing chemical regimes between the troposphere and stratosphere, based on the strong increasing or decreasing gradients of ozone, water vapor, only tropospheric tracers, or their tracer-tracer correlations (e.g., Fischer et al., 2000; Prather et al., 2011; Bauchinger et al., 2025 and citations within). The tropopause is generally highest in the tropics, reaching altitudes from 15 – 17 km, and lowest in the polar latitudes (6 – 8 km) (Wallace and Hobbs, 2006; Seinfeld and Pandis, 2016). While the tropopause is a rather thin layer (~0.5 – 2 km) in the extra-tropics, it can expand to several kilometers (2 – 4 km) in the tropics, which is also referred to as the tropical tropopause layer (TTL, Fueglistaler et al., 2009). In contrast to the stratosphere, the troposphere is characterized by convective and baroclinic processes with active vertical motion driven by surface heating and instability. On average, the temperature decreases with increasing altitude, with an environmental lapse rate of approximately $6.5\,\mathrm{K\,km^{-1}}$ (Seinfeld and Pandis, 2016). Furthermore, most of the atmospheric mass is located in the troposphere (~80%), while this layer is only a small fraction of the total height of the atmosphere. In addition, the majority of atmospheric water resides in the troposphere. Here, the hydrological cycle describes the continuous exchange of water between the atmosphere, hydrosphere, cryosphere, and land surface, driven primarily by evaporation, condensation, and precipitation. Furthermore, many sources of gases and particles originate at the surface, emitted by the biosphere, hydrosphere, and/or human activities.

The troposphere - and to a lesser extent the stratosphere - contains most of the atmospheric mass and plays a key role in the Earth's radiative budget, air quality, and climate system. Understanding how emissions, transport processes, and

temperature-dependent chemistry interact to determine atmospheric composition is therefore essential for interpreting present-day observations and projecting future changes. This thesis addresses these questions by investigating emission sources, transport pathways, and chemical interactions in the lowermost atmosphere, including the troposphere and lower stratosphere.

2.2 Dynamics of the Lower Atmosphere

Atmospheric dynamics are defined by the motion and the thermodynamic state of the air, considering temperature, pressure and density (Shepherd, 2003). An schematic illustration of the fundamental dynamical processes of the troposphere and lower stratosphere, which are important for this thesis, are shown in Figure 2.2.

In a three-dimensional rotating reference frame, such as the atmosphere, the motion is governed by the Navier-Stokes equations:

$$\frac{D\mathbf{v}}{Dt} = \frac{\partial \mathbf{v}}{\partial t} + (\mathbf{v} \cdot \nabla)\mathbf{v} = -\frac{1}{\rho}\nabla p + \mathbf{g} - 2\Omega \times \mathbf{v} + \mathbf{F_R}, \tag{2.1}$$

where (x, y, z) are the horizontal and vertical coordinates, $\mathbf{v} = (u, v, w)$ the wind vector, ρ the air density, $\mathbf{p}$ is pressure, Ω the planetary rotation vector, and the gradient operator ∇ (Navier, 1838; Foias et al., 1983). The Navier-Stokes equations describe the material derivative of the wind vector $\mathbf{v}$, resulting from the combined effects of the pressure gradient force $-\frac{1}{\rho}\nabla\mathbf{p}$, gravitational acceleration $\mathbf{g}$, the Coriolis acceleration due to Earth's rotation $-2\Omega \times \mathbf{v}$, and frictional or other forcing terms $\mathbf{F_R}$.
On synoptic and planetary scales, several simplifying balances can be assumed. When vertical accelerations are negligibly small compared to gravity, the vertical momentum equation 2.1 reduces to hydrostatic balance, which describes the balance between the upward pressure gradient force and the downward force of gravity:

$$\frac{\partial p}{\partial z} = -\rho g. \tag{2.2}$$

This hydrostatic assumption is extremely accurate in the stratosphere, which is very stable, and stratified with very little vertical acceleration. Here, transport is mostly controlled by the Brewer-Dobson circulation (Brewer, 1949; Dobson, 1956), driving upwelling processes in the tropics and poleward transport in the upper

stratosphere on a much slower timescale of month to years compared to typical tropospheric transport timescales (days to months), illustrated by large arrows in Fig. 2.2.
Away from the equator, and above the planetary boundary layer (PBL), where surface friction is small, the Coriolis force balances the horizontal pressure gradient, leading to approximate geostrophic balance:

$$f\mathbf{k} \times \mathbf{v_H} \approx \frac{1}{\rho}\nabla_{\mathbf{H}} p, \tag{2.3}$$

with the Coriolis parameter f, and $\mathbf{v_H}$ defined as the geostrophic wind component, which flows horizontally parallel to isobars (surfaces of constant pressure) (e.g., Holton et al., 1995). The zonal wind (the west-east component of the total wind) is often the dominant component of the geostrophic wind, particularly in the upper atmosphere in the mid- and high-latitudes. Balanced large-scale flow, without heat exchanges with the surrounding air, organizes transport quasi-horizontally in pressure coordinates and adiabatically along isentropes (surfaces of constant potential temperature, gray dashed lines in Fig. 2.2). This is particularly relevant in the upper troposphere-lower stratosphere (UTLS), where strong static stability suppresses vertical motion in geometric height while allowing efficient lateral redistribution along sloping isentropic surfaces (e.g., Shepherd, 2003; Gettelman et al., 2011). Here, two chemically quite different regimes can be mixed through the tropopause. The lowermost stratosphere (LMS), positioned between the tropopause and the 380 K isentropic surface (dotted area in Figure 2.2), symbolizes the area where isentropic exchange and tropopause folding can occur, mixing stratospheric and tropospheric air masses (e.g., Murgatroyd et al., 1980; Lelieveld et al., 1997; Fischer et al., 2000; Hoor et al., 2002; Joppe et al., 2024).

In the tropics, strong diabatic heating within the inter tropical convergence zone (ITCZ) drives strong deep convection and sustained upward motion (Adam et al., 2016). The high moist static energy of near-surface air promotes vertical transport of heat, moisture, and tracers into the upper troposphere. Because the Coriolis parameter f approaches zero at the equator and changes sign across it, absolute vorticity and potential vorticity also change sign, dynamically separating the two hemispheres (Shepherd, 2003). This inhibits large-scale cross-equatorial geostrophic flow and makes the ITCZ a dynamical boundary between Northern and Southern Hemisphere circulations (Seinfeld and Pandis, 2016), unless inter-hemispherical transport is dynamically forced by, e.g., eddies and wave breaking (e.g., Prather et al., 1987; Belikov et al., 2022; Schuck et al., 2024).

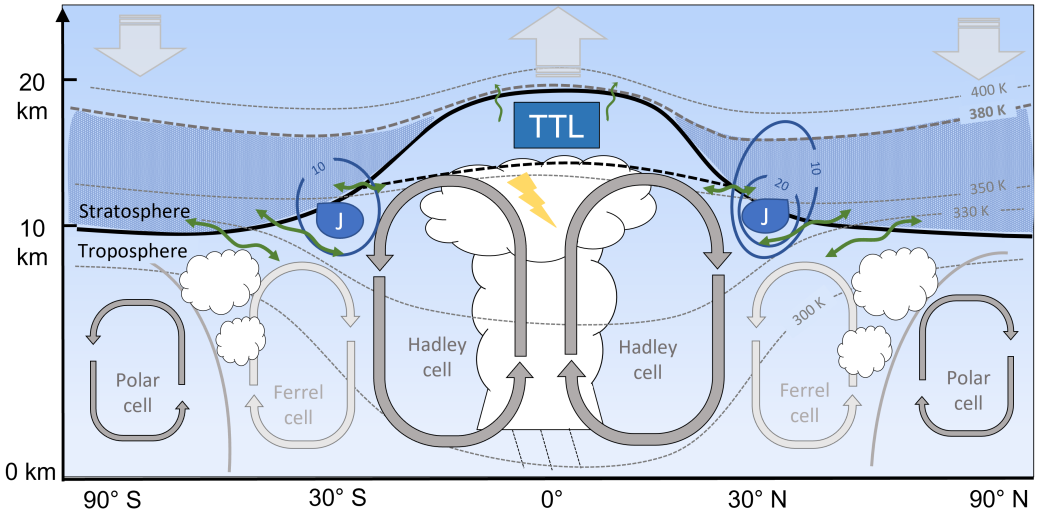

Figure 2.2: Schematic of the dynamics of the lower atmosphere in the zonal mean. Large circular arrows show the positions of the thermally direct Hadley and Polar cells in gray and the thermal indirect Ferrel cell in lighter gray. The Hadley cells connect the tropics with the subtropics, while the polar cells are situated roughly between the poles (cold air downward transport) and 60° latitude, here, supported by the frontal upward transport at the polar front (gray thick lines). The lower part of the Brewer-Dobson circulation is symbolized by large gray arrows above the tropical tropopause layer (TTL) and at the poles. Small green arrows show exchange of the air, either adiabatic (along isentopes, gray dashed lines), or induced dynamically through, e.g., Rossby waves, tropopause folds, or turbulence. The black solid line at ~10 km at the poles and ~18 km in the tropics represents the approximate tropopause height. Together with the isentopic surface at $\theta = 380$ K (thicker gray dashed line), they delimit the "lowermost stratosphere" (LMS, dotted area), which is connected to the troposphere along isentropic surfaces. J stands for jet stream, here only showing the positions of the subtropical jet streams, with strong zonal winds, symbolized as blue circular lines with typical values in m s^{-1} in a zonal mean during boreal winter (Shepherd, 2003). The clouds and the lightning sign symbolize the position of frequent (deep-) convection, either in association with the polar front at 60° latitude, or the ITCZ in the tropics, where most of the global lightning occurs (Schumann and Huntrieser, 2007). This figure was self-constructed for the needs of this study on the basis of Holton et al., 1995; Shepherd, 2003; Seinfeld and Pandis, 2016.

The persistent deep convection in the tropics further leads to a higher and colder tropopause compared to higher latitudes, forming the tropical tropopause layer

(TTL). The TTL acts like a transition region where tropospheric air enters the stratosphere (Holton et al., 1995; Fueglistaler et al., 2009). While deep convection is strongest in the tropics, convective uplift also occurs in the extra-tropics, typically associated with synoptic-scale baroclinic systems and frontal lifting, but also occurs in regions of high surface temperature and moisture. In the extra-tropics, some convective updrafts can penetrate the tropopause, generating overshoots that entrain stratospheric air and enhance vertical mixing (e.g., Frey et al., 2015).
On the large-scale, rising air in the tropics cools radiatively in the upper troposphere and subsides around 30° N and S, forming the thermally direct Hadley cells (Shepherd, 2003). Near the surface, the equatorward return flow is deflected by the Coriolis force, generating the easterly trade winds. At higher latitudes, cold and dense air descends over the poles and spreads warmer air equatorwards, giving rise to polar easterlies. Between these thermally direct circulations, a third, thermally indirect cell emerges in mid-latitudes: the Ferrel cell. Unlike the Hadley and polar cells, the Ferrel cell is not driven directly by contrast in diabatic heating but is maintained by synoptic-scale baroclinic eddies (Holton et al., 1995). These baroclinic waves develop along strong meridional temperature gradients, producing cyclones and frontal systems that transport warm, moist air poleward and cold air equatorward. Embedded within the prevailing westerly flow and propagating eastward along the jet streams, these weather systems collectively generate a net poleward heat transport which, in the zonal mean, manifests as the indirect Ferrel circulation.

The subtropics represent a dynamically sensitive transition region. Here, the poleward outflow of the Hadley circulation, angular momentum conservation, and strong meridional temperature gradients combine to form a strong wind band near the tropopause, also known as the subtropical jet streams at approximately 30° latitude (Holton et al., 1995; Stendel et al., 2021). In the vicinity of the jet streams, isentropic surfaces are strongly tilted and potential vorticity gradients are sharp, creating a dynamically distinct interface between tropospheric and stratospheric air masses. In the balanced limit, transport across this interface remains largely along isentropes.
However, atmospheric mixing and vertical exchange occur where hydrostatic and geostrophic balanced assumptions weaken. Ageostrophic accelerations become significant in regions of strong curvature, jet streams, frontal zones, and Rossby wave breaking (Holton et al., 1995; Postel and Hitchman, 2001; Domeisen and Plumb, 2012). Similarly, diabatic heating and turbulent processes violate the adiabatic constraint, allowing cross-isentropic motion. In such situations, isentropic surfaces can be distorted, folded, or irreversibly mixed, amplifying stratosphere-troposphere

exchange (STE, Holton et al., 1995).
Rossby waves emerge mostly from the tropospheric surface from orography, land-sea contrast (e.g., Held et al., 2002; Garfinkel et al., 2020), baroclinic instability (e.g., Hartmann, 1979; Boljka and Birner, 2020; Kunkel et al., 2019), or other non-linear wave-wave interactions (e.g., Domeisen and Plumb, 2012). When Rossby waves amplify and break, strong potential vorticity gradients can erode, leading to irreversible mixing across the tropopause (Krasauskas et al., 2020). Rossby wave breaking events, but also a zonal shift of the jet stream, can cause tropopause folds, mixing stratospheric air masses relatively fast into the troposphere (Danielsen, 1968; Holton et al., 1995; Postel and Hitchman, 2001; Hoor et al., 2002). Furthermore, Rossby waves are vital for connecting the lower and upper atmosphere, shaping the winter polar vortex behavior, and thereby influencing ozone distribution (Stendel et al., 2021). In the subtropics, where strong wind shear, enhanced static stability contrasts, and wave–mean flow interactions exist, Rossby waves are particularly frequent (Postel and Hitchman, 1999).

The stratosphere and troposphere can be clearly distinguished by their contrasting chemical compositions. Although the tropopause constitutes a strong dynamical barrier, transport and mixing processes between the troposphere and stratosphere can still occur. The frequency, and variability of dynamical processes, and the extent of air masses being mixed, however, remain uncertain, and are still investigated in current research (Prather et al., 2011; Škerlak et al., 2014; Müller et al., 2015; Jing and Banerjee, 2018; Schoeberl et al., 2022; Riese et al., 2025). Trace gas mixing ratios and correlations can be used to identify and quantify STE. Particularly the relation between ozone (O_3) and carbon monoxide (CO) mixing ratios provide useful information about mixing processes between the stratosphere and troposphere, as their gradients have opposite signs near the tropopause (Fischer et al., 2000; Joppe et al., 2024). However, model studies achieved better representation of observed O_3 by including tropospheric precursor emissions, hence, trace gases originating and producing O_3 within the troposphere, such as emissions of lightning strikes (Stevenson et al., 2013). In the upper tropical troposphere, lightning emissions are the major source of O_3 (Nussbaumer et al., 2023; Nussbaumer et al., 2024), which can be directly transported into the subtropics via the Hadley circulation, a region of strong STE. Particularly in a changing climate, increasing lightning emissions (Schumann and Huntrieser, 2007), and increasing STE (Hegglin and Shepherd, 2009), both lead to an increase in tropospheric O_3, merging, mostly, in the subtropics. Therefore, in Ort et al., 2025, we investigated the importance of each pathway, comparing the O_3 – CO ratio originating from STE with photochemical production

and loss processes originating from the tropical upper troposphere and transported into the subtropics via the Hadley circulation. This is present in Section 3.7.

2.3 Trace Gases of the Atmosphere

The Earth's atmosphere contains mostly nitrogen (N_2: 78%), oxygen (O_2: 21%), and argon (Ar: 1%). A small remaining fraction of less than 1% is accounted to trace gases (Singh, 1995). Even though they occur in very low abundances, expressed as ratios in mixture as one part of a trillion (ppt), a billion (ppb), or a million (ppm), they play a crucial role in the Earth's radiative balance and climate impact (Wallace and Hobbs, 2006; Seinfeld and Pandis, 2016). Particularly important are trace gases, which absorb infrared radiation from the Earth's surface and emit a portion back to the surface. These so-called greenhouse gases warm the lower atmosphere by absorbing outgoing long-wave radiation and thereby influence key atmospheric processes, including oxidation and photochemical reactions, ultimately affecting regional and global climate dynamics (e.g., Lashof and Ahuja, 1990). Water vapor (H_2O) is the most abundant greenhouse gas in the atmosphere and exerts a dominant influence on Earth's radiative balance (Wallace and Hobbs, 2006). However, its atmospheric concentration is largely controlled by temperature and the hydrological cycle, so it primarily acts as rapid climate feedback rather than as direct anthropogenic forcing (Jacob, 2001). Other greenhouse gases have risen drastically since pre-industrial times, substantially enhancing radiative forcing directly; carbon dioxide (CO_2) increased by ~50%, methane (CH_4) more than doubled (260%), and nitrous oxide (N_2O) increased by ~20% (Lan et al., 2025). Chlorofluorocarbons (CFCs), produced for long-living propellants in the industry, increased from near-zero atmospheric concentrations to significant levels, and were subsequently identified as major contributors to stratospheric ozone (O_3) depletion, endangering life on Earth (Crutzen and Ehhalt, 1977; Rowland, 1991). While this fast chemical depletion of stratospheric O_3 could be contained by a global agreement to restrict the production of the relevant compounds in 1987 (Montreal Protocol), other greenhouse gas emissions are continuing to increase. Therefore, it is crucial to understand their emission sources, global distribution, and chemical role in the atmosphere, to protect climate and life as we know it.

Trace gases can be grouped roughly into four categories, according to their chemical composition: 1) Sulfur-containing, 2) Nitrogen-containing, 3) Carbon-containing, 4) Halogen-containing (Seinfeld and Pandis, 2016). Those classifications are not exclusive, as combinations of those chemical compounds are possible as well. There

are also other compounds like, e. g., hydrogen peroxide (H_2O_2), H_2O, or hydroxyl radicals (OH), which are not included in those compound classes.
Strong emitting regions, where concentrations are elevated relative to typical ambient levels, can be natural or urban regions, depending on the trace gas. Direct pollutants, mostly in anthropogenic areas, such as sulfate-containing (sulfur, SO_2), nitrogen oxides (NO_x), and organic compounds, emitted by, e.g., coal and fuel combustion, are photochemically converted to secondary pollutants, such as O_3, or further oxidize, and aggregate to ultra-fine aerosol particles, both reducing air quality (Tiao et al., 1975). Hence, all trace gases play a crucial and complex role in chemical interactions, can be indirect sources and sinks of greenhouse gases, and are crucial for understanding our changing atmosphere.

2.3.1 Temporal and Spatial Scales

The complex dynamical and chemical regime of the atmosphere is highly variable in time and space. In Figure 2.3, an overview of temporal and spatial scales is illustrated, showing the ranges and lifetimes of atmospheric constituents and atmospheric transport and mixing. Every trace gas emitted into the atmosphere is eventually removed over time, stored in a reservoir system (atmosphere, sediment, ocean, living organism) (Rodhe, 1992), or converted to another species. This is part of the biogeochemical cycle that every element experiences (Seinfeld and Pandis, 2016). Depending on their "lifetime" in the atmosphere, compounds are divided into three main groups: 1) Short-lived species (seconds to minutes), 2) Moderately long lived species (hours to months), and 3) Long-lived species (> 1 year). Accordingly, their spatial distribution increases with increasing lifetime, allowing the gas to distribute to larger scales, when they live long enough. Therefore, long-lived species, usually appear homogeneously distributed throughout the troposphere, without having large gradients horizontally or vertically, except near strong source or sink regions. Hence, depending on their lifetimes, trace gases are well mixed within the boundary layer, hemisphere, or globally, following turbulent mixing and transport throughout the atmosphere. Dynamical processes are separated into microscale (1 – 100 m), local scale (~100 m –10 km, urban), mesoscale (~10 km – 1000 km, regional) and global scales (≥1000 km, synoptic) (Seinfeld and Pandis, 2016).

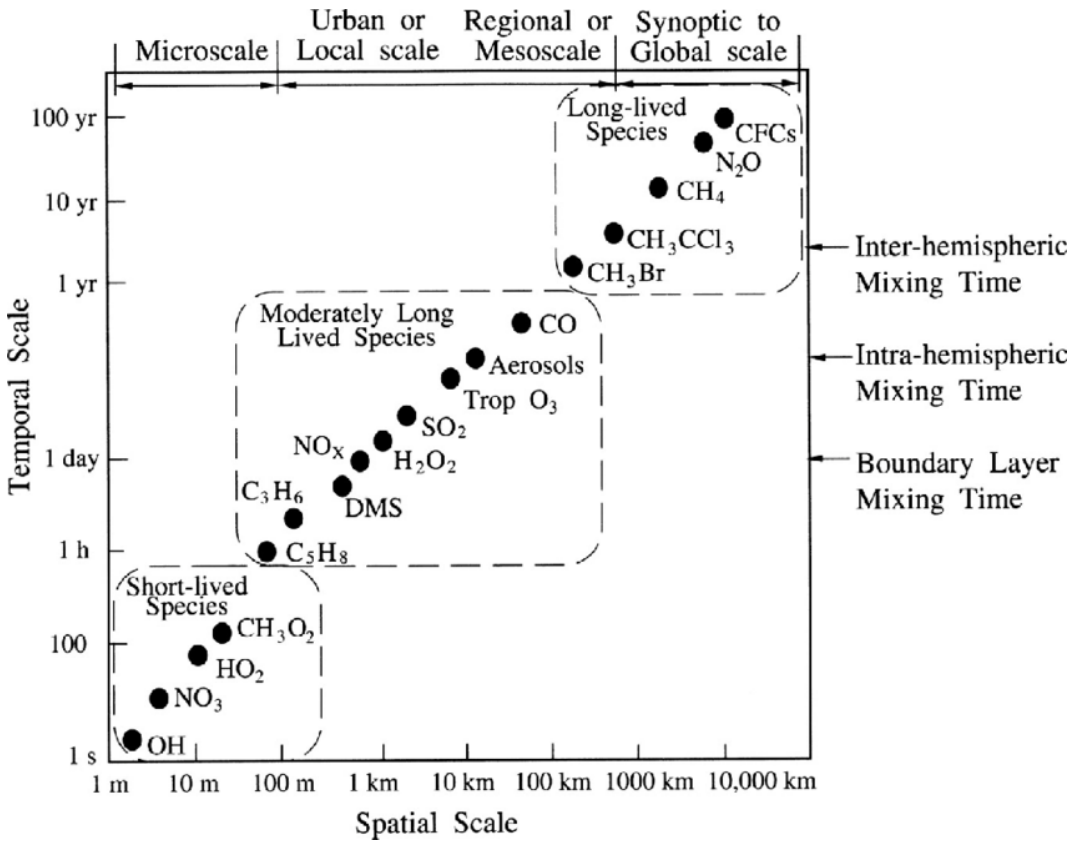

Figure 2.3: Spatial and temporal scales of atmospheric constituents, demonstrating variability in lifetimes and distribution. (Taken from Brasseur et al., 1999).

2.3.2 Important Trace Gases

In the following, a few trace gases are introduced in more detail, which are important for the results of this thesis (O_3, NO_x, OH, CH_4, CO). Their sources and sinks, global distribution, and most important chemical reactions are presented.

Ozone (O_3):

A key role of atmospheric chemistry plays the formation and removal of O_3. Ozone is besides H_2O, CO_2, and CH_4 one of the four most important greenhouse gases of the atmosphere, protecting and endangering life on Earth at the same time. Stratospheric O_3 absorbs highly energetic UV radiation emitted by the sun, which warms the stratosphere, and resulting in a stable layering of the atmosphere (Chapman, 1930; Caldwell et al., 1998). Tropospheric O_3 is a potent greenhouse gas and harmful

to human health, vegetational photosynthesis, and global warming due to radiative forcing (e. g., Lelieveld and Dorland, 1995; Staehelin et al., 2001; Norval et al., 2011; Ainsworth et al., 2012; Nuvolone et al., 2018). O_3 chemistry is highly important in both, the troposphere and stratosphere (Rowland, 1991; Tang et al., 1998; Staehelin et al., 2001).
Stratospheric O_3 is primarily produced in the tropical upper stratosphere through photolysis of molecular oxygen O_2:

$$O_2 + h\nu \longrightarrow O(^3P) + O(^3P), \tag{2.4}$$

followed by three-body recombination:

$$O_2 + O(^3P) + M \longrightarrow O_3 + M. \tag{2.5}$$

Here, short-wave solar UV radiation photodissociates an oxygen molecule into two highly reactive oxygen atoms $O(^3P)$, which quickly collide with O_2 molecules to form O_3 and in the presence of a third body (M), which is typically an inert molecule such as N_2 or O_2 that stabilizes the newly formed O_3 by carrying away excess energy. Ozone can also photolyze back to O_2 and O, completing the dynamic equilibrium of this so-called Chapman cycle (Johnston, 1975). About 90% of atmospheric O_3 is found in the stratosphere (Seinfeld and Pandis, 2016).
Tropospheric O_3 either originates from the stratosphere or is photochemically produced in the presence of nitrogen oxides (NO_x) and volatile organic compounds (VOCs) under sunlight, with peroxy radicals (RO_2, HO_2) enabling net ozone formation. In this process, photodissociation of nitrogen dioxide (NO_2) produces atomic oxygen, which then produces O_3 via Reaction 2.5. Net production of O_3 only occurs, because peroxy radicals, which are formed during the oxidation of CO and VOCs, convert NO to NO_2 without destroying O_3 (Seinfeld and Pandis, 2016).
Ozone is typically enhanced in urban polluted regions, where photochemical reactions lead to the formation of photochemical smog (first time measured in Los Angeles, Tiao et al., 1975). In the tropics, elevated O_3 can be produced through biomass burning events (Bourgeois et al., 2021). Average background levels are reported to be in the range of 10 ppbv in remote regions, up to 500 ppbv in polluted regions, strongly increasing up to 0.5 – 10 ppmv in the stratosphere (Fried and Richter, 2006).

Nitrogen oxides (NO_x):

Nitrogen oxides play an important role in atmospheric chemistry. They are usually designated as NO_x, which is the sum of nitric oxide (NO) and nitrogen dioxide (NO_2). NO is the primary oxide, which is emitted during high-temperature fossil fuel combustion, where an interaction of nitrogen in the fuel and atmospheric oxygen can take place, or when chemical conversion of atmospheric nitrogen and oxygen occurs during a burning process (e.g., of biomass) (Seinfeld and Pandis, 2016). Small amounts of NO_2 can also form during combustion, but the majority is created by oxidation of NO. Therefore, NO_x sources in the troposphere are from fossil-fuel combustion, biomass burning, aircraft emissions, lightning emissions, but can also be released from the soil, transported from the stratosphere into the troposphere, or be produced through oxidation of ammonia (NH_3) (Delmas et al., 1997). There are also several other oxides of nitrogen in the atmosphere, which are commonly referred to as reactive odd nitrogen, such as nitrate radicals (NO_3), nitric acid (HNO_3), or peroxyacetyl nitrate (PAN).
In the stratosphere, NO_x is primarily produced through the reaction of nitrous oxide (N_2O) with electronically excited oxygen $O(^1D)$, which is generated by ozone photolysis:

$$O_3 + h\nu \longrightarrow O_2 + O(^1D), \tag{2.6}$$

$$O(^1D) + N_2O \longrightarrow 2NO. \tag{2.7}$$

This reaction constitutes the dominant natural source of stratospheric NO_x, while most N_2O loss occurs via photolysis to N_2 and $O(^1D)$ (Wallace and Hobbs, 2006).
Once produced, NO_x plays an important role in tropospheric photochemistry. Nitric oxide rapidly reacts with O_3 to form NO_2 and O_2 via Reaction 2.8:

$$NO + O_3 \longrightarrow NO_2 + O_2. \tag{2.8}$$

Then, NO_2 can be photolyzed:

$$NO_2 + h\nu \xrightarrow{O_2} NO + O(^3P), \tag{2.9}$$

followed by ozone formation via Reaction 2.5 (Johnston, 1975; Seinfeld and Pandis, 2016). In a photostationary state, there is no net change in the NO and O_3 budget within this NO_x cycle. However, in polluted regions, i.e., in the presence of peroxy radicals, more NO_2 is produced (see Reaction 2.12), resulting in more O_3, as explained above.
Typical mixing ratios for NO and for NO_2 in the troposphere range from 0 –

1450 pptv, and from 0 – 3349 pptv, respectively (Fried and Richter, 2006), while peak values can reach mixing ratios of 10 – 1000 ppbv. In the upper troposphere, NO_x production by aircraft or lightning emissions can increase O_3 production, along with stratospheric entrained O_3 or NO_x resulting in O_3. In the study of Ort et al., 2025, presented in Section 3.7, we address the quantity of O_3 production from lightning in comparison to stratospheric O_3 mixed into the troposphere.

Hydroxyl radicals (OH):

Hydroxyl radicals are also known as the "cleanser" of the atmosphere. Once they are created in the atmosphere, they attack partially oxidized gases containing hydrogen (H), carbon (C), nitrogen (N), oxygen (O), and sulfur (S) (e.g., CO, CH_4), as well as halogens (except N_2O and CFCs), within one to two seconds. These gases are then converted into products that are more easily removed by wet or dry deposition (Lelieveld et al., 2004; Wallace and Hobbs, 2006). Even with their typical average mixing ratios in the troposphere of only a few tens of pptv, they are the major atmospheric sink for CH_4, and preferably reacting with CO (39%, Lelieveld et al., 2016), but also react with NO_x and other VOCs, such as isoprene (C_5H_8).
The interaction and sum of OH radicals and hydroperoxyl radicals (HO_2) is also known as HO_x cycle. It represents how an OH radical catalyzes the formation of O_3 from NO and a VOC (Seinfeld and Pandis, 2016).
Production of OH radicals is divided into primary and secondary production. Primary OH production dominates under conditions where UV radiation is present, as ozone photolysis generates electronically excited oxygen atoms $O(^1D)$, which subsequently react with H_2O to produce two OH radicals via Reactions 2.6 and 2.10:

$$O(^1D) + H_2O \rightarrow 2OH. \tag{2.10}$$

The reaction of $O(^1D)$ with CH_4 can also result in a OH radical, along with a methyl radical (CH_3) via Reaction 2.11 and represents an important source of OH in the stratosphere:

$$O(^1D) + CH_4 \rightarrow OH + CH_3. \tag{2.11}$$

Here, the methyl radical further reacts with O_2 to produce methylperoxy radicals (CH_3O_2), an important organic peroxy radical that is crucial for tropospheric O_3 production via the catalytic cycle of nitrogen oxides (Reactions 2.5, 2.9) (Seinfeld and Pandis, 2016).
Secondary production appears as a recycling mechanism, which can be catalyzed by NO_x, O_x, and OVOC (Lelieveld et al., 2016). Which mechanism dominates depends on the environmental conditions. While most OH recycling in forests occurs with

OVOC, the NO_x mechanism dominates in anthropogenically polluted environments or in the upper troposphere due to lightning emissions producing NO_x, following the Reaction 2.12:

$$NO + HO_2 \rightarrow NO_2 + OH. \tag{2.12}$$

The influence of lightning-induced NO_x emissions on OH recycling via depletion of CO is discussed in more detail in Ort et al., 2025 and Section 3.7.

Methane (CH_4):

Methane is the second most important anthropogenic greenhouse gas, after CO_2, due to its strong radiative forcing and relatively short lifetime of approximately 9 years (Shindell et al., 2012; Jackson et al., 2020; Pérez-Domínguez et al., 2021; Szopa et al., 2021; Uluocak, 2025). As shown in the global CH_4 mixing ratios in Figure 2.4, after a brief stabilization of global CH_4 mixing ratios in the early 2000s, a pronounced increasing trend continued since 2007, exceeding worst-case scenarios of climate model predictions in the early 2020s (Saunois et al., 2016; Saunois et al., 2020; Nisbet et al., 2019). Global mean surface mixing ratios of methane have nowadays exceeded values higher then 1946.47 ppb (October 2025, Lan et al., 2025). The strong increase of global CH_4 correlates with a decrease in the global methane carbon isotope ratio C^{13}/C^{14} ($\delta^{13}C$, Fig. 2.4, lower panel). Depending on its source, carbon isotopes differ, which provides insights of what may have changed since 2007. Anthropogenic sources include emissions from fossil fuel extraction and use (gas, oil, and coal), livestock, rice cultivation, wastewater, landfills, biomass and biofuel burning. Natural CH_4 emissions arise mainly from wetlands, geological seeps, termites, inland freshwater such as rivers and lakes, and thawing permafrost (i. e., Saunois et al., 2025; Hancock et al., 2025). A decrease of $\delta^{13}C$, can be caused by either a decrease of the atmospheric sink (oxidation by OH) or a change in relative proportions of sources, which would suggest an increase in biogenic emissions (by wetlands or cattle), or a combination of both (Nisbet et al., 2019; Peng et al., 2022).

The strongest atmospheric sink of CH_4, also mostly controlling its lifetime (Niwa et al., 2025), is through oxidation with OH radials, which dominates in both, the troposphere and stratosphere (Lelieveld et al., 2018). OH reacts with CH_4, forming methyl radicals (CH_3), which almost instantaneously reacts with O_2 to yield methyl peroxy radicals (CH_3O_2), thus can be formulated as:

$$CH_4 + OH \xrightarrow{O_2} CH_3O_2 + H_2O. \tag{2.13}$$

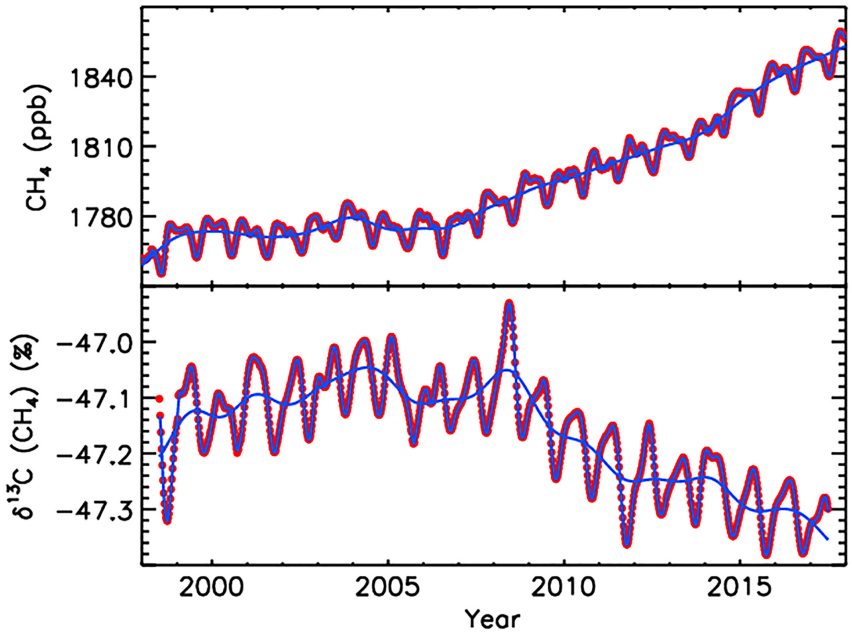

Figure 2.4: Atmospheric methane at Earth's surface in the remote marine troposphere. Upper panel shows globally averaged surface atmospheric CH_4 at weekly resolution (red and blue) and deseasonalized trend (blue), 2000–2017. Lower panel as above, but for globally averaged surface atmospheric $\delta^{13}C$ (CH_4). Data from NOAA (Lan et al., 2025). Figure taken from Nisbet et al., 2019.

Methane oxidation feeds into the coupled HO_x and NO_x cycles by producing peroxy radicals, thereby promoting net tropospheric ozone formation in the presence of NO_x (Reactions 2.5, 2.9) (Lelieveld et al., 2016). Furthermore, methane oxidation by OH produces formaldehyde and subsequently CO before its eventual conversion to CO_2. This indirect CH_4–CO coupling strongly influences the atmospheric oxidative capacity by modulating OH mixing ratios (Seinfeld and Pandis, 2016). Other atmospheric loss processes include reactions with chlorine atoms (Cl), or $O(^1D)$ (Reaction 2.11). CH_4 can also be taken up by the soil, which is a relatively small fraction of atmospheric CH_4 loss, but also highly uncertain regarding the environmental conditions, such as moisture, soil texture, temperature, and nitrogen content (Murguia-Flores et al., 2018). Soil uptake is the only known biological sink of atmospheric CH_4 where microbes in the soil, the so-called methanotrophs, consume CH_4 and oxidize it to methanol (aerobic methanotrophy), or use it as an energy source, coupling it with electron acceptors such as nitrogen or sulfate (anaerobic methanotrophy), depending on if oxygen is available, respectively. This sink is therefore strongly coupled with main sources of CH_4, such as rice paddies, wetlands, and flooded forests (Conrad, 1989), and is not yet well understood in every ecosystem (Saunois et al., 2025). The study of Ort et al., 2026a, presented in Section 3.5, addresses this research gap in a flux analysis investigating CH_4 emissions in the Amazon, a tropical ecosystem containing large areas of wetlands and flooded forests.

Anthropogenic emissions contribute approximately 60% to the global CH_4 budget, while the remaining 40% originate from natural sources. However, natural sources can be influenced indirectly, to some extent, also by anthropogenic activities such as climate change feedbacks or land-use change (Zhang et al., 2017; Franco et al., 2025). The global mean budget of methane emissions for the 2010–2019 decade is reported by Saunois et al., 2025, who combined several studies achieving mean total methane emissions of 575 Tg yr^{-1} (553-586) and 669 Tg yr^{-1} (512-849) from top-down and bottom-up approaches, respectively. Here, the uncertainty is given by the minimum and maximum mean total emissions of those studies, shown in the brackets. Top-down estimates infer emissions from atmospheric observations using inverse modeling, while bottom-up estimates calculate emissions from activity data and emission factors based on known sources. However, those two approaches have improved over the last decades in narrowing the gap between their methane emission estimates (Saunois et al., 2016; Saunois et al., 2020; Saunois et al., 2024; Saunois et al., 2025). Nevertheless, large differences remain, not only between bottom-up and top-down approaches, but also throughout different studies, not even considering uncertainties of the individual estimates.
In Table 2.1 the contribution to the total methane budget from different sources

Table 2.1: Bottom-up and top-down global methane emissions in the 2010–2019 decade. Estimates are averaged over several studies, and given in Tg CH_4 yr^{-1}, with uncertainties (in brackets) representing the minimum and maximum mean emission estimates over all studies. These numbers are adapted from Saunois et al., 2025, Figure 7.

Fluxes	Source	Bottom-up	Top-down
Anthropogenic	Fossil fuel production and use	120 (117-125)	115 (100-124)
	Agriculture and waste	211 (195-231)	228 (213-242)
	Biomass and biofuel burning	28 (21-39)	27 (26-27)
Natural and indirect anthropogenic	combined wetland and inland freshwaters	248 (159-369)	165 (145-214)
Natural	other natural emissions (permafrost, termites, etc.)	63 (24-93)	43 (40-46)
	Sink		
	atmospheric (mainly OH, Cl)	602 (496-747)	521 (485-532)
	soil absorption	31 (11-49)	35 (35-36)

and sinks are listed. Global emission inventories of CH_4 are lacking the capability of reproducing the strong increasing trend of global CH_4 concentrations (Saunois et al., 2020; Saunois et al., 2024; Saunois et al., 2025). While anthropogenic emissions from bottom-up and top-down estimates differ within the uncertainties, as shown in Table 2.1, large discrepancies remain between bottom-up and top-down emission totals for the natural and indirect anthropogenic emissions with 248 Tg CH_4 yr^{-1} and 165 Tg CH_4 yr^{-1}, respectively. Largest uncertainties remain in combined wetland and inland freshwater emissions and atmospheric sinks.

The global distribution of atmospheric CH_4 mixing ratios is determined by its atmospheric lifetime and location of its major source regions. As a result, CH_4 is relatively homogeneously distributed throughout each hemisphere, particularly in absence of major sources such as over oceans. Within the troposphere, higher CH_4 mixing ratios are observed in the northern hemisphere than in the southern hemisphere due to the greater land-to-ocean ratio and the predominance of anthropogenic emissions in the north. In the tropics, where extensive wetlands and seasonally strong biomass burning occur, CH_4 is elevated near the surface (Basso et al., 2021; Shaw et al., 2022; Niwa et al., 2025; Hancock et al., 2025; Balasus et al.,

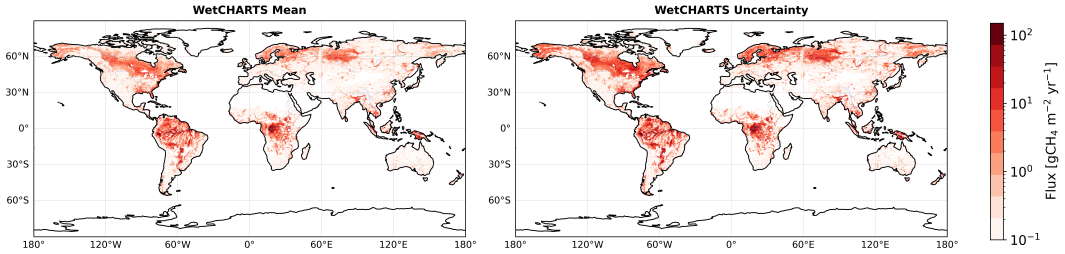

Figure 2.5: Global bottom-up estimates of wetland methane emissions by WetCHARTs (Bloom et al., 2017; Zhu et al., 2025). Displayed are the annual mean (left panel) and uncertainty (right panel), derived from averages over 18 ensemble simulations, with added noise, as described in Zhu et al., 2025. WetCHARTs uses empirical biogeochemical modeling with remote sensed inundation, model-driven relative humidity fluxes and a temperature sensitivity factor to achieve CH_4 fluxes from not only wetlands, but also other freshwater surfaces, such as reservoirs, seeps, rivers, and lakes.

2026). In the stratosphere, the lack of sources and the dominance of chemical sinks lead to lower CH_4 mixing ratios than in the troposphere.
Wetlands are the largest natural CH_4 source in the atmosphere and are mainly located in the tropics (Jackson et al., 2020). However, they are also the most uncertain (Dean et al., 2018; Zhu et al., 2025), and highly variable spatially and temporally (Nisbet et al., 2019; Saunois et al., 2020). Figure 2.5 shows a map of annually averaged global wetland methane emissions (2002–2020) estimated from a bottom-up approach using empirical data from satellites, including, among others, surface humidity, temperature factors and land-cover types. Several ensemble simulations were simulated to achieve the mean (left plot) and the standard deviation (right plot) of this bottom-up estimate named WetCHARTs (Bloom et al., 2017; Zhu et al., 2025). Methane emissions are strongest in the tropics, mainly in the Amazon and Congo. Emission uncertainties are in the same order of magnitude then the mean emissions, exceeding over 100%, especially where emissions are large (see Figure 2.5). This motivates the need to better understand emissions from wetlands in source regions. The study of Ort et al., 2026a, presented in Section 3.4, investigates regional emissions of methane over the Amazon by using airborne CH_4 observations to evaluate WetCHARTs bottom-up estimates.

Carbon Monoxide (CO):

Carbon monoxide is mainly produced by combustion, such as biomass burning or industrial emissions at surface-level (Crutzen and Andreae, 1990). Atmospheric in-situ production of CO also occurs during the oxidation of CH_4 to CO_2. Oxidation

is initiated by reaction with OH, forming a methyl radical (CH_3) that rapidly reacts with O_2 to produce the methyl peroxy radical (CH_3O_2, Reaction 2.13). In the presence of NO_x, CH_3O_2 is converted to formaldehyde (HCHO), a key intermediate toward CO formation:

$$CH_3O_2 + NO \rightarrow CH_3O + NO_2, \tag{2.14}$$

$$CH_3O + O_2 \rightarrow HCHO + HO_2. \tag{2.15}$$

Then, HCHO is subsequently oxidized or photolyzed, producing CO (Wallace and Hobbs, 2006; Strode et al., 2018).

Its atmospheric lifetime ranges between 1 to 3 months and is mostly controlled by its major sink, i.e., the oxidation by OH radicals (Pressman and Warneck, 1970; Lelieveld et al., 2016):

$$CO + OH \rightarrow H + CO_2. \tag{2.16}$$

Hence, in the tropical upper troposphere, where secondary recycling of OH via lightning-induced NO_x appears (Reaction 2.12), CO lifetimes are typically shorter, while at the poles, CO lifetimes are longer. The shortening of the lifetime of CO through the OH sink in the tropics is demonstrated and discussed in more detail in the study of Ort et al., 2025, see Section 3.7. Due to its lifetime, CO has a dominant seasonal cycle, depending on biomass burning events in the tropical dry season, and the low sink through low mixing ratios of OH during winter in extra-tropical regions (e.g., Seiler, 1974; Lelieveld et al., 2016).
Typical CO background mixing ratios vary from 80 – 150 ppbv in the northern and 40 – 90 ppbv in the southern troposphere and usually decrease with increasing altitude in the troposphere, when strong vertical uptake is not present Herman et al., 1999; Froidevaux et al., 2025. Inside pollution plumes, CO can reach mixing ratios of more than 1000 ppbv (Fried and Richter, 2006).

2.4 In-Situ Measurement Techniques of Trace Gases in the Atmosphere

In-situ measurements of trace gases provide essential constraints on atmospheric composition, chemical processes, and surface-atmosphere interaction processes. Compared to remote sensing platforms, which are able to retrieve global column-

averaged information (Clerbaux et al., 2003), in-situ instruments can sample air directly with much higher temporal and spatial resolution. Those measurements are able to detect micro- to continental-scale processes with high accuracy and precision (Heard, 2006). Therefore, in-situ instruments play a central role in validating satellite retrievals, evaluating atmospheric transport and chemistry models, and supporting inverse modeling approaches aimed to estimate surface emissions (Andreae et al., 2012; Turner et al., 2020; Niwa et al., 2025).

In-situ trace gas observations are conducted across a range of measurement platforms, each addressing different spatial and temporal scales. Ground-based stations provide long-term, highly precise measurements that are crucial for trend detection and baseline monitoring, but are limited in their spatial representativeness.
Aircraft-based measurements bridge this gap by enabling regional to continental-scale observations with high spatial resolution, including vertical profiling of the troposphere and lower stratosphere, targeted sampling of emission plumes, or following aged air-masses (e.g., Müller et al., 2015; Müller et al., 2016b; Müller et al., 2016a; Thompson et al., 2022; Riese et al., 2025; Ray et al., 2024). Airborne observations are particularly valuable in regions with low data coverage, such as the tropics. Here, only few ground stations exist, and remote sensing deployed on satellites is facing the difficulty to penetrate the persistent deep cloud cover within the ITCZ, and hence are often combined and averaged over longer time periods to achieve spatial data coverage (Reiche et al., 2016; Turner et al., 2018). Aircraft measurements can provide valuable data from the surface to the lower stratosphere, and from the poles to the tropics. However, this goes hand in hand with demanding environmental conditions for the measuring devices. Airborne instrumentation must overcome extreme challenges on a moving platform, including additional limitations of size, weight, and user friendly operation (Röder et al., 2024; D'Amato et al., 2025). Therefore, continuous improvements and characterizations of instruments on aerial platforms are crucial to continue providing that valuable in-situ data. In the study of Ort et al., 2024, presented in Section 3.2, a newly build airborne instrument is described and characterized, able to provide such high precision data of, e.g., CO and CH_4.
Additional platforms, including ships, balloons, vehicles, drones, or other moving platforms, complement the observational network by extending coverage to marine, remote, or other inaccessible environments, but are not in focus of this work (Heard, 2006).

2.4.1 Measurement principles for CO, O_3, and CH_4

In this work, the focus lies on in-situ measurement techniques, able to observe CO, O_3, and CH_4 in the atmosphere, as those species are central to this work. Particularly, the focus lies on infrared absorption spectroscopy, key to the airborne instrument characterization presented in Section 3.2, and used to capture atmospheric CH_4 and CO, which is analyzed in Section 3.5, and Section 3.7.

There are various techniques to measure trace gases in situ. To detect such small compounds in the air, their physical and chemical properties are used, including their optical, chemical, photochemical, and electrochemical properties. The choice of measurement principle depends on the required precision, temporal resolution, robustness, and suitability for different platforms such as ground stations, aircraft, or mobile laboratories (Heard, 2006). For CO, CH_4, and O_3, several well-established techniques are widely used in atmospheric research, but we will focus here on optical measurement techniques. The most important measurement techniques generally used for CH_4, CO, and O_3, are briefly summarized in Table 2.2.

One feature most of the optical in-situ measurement techniques have in common, is the ability for atmospheric molecules to absorb electromagnetic radiation at discrete, molecule-specific wavelength, mostly spanning from the infrared (IR) to visible, and ultraviolet (UV) electromagnetic spectrum. This optical absorption spectroscopy allows quantitative determination of gas mixing ratios when absorption cross-sections and path lengths are known. This follows the Beer-Lambert law (Swinehart, 1962; Mayerhöfer et al., 2020), which relates molecular parameters with measured light intensities:

$$I(v) = I_0(v) \cdot exp[-NS(v)l] = I_0(v) \cdot exp[-A(v)]. \tag{2.17}$$

Here, N represents the total number density of the molecules within the sampling volume, l the optical path length, and $S(v)$ the spectral line intensity of the absorbing molecule at wavenumber v. The exponent can also be combined to $A(v)$, which describes the optical depth, also known as optical density, optical mass, or more commonly referred to the "absorbance" of the molecule at wavenumber v (Fried and Richter, 2006).
In Figure 2.6, a low-resolution display of vibrational-rotational lines of six selected atmospheric trace gases from wavenumber 400 to 4000 cm^{-1} are shown, taken from the HITRAN database (Gordon et al., 2022).

Table 2.2: Common in-situ measurement techniques for CO, CH_4, and O_3 on airborne platforms.

Species	Technique	Key advantages	Main limitations	Key References
CO, CH_4	TDLAS / QCLAS (IR absorption)	High sensitivity and selectivity; fast time response	Sensitive to optical alignment and pressure/temperature variations; requires calibration	Fried and Richter (2006)
CO	NDIR absorption	Robust and simple; long-term stability	Lower selectivity; potential cross-sensitivity to other IR-active gases	Jha (2022)
CH_4	CRDS / OA-ICOS / CEAS (cavity-enhanced IR absorption)	Very high precision and stability; low drift	Larger optical complexity; sensitivity to contamination and cavity losses	Plane and Saiz-Lopez (2006)
CH_4	FTIR absorption	Simultaneous multi-species detection	Lower temporal resolution; larger instrument size and complexity	Bacsik et al. (2004)
O_3	UV absorption spectroscopy	Highly selective; robust and well established; minimal interference	Limited to ozone only; requires UV optics and stable lamp source	Plane and Saiz-Lopez (2006)
O_3	Chemiluminescence	Very fast time response	Requires reagent gases; higher operational complexity	Weinheimer (2006)

Typical wavenumbers to measure CO are at 2000 – 2300 cm^{-1}. For CH_4, two strong spectral windows are commonly used in absorption spectroscopy: 1200 – 1400 and 2900 – 3200 cm^{-1}. Even though O_3 shows absorption at around 1000 cm^{-1}, it is most commonly measured in the ultraviolet (UV) spectral range at wavelengths near 254 nm (~ 40 cm^{-1}). Alternative methods for O_3 include chemiluminescence techniques, where ozone reacts with a suitable reagent, such as NO (Reaction 2.8), to emit light proportional to its mixing ratio. While highly sensitive, these systems are more complex and less common in routine atmospheric monitoring compared to UV absorption instruments (Silveira Petruci et al., 2022).

Optical spectroscopy uses different light sources, which depict certain spectral windows, where absorption lines are strong enough for detection and atmospheric interference (by e.g., H_2O, CO_2) is manageable (Tittel et al., 2003). While some measurement techniques use natural light sources such as the sun, moon, stars, or the Earth itself to capture trace gas absorption, others employ artificial light sources instead, for instance lasers or lamps. The optical path length depends on the guidance of the light source, which either traverses in a well-defined optical path through the atmosphere of usually several kilometers or is reflected or scattered within multi-pass cells (typically by the type of White (White, 1957) or Herriott (Herriott and Schulte, 1965; McManus et al., 1995) for absorption spectroscopy), or in between mirrors to produce measurable absorption. The differences in the choice of the light source, spectral resolution, and guidance of the light are key for the various optical applications existing (Fried and Richter, 2006). While Tunable Diode Laser Absorption Spectroscopy (TDLAS, e.g., Wienhold et al., 1998; Holloway et al., 2000; Fried et al., 2008) uses narrow-band laser to scan dedicated gases through multi-pass cells, Fourier Transform Infrared (FTIR, e.g., Bacsik et al., 2004; Ortega et al., 2025) spectrometer can detect multiple gases over broadband mid-IR absorption using the optical interference of one fixed and one moving mirror.

Quantum cascade lasers have further improved absorption spectroscopy in the mid-IR (QCLAS), providing higher optical output powers and room-temperature operation, making them indispensable for airborne platforms (Faist et al., 1994; Pal and Pradhan, 2021; D'Amato et al., 2025). Non-dispersive infrared gas sensing (NDIR) measures the attenuation of broadband infrared radiation at characteristic absorption bands using optical filters (Jha, 2022). Differential Optical Absorption Spectrometer (DOAS, e.g., Plane and Saiz-Lopez, 2006; Heue et al., 2008) have a variety of technical setups. They mostly use broadband light sources, either extra-terrestrial or artificial, which traverse the atmosphere or are scattered within multi-pass cells. DOAS techniques use differential absorption, also based on the

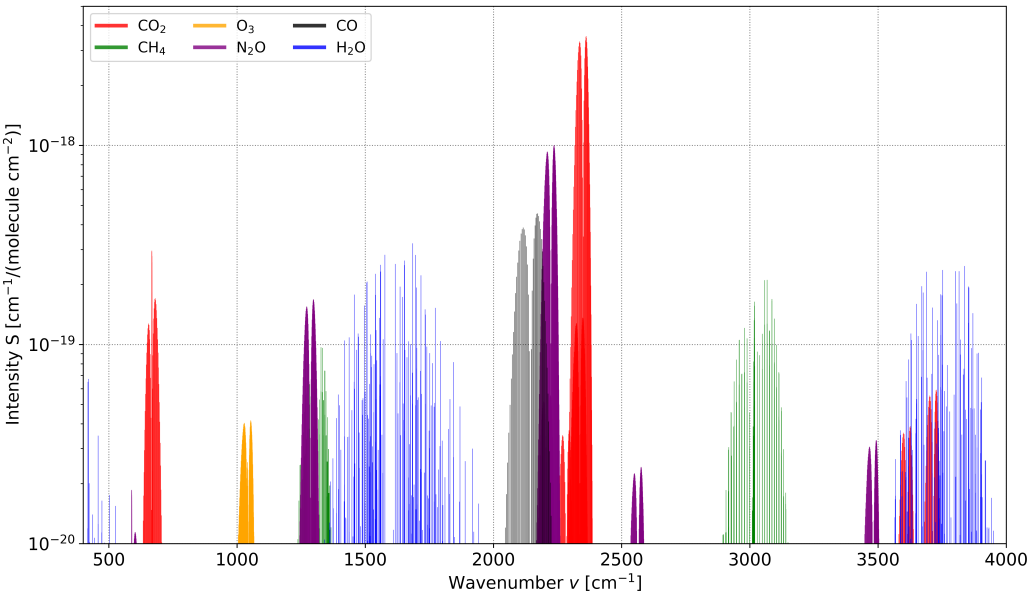

Figure 2.6: Line spectrum of selected strong absorber in the IR range (CO_2: red, CO: black, CH_4: green, N_2O: purple, O_3: orange). Data for the absorption lines are taken from the HITRAN database (Gordon et al., 2022). Line intensities are shown for temperatures of 296 K, intensities higher than 10^{-20} $cm^{-1}/(molecules\,cm^{-2})$, and wavenumbers υ between 400 and 4000 cm^{-1}, which spans wavelengths λ from 2.5 μm to 25 μm.

Beer-Lambert law (Eq.: 2.17), but include extinction, which next to absorption considers Rayleigh and Mie scattering. DOAS techniques are also used in cavity ring-down spectroscopy (CRDS), cavity-enhanced absorption spectroscopy (CEAS), or off-axis integrated cavity output spectroscopy (OA-ICOS), all also common to measure CH_4 (Berden et al., 2000; Berden and Engeln, 2009; Rella et al., 2015). Mass spectroscopy uses ionization to separate gas molecules prior to their light absorption, achieving a whole spectrum of different compounds, applicable to all elements (Williams, 2006).

Each optical in-situ technique has its advantages and disadvantages. Quantum cascade laser absorption spectrometers are widely used for airborne in-situ trace gas measurements (e.g., CO and CH_4) because they provide high sensitivity and fast response in the mid-infrared, where these species have strong absorption features (see Fig. 2.6). The two QCLAS used in this study provide measurements of 1 Hz resolution, which is ideal for resolving small-scale turbulence, plumes, and vertical gradients. Furthermore, they provide the opportunity for a compact optical path (e.g., multi-pass cells), particularly relevant for airborne measurements, which often demand weight and size limitations.
However, their operation requires careful control of pressure, temperature, and calibration, along with accurate line parameters and humidity corrections (Fried and Richter, 2006; Röder et al., 2024; D'Amato et al., 2025). Therefore, it is crucial to carefully characterize QCLAS, best on the platform where they will be used for in-situ observations. This thesis quantifies the performance of a newly build QCLAS on a basis of a dedicated test-flight (Sec. 3.2), understanding its limitations and possible correction methods for, i.e., temperature, pressure, humidity, before using its in-situ observations for atmospheric analysis (Sec. 3.4). This particular QCLAS stands out with its small and simple design, low power demand, multi-species capability (simultaneously), and sufficient pressure control throughout the lower atmosphere able to reach altitudes with ambient pressure past ~100 hPa.

2.5 Thesis Structure and Research Perspective

Understanding the complex interactions between emissions, atmospheric transport and chemistry is fundamental for constraining the distribution and development of trace gases in the atmosphere. Those interactions determine the spatial and temporal variability of climate-relevant species, crucial for climate and mankind future. However, disentangling their relative contributions remains challenging due to nonlinear chemical processes, variable meteorological conditions, and un-

certainties in observations and emission inventories.

Airborne observations offer a unique perspective to bridge this gap by directly sampling the atmosphere across vertical and horizontal gradients, thereby capturing both local emission signals and large-scale transport patterns. When combined with advanced modeling tools such as transport and chemistry coupled models, inverse methods, and Lagrangian particle dispersion models, these measurements enable a quantitative assessment of emission strengths, transport pathways, and the importance of chemical processes in shaping the atmosphere.

This thesis investigates the role of surface emissions, atmospheric transport and photochemistry on observed trace gas variability in the troposphere, with particular emphases on airborne measurements. In Figure 2.7, a schematic overview of the

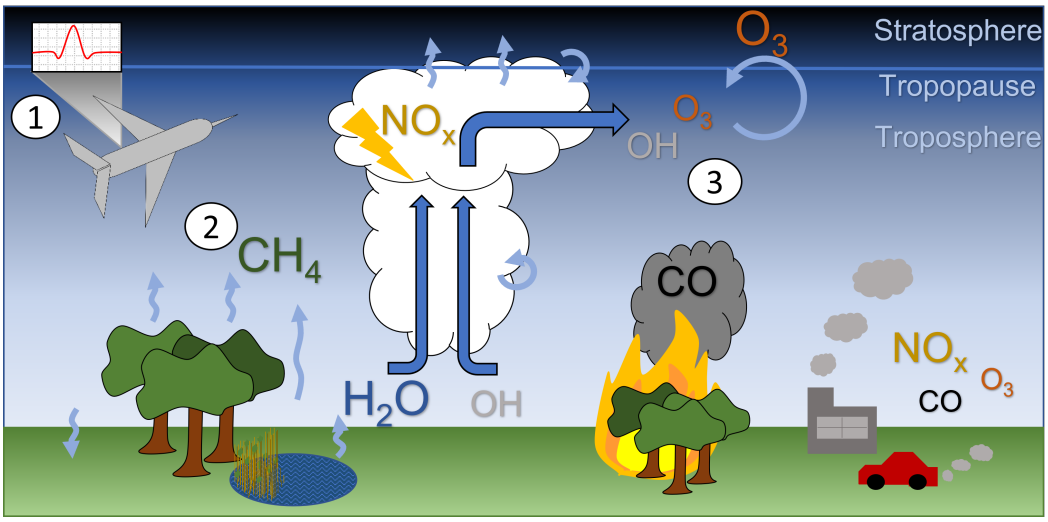

Figure 2.7: Thesis overview figure, combining schematically the studies of airborne in-situ observations (1), regional flux estimates (2), and of the role of transport and chemistry within the troposphere (3). This figure was self-constructed.

lower atmosphere is illustrated, combining the three interconnected studies of this thesis. This work builds from instrument-level performance (1) to regional interpretation of emissions (2) and global-scale trace gas transport along with chemistry (3). By combining in-situ observations with atmospheric chemistry and transport modeling tools, this thesis aims to improve the representation of trace gas sources and sinks and to assess their sensitivity to dynamical and chemical processes.

The thesis started with an introduction into the topic, followed by the three interconnected studies:

1. **Airborne Instrument Characterization**
   The first study characterizes a newly developed quantum cascade laser absorption spectrometer, which is used to measure trace gases in the infrared range deployed on a research airplane. This includes the detailed description of the instrumental setup, and further investigates its performance under variable environmental conditions during in-flight operation. These results establish the quality and limitations of the observational data used throughout the thesis, and they provide the uncertainty framework required for subsequent inversion analyses, presented in the second study.

2. **Regional Flux Estimation**
   In the second study, methane emission estimates are derived from using airborne observations, back-trajectory based footprints, and Bayesian inversion, combining in-situ concentrations, prior information from bottom-up emission inventories with surface fluxes. This analysis quantifies regional fluxes of the Amazon basin, and examines the contributions of major source categories of wetland classifications. This part demonstrates how airborne measurements can reduce uncertainties in regional methane budgets, and highlights the importance of atmospheric observations to evaluate and improve emission inventories.

3. **The Role of Transport and Chemistry**
   The third study investigates how atmospheric dynamics and chemical processes shape trace gas distributions observed during several combined airborne data sets on a global-scale, with a focus on the ozone-to-carbon-monoxide-ratio. Using a transport and chemistry model, the study quantifies the role of lightning emissions on trace gases transported via deep convection, and large-scale dynamical patterns within the troposphere in relation to mixing processes with the stratosphere. By using a sensitivity study excluding lightning emissions, the analysis identifies regimes where chemical production and loss processes contribute significantly to the trace gas composition of the troposphere, which needs to be taken into account for future studies.

Together, these three studies create a coherent framework: robust instrument characterization enables reliable observational constraints; an inverse analysis of airborne observations provide improved regional flux estimates; and convective transport of surface emissions enables important chemical interactions conditioning the troposphere. This thesis concludes with a discussion of remaining uncertainties and outlines the implications for future work on integrating high-resolution airborne data with chemical transport and inverse modeling frameworks to improve our understanding of source–sink dynamics and their feedback's under a changing climate.

3 Results

Part I

Airborne Instrument Characterization

3.1 The CAFE Brazil campaign

The Chemistry of the Atmosphere Field Experiment in Brazil (CAFE Brazil) is an airborne measurement campaign conducted in December 2022 to January 2023 in Manaus, Brazil. On board of the High-Altitude LOng range (HALO) research aircraft, run by the German Aerospace Center (DLR, Obepfaffenhofen), a large number of instruments were deployed, measuring various trace gases, aerosol particles and greenhouse gases. In the scope of the campaign, two test flights, four transfer flights from Germany to Brazil and 16 local research flights were conducted, covering an altitude range from the surface up to 14.5 km. The flight tracks are shown in Figure 3.1.

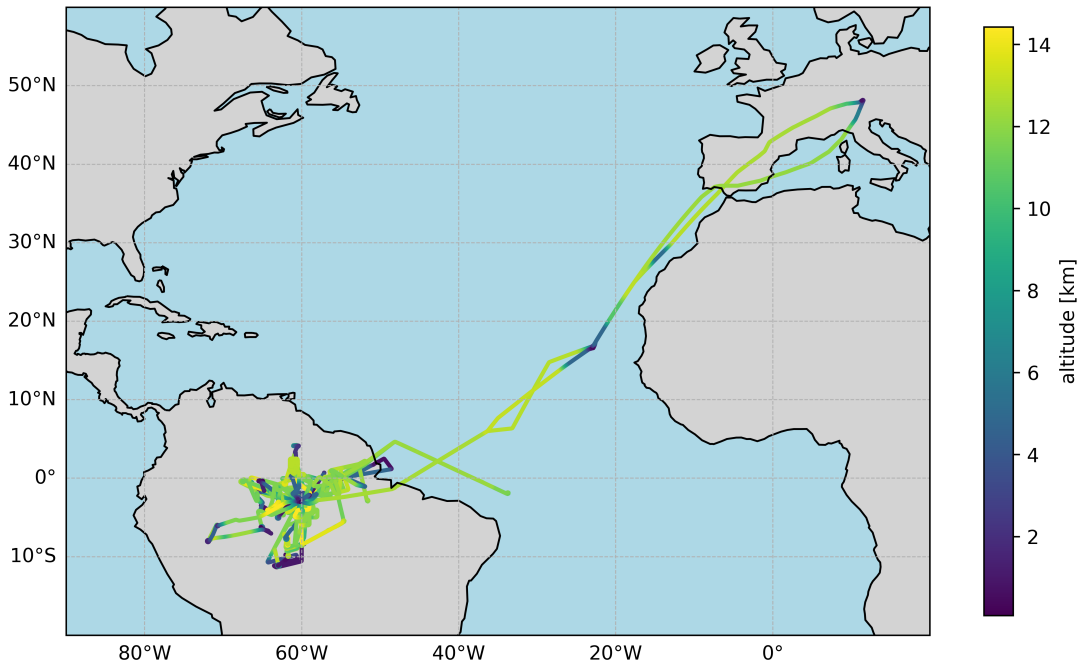

Figure 3.1: Flight tracks of the CAFE Brazil campaign, color-coded by the GPS altitude. Note that the test flights previous to the campaign are not included.

3.2 In-flight characterization of a compact airborne quantum cascade laser absorption spectrometer

This chapter presents a characterization of a newly developed absorption spectrometer based on a test flight conducted previous to the CAFE Brazil campaign. I am the first author of this study, which was published on the 11 June 2024 in the journal *Atmospheric Measurement Techniques* as a research article. Together with Dr. Lenard Lukas Röder, I performed the measurements and the data processing. I analyzed all data presented. Supported by Dr. Horst Fischer, I designed the study and wrote the manuscript. All co-authors contributed to the design and development of the instrument, proof-read the manuscript, or participated in the CAFE Brazil campaign. Detailed author contributions are provided in the paper under *Author contributions*. All data used for this study has been uploaded on the HALO database accessible via DLR, 2023.

The article illustrates the performance of the absorption spectrometer ATTILA measuring CO and CH_4, quantifies its capabilities, and discusses its limitations during in-situ airborne observations. Furthermore, a direct comparison is made with an established absorption spectrometer (TRISTAR), which conducted simultaneous CO measurements during the CAFE Brazil campaign above the Amazon Basin. In addition to the good agreement in observed atmospheric CO between the two instruments, this study reports the first CO and CH_4 spatial distributions of that campaign, which indicate a strong impact of convection, as seen in a C-shaped CO vertical profile and enhanced CH_4 mixing ratios toward the surface of the Amazon region. The latter aspect is further investigated in the next chapter.

The supplemental material can be found in Section 3.3.

Atmos. Meas. Tech., 17, 3553–3565, 2024
https://doi.org/10.5194/amt-17-3553-2024

Atmospheric Measurement Techniques
Open Access
EGU

In-flight characterization of a compact airborne quantum cascade laser absorption spectrometer

Linda Ort[1], Lenard Lukas Röder[1], Uwe Parchatka[1], Rainer Königstedt[1], Daniel Crowley[2], Frank Kunz[3], Ralf Wittkowski[3], Jos Lelieveld[1,4], and Horst Fischer[1]

[1]Atmospheric Chemistry Department, Max Planck Institute for Chemistry, 55128 Mainz, Germany
[2]Department of Dynamics at Surfaces, Max Planck Institute for Multidisciplinary Sciences, 37077 Göttingen, Germany
[3]Mechanical Support Department, Max Planck Institute for Chemistry, 55128 Mainz, Germany
[4]Climate and Atmosphere Research Center, The Cyprus Institute, Nicosia, 1645, Cyprus

Correspondence: Linda Ort (linda.ort@mpic.de) and Horst Fischer (horst.fischer@mpic.de)

Received: 29 November 2023 – Discussion started: 30 November 2023
Revised: 26 April 2024 – Accepted: 29 April 2024 – Published: 11 June 2024

Abstract. Here, we report on the development of a new quantum cascade laser infrared absorption spectroscopy (QLAS) instrument, the Airborne Tropospheric Tracer In-situ Laser Absorption spectrometer (ATTILA), for atmospheric trace-gas measurements on board of the German High-Altitude Long-range Observatory (HALO) aircraft. Its small and light design makes it suitable for airborne measurements up to approximately 150 hPa of ambient pressure (13–14 km). The dual laser instrument can measure several trace gases simultaneously in two 36.4 m path astigmatic Herriott cells with a data acquisition frequency of 1 Hz. We describe the measurement method and the data acquisition of ATTILA and its in-flight performance by focusing on potential sources of influences on the signal, which we investigated with a dedicated test flight during which the instrument sampled from a constant source. We show that linear critical influences associated with challenging movement patterns can be corrected afterwards, while nonlinear limitations can be minimized by appropriate calibration frequencies and integrated time intervals. During the recent aircraft campaign CAFE Brazil (Chemistry of the Atmosphere Field Experiment in Brazil) from December 2022 to January 2023, carbon monoxide (CO) measurements from ATTILA show a good agreement of a R^2 of 0.89 with simultaneous CO measurements from an established IR spectrometer for airborne measurements, the TRacer In Situ TDLAS (tunable diode laser absorption spectroscopy) for Atmospheric Research (TRISTAR), at a 10 s time resolution. First dynamical characteristics and tracer distributions of CO and methane (CH_4) over the Amazon rainforest can be identified with ATTILA measurements with a total measurement uncertainty of 10.1 % and 17.5 % for calibration gas mixing ratios of 153 and 1990 ppbv and a data accuracy of 0.3 % and 5.5 % for a data acquisition frequency of 1 Hz for CO and CH_4, respectively.

1 Introduction

Laser spectroscopic measurement techniques have been developed considerably in the past 2 decades, improving their resolution, accuracy, and stability for trace-gas measurements in the atmosphere (Werle, 1998). These advantages, and many more, make laser spectroscopy a highly efficient technique for measuring trace gases compared to classic chemical and chromatographic measurement techniques (Li et al., 2013). Tunable diode laser absorption spectroscopy (TDLAS) and the more efficient quantum cascade laser infrared absorption spectroscopy (QLAS) have been proven to be reliable measurement techniques in numerous publications (Faist et al., 1994; Kormann et al., 2002; Fried and Richter, 2006; McManus et al., 2010; Tuzson et al., 2020; Pal and Pradhan, 2021, and citations within). Especially for airborne measurements, a lightweight and compact design that can withstand the extremely difficult measurement conditions caused by abrupt changes in acceleration, direction, and height is very important (Richter et al., 2015; Catoire et al., 2017). Through the work of Röder et al. (2024) we also know that on airborne-platform instrumental characteristics

can behave differently compared to the laboratory. QLAS and TDLAS trace-gas measurements have been proven to be very valuable for detecting and understanding small-scale atmospheric chemistry, radiative effects, transport processes, and their overall impact on the Earth's climate (Fried et al., 2008). A reliable spectrometer for airborne measurements is the TRacer In Situ TDLAS for Atmospheric Research (TRISTAR), which performed successfully in a large number of field campaigns and research flights measuring tropospheric and stratospheric carbon monoxide (CO), carbon dioxide (CO_2), methane (CH_4), nitrous oxide (N_2O), and formaldehyde (HCHO) (Wienhold et al., 1998; Schiller et al., 2008; Tadic et al., 2017; Tomsche et al., 2019). Since the work of Tomsche et al. (2019), TRISTAR has been further improved, which is described in the study of Röder et al. (2024).

Airborne measurements can generate high-resolution and small-scale data even in remote locations, for example, in the tropics, where high cloud coverage complicates satellite-based measurements (Reiche et al., 2016, and citations within). Nevertheless, besides these advantages, experimental challenges such as vibrations, weight, and size limitations, pressure and temperature fluctuations during research flights, and complicated measurement modes for operation have prompted further investigations for suitable instrumentation (Li et al., 2013).

In the following, we present the Airborne Tropospheric Tracer In-situ Laser Absorption spectrometer, in short ATTILA, which has been specifically developed for airborne trace-gas measurements on board of the High-Altitude Long-range Observatory (HALO) aircraft. It is equipped with two room-temperature quantum cascade lasers that measure CO, CH_4, and N_2O in a two-cell system, which is described in more detail in Sect. 2. ATTILA conducted measurements during the CAFE Brazil (Chemistry of the Atmosphere Field Experiment in Brazil) campaign in December 2022 and January 2023, which took place above the Amazon rainforest region. In the scope of the campaign, a test flight was performed to investigate instrument behavior in the face of extreme airborne challenges in more detail. The doubling of simultaneous trace-gas measurements of the well-known TRISTAR spectrometer and the newly developed spectrometer ATTILA allows a comparison and quantification of the data quality, as well as some first insights into the atmospheric composition and trace-gas distribution over the Amazon rainforest.

2 The ATTILA instrument

ATTILA is a custom-built two-cell mid-infrared room-temperature quantum cascade laser absorption spectrometer constructed in 2019 at the Max Planck Institute for Chemistry to measure trace gases in the atmosphere on board of the research aircraft HALO. It is designed to further improve airborne measurements considering the limitations of weight and size for small aircraft. ATTILA is mounted in a 19 in. (48.26 cm) box and is small in size (48 cm × 27 cm × 55 cm) with a total weight of only 20.6 kg (excluding the pump). It holds two optical frames mounted in parallel inside of it. Figure 1 shows a picture of the instrument setup inside the box. The instrument is layered into two sections. On the top layer, the two optical frames, the flow systems, and the tubing are mounted. In the bottom layer the electronic devices are located. Those two layers are separated by a 4.5 mm thick aluminum plate and are ventilated by four fans located on the front of the instrument, which is in the picture on the right-hand side.

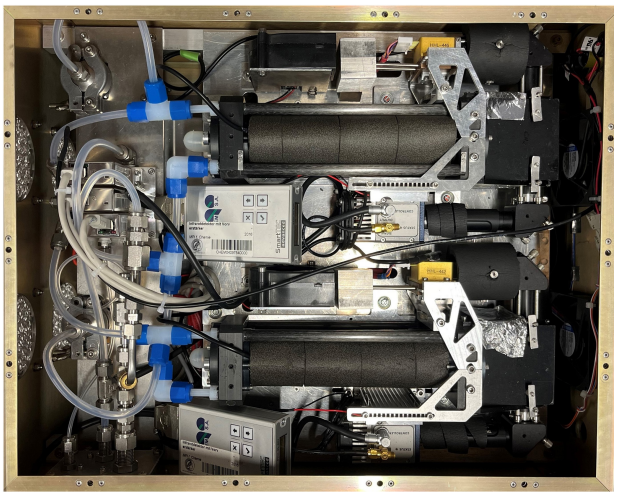

Figure 1. Picture of the top view of the measurement setup of ATTILA with the front of the instrument directed towards the right side. In the upper part of the picture the optical unit measuring CH_4 and N_2O with the laser HHL-446 is located, and in the lower part, CO and N_2O can be measured with the HHL-442 laser.

In the following the individual parts of the ATTILA instrument are described in more detail.

2.1 Optical and electrical setup

Figure 2 shows an overview of the schematic setup of the IR spectrometer. The two optical frames each consist of an astigmatic Herriott cell (HC; Herriott and Schulte, 1965; McManus et al., 1995), a quantum cascade laser (QCL), and a mid-infrared detector, as well as mirrors and lenses directing the laser beam in the optical section. Multipass absorption cells are often used to provide long optical pathways in an optimized compact volume (Zahniser et al., 1995). The total airflow of 0.2 L min^{-1} is controlled by two compound mass flow controllers (MFCs) (Bronkhorst, IQ+FLOW) separating the gas flow into the two cells with 0.1 L min^{-1} each. Furthermore, for calibration measurements another MFC leads 0.3 L min^{-1} of an external gas bottle into the ambient tube,

where 0.2 L min^{-1} is separated into the two HCs again and 0.1 L min^{-1} prevents ambient air influence.

The two QCLs (Alpes Lasers, HHL-series, Lausanne, Switzerland) can measure CO (2190.0175 cm^{-1}; Li et al., 2015) and N_2O (2190.3498 cm^{-1}; Toth, 2004) in one cell (Li et al., 2013) and CH_4 (1256.6 cm^{-1}; Ba et al., 2013) and N_2O (1255.42 cm^{-1}; Toth, 2004) in the second cell. The N_2O lines are mainly used to track the line center position of the spectra throughout atmospheric measurements due to its long lifetimes in the troposphere with only a small vertical gradient (Crutzen and Ehhalt, 1977). Both lasers are functional for laser temperatures up to 60 °C but are cooled down to 26.5 °C for operation. Each laser is controlled by a laser controller (Wavelength Electronics, WTC3243 and WTC3293), which adjusts the current and temperature of the laser. An integrated Peltier junction and an NTC temperature sensor (model 10K4CG) together with the above-mentioned fans ensure temperature stability. As the two optical frames are identical in their setup, the following description will focus only on one frame, as shown schematically in Fig. 3.

First, the laser beam passes two anti-reflection-coated plano-convex lenses to compensate for the divergence and focus it onto an adjustable plane mirror with an elliptical shape (Thorlabs, 12.7 mm (PFE05-P01)), which projects the laser beam on a right-angle prism mirror (Thorlabs, 12.5 mm (MRA12-P01)). Here, the laser beam is guided through an entrance window (Edmund Optics, TECHSPEC CaF_2 20 mm) and a coupling hole of the front mirror onto the left side of the back mirror of the two opposing astigmatic mirrors (Aerodyne, AMAC-36) of the HC. The correct adjustment of the HC is done with an optical visible adjustment laser at 635 nm (Thorlabs, HLS635) to see and achieve the specifically needed Lissajous pattern (Zahniser et al., 1995) on the two mirrors. This pattern is formed by the different horizontal and vertical radii of the curvature of $R_x = 246.0$ mm and $R_y = 269.4$ mm, respectively, of the two concave mirrors with diameters of 3.8 cm. They need to be rotated exactly by 62.55° to each other, considering their orientation, with the focus of the first entering beam in the middle of the cell. This alignment results in a multipass state where the laser beam is reflected 182 times back and forth which covers a distance of 36.4 m inside the compact HC with a length of 199.91 mm. With increasing path length, the signal-to-noise ratio (SNR) increases until the loss of the many reflections becomes important (Werle and Slemr, 1991). With a volume of 250 mL, the astigmatic HC provides an effective SNR compared to other HC types (Zahniser et al., 1995). Furthermore, between 3 to 10 µm the mirrors for the CO–N_2O cell are coated with silver, which provides a reflectivity of 99.2 % with a minimum of 99 % (Tafelmaier, Dünnschicht-Technik GmbH, Germany). For the same range but with a golden coating, the mirrors of the CH_4–N_2O cell have a reflectivity of around 99 % (Tafelmaier, Dünnschicht-Technik GmbH, Germany). One potential limitation of the HC can be optical interference fringes produced by scattering in the cell which degrade the effective SNR and can disturb the molecular absorption lines through a similar free spectral range. More features of the HC can be found in McManus et al. (1995) and Zahniser et al. (1995).

When the laser beam passes the HC, it gets partly absorbed by the trace gas of interest until it exits the cell through the entrance hole again. Through two valves above the back mirror side of the HC the sampled air inside the cell can be exchanged. The input valve which is controlled by the above-mentioned MFCs brings either ambient or calibration gas into the cell on the front mirror side. Behind the output valve a pump (VACUUBRAND, diaphragm pump – MD 1 VARIO-SP) is attached to reduce and keep the pressure inside the cells at 50 hPa continuously, which is detected by a pressure sensor (Dekont, VCC200) connected to the input valve. Furthermore, a PT-100 temperature sensor is mounted on top of the HC, detecting the temperature of the cell.

After exiting the HC through the front mirror hole the laser beam is directed with a prism and an adjustable elliptical mirror through a single lens and focused onto a room-temperature infrared-sensitive photovoltaic semiconductor detector (VIGO System S.A., PIP-DC-20M-F-M4). The beam slightly overshoots the detector entrance to compensate for potential beam misalignment due to vibrations.

For improved stability of the signal during vibrations and movements the optical frame is equipped with bracket reinforcements. Furthermore, several black isolating covers on top of the laser pathways reduce temperature fluctuations and laser scattering.

2.2 Signal processing and analysis software

The characteristics of the signal are processed, controlled, and read out by a single-board controller (National Instruments, CompactRIO sbRIO-9627). The controller includes a real-time processor, a field-programmable gate array (FPGA), which modulates the frequency on top of a voltage ramp including an offset to scan the targeted spectrum range. This is done by using the wavelength modulation spectroscopy (WMS) technique, described in Fried and Richter (2006). The triangular ramp provides two spectra, an upwards- and downwards-directed spectrum of the measured signal. With a sine wave modulation frequency of 17.86 kHz, a ramp is generated with 4096 discrete steps and scanned within 28.7 ms in each direction. Therefore, the frequency of the triangular wave is 17.4 Hz. This provides a scanning frequency of approx. 35 000 samples per second for each tracer of interest, after which the ramp is reduced by a quarter resulting in a 1024-point spectrum. The modulation depths for CO and CH_4 have been chosen empirically to maximize the signal-to-noise ratio. This digital command is converted into an analogue signal via a digital–analog converter (DAC) and transferred through an analog output to the laser controller. Then, the laser controller can adjust the temperature and current of the infrared laser to perform the wavelength

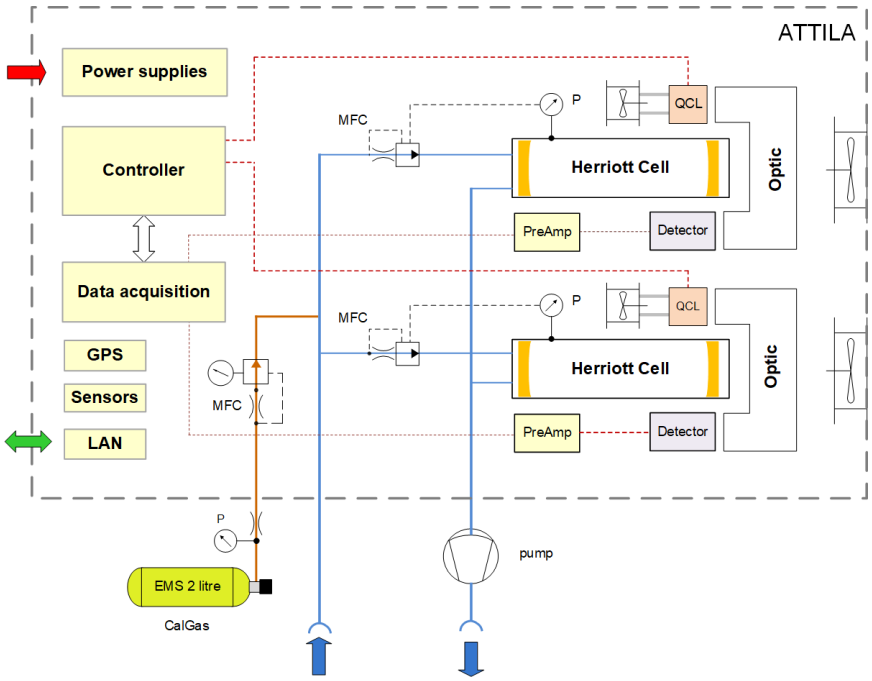

Figure 2. Schema of the measurement setup of ATTILA with the electrical and optical components.

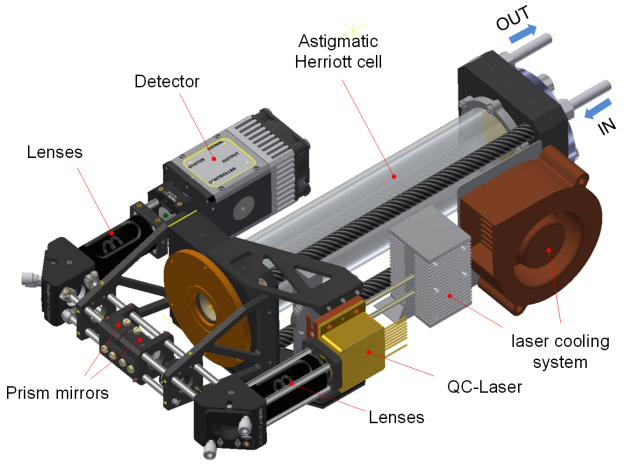

Figure 3. Sketch of the full optical setup for one cell including the astigmatic Herriott cell, the laser, and detector as well as the directing mirrors.

scan of the signal to generate an absorption spectrum when passing the HC. After detecting the absorbed signal, a preamplifier forwards the amplified signal through an analog input back into the sbRIO-9627, where the signal gets digitized by an analog–digital converter (ADC) again. Here, a digital lock-in amplifier demodulates and phase shifts the signal with the doubled initial modulation frequency ($2f$) to match the phase of the measured signal. Both the modulation and demodulation are performed by a LabVIEW (Laboratory Virtual Instrument Engineering Workbench)-controlled real-time FPGA system that is free of any jitter caused by software processes. The $2f$ harmonic signal provides a nearly constant baseline in the absorption-free region and a maximum at the center of the line (Fried and Richter, 2006). This ensures a minimization of electronic noise and an independency of the baseline of the spectra. Therefore, background calibrations and background subtraction are not necessary. Only a source with constant and known gas concentrations is needed to calculate the final gas mixing ratios. After the lock-in amplifier, a low-pass filter generates the DC signal with 1024 channels and an absorption spectrum which can be visualized in the corresponding software LabVIEW. The signal processing methodology and setup have a resolution time of 1 Hz with a duty cycle of 100 % for each tracer of interest, thereby facilitating the real-time visualization of precise concentrations of trace gases present in the sampled air. Additionally, a linear regression scheme calculates real concentration values, c_s, with the slope of the correlation between the fit of the $2f$ absorption spectrum S_s and the calibration spectrum S_{cal} multiplied by the known calibration gas concentration c_{cal} as follows (Fried and Richter, 2006):

$$c_s = c_{cal} \cdot \mathrm{corr}(S_s, S_{cal}). \quad (1)$$

A huge advantage of the processing is the flexibility of the modulation and fitting settings. Every parameter can be digitally adjusted to achieve the best result. The current settings

have been chosen after intensive laboratory test runs and have proven themselves during the campaign.

In addition to the online signal processing, a specialized analysis software was developed using IGOR Pro (WaveMetrics) for comprehensive postprocessing of the raw spectra. The software features automated filtering, exact positioning of the absorption lines, and background subtraction, if necessary, while also facilitating a precise linear fit to a calibration spectrum. Moreover, linear cell pressure variances as well as nonlinear Lambert–Beer effects can be corrected and overall precise mixing ratios of a species of interest can be determined. Furthermore, 1D and 2D visualization of the spectra with time can be used to recapitulate and correct for drift behavior or abrupt changes in the background induced by, e.g., temperature and pressure changes as well as the movements of the aircraft (Schiller et al., 2008). Further analysis and noise reduction opportunities have been discussed in Röder and Fischer (2022) and citations within.

2.3 Instrument setup on board of HALO

ATTILA is developed for aircraft measurements, specifically on board of the research aircraft HALO. During field campaigns, it is mounted in a 19 in. (48.26 cm) measurement frame rack together with the Nitrogen Oxide Analyzer for HALO (NOAH), described by Tadic et al. (2020) and Nussbaumer et al. (2021). Both instruments sample continuously over a 6.28 m long bypass from the top of the aircraft through a forward-facing stainless steel trace-gas inlet (TGI). The Teflon-coated tubing channels the ambient air through 1/2 in. (1.27 cm) PFA (perfluoroalkoxy alkane) tubes until it exits the aircraft again through a second TGI. After 4.57 m of this tubing, 0.2 L min^{-1} is led through a 1.27 m long 1/4 in. (0.635 cm) tube into the ATTILA instrument, located 0.16 m before the nitrogen oxide analyzer samples 3.0 L min^{-1} from the bypass. Figure 4 shows a sketch of the gas flow. As the ambient air enters the spectrometer, the air is separated into the two HCs through two MFCs as described above.

For in-flight calibrations, a 2 L EMS gas bottle filled with compressed air is used. It is stored below the rack during the flight. The exact concentrations of the compressed air are characterized with a primary standardized gas bottle beforehand. During the calibration mode, one MFC leads the calibration gas with a flow of approximately 0.3 L min^{-1} into the other two MFCs, which separate the flow into the cells with 0.1 L min^{-1} each. Due to this overflow of 0.1 L min^{-1} between calibration and ambient measurements, the calibration gas steams slightly into the ambient and exhaust lines which prevents these lines from influencing the measurements. A critical orifice is built inside the connecting tube towards the exhaust so that the latter does not influence ambient measurements.

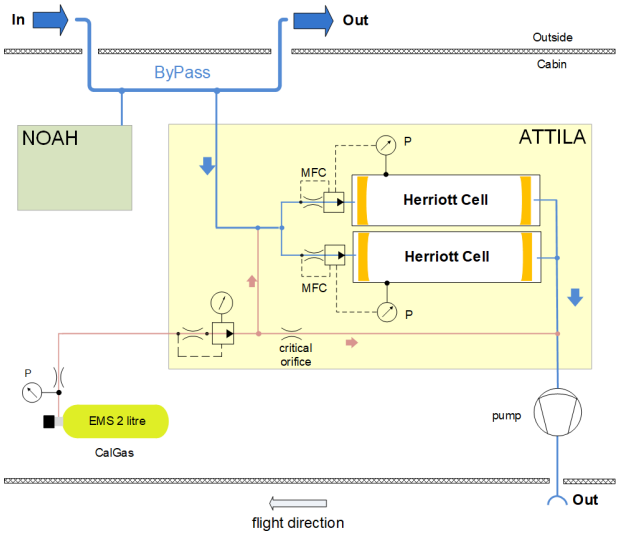

Figure 4. Flow chart of ATTILA setup on the HALO aircraft.

3 Instrument performance based on test flight

Within the CAFE Brazil campaign from November 2022 to January 2023, 22 flights have been performed with HALO, including 2 test flights during the preparation phase at the German Aerospace Center (DLR) in Oberpfaffenhofen, Germany; 4 transit flights with a stop-over at Sal, Cabo Verde; and 16 research flights over the Amazon rainforest based in Manaus, Brazil. The first test flight was used to investigate the in-flight behavior of ATTILA. Therefore, continuous calibration gas measurements were performed during this test flight on 22 November 2022 in the preparation phase of the CAFE Brazil campaign. This test flight was specifically planned to investigate the behavior of individual instruments in response to in-flight environmental changes like temperature and pressure, as well as extreme aircraft movements, and has already been used for instrument characterization in the studies of Hamryszczak et al. (2023) and Röder et al. (2024). Hence, various flight levels and different vertical velocities and accelerations, as well as the variation in yaw, pitch, and roll angles, have been performed. At 10:30 UTC the aircraft departed. Before, the instrument was running for approx. 2 h in the aircraft to warm up. The final approach of HALO for that test flight was at 14:23 UTC. Several instrument flight parameters are shown in Figs. 5 and 6 and are discussed to determine the systematic influences on the signal.

Starting with Fig. 5, the 2D 2f raw spectra with the absorption lines of CO and N_2O are shown in blue in the channels 200 and 800, respectively, over time. Additionally, the temperature of the HC T_{HC} and the cabin pressure p_{cab} of the aircraft measured at the rack are added as yellow and grey lines, respectively. Please note that the spectrum in Fig. 5 is already processed with a pre-filter and the absorption lines are locked and shifted according to their line maximum. The

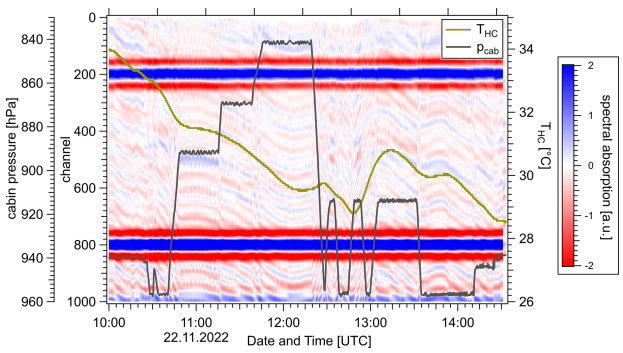

Figure 5. The 2D spectrum of the upwards-directed ramp signal of the CO–N_2O laser showing the channels versus the time of the first test flight on 22 November 2022 with the N_2O absorption line in the bottom (channel 800) and the CO absorption line displayed in the top (channel 200) of the graph. The color scale is adjusted to values close to zero to show a stronger contrast of the background signal. Blue colors indicate positive values, hence absorption of the signal, and red colors negative values of the $2f$ spectrum. The yellow line shows the temperature on top of the HC during the whole flight. In grey, the cabin pressure is displayed, measured at the ATTILA rack. The HALO aircraft was in the air from 10:30–14:23 UTC.

background signal has not been shifted. By focusing on the background signal between channels 300 and 700, thus between the absorption lines of CO and N_2O, interference on the signal can be addressed. The long-term drift behavior of the spectra correlates well with the change in the temperature inside the HC. T_{HC} changes during the test flight by about 6 °C peak to peak. These changes are influenced by the cabin temperature which fluctuates in the same range even with the air conditioning control system on board of the HALO aircraft. The postprocessing of the signal includes a shift in the absorption lines by locking the signal on its line maximum. With this, the drift behavior of the signal can be corrected, which can be seen in Fig. 5. Furthermore, temperature changes have a small impact on the laser temperature and its operating point and therefore the intensity of the signal. Looking at the laser temperature of the CO–N_2O laser in Fig. 6 in the lowermost panel, the temperature change correlates well with the one from T_{HC}. A variation in temperature further influences the optical setup by expansion of the material to induce etalon structures through interference. These interference fringes can influence the absorption signal amplitude via nonlinear constructive and destructive interference, which are much harder to identify. Slow changes in the fringe structure, such as temperature changes mentioned above, can be approximated linearly and thus be counteracted by frequent calibrations.

Moreover, a change in pressure can have an influence on the signal. There are two influences known which lead to different assumptions: first a change in ambient pressure and second a change in cabin pressure. First, when the ambient pressure changes, the pumping has to adjust to the new pressure gradient to keep the flow stable. This is done by varying the voltage of the pump from approx. 4 V up to its maximum of 10 V. The pump voltage, the HC pressure, and the pressure gradient calculated from the ratio of the ambient to the cabin pressure are shown in Fig. 6. Especially for fast altitude changes during, e.g., departure or landing, these disturbances are visible in the cell pressure, spectra, and concentration. At constant flight levels and slow altitude changes, the pump can easily regulate the cell pressure to keep it constant at 50 hPa. Cell pressure instabilities are linear and hence can be corrected in the data processing.

Secondly, Fig. 5 shows that the cabin pressure of the aircraft fluctuates even in constant flight levels of about 4 hPa. This influences the spectra and hence the measured concentration by inducing sine-structured short-term fluctuations. This can be seen especially between 10:48 and 11:15 UTC. Looking at the three different flight levels between 10:48 and 12:18 UTC, the cabin pressure fluctuations do not change but their influence on the signal does, as can be seen in the mixing ratio in Fig. 6. Hence, we see that pressure instability has an effect on the interference fringes. This effect is not linear and still needs to be investigated.

In the first half of the test flight the aircraft mostly flies straight, which can be seen from the roll and pitch angles and the yaw angle rate displayed in Fig. 6. Small aircraft movements only have minor influences on the signal. In the second half of the flight from 12:30 UTC onwards extreme aircraft movements involving abrupt changes to varying roll, pitch, and yaw angles are carried out. These aircraft movements create disturbances in the signal through, e.g., centrifugal forces which can have an effect on the optical setup and hence the signal. The mixing ratio in Fig. 6 shows a strong impact of aircraft movements on the signal. However, these extreme aircraft movements are, if possible, avoided during measurement flights to provide as stable conditions as possible for airborne measurements. Nevertheless, another important factor causing small instrumental movements might be atmospheric turbulence, which is not shown here.

In general, influences on the signal are mostly induced by temperature and pressure changes and aircraft movements (Fried and Richter, 2006), which create linear and nonlinear effects, as described above. As it is mostly a combination of variables that influence the signal, disentangling these effects of individual parameters is difficult. Nevertheless, temperature drift behavior, pressure effects, and short-term disturbances can be corrected by frequent calibration measurements and averaging (Richter et al., 2015). To investigate the appropriate calibration frequency, different calibration intervals have been tried out in the postprocessing of the test flight, assuming that parts of the calibration gas measurements are calibrations and others are ambient measurements. The tracer concentrations shown in Fig. 6 are not yet drift-corrected. Their mean values are 163 ± 14, 378 ± 30, and 1768 ± 235 ppbv for CO, N_2O, and CH_4, respectively.

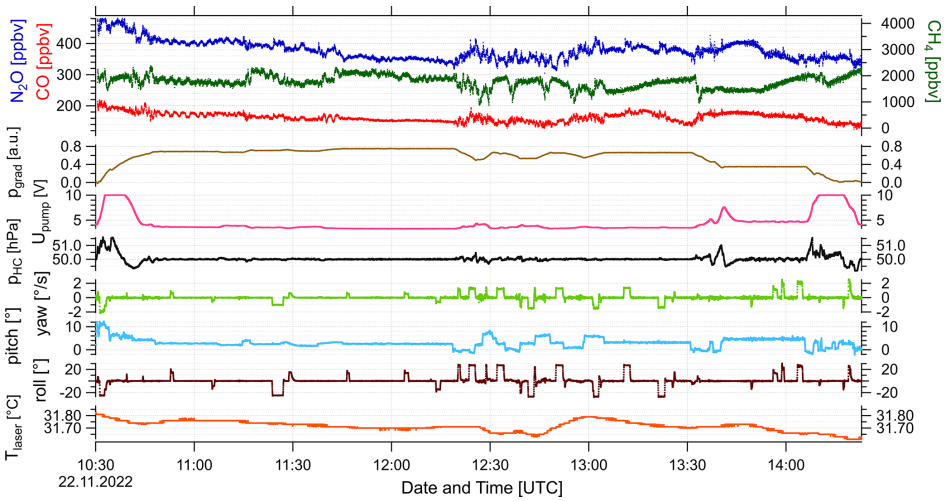

Figure 6. Compilation of instrument and flight parameters over time from the test flight on 22 November 2022. Shown are the laser temperature of the CO–N_2O laser (T_{laser}, orange line), the voltage of the pump (U_{pump}, pink line), the mean HC pressure calculated over both cells (p_{HC}, black line), and the roll (dark red line) and pitch (light blue) angles as well as the yaw angle rate per second (light green) of the HALO aircraft during that flight. As the ocher line the pressure gradient calculated as the ratio of the ambient pressure and the cabin pressure as $p_{grad} = 1 - p_{ambient}/p_{cabin}$ is displayed. Note that the tracer concentrations of CO in red, N_2O in blue, and CH_4 in green in the top panel of the graph are not yet corrected by pressure and Lambert–Beer. A linear calibration fit has been used from only one calibration before the flight. Throughout the whole flight ATTILA was running on calibration mode sampling only from a gas bottle with 161 ± 9 ppbv of CO, 358 ± 22 ppbv of N_2O, and 2025 ± 7 ppbv of CH_4, including the accuracy of the bottle.

For the optimal drift correction different calibration intervals have been tried out in the postprocessing of the test flight data. The drift-corrected mixing ratios for different calibration intervals for CO, N_2O, and CH_4 can be found in the Supplement in Figs. S1, S2, and S3, respectively. The higher the interval, the better drift influences can be corrected, but fewer ambient measurements are done and more calibration gas is needed. The drift correction clearly depends on the positioning of the calibrations and the interference at that time. A measure for this is the reproducibility R. For this, a mean value of each calibration measurement is calculated and investigated for their accuracy and shift over time. Low R indicates similar mean values of each calibration and hence small drift behavior. R varied from 0.71 % to 8.54 % for different calibration frequency scenarios from every 85 min to every 2 min. After drift correction, the relative statistical error of the calibrations provides the mean precision P, which is 2.63 ± 0.47 % for all scenarios. For the choice of the appropriate calibration interval those different scenarios have been compared and an automated interval of 20 min was chosen as an optimal trade-off between drift counteraction, duty cycle, and calibration gas consumption. The duration of the calibrations are 60 s, where the first 15 s are not taken into account in the analysis to ensure sufficient flushing time of the cell. With 20 min of calibration frequency the mean values of the corrected mixing ratios are 160 ± 10, 357 ± 14, and 2029 ± 197 ppbv for CO, N_2O, and CH_4, respectively. Therefore, they are in the range of the standard errors of the calibration gas, which are for CO 161 ± 9 ppbv, for N_2O 358 ± 22 ppbv, and for CH_4 2025 ± 7 ppbv. This calibration setting was adopted for the rest of the campaign.

4 Instrument comparison for ambient data

The long-established TRISTAR instrument (e.g., Wienhold et al., 1998; Schiller et al., 2008; Tadic et al., 2017; Tomsche et al., 2019) was deployed simultaneously to ATTILA within the CAFE Brazil campaign, measuring also CO and N_2O. Both IR spectrometers operated throughout the whole campaign without any technical malfunctions. A comparison of these two IR spectrometers has been done to investigate the instrumental performance of the newly developed spectrometer. This is especially important for future planning, as ATTILA can take over CO measurements and TRISTAR could be modified to measure other trace gases like, e.g., formaldehyde due to its high stability and precision. Please note that the general measurement focus of the instrument is on CO, as the N_2O absorption line is only used to track the spectra on its right position, especially at high altitudes where CO concentrations are markedly lower. The CH_4 data will be shown in the next section.

The total in-flight measurement uncertainty MU over the whole campaign is estimated by using R and P, described in Sect. 3 and calculated as follows:

$$\mathrm{MU} = \sqrt{P^2 + R^2}. \quad (2)$$

Table 1. Mean precision P, reproducibility R including their 1σ, and the total measurement uncertainty MU calculated using Eq. (2) for all research flights of the CAFE Brazil campaign for the ATTILA and TRISTAR spectrometers. The accuracy Acc of the secondary standard used as calibration gas during the flights is calculated using Eq. (3).

Tracer	$P \pm \sigma$ (%)	$R \pm \sigma$ (%)	MU (%)	Acc (%)
CO (ATTILA)	2.6 ± 1.2	9.8 ± 3.9	10.1	0.3
N_2O (ATTILA)	1.4 ± 0.3	9.1 ± 4.2	9.2	0.1
CH_4 (ATTILA)	4.2 ± 1.5	17 ± 9.5	17.5	5.5
CO (TRISTAR)	0.3 ± 0.04	3.5 ± 1.9	3.5	0.3
N_2O (TRISTAR)	0.2 ± 0.04	2.97 ± 2.05	3.0	0.1

Another measure for data comparison is the accuracy Acc, representing the standard error of the in-flight calibration gas. Acc of the secondary standard used as calibration gas during the flights is calculated via

$$\mathrm{Acc} = \sqrt{(R_F)^2 + \left(\frac{\sigma}{N}\right)^2 + \left(\frac{F_{\mathrm{err}}}{F_{\mathrm{mean}}}\right)^2}, \quad (3)$$

including the reproducibility of the primary standard measurements R_F, the standard deviation divided by the number of points of the secondary standard measurements, and the primary standard error over its mean content. The primary standard errors are given by the manufacturer (Luxfer Gas Cylinders Ltd., Colwick, Nottingham, England) as 0.36, 0.21, and 0.24 ppbv for CO, N_2O, and CH_4, respectively.

MU is in the lower percent range for both instruments, as shown in Table 1. In comparison to the performance of TRISTAR, ATTILA's MU is increased by a factor of 3. Acc is for all tracers in the per mille range, except for CH_4 which is at 5.5 %.

For the comparison, a time resolution adjustment has been made. As an example, a section of the research flight number 14 on 12 January 2023 is shown in Fig. 7 where extreme CO concentrations could be measured with both instruments, as the aircraft flew through several fresh biomass burning plumes at a low altitude in the boundary layer of about 760 m. In Fig. 7 two smaller plumes are displayed with high concentrations above 1000 ppbv. There is a delay of 5 s visible between the two instruments, which is due to the differences in their flow rate and cell volumes. TRISTAR has a flow rate of $3\,\mathrm{L\,min^{-1}}$ and hence exchanges the sampled air much faster than ATTILA. This time delay of 5 s has been corrected for further analysis of the ATTILA data. Another consequence of the time resolution difference is that TRISTAR measures higher concentrations in a short extreme event which ATTILA can only see smoothed out with its flow of $0.2\,\mathrm{L\,min^{-1}}$. High-frequency features below 5 s cannot be measured with ATTILA. This, specifically, shows the first peak at 16:47:45 UTC of the biomass burning event displayed in Fig. 7. Nevertheless, these flow limitations are only a few seconds, which is still a good time resolution for airborne measurements.

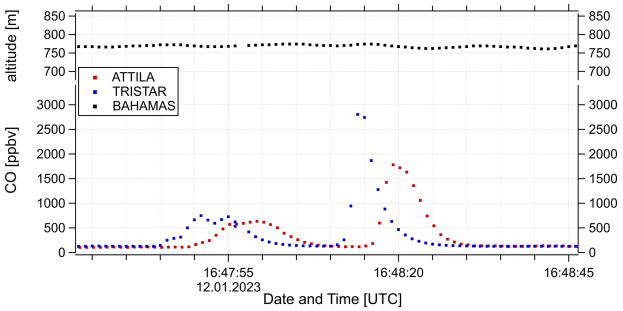

Figure 7. Timeline of CO mixing ratios from ATTILA in red and TRISTAR in blue measured during flight number 14 on 12 January 2023. In black, the GPS altitude from the BAHAMAS instrument (DLR, Oberpfaffenhofen, Germany) during the flight is displayed. All data are at 1 Hz resolution. The CO measurements have been fully processed and corrected by drift, pressure change, and Lambert–Beer.

In Fig. 8 the correlation of all CO measurements throughout the whole campaign from both IR spectrometers is displayed. Additionally, a least orthogonal distance fit has been performed, including their MUs (Table 1). The scale has been slightly adjusted to focus on typical atmospheric concentrations instead of extreme events. Except for some outliers, which can be related to extreme aircraft movements and changes during some takeoffs and landings, the 1 Hz measurements agree quite well with a slope of 1.0022 ± 0.0004 and a R^2 of 0.83. The differences in the data sets are mainly due to their different instrumental noise. TRISTAR features a more robust design, a better insulation and temperature control through a heating plate, and a stabilized and more extensive optical system, and its operation can profit from many years of experience and further improvement of the spectrometer throughout numerous campaigns (Tomsche et al., 2019; Tadic et al., 2017; Schiller et al., 2008, and citations within). Therefore, fast atmospheric changes and unusual extreme events in the boundary layer with CO measurements higher than 600 ppbv can be better detected by the TRISTAR instrument. Nevertheless, an averaged time resolution of 10 s provides a R^2 of 0.89 with a slope of 0.9811 ± 0.0003 and is an adequate time resolution eliminating nearly all the instrumental noise. The correlation of the 10 s averaged data is displayed in Fig. S4 in the Supplement.

In Fig. 9 the 1 Hz data have been binned into 500 m boxes from the whole campaign data set excluding the two test flights. In green and black the mean, median, and standard deviation of ATTILA and TRISTAR, respectively, are shown. A few assumptions can be made. First of all, below 1 km several extreme events have been measured due to anthropogenic emissions and biomass burning events. As explained

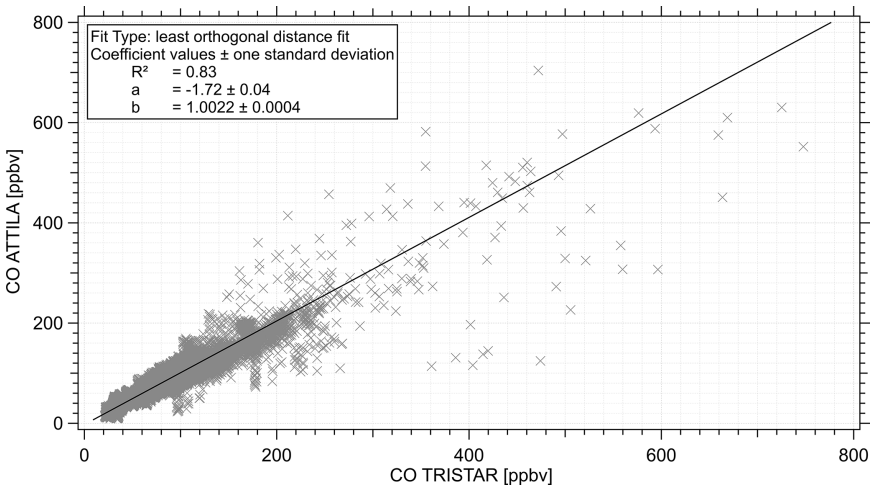

Figure 8. Correlation of all CO ambient measurements from ATTILA on the y axis and from TRISTAR on the x axis over the whole CAFE Brazil campaign, excluding the two test flights. The data have been fully processed and corrected. A least orthogonal distance fit, displayed as a black line, has been performed, including the MU values presented in Table 1. Outliers are mostly related to extreme aircraft movements during takeoffs and landings.

above, due to TRISTAR's higher time resolution and flow, short-term changes in extreme mixing ratios can be detected better with TRISTAR, leading to a higher variation in the standard deviation near the surface compared to ATTILA CO measurements. Nevertheless, their mean values differ only by 7 ppbv. Furthermore, throughout the free troposphere above 2 km the instruments agree quite well in their mean values of differences up to maximum ±2 ppbv. Especially above 12 km the measurements are almost identical even with respect to their standard deviations and median values.

In conclusion, the ATTILA instrument is suitable for high-resolution measurements of atmospheric variations and can reliably detect atmospheric features during airborne measurements. In large part, due to its minimalist and robust design during airborne measurements, this instrument can be used for dynamical and chemical investigations of the atmosphere. Therefore, atmospheric spatial tracer distributions, vertical profiles, and qualitative indication of potential source and sink regions through chemical reactions can be investigated. For example, for flux measurements which require time resolutions smaller than 1 Hz and a high data quality (Nussbaumer et al., 2023), the ATTILA instrument still has to be improved.

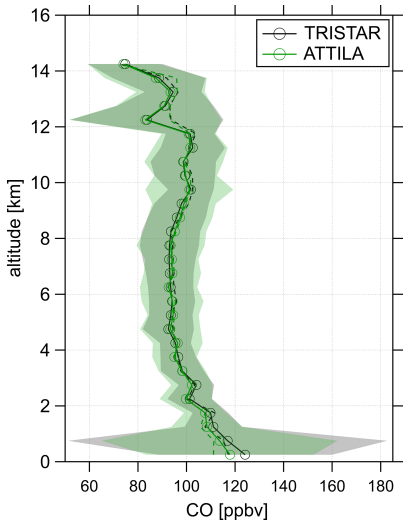

Figure 9. Vertical profile of all CO measurements over the whole campaign, excluding the two test flights. Both profiles are binned in 500 m boxes measured by TRISTAR with black and ATTILA with green lines. Additionally, the medians are shown with dashed lines and the standard deviation of the measurements as shaded areas.

5 Results from CAFE Brazil

With a base in Manaus, Brazil (3°6′ S, 60°1′ W), the CAFE Brazil aircraft campaign was carried out over the Amazon rainforest from December 2022 until the end of January 2023. Various instruments on board of the HALO aircraft measured about 50 different trace gases, radicals, and aerosol particle properties in 16 local flights over the Amazon rainforest region from a few meters above the forest up to about 15 km in altitude. In additional to the local research flights, four transfer flights with a stopover in Sal, Cabo Verde, and two test flights over Germany were carried out within the campaign. The main research focus lay on the investigation of oxidation processes and their control of new particle formation and particle growth over the rainforest region. Further objectives of the campaign were the investigation of the gen-

eral distribution of the measured variables over the pristine forest as well as over regions influenced by anthropogenic activity and their transport through deep convection into the tropical tropopause layer (TTL) (Fueglistaler et al., 2009).

In Fig. 10 meridional profiles of CO (left panel) and CH_4 (right panel) measured by ATTILA over the Amazon rainforest from the CAFE Brazil campaign are shown. The bin size of those distributions was chosen according to the individual MUs of the trace-gas measurements presented in Table 1. Therefore, CO is binned into $1\,^\circ \times 0.5$ km bins and CH_4 into $2\,^\circ \times 2$ km bins. All data are corrected by drift, cell pressure variations, and Lambert–Beer. The CH_4 data are additionally corrected according to the water dilution effect, which is described in more detail in the study of Haracono et al. (2015).

Focusing on CO in the left panel of Fig. 10, we can see three regions of enhanced and two regions of lower CO concentrations. The enhanced values originate from anthropogenic emissions and biomass burning events which can be vertically transported by convection. Specifically, in the lower altitudes below approx. 3 km, in the boundary layer, mean values reach 140 ppbv. Mostly, these are located around 60° W, which indicates anthropogenic emissions of the city Manaus (3°6′ S, 60°1′ W) as well as extreme single biomass burning events, which have been captured around 4°5′ S, 62°5′ W. Those elevated concentrations are vertically transported from the boundary layer into the free troposphere through deep convection and could be probed in the outflow of those convective cells several times between 10 and 13 km mostly west of Manaus. During one research flight towards the east, another strong outflow event could be measured up to 14 km.

The lower concentrations are influenced by stratospheric air which gets transported and mixed downwards into the TTL. Two regions which are dominated by stronger stratospheric influence during the campaign are between 55 and 60° W above 13 km and around 69° W down to 12 km. That influence propagates quite deep into the free troposphere. This might be affected by gravity waves in the lee of the Andes but has not been investigated further in this study.

The mean concentration of CH_4 over the whole meridional profile above the Amazon rainforest is 1932 ppbv. According to the NOAA database the monthly mean values for December 2022 and January 2023 are 1924.72 and 1922.16 ppbv, respectively (Lan et al., 2023). With an accuracy of 5.5 % (Table 1) for the CH_4 data and taking into account that the NOAA mean value has been measured over the whole vertical atmospheric column above the remote marine surface, these values are in quite good agreement. Nevertheless, the vertical profile of CH_4 also shows a different vertical distribution. Below 4 km the mean value is 2030 ppbv, and above it is 1907 ppbv. Hence, there might be a source of CH_4 over the Amazon rainforest region. According to the global database from NOAA (Lan et al., 2023) there is a drastically increasing trend in atmospheric methane in the recent years. A modeling study by Zhang et al. (2023) using a wetland model, referring to the years 2000 to 2021, reports large increases in CH_4 emissions since 2000 with the strongest increase in the years 2020 and 2021. Based on the satellite-borne NOAA database, Peng et al. (2022) suspected higher natural methane emissions, while anthropogenic emissions probably decreased over the COVID-19 lockdown. The positive feedback of natural methane emissions is suggested to be mostly from wetlands, as warming and more moisture through climate change can contribute to this effect. However, as the CAFE Brazil campaign generated a statistically representative and unique data set of in situ measurements over the Amazon rainforest, those increased CH_4 values will be further investigated in another study.

6 Conclusions

In this study, a newly developed quantum cascade laser absorption spectrometer, named ATTILA, has been presented and intensively characterized in its in-flight measurement performance. This work not only describes the instrument's functional properties and technical setup, but it identifies possible data interference for airborne trace-gas measurements.

The advantages of the instrumental design are its low weight, size, and costs and its simplicity, which makes it an ideal airborne trace-gas IR spectrometer and possibly attractive for commercial use. This instrument features two cells, which allows simultaneous measurements of a minimum of two tracers. Based on a test flight from a recent airborne research campaign, CAFE Brazil, the instrument has been characterized and influences of extreme environmental changes on the signal could be identified. By identifying these influences, postprocessing of the signal allows for improvement in the data quality. Therefore, temperature drift behavior, linear pressure changes, and short-term fluctuations can be corrected to some extent through frequent calibrations, line-shifting, and appropriate averaging of the data. A comparison with a similar, more established IR spectrometer, TRISTAR, has been used to verify the overall assumption of the quality of the data set. It has been shown that despite ATTILA's minimalist design and the challenges of an airborne platform, the measurements are of high quality, especially at constant flight levels and high altitudes, as its main shortcomings are related to abrupt changes in altitude and extreme aircraft movements. Therefore, the compact IR spectrometer ATTILA is capable of providing detailed information about spatial distributions in the atmosphere. The data set from the CAFE Brazil campaign has been briefly presented and discussed, and atmospheric features could be derived in the CO and CH_4 measurements over the Amazon rainforest. Especially for CO, only minor limitations of the data quality could be identified, and detailed atmospheric variations driven by dynamical processes could be located. For CH_4, there are more limitations than for the CO mea-

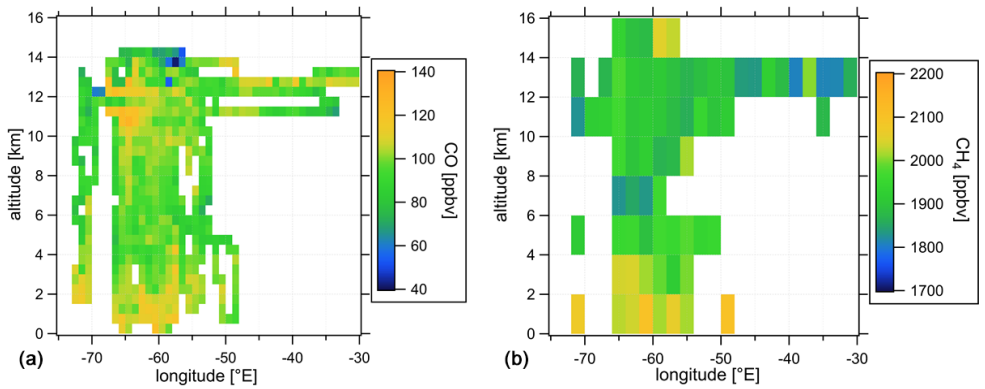

Figure 10. Median of the meridional profiles of the CO **(a)** and CH_4 **(b)** measurements of the CAFE Brazil campaign over the Amazon rainforest derived from ATTILA. The 1 Hz data are binned into a $1^\circ \times 0.5$ km subset for CO and into a $2^\circ \times 2$ km subset for CH_4 due to differences in their MU values. Additionally, for methane the bins with less than 1000 data points have been removed for a better statistical representation.

surements due to the optical setup. Nevertheless, a general overview of the CH_4 vertical distribution over the Amazon rainforest with enhanced concentrations in lower altitudes could be shown.

Through more field experience, ATTILA can be further improved. The main limitations are the influences of abrupt aircraft movements which cause nonlinear etalon structures. These drawbacks can be addressed by more precise adjustment and improvement in the optical setup. With a more stable optical adjustment, the influences on the signal caused by fluctuating temperature and pressure or strong aircraft movements will be further reduced.

Code and data availability. All data measured during the CAFE Brazil campaign and codes which have been used are available upon request. The BAHAMAS data can be found in the HALO database (https://doi.org/10.17616/R39Q0T, Gottschaldt and Rapp, 2017). The CO and CH_4 data will be uploaded by the end of 2024.

Supplement. The supplement related to this article is available online at: https://doi.org/10.5194/amt-17-3553-2024-supplement.

Author contributions. HF and LO designed the study; JL and HF planned the campaign; LO and LLR performed the measurements; LO and LLR processed and analyzed the data; UP, RK, DC, FK, RW, and HF designed the instrument; UP, RK, DC, LLR, and LO optimized the instrument; LO wrote the manuscript draft with contributions from all co-authors.

Competing interests. The contact author has declared that none of the authors has any competing interests.

Disclaimer. Publisher's note: Copernicus Publications remains neutral with regard to jurisdictional claims made in the text, published maps, institutional affiliations, or any other geographical representation in this paper. While Copernicus Publications makes every effort to include appropriate place names, the final responsibility lies with the authors.

Acknowledgements. The authors gratefully acknowledge the whole CAFE Brazil team, including the atmospheric department of the University of Frankfurt, Karlsruhe Institute of Technology, and the Deutsches Zentrum für Luft- und Raumfahrt (DLR) in Oberpfaffenhofen, whose support was essential for the project.

Financial support. The article processing charges for this open-access publication were covered by the Max Planck Society.

Review statement. This paper was edited by Glenn Wolfe and reviewed by two anonymous referees.

References

Ba, Y. A., Wenger, C., Surleau, R., Boudon, V., Rotger, M., Daumont, L., Bonhommeau, D. A., Tyuterev, V. G., and Dubernet, M.-L.: MeCaSDa and ECaSDa: Methane and ethene calculated spectroscopic databases for the virtual atomic and molecular data centre, J. Quant. Spectrosc. Ra., 130, 62–68, https://doi.org/10.1016/j.jqsrt.2013.05.001, 2013.

Catoire, V., Robert, C., Chartier, M., Jacquet, P., Guimbaud, C., and Krysztofiak, G.: The SPIRIT airborne instrument: a three-channel infrared absorption spectrometer with quantum cascade lasers for in situ atmospheric trace-gas measurements, Appl. Phys. B, 123, 1–12, https://doi.org/10.1007/s00340-017-6820-x, 2017.

Crutzen, P. J. and Ehhalt, D. H.: Effects of nitrogen fertilizers and combustion on the stratospheric ozone layer, Ambio, 6, 112–117, https://www.jstor.org/stable/4312257 (last access: 18 August 2023), 1977.

Faist, J., Capasso, F., Sivco, D. L., Sirtori, C., Hutchinson, A. L., and Cho, A. Y.: Quantum cascade laser, Science, 264, 553–556, https://doi.org/10.1126/science.264.5158.553, 1994.

Fried, A. and Richter, D.: Infrared absorption spectroscopy, in: Analytical Techniques for Atmospheric Measurement, Wiley Online Library, 72–146, https://doi.org/10.1002/9780470988510.ch2, 2006.

Fried, A., Diskin, G., Weibring, P., Richter, D., Walega, J., Sachse, G., Slate, T., Rana, M., and Podolske, J.: Tunable infrared laser instruments for airborne atmospheric studies, Appl. Phys. B, 92, 409–417, https://doi.org/10.1007/s00340-008-3136-x, 2008.

Fueglistaler, S., Dessler, A., Dunkerton, T., Folkins, I., Fu, Q., and Mote, P. W.: Tropical tropopause layer, Rev. Geophys., 47, 8755–1209, https://doi.org/10.1029/2008RG000267, 2009.

Gottschaldt, K.-D. and Rapp, M.: HALO database (last update: 1 October 2020), German Aerospace Center (DLR) [data set], https://doi.org/10.17616/R39Q0T, 2017.

Hamryszczak, Z., Dienhart, D., Brendel, B., Rohloff, R., Marno, D., Martinez, M., Harder, H., Pozzer, A., Bohn, B., Zöger, M., Lelieveld, J., and Fischer, H.: Measurement report: Hydrogen peroxide in the upper tropical troposphere over the Atlantic Ocean and western Africa during the CAFE-Africa aircraft campaign, Atmos. Chem. Phys., 23, 5929–5943, https://doi.org/10.5194/acp-23-5929-2023, 2023.

Haracono, Y., Iwata, H., Sakabe, A., Ueyama, M., Takahashi, K., Nagano, H., Nakai, T., and Kosugi, Y.: Effects of water vapor dilution on trace gas flux, and practical correction methods, J. Agr. Meteorol., 71, 65–76, https://doi.org/10.2480/agrmet.D-14-00003, 2015.

Herriott, D. R. and Schulte, H. J.: Folded Optical Delay Lines, Appl. Opt., 4, 883–889, https://doi.org/10.1364/AO.4.000883, 1965.

Kormann, R., Fischer, H., Gurk, C., Helleis, F., Klüpfel, T., Kowalski, K., Königstedt, R., Parchatka, U., and Wagner, V.: Application of a multi-laser tunable diode laser absorption spectrometer for atmospheric trace gas measurements at sub-ppbv levels, Spectrochim. Acta A, 58, 2489–2498, https://doi.org/10.1016/S1386-1425(02)00066-5, 2002.

Lan, X., Thoning, K., and Dlugokencky, E.: Trends in globally-averaged CH_4, N_2O, and SF_6, NOAA Global Monitoring Laboratory measurements, https://doi.org/10.15138/P8XG-AA10, 2023.

Li, G., Gordon, I. E., Rothman, L. S., Tan, Y., Hu, S.-M., Kassi, S., Campargue, A., and Medvedev, E. S.: Rovibrational line lists for nine isotopologues of the CO molecule in the X1Σ+ ground electronic state, Astrophys. J. Suppl. S., 216, 15, https://doi.org/10.1088/0067-0049/216/1/15, 2015.

Li, J., Parchatka, U., and Fischer, H.: Development of field-deployable QCL sensor for simultaneous detection of ambient N_2O and CO, Sensor. Actuat. B-Chem., 182, 659–667, https://doi.org/10.1016/j.snb.2013.03.073, 2013.

McManus, J. B., Kebabian, P. L., and Zahniser, M. S.: Astigmatic mirror multipass absorption cells for long-path-length spectroscopy, Appl. Opt., 34, 3336–3348, https://doi.org/10.1364/AO.34.003336, 1995.

McManus, J. B., Zahniser, M. S., Nelson Jr., D. D., Shorter, J. H., Herndon, S. C., Wood, E. C., and Wehr, R.: Application of quantum cascade lasers to high-precision atmospheric trace gas measurements, Opt. Eng., 49, 111124, https://doi.org/10.1117/1.3498782, 2010.

Nussbaumer, C. M., Parchatka, U., Tadic, I., Bohn, B., Marno, D., Martinez, M., Rohloff, R., Harder, H., Kluge, F., Pfeilsticker, K., Obersteiner, F., Zöger, M., Doerich, R., Crowley, J. N., Lelieveld, J., and Fischer, H.: Modification of a conventional photolytic converter for improving aircraft measurements of NO_2 via chemiluminescence, Atmos. Meas. Tech., 14, 6759–6776, https://doi.org/10.5194/amt-14-6759-2021, 2021.

Nussbaumer, C. M., Place, B. K., Zhu, Q., Pfannerstill, E. Y., Wooldridge, P., Schulze, B. C., Arata, C., Ward, R., Bucholtz, A., Seinfeld, J. H., Goldstein, A. H., and Cohen, R. C.: Measurement report: Airborne measurements of NO_x fluxes over Los Angeles during the RECAP-CA 2021 campaign, Atmos. Chem. Phys., 23, 13015–13028, https://doi.org/10.5194/acp-23-13015-2023, 2023.

Pal, M. and Pradhan, M.: Quantum Cascade Laser Spectroscopy, Modern Techniques of Spectroscopy: Basics, Instrumentation, and Applications, Springer, 363–387, https://doi.org/10.1007/978-981-33-6084-6_14, 2021.

Peng, S., Lin, X., Thompson, R. L., Xi, Y., Liu, G., Hauglustaine, D., Lan, X., Poulter, B., Ramonet, M., Saunois, M., Yin, Y., Zhang, Z., Zheng, B., and Ciais, P.: Wetland emission and atmospheric sink changes explain methane growth in 2020, Nature, 612, 477–482, https://doi.org/10.1038/s41586-022-05447-w, 2022.

Reiche, J., Lucas, R., Mitchell, A. L., Verbesselt, J., Hoekman, D. H., Haarpaintner, J., Kellndorfer, J. M., Rosenqvist, A., Lehmann, E. A., Woodcock, C. E., Seifert, F. M., and Herold, M.: Combining satellite data for better tropical forest monitoring, Nat. Clim. Change, 6, 120–122, https://doi.org/10.1038/nclimate2919, 2016.

Richter, D., Weibring, P., Walega, J. G., Fried, A., Spuler, S. M., and Taubman, M. S.: Compact highly sensitive multi-species airborne mid-IR spectrometer, Appl. Phys. B, 119, 119–131, https://doi.org/10.1007/s00340-015-6038-8, 2015.

Röder, L. L. and Fischer, H.: Theoretical investigation of applicability and limitations of advanced noise reduction methods for wavelength modulation spectroscopy, Appl. Phys. B, 128, 1–10, https://doi.org/10.1007/s00340-021-07737-z, 2022.

Röder, L. L., Ort, L. M., Lelieveld, J., and Fischer, H.: Determination of Temporal Stability and Instrument Performance of an airborne QCLAS via Allan-Werle-plots, Appl. Phys. B, https://doi.org/10.21203/rs.3.rs-3619758/v1, in review, 2024.

Schiller, C., Bozem, H., Gurk, C., Parchatka, U., Königstedt, R., Harris, G., Lelieveld, J., and Fischer, H.: Applications of quantum cascade lasers for sensitive trace gas measurements of CO, CH_4, N_2O and HCHO, Appl. Phys. B, 92, 419–430, https://doi.org/10.1007/s00340-008-3125-0, 2008.

Tadic, I., Parchatka, U., Königstedt, R., and Fischer, H.: In-flight stability of quantum cascade laser-based infrared absorption spectroscopy measurements of atmospheric carbon monoxide, Appl. Phys. B, 123, 1–9, https://doi.org/10.1007/s00340-017-6721-z, 2017.

Tadic, I., Crowley, J. N., Dienhart, D., Eger, P., Harder, H., Hottmann, B., Martinez, M., Parchatka, U., Paris, J.-D., Pozzer,

A., Rohloff, R., Schuladen, J., Shenolikar, J., Tauer, S., Lelieveld, J., and Fischer, H.: Net ozone production and its relationship to nitrogen oxides and volatile organic compounds in the marine boundary layer around the Arabian Peninsula, Atmos. Chem. Phys., 20, 6769–6787, https://doi.org/10.5194/acp-20-6769-2020, 2020.

Tomsche, L., Pozzer, A., Ojha, N., Parchatka, U., Lelieveld, J., and Fischer, H.: Upper tropospheric CH_4 and CO affected by the South Asian summer monsoon during the Oxidation Mechanism Observations mission, Atmos. Chem. Phys., 19, 1915–1939, https://doi.org/10.5194/acp-19-1915-2019, 2019.

Toth, R.: Linelist of N_2O parameters from 500 to 7500 cm^{-1}, JPL online, https://mark4sun.jpl.nasa.gov/n2o.html (last access: 10 October 2023), 2004.

Tuzson, B., Graf, M., Ravelid, J., Scheidegger, P., Kupferschmid, A., Looser, H., Morales, R. P., and Emmenegger, L.: A compact QCL spectrometer for mobile, high-precision methane sensing aboard drones, Atmos. Meas. Tech., 13, 4715–4726, https://doi.org/10.5194/amt-13-4715-2020, 2020.

Werle, P.: A review of recent advances in semiconductor laser based gas monitors, Spectrochim. Acta A, 54, 197–236, https://doi.org/10.1016/S1386-1425(97)00227-8, 1998.

Werle, P. and Slemr, F.: Signal-to-noise ratio analysis in laser absorption spectrometers using optical multipass cells, Appl. Opt., 30, 430–434, https://doi.org/10.1364/AO.30.000430, 1991.

Wienhold, F., Fischer, H., Hoor, P., Wagner, V., Königstedt, R., Harris, G., Anders, J., Grisar, R., Knothe, M., Riedel, W., Liibken, F.-J., and Schilling, T.: TRISTAR-A tracer in-situ TDLAS for atmospheric research, Appl. Phys. B, 67, 411–417, http://hdl.handle.net/10315/4208 (last access: 18 September 2023), 1998.

Zahniser, M. S., Nelson, D. D., McManus, B., Kebabian, P. L., Lloyd, D., Fowler, D., Jenkinson, D. S., Monteith, J. L., and Unsworth, M. H.: Measurement of trace gas fluxes using tunable diode laser spectroscopy, Philos. T. Roy. Soc. A, 351, 371–382, https://doi.org/10.1098/rsta.1995.0040, 1995.

Zhang, Z., Poulter, B., Feldman, A. F., Ying, Q., Ciais, P., Peng, S., and Li, X.: Recent intensification of wetland methane feedback, Nat. Clim. Change, 13, 430–433, https://doi.org/10.1038/s41558-023-01629-0, 2023.

3.3 Supplement of "In-flight characterization of a compact airborne quantum cascade laser absorption spectrometer"

Supplement of Atmos. Meas. Tech., 17, 3553–3565, 2024
https://doi.org/10.5194/amt-17-3553-2024-supplement

Atmospheric Measurement Techniques
Open Access
EGU

Supplement of

In-flight characterization of a compact airborne quantum cascade laser absorption spectrometer

Linda Ort et al.

Correspondence to: Linda Ort (linda.ort@mpic.de) and Horst Fischer (horst.fischer@mpic.de)

Supplemental Materials

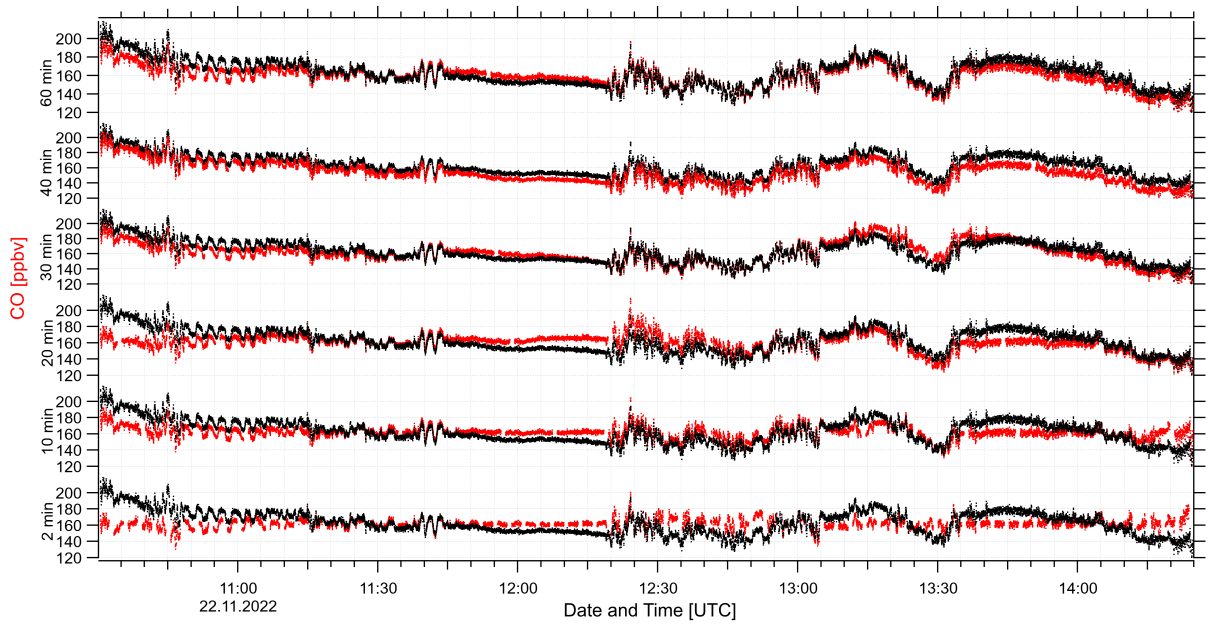

Figure S1. Comparison of calibration frequencies of CO with data from the test flight on the 22nd of November 2022. Black lines indicate measurements of constant calibration gas processed with only one virtual calibration before the flight of 60 seconds length. In red the same measurements are shown processed and drift-corrected with virtual calibrations set every 2, 10, 20, 30, 40 and 60 minutes from bottom to top, accordingly. The volume mixing ratio of CO which is supposed to be measured is 161 ppbv.

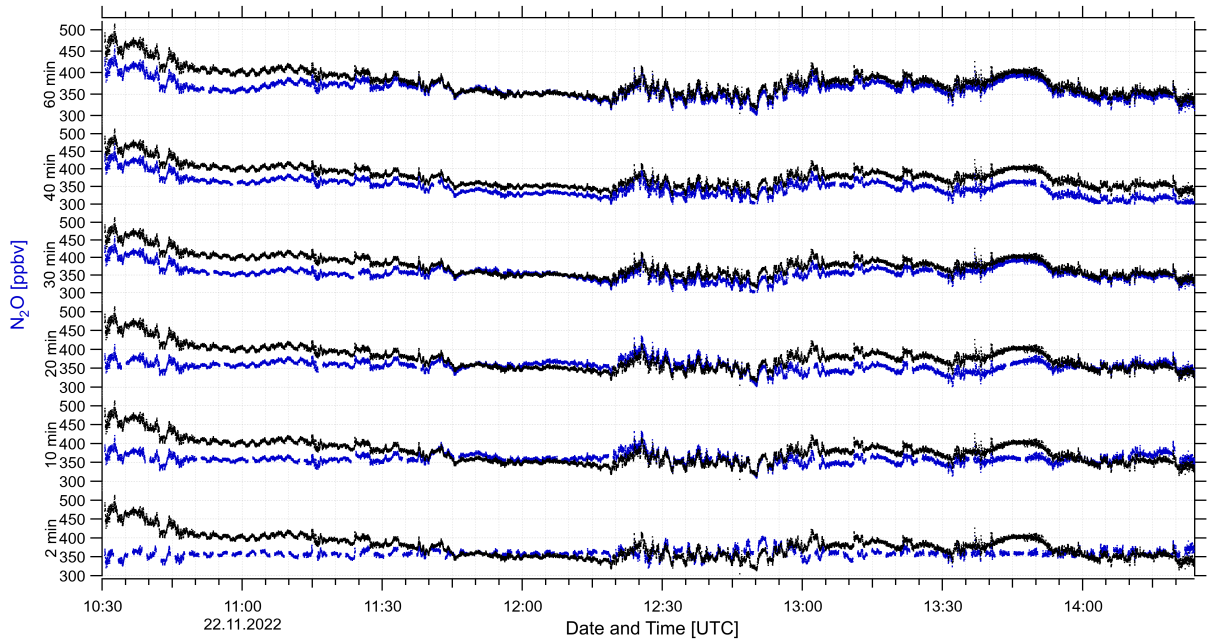

Figure S2. Comparison of calibration frequencies of N_2O with data from the test flight on the 22nd of November 2022. Black lines indicate measurements of constant calibration gas processed with only one virtual calibration before the flight of 60 seconds length. In red the same measurements are shown processed and drift-corrected with virtual calibrations set every 2, 10, 20, 30, 40 and 60 minutes from bottom to top, accordingly. The volume mixing ratio of N_2O which is supposed to be measured is 358 ppbv.

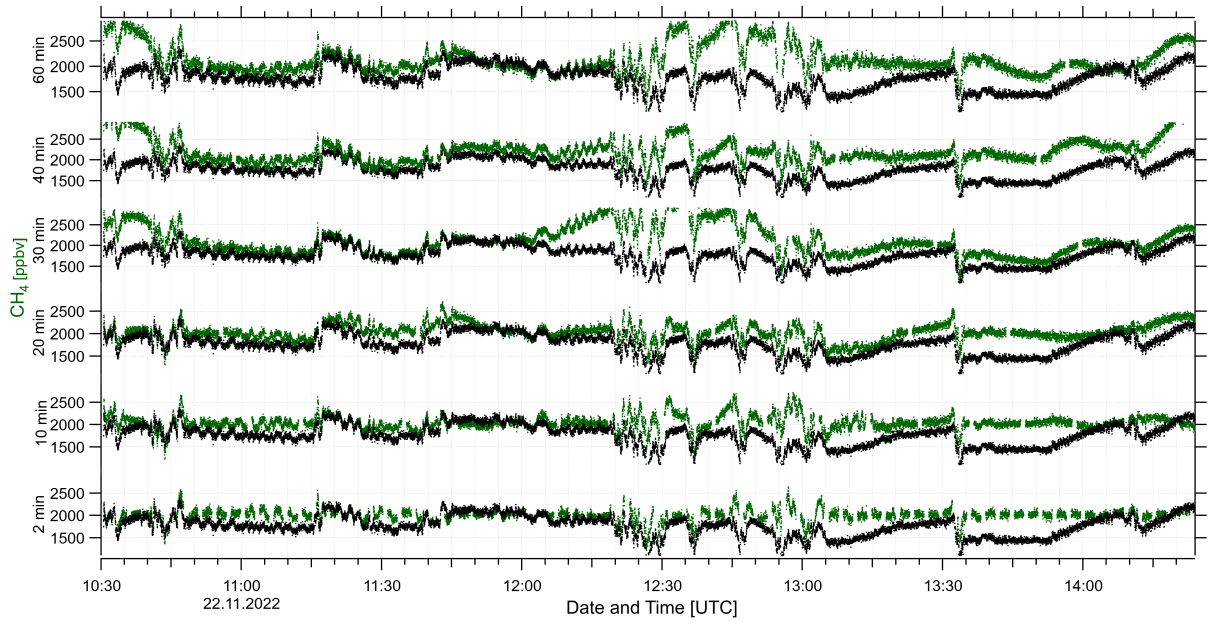

Figure S3. Comparison of calibration frequencies of CH_4 with data from the test flight on the 22nd of November 2022. Black lines indicate measurements of constant calibration gas processed with only one virtual calibration before the flight of 60 seconds length. In red the same measurements are shown processed and drift-corrected with virtual calibrations set every 2, 10, 20, 30, 40 and 60 minutes from bottom to top, accordingly. The volume mixing ratio of CH_4 which is supposed to be measured is 2025 ppbv.

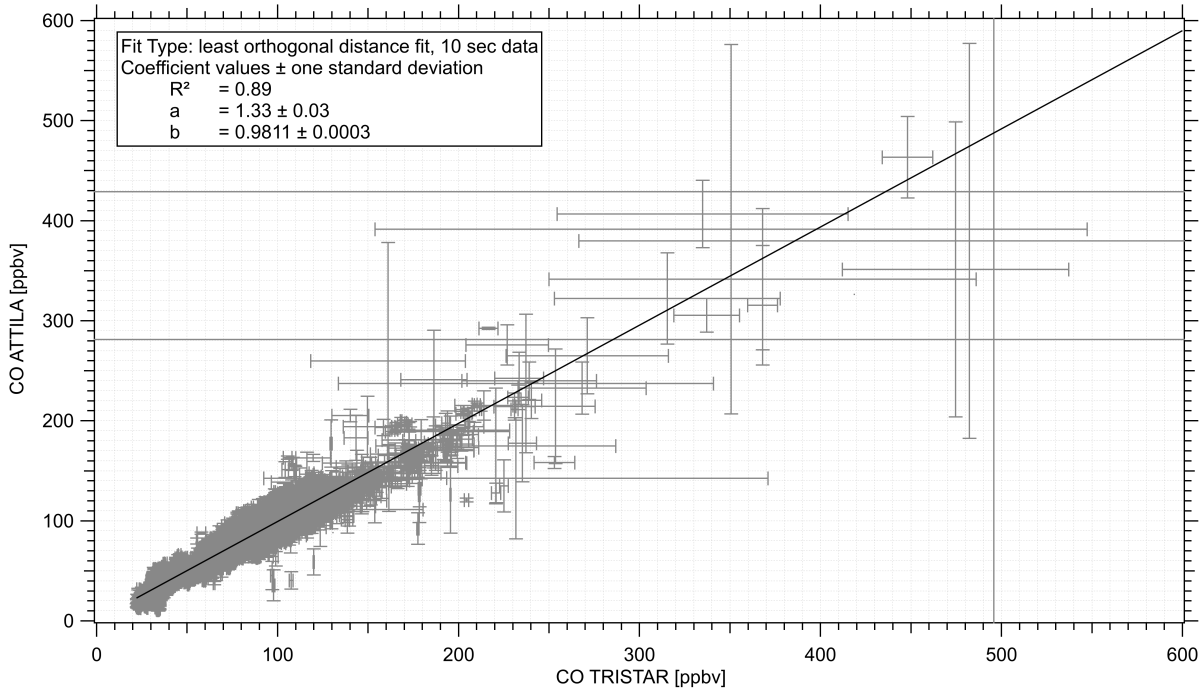

Figure S4. Correlation of all 10 seconds averaged CO ambient measurements from ATTILA on the y-axis and from TRISTAR on the x-axis over the whole CAFE Brazil campaign, excluding the two test flights. The data has been fully processed and corrected. A least orthogonal distance fit has been performed, including the standard deviation of the averaged data.

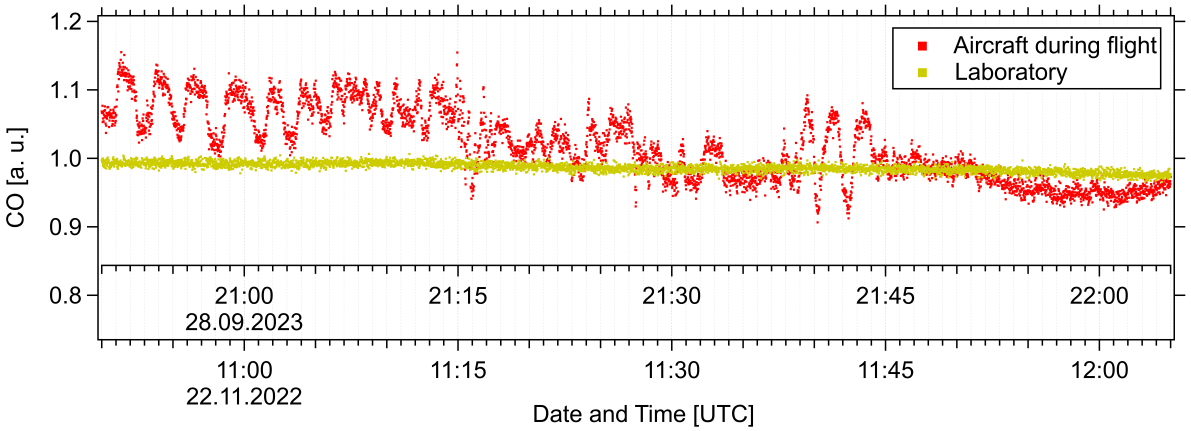

Figure S5. Two time series of constant gas measurements of CO while the ATTILA instrument was built in the rack and located in the laboratory (yellow) and inside the aircraft HALO during the test flight on the 22nd of November 2022 (red). Both time series have been normalized to the standard concentration of the gas bottles used for a better comparison. The concentrations of the standard gas bottles are at 156 ppbv and 245 ppbv for the flight and laboratory, respectively. The measurement uncertainties for the laboratory CO measurements are 1.6 ppbv (0.665 %) and for the aircraft on ground measurement at 8.2 ppbv (5.3 %).

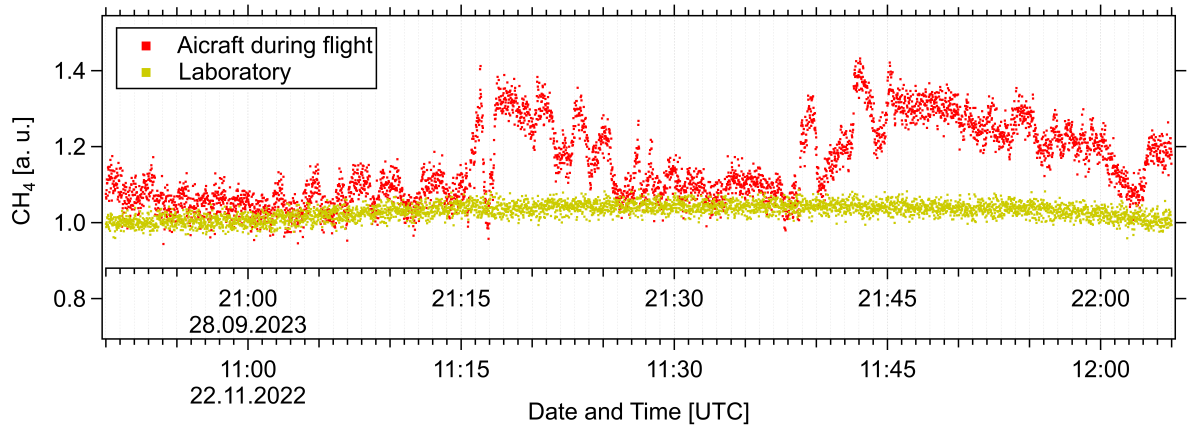

Figure S6. Two time series of constant gas measurements of CH_4 while the ATTILA instrument was built in the rack and located in the laboratory (yellow) and inside the aircraft HALO during the test flight on the 22nd of November 2022 (red). Both time series have been normalized to the standard concentration of the gas bottles used for a better comparison. The concentrations of the standard gas bottles are at 1920 ppbv and 2024 ppbv for the flight and laboratory, respectively. The measurement uncertainties for the laboratory CH_4 measurements are 42.52 ppbv (2.1 %) and for the aircraft measurement at 195 ppbv (10.2 %) for the shown period.

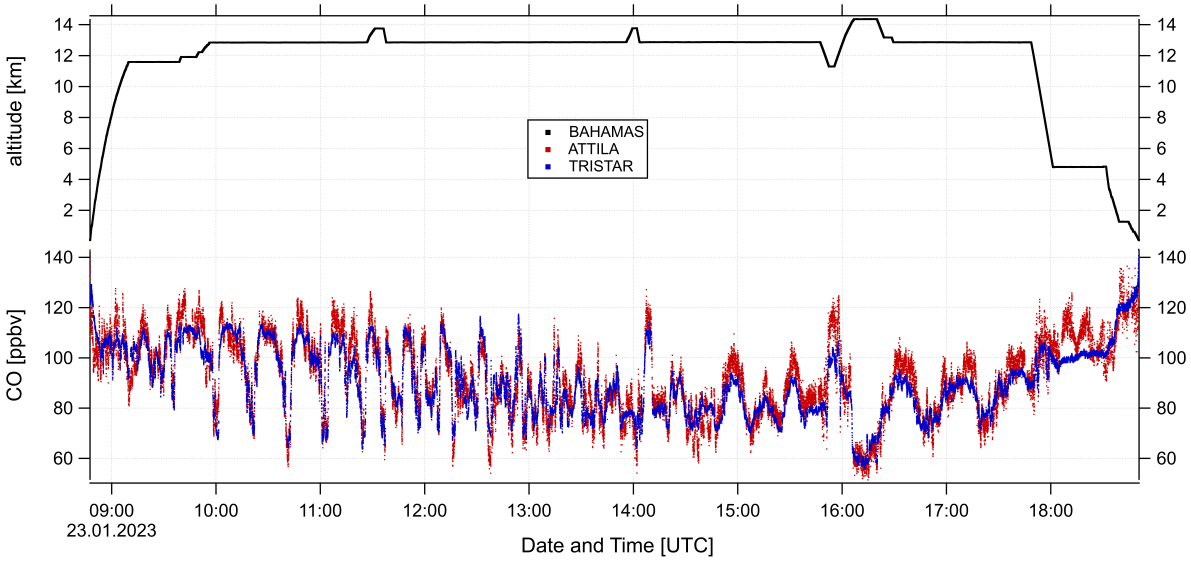

Figure S7. An example research flight (RF19) of fully processed ambient CO data during the CAFE Brazil campaign is shown. The CO mixing ratios of ATTILA are shown in red and from TRISTAR are shown in blue. Additionally, the GPS altitude given by the BAHAMAS instrument (DLR, Oberpfaffenhofen, Germany) is displayed in black. The measurement uncertainty of this flight was at 2.5 % and 7.8 % for TRISTAR and ATTILA CO measurements, respectively.

Part II

Regional Flux Estimation

3.4 Methane global distribution - observed and modeled

Global methane concentrations can be captured with various measurement techniques, either ground-based, in situ or remote-sensed. Long-term measurements of global surface CH_4 are collected by the NOAA network (National Oceanic and Atmospheric Administration, Lan et al., 2025), mostly from marine areas, where no strong source is expected. This data set represents the atmospheric background CH_4 mixing ratios and observes a strong increasing global trend since pre-industrial times.

Remote-sensed observations from satellites can provide details regarding large-scale spatial patterns; however, they often are limited by clouds or in their small spatial-temporal resolution, distinguishing small-scale details. Especially in a strong emitting region, such as in the topics, where most of the wetlands are located, only sparse data from satellites is provided, despite accumulated data sets (Turner et al., 2018; Stendel et al., 2021). Direct in-situ measurements in the troposphere and lower stratosphere can be done by airborne platforms, e.g., aircrafts, which can provide such high-resolution measurements, capturing small-scale atmospheric details. Those airborne observations, combined with analytical approaches and transport models, can provide the insights in understanding complex atmospheric sink-source interactions.

In Figure 3.2, a zonal gradient of CH_4 mixing ratios is shown, derived from a combination of twelve aircraft observations conducted around the globe. The individual campaigns are explained in more detail in Section 3.7. As those campaigns took place in different times of year between 2012 – 2024, their zonal gradients can be interpreted as an annual mean, and were trend-corrected beforehand. This trend-correction was made by using NOAA global monthly mean values, comparing those to a reference month value (January 2022), and then multiplying the factor of the resulting ratio onto the observations of the corresponding months, i.e., when the data was collected. Therefore, all campaign data was transformed to hypothetically being measured in January 2022 with a global background CH_4 mixing ratio of 1906.32 ppbv (Lan et al., 2025).
The zonal distribution of CH_4 shows a few features, which are not directly expected by a trace gas with a lifetime of approximately 9 years, which should be long enough to be well mixed in the troposphere (Shindell et al., 2012; Jackson et al., 2020).
In the northern hemisphere, CH_4 is overall higher than in the southern hemisphere,

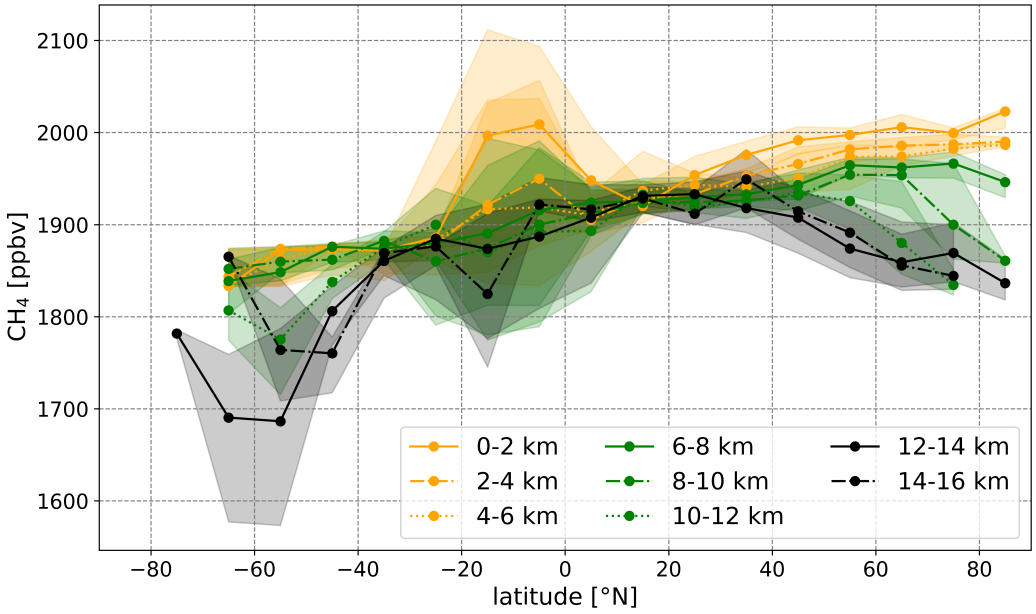

Figure 3.2: Zonal annually averaged gradients of CH_4 from aircraft measurements. Airborne data sets were combined, trend-corrected according to the NOAA monthly mean values onto January 2022 and averaged into 2 km and 10° latitude from twelve different campaigns conducted in the period from 2012–2024 at different locations around the world. Shown are the medians for low altitudes (orange), free to upper tropospheric altitudes in green, and for upper tropospheric and lower stratospheric altitudes in black. Shaded areas represent the 25^{th} and 75^{th} percentiles, respectively. The CH_4 data set from one tropical campaign (CAFE Brazil) is presented in more detail in Section 3.2, and 3.5. All campaigns are presented in more detail in Section 3.7, but without the CH_4 data set.

showing the difference in the land-ocean ratio and population density of both hemispheres, indicating generally stronger emissions in the northern hemisphere. Towards the surface, indicated by orange lines in Figure 3.2, there is an increasing gradient in CH_4 mixing ratios towards the northern high latitudes, likely due to melting permafrost, and anthropogenic emissions such as fossil fuel burnings, releasing large amounts of CH_4. Towards higher altitudes (black lines), dilution with stratospheric air is possible, especially towards the poles due to the lower tropopause, which decreases CH_4 mixing ratios. In the tropics, highest surface CH_4 mixing ratios are observed, which will be further investigated in the next Section 3.5. Here, strong emitters of CH_4 are attributed to wetlands, livestock, and seasonally biomass burning (Basso et al., 2021; Shaw et al., 2022; Hancock et al., 2025; Balasus et al., 2026).

3.5 Airborne observations reveal underestimated riverine methane emissions across the Amazon

This chapter presents an analysis of CH_4 emissions in the Amazon region based on airborne observations and an analytical approach. Simulations of back-trajectories using the STILT model provide footprints of the whole CAFE Brazil campaign, which was further used to evaluate surface fluxes of CH_4 based on current bottom-up estimates. The approach uses Bayesian inversion to evaluate the prior bottom-up estimates with the observations of the CAFE Brazil campaign and achieved improved CH_4 flux maps of the Amazon Basin.

This study was submitted for peer-reviewed publication to *Geophysical Research Letters* on 19 February 2026 and I am the first author of this work. This manuscript has been published on the preprint server *ESS Open Archive* on the 2 March 2026, within the process of submission. I measured, analyzed and processed the CH_4 data, scripted and computed the Bayesian inversion (over HPC, Viper, Garnish), and produced all results presented in the manuscript. The STILT simulations were performed for the CAFE Brazil campaign in cooperation with Dr. Alex J. Turner and Nikhil Dadheech and provided for Bayesian inversion. The modeled data used in this study was simulated and provided by Dr. Anthony A. Bloom (WetCHARTs), James Yoon (GEOS-Chem), Hans-Christoph Lachnitt, and Dr. Paul Konopka (ERA5, CLaMS), or downloaded from open data platforms (CAMS, ECMWF). All data used is publicly available over Zenodo via Ort et al., 2026b. All co-authors reviewed and edited the manuscript prior to submission. In cooperation with Prof. Dr. Christian Frankenberg (California Institute for Technology, Pasadena, USA) and supported by Dr. Horst Fischer, I designed the study and wrote the manuscript with proof-readings of all co-authors. Please note, that during review process parts of the text and content can change.

This article shows a strong underestimation of bottom-up methane emissions, particularly at a wetland-riverine continuum. Those results highlight the spatial variability of tropical ecosystems regarding methane emissions, and hence, the need to improve data coverage and knowledge about underlying processes, and spatial-temporal resolution in state-of-the-art bottom-up estimates.

The supporting information of this study can be found in Section 3.6.

Airborne observations reveal underestimated riverine methane emissions across the Amazon

Linda Ort[1], Christian Frankenberg[2,3], Nikhil Dadheech[4], James (Young Suk) Yoon[4], Alexander J. Turner[4], A. Anthony Bloom[3], Paul Konopka[5], Hans-Christoph Lachnitt[6], Peter Hoor[6], Jos Lelieveld[1,7], Eric A. Kort[1,8], Horst Fischer[1]

[1]Atmospheric Chemistry Department, Max Planck Institute for Chemistry, Mainz, 55128, Germany
[2]Division of Geological and Planetary Sciences, California Institute of Technology, Pasadena, CA, 91125, USA
[3]Jet Propulsion Laboratory, California Institute of Technology, Pasadena, California, 91109, USA.
[4]Department of Atmospheric and Climate Science, University of Washington, Seattle, Washington, 98195, USA
[5]Institute of Climate and Energy Systems, Stratosphere (ICE-4), Forschungszentrum Jülich, 52428, Germany
[6]Institute for Atmospheric Physics, Johannes Gutenberg University, Mainz, 55128, Germany
[7]Climate and Atmosphere Research Center, The Cyprus Institute, Nicosia, 1645, Cyprus
[8]Climate and Space Sciences and Engineering, University of Michigan, Ann Arbor, 48109, USA

Key Points:

- Regionally enhanced methane mixing ratios have been observed over the Amazon Basin about twice those simulated by bottom-up models.
- Wetland emissions are underestimated by a factor up to four in and near rivers.
- Largest fractional methane flux underestimations are linked primarily to large river deltas, reservoirs, and flooded areas in the Amazon.

Corresponding author: Linda Ort, linda.ort@mpic.de

Abstract

Strongly increasing trends in global methane in recent decades highlight the importance of understanding source-sink attributions and climate feedback mechanisms, especially for large natural sources like wetlands. Here, we present an analysis of airborne methane observations above the Amazon Basin conducted from December 2022 through January 2023 that reveal enhanced methane concentrations, especially below 6 km. Using Bayesian inversion with the atmospheric transport model STILT, we optimize surface fluxes to match our observations, starting from prior bottom-up flux estimates by WetCHARTs. The posterior suggests underestimated emissions across the Amazon basin. The largest underestimates occur along rivers and tributaries, where emissions exceeded model values by up to a factor of four. River deltas make up 26% of the underestimated fluxes with reservoirs, and regularly flooded riverine areas contribute 19% and 13%, respectively. This highlights the need for improved understanding of the continuum across wetlands and freshwater bodies for tropical methane emissions.

Plain Language Summary

Methane is a powerful greenhouse gas, and its rapid increase in the atmosphere over recent decades highlights the need to better understand its sources and how it influences the climate. In this study, we analyzed methane measurements taken from aircraft over the Amazon Basin between December 2022 and January 2023. The data showed high methane levels, especially in the lower atmosphere below 6 kilometers. We found the methane emissions were previously underestimated by up to a factor of four. The underestimates were predominately along rivers and tributaries. Our work highlights the need for improved understanding of methane emissions from river systems in the tropics.

1 Introduction

Methane (CH_4), the second most important anthropogenic greenhouse gas after CO_2, has a global warming potential of approximately 25 over a 100-year time horizon, and its atmospheric concentration is projected to continue rising (Dhakal et al., 2022; Uluocak, 2025). The renewed growth of atmospheric methane since 2007 has coincided with isotopic lightening (declining $\delta^{13}C$–CH_4) (Nisbet et al., 2019; Lan et al., 2025), suggesting a shift toward stronger biogenic sources, such as from wetlands or cattle (Turner et al., 2019; Niwa et al., 2025). Alternatively, variations in methane's chemical lifetime of roughly nine years (Prather et al., 2012), which is primarily controlled by its oxidation by the hydroxyl radical (OH), (Lelieveld et al., 2016; Szopa et al., 2021), could contribute to the isotopic trend via kinetic fractionation (Karandashev et al., 2017). However, global OH remains poorly constrained, leaving its role in recent methane growth uncertain (Turner et al., 2017; Rigby et al., 2017; Szopa et al., 2021). Owing to its strong radiative forcing and relatively short atmospheric lifetime compared to most other greenhouse gases, methane is a key target for near-term climate mitigation, as emission reductions can rapidly lower atmospheric concentrations and limit additional warming (Shindell et al., 2012; Jackson et al., 2020; Pérez-Domínguez et al., 2021; Predybaylo et al., 2025). Realizing this potential, however, requires a robust understanding of the spatiotemporal balance between methane sources and sinks.

Methane emissions arise from both anthropogenic (65% of total emissions, e.g., agriculture, fossil fuel exploitation, biomass burning, waste management) and natural sources (35%, e.g., wetlands, inland freshwater, permafrost, microbial activity). As international agreements (e.g., Paris Agreement, Global Methane Pledge, i.e., (Malley et al., 2023)) aim to regulate anthropogenic methane emissions, uncertainties in natural sources may become an even stronger limiting factor in constraining the global methane budget. In addition, wetland and freshwater environments are increasingly sensitive to human in-

fluences, such as climate change, land-use change, and eutrophication (Zhang et al., 2017; Saunois et al., 2020, 2024, 2025; Zhu et al., 2025).

Global methane emission estimates have improved substantially in recent years, as reflected by the narrowing gap between top-down ($575\,\mathrm{Tg\,yr^{-1}}$) and bottom-up ($669\,\mathrm{Tg\,yr^{-1}}$) estimates for global methane emissions between 2010 – 2019 (Saunois et al., 2025). This smaller 16% overestimate in current bottom-up estimates, which is half that of the 30% overestimate in previous bottom-up inventories (Saunois et al., 2020), was mainly from adding new parameters to natural emissions, e.g., reservoirs, lakes, ponds, streams and rivers, and hysteretic temperature sensitivity (Delwiche et al., 2022; Saunois et al., 2024; S. Chen et al., 2025; Saunois et al., 2025). This improvement reduced double counting between freshwater and wetland emissions, considered feedback mechanisms from anthropogenic activities on natural methane emissions (Saunois et al., 2025), and assimilated more methane observations in the inverse system from satellites, surface networks (FLUXNET-CH_4), or other in-situ (e.g., airborne) data (Knox et al., 2019; Delwiche et al., 2021; Lu et al., 2021). However, large uncertainties still remain in natural emissions, such as those from wetlands or inland freshwater (Zhu et al., 2025). Moreover, methane emissions can be highly variable, and localized point source emissions may dominate the total emission budget (Frankenberg et al., 2016; Cusworth et al., 2022; Jacob et al., 2022; He et al., 2024). This is particularly important for ecosystems such as tropical rainforests and the Arctic, where climate induced feedbacks can amplify emissions in ways that are difficult to detect and manage. For example, the balance of production (methanogenesis) and loss (oxidation by methanotrophs) through soils is highly dependent on temperature and soil moisture, which makes it spatiotemporally variable and results in large uncertainties of flux estimates, especially for wetland regions (Murguia-Flores et al., 2018; Turner et al., 2019). Therefore, additional high-resolution observations are crucial to improve knowledge of surface fluxes, which can be used in climate modeling and predictions.

Tropical wetlands account for the largest share of global methane emissions, but limited ground stations and persistent deep cloud cover pose major challenges for ground and satellite observational data coverage, respectively (Asner, 2001). Airborne measurements, on the other hand, have advantages in tropical regions as they are able to collect high-resolution *in-situ* data independent from the infrastructure and cloud cover. Airborne measurements can resolve boundary layer structure, the free troposphere, and entrainment zones vertically, spatially, and temporally (Andreae et al., 2012; Beck et al., 2012; Basso et al., 2021; France et al., 2022). Combined with transport models and inverse simulation methods (e.g., Bayesian inversion), airborne observations can provide valuable insights on regional surface fluxes.

The Amazon rain forest is known to be a strong methane emitter due to its high wetland emissions (Pangala et al., 2017; Saunois et al., 2025; Zhu et al., 2025). Here, wetlands contribute to 83% of the forest's total methane emissions, followed by seasonal biomass burning emissions (17%) that occur largely during the region's dry fire season (Jul-Oct) (Basso et al., 2021; Saunois et al., 2020). Several previous airborne campaigns have identified large fluxes from wetlands in Bolivia or south-east Amazonia (France et al., 2022; Basso et al., 2021). However, the high complexity of wetland regions in parameters such as soil physical properties, vegetation type and water availability through flooding and precipitation, are not fully captured by the spatiotemporal resolution of current models (Dutaur & Verchot, 2007). Therefore, more observations are crucial to understand the Amazon methane budget and its changes over time due to human activity, such as large-scale deforestation (Silva Junior et al., 2021), floodings through hydropower stations (Michael Keller, 1994; Caldas et al., 2023), and a changing climate.

In this study, we use dense *in-situ* observations of methane from a recent airborne campaign over the Amazon with observations ranging from the planetary boundary layer (PBL) to the upper troposphere, covering altitudes between 200 m up to 14.5 km. We

use this spatially-dense set of observations to evaluate current wetland emission inventories, which is the dominant methane source in the Amazon Basin. We also use a high resolution Lagrangian Particle Dispersion Model (LPDM) to relate these airborne observations to surface fluxes. Finally, we identify regions that are over- or underestimated in the process-based wetland model via Bayesian inference.

2 Data and Methods

In a previous study (Ort et al., 2024), we observed regional enhancements of dry methane mixing ratios over the Amazon Basin from December 2022 to January 2023 during the Chemistry of the Atmosphere Field Experiment in Brazil (CAFE Brazil) (Nussbaumer et al., 2024; Curtius et al., 2025), measured by the Airborne Tropospheric Tracer In-situ Laser Absorption spectrometer (ATTILA) via infrared quantum cascade laser absorption spectroscopy (QLAS) (Ort et al., 2024). Via frequent, in-flight calibrations, we derive a measurement uncertainty of $\sigma = \pm 67.69$ ppb for one-minute averaged data over the whole campaign. Higher uncertainties are expected during rapid ascents and descents. Therefore, data taken during those periods were set to the maximum possible uncertainty of $\sigma = \pm 315.35$ ppb, which is derived from the in-flight calibrations before linear correction. See Supporting Information (SI) Section S1 for further details.

Figure 1 shows a comparison of the airborne observations from CAFE Brazil with three different models: CAMS (Copernicus Atmosphere Monitoring Service, Bergamaschi et al. (2013)), GEOS-Chem (Bey et al., 2001; Henze et al., 2007; Maasakkers et al., 2019), and CLaMS (Chemical Lagrangian Model of the Stratosphere, version 3.0, McKenna, Konopka, et al. (2002); McKenna, Grooß, et al. (2002); Konopka et al. (2025)). We find systematic enhancements in the airborne observations from the surface up to 6 km compared to all three models, with the largest enhancements below 4 km. Above ∼6 km, all models and the aircraft observations show a uniform profile with comparable variability (background = 1907 ppb). In the aircraft observations, we observed a mean enhancement of approximately 135 ppb at the lowest altitudes (below 1 km) relative to the free tropospheric background in both months of observations (Dec: 2042.98 ppb; Jan: 2041.13 ppb). We expected stronger variability at higher altitudes due to convective activity, which has also been observed through elevated carbon monoxide and isoprene mixing ratios in the free and upper troposphere (see Ort et al. (2024); Curtius et al. (2025)). However, convection is often poorly represented in models (i.e., (Prein et al., 2015)).

CAMS, GEOS-Chem, and CLaMS differ in their treatment of transport and emissions. CAMS provides operational, globally consistent methane fields constrained by satellite data, but relies on relatively coarse prior emission inventories, limiting regional detail over the Amazon (Bergamaschi et al., 2013). GEOS-Chem allows flexible testing of wetland and anthropogenic inventories, though Amazonian fluxes remain highly sensitive to wetland parameterizations (Maasakkers et al., 2019; Delwiche et al., 2022). CLaMS uses a Lagrangian transport framework with detailed mixing representation suited for inversions, while surface emissions are prescribed from external inventories (e.g., EDGAR and wetland datasets), which constitute a major source of uncertainty (McKenna, Konopka, et al., 2002; McKenna, Grooß, et al., 2002). Additional information is provided in SI Text S2.

The upwind region of the measurements that influence the observed concentration, known as the measurement "footprint", is calculated with the STILT model, a Lagrangian model built upon the Hybrid Single-Particle Lagrangian Integrated Trajectory (HYSPLIT) model (Lin et al., 2003; Turner et al., 2018; Dadheech et al., 2025). STILT can generate time-resolved footprints (e.g., hourly) using meteorological data from the GFS (Global Forecast System) and particle dispersion from a starting location. This produces a 3-D array (x, y, t) that can be integrated over time to yield a two-dimensional footprint

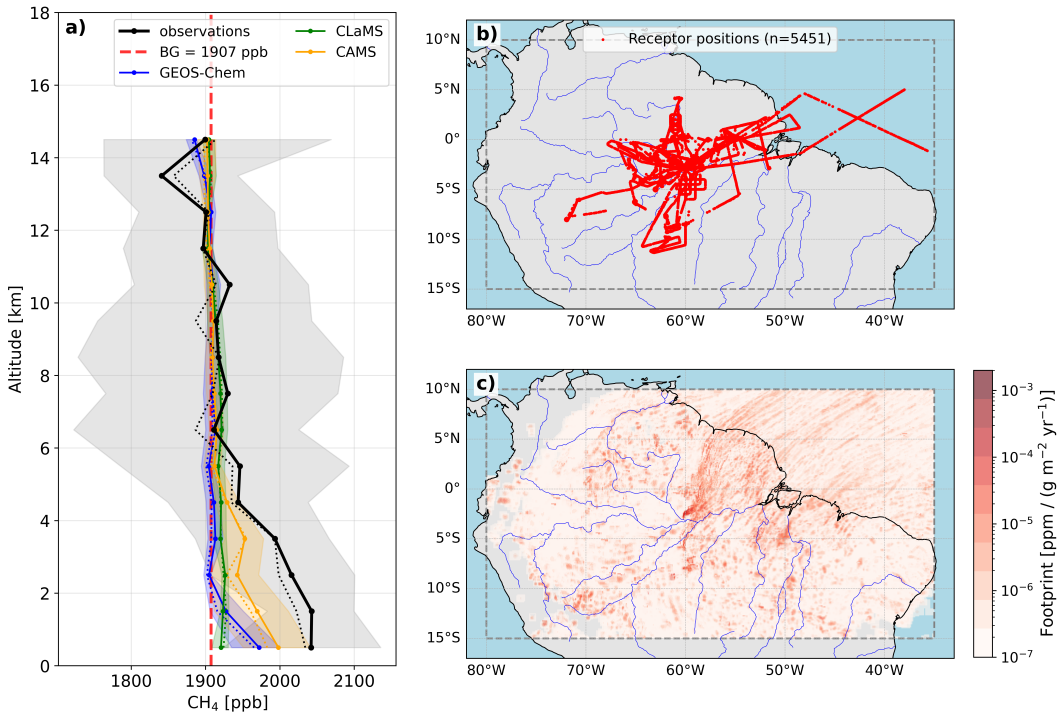

Figure 1. Methane observations and their footprints. Panel a) shows the mismatch between observed methane vertical profiles (black lines) and three model simulations (CAMS: orange lines, GEOS-Chem: blue lines, CLaMS: green lines), each interpolated along the flight tracks. The vertical profiles are derived from the 60 s-data points, averaged over 1 km-boxes over the whole Amazon region, defined from 80°W–35°W and 15°S–10°N (gray grid box in b, c). Solid and dotted lines represent the means, and medians, respectively, and the shaded areas the 25$^{\text{th}}$ and 75$^{\text{th}}$ percentiles. The three modeled data sets were intentionally merged with the free tropospheric mean value of the observations (background; BG = 1907.46 ppb; red line) by applying a relative factor shifting the vertical profile to match the BG. Panels b) shows the receptor positions (60 s data point aircraft position) that result in a valid footprint, superimposed in panel c). The footprints are purely dynamical, meaning they represent any gas particle concentration per unit flux over the whole CAFE Brazil campaign. Units were converted to ppm $(\mathrm{g\,m^{-2}\,yr^{-1}})^{-1}$ using the molar mass of methane for consistency.

matrix unique to each observation. This footprint matrix relates surface fluxes to the *in-situ* airborne observations.

The spatial domain of our study ranges from 80°W–35°W and 15°S–10°N (marked as gray dashed box in Figures 1b and c) with a horizontal grid resolution of 0.1°×0.1°. This domain contains a total number of grid cells (m) on the order of 10^5 ($m = \text{latitudes} \times \text{longitudes} = 249 \times 449 = 111{,}801$). For this spatial domain, footprints were calculated for each 60 s-data point airborne position shown in Figure 1b, hereby referred to as the receptor positions. In total, we have 7,620 60-s averaged airborne observations. Of these, the back trajectories for 2,169 receptors do not reach the surface and have no sensitivity to surface emissions within the defined spatial domain. As such, we use $n = 5{,}451$ receptors with non-zero surface sensitivity for this analysis. A superposition of all footprints is shown in Figure 1c. Approximately 89% of the domain is covered with at least one trajectory endpoint per cell; however, we focus on regions with the 40% highest sensitivity from the observations, quantified by the total number of trajectory-endpoints and total fraction of particles arriving in each cell (see Figure S4). The large number of observations within this region enhances statistical robustness and thereby reduces observational uncertainty. See SI Text S3 for details.

As mentioned above, we relate the observational enhancement towards the background concentration $\mathbf{y}$ ($n \times 1$) to the surface emissions $\mathbf{x}$ ($m \times 1$) using the footprint matrix: $\mathbf{y} = \mathbf{Hx}$, where $\mathbf{H}$ being the footprint matrix of shape ($n \times m$). To infer the emissions $\mathbf{x}$ from the observed concentrations, we can minimize a cost function following Rodgers (1990, 2000). The resulting solution (posterior emissions; $\hat{\mathbf{x}}$) to this inverse problem can be estimated as follows:

$$\hat{\mathbf{x}} = \mathbf{x}_p + \mathbf{B}\mathbf{H}^T(\mathbf{H}\mathbf{B}\mathbf{H}^T + \mathbf{R})^{-1}(\mathbf{y} - \mathbf{H}\mathbf{x}_p). \tag{1}$$

Here, $\mathbf{x}_p$ is the prior emission inventory and is used to provide a baseline estimate of the emissions, weighted with its error covariance matrix $\mathbf{B}$. The observational uncertainty is provided with the observational covariance matrix $\mathbf{R}$. The inversion was solved in observation space by forming the innovation covariance matrix $\mathbf{H}\mathbf{B}\mathbf{H}^T + \mathbf{R}$ and solving the resulting linear system directly, thereby avoiding explicit matrix inversion. The posterior state was obtained by weighting the innovation with the prior covariance and adjoint transport operator, yielding a solution equivalent to the classical Bayesian formulation (Tarantola, 2005; Rodgers, 2000) but computationally efficient for large state dimensions.

We use WetCHARTs (v1.3.3, spatial resolution: 0.5°×0.5°, Bloom et al. (2024)) bottom-up estimates as our prior emission inventory, as it was proven before to capture regional-scale spatial distribution of methane wetland emission fluxes over South America (Zhu et al., 2025; Hancock et al., 2025). Furthermore, biomass burning emissions can be neglected as we observed nearly no biomass burning influence during the CAFE Brazil campaign (Curtius et al., 2025). For the prior state vector $\mathbf{x}_p$ we use the ensemble mean of December and January WetCHARTs simulations (2001-2022) that were generated, i.e., from different wetland extents, terrestrial biosphere models, and CH_4:C temperature dependencies. Therefore, when using WetCHARTs, we do not differentiate between wetland and inland freshwater emissions (e.g. from lakes, reservoirs and rivers).

Additional consideration was given to the construction of the prior error covariance matrix ($\mathbf{B}$, $m \times m$) and the observational covariance matrix ($\mathbf{R}$, $n \times n$). For the prior error covariance matrix, fine-grid ensemble variances are scaled first such that aggregation of the covariance within each coarse grid cell reproduces the original WetCHARTs ensemble uncertainty. Afterwards, we follow prior covariance construction of Turner et al. (2020) by conditional spatial correlations on land-cover similarity. Here, we use Global Lakes and Wetlands Database (GLWD, version 2, Lehner et al. (2025a)) and exponentially decay correlations in distance, such that approximately one-and-a-half coarse grid cells are covered. This spatial correlation ensures that when the inversion increases emis-

sions in a given grid cell, neighboring cells of the same land-cover type within a defined radius also adjust their emissions, with the magnitude of the adjustment decreasing with distance (see SI Section S4.1 and Figure S6 for more detail). For $\mathbf{R}$, we take the variance over all in-flight calibrations ($\mathrm{diag}(\mathbf{R}) = \sigma^2$) while assuming no correlation between each observation, resulting in a diagonal covariance matrix ($n \times 1$) for the inversion.

For large systems, it is computationally infeasible to store the posterior flux uncertainty $\mathbf{P}$ explicitly. Therefore, the random probe Hutchinson estimator was used to approximate its diagonal elements, providing grid-level posterior standard deviations ($\hat{\sigma}_{i,i} \approx \sqrt{\mathbf{P}_{i,i}}$). This stochastic trace estimation method efficiently samples random perturbations to estimate the variance reduction in each grid cell (Scheuer & Stoller, 1962; Hutchinson, 1989). Furthermore, we calculate the averaging kernel sensitivity, which is a dimensionless measure of information gain that indicates the fraction of the posterior flux signal driven by the observations, as the diagonal elements of the posterior averaging kernel mapped onto the coarse flux grid. More details on the inversion settings are available in SI Text S4.

3 High Resolution Methane Fluxes

The resulting posterior emissions using airborne observations and WetCHARTs bottom-up estimates are shown in Figure 2. The left panels present the results for the entire domain, while the right panels provide a detailed analysis of the most affected areas, largely within the highest 40% of observation sensitivity as indicated by the green contour lines. The posterior fluxes are shown in Fig 2a and 2b, the flux differences between the posterior and prior in 2c and 2d, their ratio can be found in 2e and 2f, and the diagonal elements of the averaging kernel matrix in 2g and 2h. The averaging kernel sensitivity indicates where the inversion effectively updates the prior emissions based on observational constraints in the prior grid resolution. Error statistics on our inversion indicates that it provides eight independent pieces of information for the whole domain (measured by degrees of freedom for signal, DOFS). Overall, the inversion increases the regional methane flux from 62.23 ± 5.04 to $65.68 \pm 4.95\,\mathrm{Tg\,yr^{-1}}$, with the uncertainty calculated from Monte Carlo–derived 1σ error. A detailed view on prior and posterior uncertainties can be found in the SI Figure S7.

We first focus on Figure 2a, b. In general, posterior emissions reflect the spatial pattern of the prior emissions, which capture the regional-scale spatial distribution of methane emission fluxes over Brazil (Zhu et al., 2025; Hancock et al., 2025). However, more detail in spatial flux variability could be achieved after the inversion due to the higher spatial resolution provided by the footprint matrix.

Regions with low observational sensitivities, which occur mainly the northwestern and southern part of our domain, show little change in emission after the inversion (Fig 2c, d). Nevertheless, a few exceptions can be found in the east of Peru - a large wetland area - as well as in the large river delta of Venezuela on the northern edge of our domain, with changes up to $50\,\mathrm{g\,CH_4\,m^{-2}\,yr^{-1}}$.

Within the region most strongly constrained by observations, we qualitatively see the largest previous underestimates in methane fluxes close to large river streams (e.g., the Amazon river) and in the Amazon delta, with posterior fluxes of up to $227.51\,\mathrm{g\,CH_4\,m^{-2}\,yr^{-1}}$. For comparison, the prior emissions within the spatial domain had a maximum methane flux of $103.45\,\mathrm{g\,CH_4\,m^{-2}\,yr^{-1}}$. The largest change in the posterior emissions relative to the prior is $152\,\mathrm{g\,CH_4\,m^{-2}\,yr^{-1}}$, which occurs southwest of the city of Manaus, Brazil, where large areas of seasonally flooded forests persist (3.7°S, 61.3°W). In general, the prior emissions inventory underestimated methane emissions across riverine systems.

However, our inversion shows some regions where the WetCHARTs prior emissions are up to $50\,\mathrm{g\,CH_4\,m^{-2}\,yr^{-1}}$ higher than the posterior, as indicated by blue colors in Fig. 2c, d. In these regions, the bottom-up estimates seem to overestimate methane emissions, which may be due to higher surface complexity and vegetation properties, or under-constrained climate-induced feedback mechanisms such as localized drying of riverbeds resulting in more methane oxidation within soils (Stanley et al., 2016). WetCHARTs uses empirical, biogeochemical modeling with remotely sensed inundation, model-driven relative humidity fluxes, and a temperature sensitivity factor to estimate methane fluxes (Bloom et al., 2017; Zhu et al., 2025). Although WetCHARTs still captures small spatial details (see Fig. S7 in SI), our inversion finds even stronger spatial heterogeneity, especially close to large river systems, mostly due to the inversion's higher resolution. However, WetCHARTs does not explicitly represent several processes that may contribute to the spatial heterogeneity of wetland–river methane emissions, including vegetation composition, macrophyte presence, hydrological state, flow velocity, and water depth.

Comparing the ratio of posterior and prior fluxes (Fig. 2e, f), we find that methane emissions are underestimated by the prior by up to a factor of four, mostly north of Manaus and in the Amazon river delta. Most efficiently updated by the inversion is the region southwest of Manaus, with AK sensitivities up to 0.48 (48% constrained by observations), which coincides with the area of highest fluxes in the posterior.

To identify which surface types drive the regional emission adjustment, we decompose the inversion-derived flux changes by land-cover class and quantify both their absolute and relative contributions. Figure 3 shows class-integrated absolute changes in methane emissions ($\mathbf{\Delta F}$=$\hat{\mathbf{F}}$-$\mathbf{F}_p$; $\mathrm{Tg\,yr^{-1}}$) with 1σ Monte Carlo uncertainties, together with the prior-weighted relative changes (%) for all land-cover types within the well-constrained area. Surface classifications are from GLWD (500 m at the equator) and re-gridded to our resolution via nearest-neighbor interpolation, assigning each cell the dominant land-cover class (see Figure S5). We subdivide the land-cover types into colored main groups, according to Lehner et al. (2025b).

The strongest absolute change in wetland classifications can be found in coastal wetland regions, e.g., large river deltas, mangroves, and large estuarine rivers. Notably, the spatially-averaged percentage corrections applied to the prior emissions were high for large river deltas (26%) and major estuarine rivers (10%), with changes in total emissions after the inversion of $+0.40\pm0.009\,\mathrm{Tg\,yr^{-1}}$ and $+0.05\pm0.002\,\mathrm{Tg\,yr^{-1}}$, respectively. Methanogens decompose organic matter in waterlogged, anaerobic soils, producing methane via methanogenesis from substrates such as acetate and hydrogen. Conversely, methanotrophic bacteria oxidize methane to CO_2 or CH_3OH under oxic conditions (Murguia-Flores et al., 2018). Tropical soils exhibit intense microbial activity, often isolated from oxygen by extensive water bodies. River transport and deposition of organic matter can further distribute carbon substrates downstream. Methanogenesis in river sediments is strongly temperature-dependent and intensifies with warming (Yvon-Durocher et al., 2014). Rising temperatures enhance microbial metabolism and anaerobic carbon mineralization, increasing methane production. The growing frequency and intensity of river heatwaves, particularly in the Amazon and Congo Basin (Y. Chen et al., 2026), elevate sediment temperatures and may reduce oxygen availability, potentially shifting rivers toward sustained methane production with distinct temporal emission regimes.

Furthermore, we observe strong relative changes and moderate absolute changes in methane fluxes in inland waterbodies, e.g., reservoirs, large rivers, and permanent waterbodies. In particular, large rivers contribute $+0.07\pm0.001\,\mathrm{Tg\,yr^{-1}}$ to the change in the regional budget, and reservoirs show a strong relative change of up to 19% in methane emissions, even though their absolute contribution is minor ($+0.029\pm0.0004\,\mathrm{Tg\,yr^{-1}}$). While there are limited studies about methane emissions from reservoirs (Michael Keller, 1994; Delwiche et al., 2022), there are growing concerns about the impact of the increasing number of hydropower stations in the Amazon (Flecker et al., 2022; Caldas et al.,

2023). Early studies found that newly-built reservoirs in tropical regions (Gatun Lake, Panama) emit large amounts of methane through bubbling of up to $3.65-73\,\mathrm{g\,CH_4\,m^{-2}\,yr^{-1}}$ at deeper sites ($>7\,\mathrm{m}$) and $730\,\mathrm{g\,CH_4\,m^{-2}\,yr^{-1}}$ at shallow sites ($<2\,\mathrm{m}$) (Michael Keller, 1994). Furthermore, substantial inundation of forested regions for hydropower energy recovery often results in dead trees in the lakes due to deficient forest clearing (Caldas et al., 2023). Consequently, the presence of dead tree-stumps in the inundated area could function as a carbon conduit, facilitating the transfer of microbial matter from the underlying soil.

Across forested and non-forested zones with both organic and mineral soils (e.g., riverine, regularly flooded, forested; palustrine, non-forested, seasonally-flooded; Lacustrine, forested; tropical/subtropical peatland, forested), methane emissions show moderate increases after inversion. Of these biomes, regularly-flooded riverine and tropical peatland contribute most to the regional budget adjustment, with absolute and relative changes of $+0.25\pm0.005\,\mathrm{Tg\,yr^{-1}}$ (13%), and $+0.28\pm0.009\,\mathrm{Tg\,yr^{-1}}$ (7%), respectively. Non-forested, seasonally-flooded palustrine areas show a strong relative change (36%) due to a small prior total emission flux (not shown); however, their absolute contribution is nearly zero ($+0.003\pm0.00005\,\mathrm{Tg\,yr^{-1}}$).

We expect pronounced seasonal variability in this wetland group according to WetCHARTs (Fig. S12), which simulates peak emissions during the wet season (March–April) and minima in the dry season (July–October), which is also in agreement with biweekly multi-year airborne observations from Basso et al. (2021). During the dry season, regional methane fluxes are increasingly influenced by biomass burning. Comparing annual WetCHARTs means to the December–January fluxes used here reveals a north–south contrast: December–January fluxes are $\sim30\,\mathrm{g\,CH_4\,m^{-2}\,yr^{-1}}$ higher than the annual average south of the Amazon River and $\sim30\,\mathrm{g\,CH_4\,m^{-2}\,yr^{-1}}$ lower in the northern Amazon (Fig. S8). Tropical ecosystems are changing rapidly through warmer temperatures and altered precipitation patterns, resulting in strong seasonal and regional differences in water levels, temperatures, and methane emissions. Anthropogenic land-use in the Amazon has increased dramatically over the last decades, increasing not only methane emissions from livestock, but also impacting forested peatlands, which contain large amounts of carbon (Girkin et al., 2022).

Additionally, we find the strongest change in methane total emissions in dryland cells ($+1.14\pm0.015\,\mathrm{Tg\,yr^{-1}}$ or +14%). Possible reasons can not be evaluated in this study, as this could include methane emissions from other sources than wetlands, such as livestock, biomass burning, or other anthropogenic sources. However, those enhanced posterior emissions may also arise, to some extent, from spatial aggregation effects, namely mixing dryland with wetland fractions which would bias grid-scale fluxes high. Moreover, methane emissions coming from regions GLWD have not classified at wetlands might be experiencing inundation (Balasus et al., 2026). Possible surface property changes may also contribute to that enhancement, as those are highly affected by climate change (Franco et al., 2025) and are not considered in the WetCHARTs inventory.

4 Conclusions and Outlook

The tropics are important methane source regions. In particular, the Amazon rain forest is a highly complex region with a variable and sensitive ecosystem, particularly in the context of climate change. Better quantifying its changing contribution to greenhouse gas fluxes is key in global total emissions and carbon cycling. In this study, we used airborne observations of methane from the early wet season (December 2022 - January 2023) above the Amazon rain forest to evaluate current bottom-up methane emission estimates using a footprint analysis and a Bayesian inversion. We focused on wetland emissions, which are the strongest methane emitters in the tropics. While WetCHARTs bottom-up emissions provided a good estimate of methane fluxes for most of the Amazon Basin

after our inversion, some regional fluxes were estimated to be up to four times larger than WetCHARTs. We found the largest changes between the prior and posterior in large river deltas, reservoirs, and river systems in the Amazon. Spatial variability of methane fluxes highly depend on small-scale surface properties (e.g., microbial activity, saturation), where even small rivers and lakes can emit large amounts of methane.

Our inversion results suggest large underestimations of methane fluxes across wetland-river continuum, particularly at the estuaries of the Amazon, where large volumes of freshwater enters the Atlantic. Beyond revealing previously unobserved fluxes, our results highlight the urgent need to better characterize the processes controlling methanogenesis across the tropical aquatic continuum. The important role of soil microbes as sources and sinks of methane is not yet well understood, especially in a changing climate. Temperature sensitivity and deposition of eroded soils containing large amounts of organic matter in coastal regions needs to be considered for carbon emissions, and not only for the Amazon. Similar biases could extend to other tropical river systems in Central Africa (Balasus et al., 2026), and Southeast Asia, where observational constraints remain sparse and process representation is uncertain. Anthropogenic activities are increasingly affecting tropical ecosystems, underscoring the need for more accurate attribution of top-down fluxes to the multiple, overlapping processes contributing to methane emissions (Pangala et al., 2017). Improved observational coverage and model representation of tropical large rivers, deltas, flooded forests, peatlands, and reservoirs, are therefore critical for reducing uncertainties, capturing small-scale variability, and solving temporal dynamics in the global methane budget.

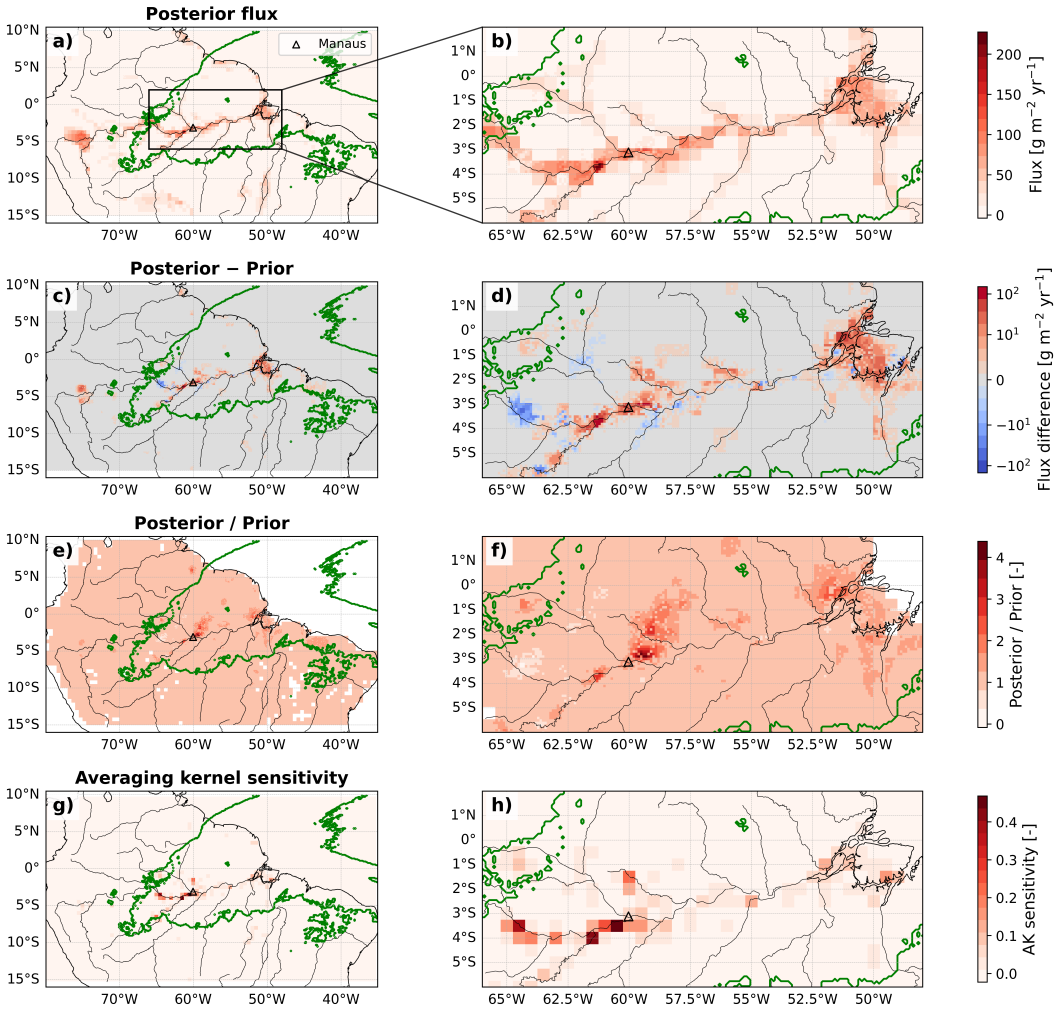

Figure 2. Posterior methane emissions over Amazonian basin. The left panels show posterior methane fluxes over the full Amazonian domain, with a close-up (black rectangle in panel a) shown on the right, both at 0.1°×0.1° resolution. The posterior fluxes represent our optimized emission estimates obtained from the inversion, which uses WetCHARTs bottom-up fluxes as priors and is constrained by airborne methane observations (a, b). The difference between the posterior and the prior (c, d), and the ratio between the posterior and the prior (e, f), indicate the strongest change in emissions after the inversion in the Amazon delta and river regions. The averaging kernel (AK) sensitivities represent the ability of the observations to quantify emissions independently from the prior estimates on the prior grid resolution (0.5°×0.5°, g, h). The green contour lines surround the area of the 40% strongest observational influence. The triangle marks the location of the city Manaus.

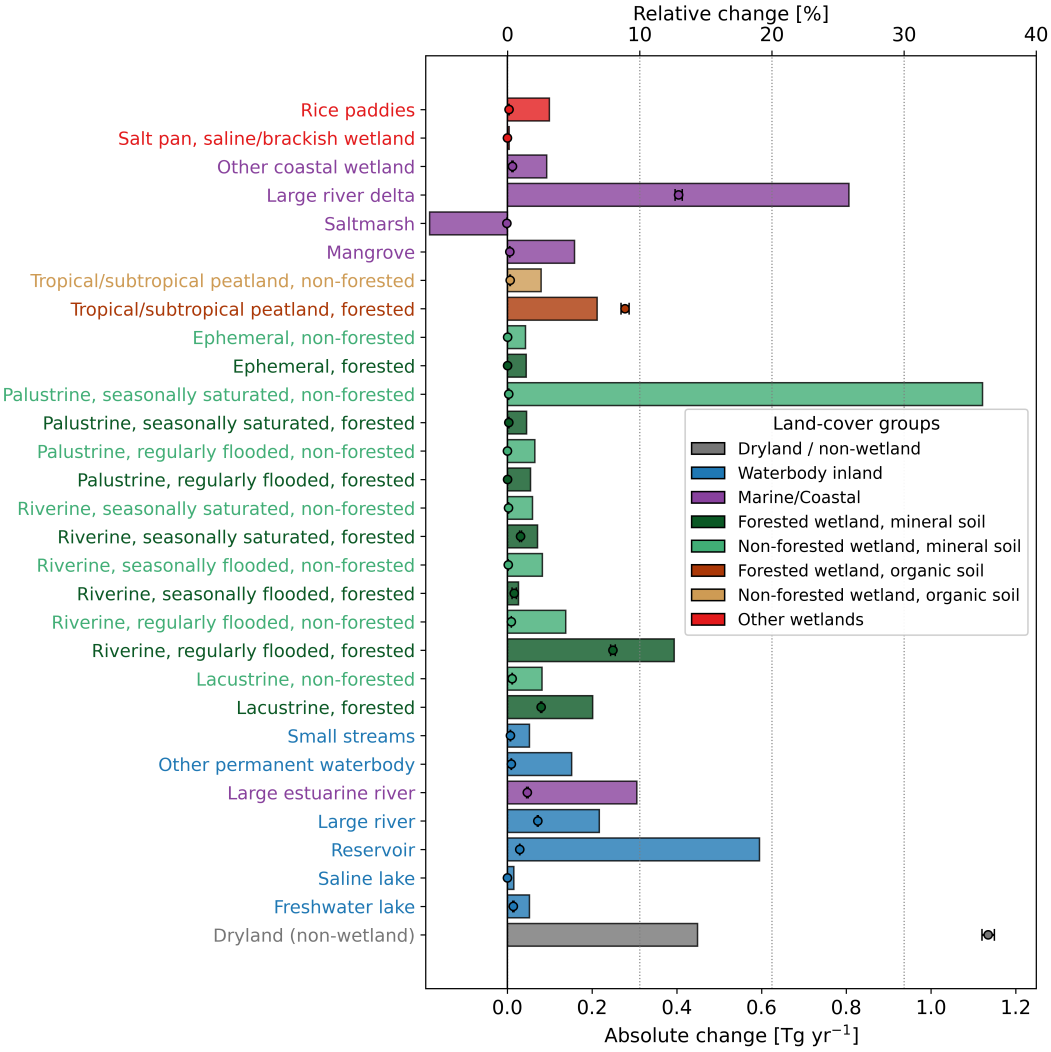

Figure 3. Land-cover–specific changes in methane emissions after inversion within the area of 40% highest observational sensitivity. Horizontal bars (top x-axis) show the prior-weighted relative change (%), where grid-cell contributions are weighted by their prior absolute flux within each land-cover classification by GLWD (same as used for spatial correlations of prior covariance matrix). Dots indicate the corresponding absolute change in class-integrated emissions ($\Delta\mathbf{F}=\hat{\mathbf{F}}$-$\mathbf{F}_p$; Tg yr^{-1}), with black error bars representing the 1σ uncertainty of total fluxes derived from 100 Monte Carlo realizations of the spatially correlated flux perturbations consistent with the inversion error covariance. Bar and dot colors indicate land-cover groupings (e.g., waterbody inland or marine/coastal, forested/non-forested, organic/mineral soils), adapted from Lehner et al. (2025b). A similar figure for the full domain can be found in Figure S11.

Open Research Section

Observational data used in this study can be obtained on the HALO database platform by signing a data contract (DLR, 2023) or can be found, together with the model data used in this study on Zenodo via Ort et al. (2026). CAMS data (release: v23r1, source: TM5-MP 4D-Var) was downloaded via (Copernicus Atmosphere Monitoring Service, 2020) [last access: 7 March 2025]. WetCHARTs ensemble simulations can be accessed via Bloom et al. (2024) and are explained in detail in Bloom et al. (2017). The GLWD data set can be found via Lehner et al. (2025a), and is explained in Lehner et al. (2025b); Lehner and Döll (2004).

As Applicable – Inclusion in Global Research Statement

Acknowledgments

We acknowledge all participants from the CAFE Brazil campaign and those who helped developing the models. We thank Uwe Parchatka and Lenard Röder for their technical and analytical support with the methane measurements. ND, JYY, and AJT were supported by Schmidt Sciences through the VESRI program and the $FETCH_4$ project. Part of this research was carried out at the Jet Propulsion Laboratory, California Institute of Technology, under a contract with the National Aeronautics and Space Administration.

References

Andreae, M. O., Artaxo, P., Beck, V., Bela, M., Freitas, S., Gerbig, C., ... Wofsy, S. C. (2012). Carbon monoxide and related trace gases and aerosols over the amazon basin during the wet and dry seasons. *Atmospheric Chemistry and Physics*, *12*(13), 6041–6065. Retrieved from `https://acp.copernicus.org/articles/12/6041/2012/` doi: 10.5194/acp-12-6041-2012

Asner, G. P. (2001). Cloud cover in landsat observations of the brazilian amazon. *International Journal of Remote Sensing*, *22*(18), 3855–3862. Retrieved from `https://doi.org/10.1080/01431160010006926` doi: 10.1080/01431160010006926

Balasus, N., Jacob, D. J., Bloom, A. A., East, J. D., Estrada, L. A., Hancock, S. E., ... Worden, J. R. (2026). 2019–2024 trends in african livestock and wetland emissions as contributors to the global methane rise. *EGUsphere*, *2026*, 1–30. Retrieved from `https://egusphere.copernicus.org/preprints/2026/egusphere-2025-6251/` (preprint) doi: 10.5194/egusphere-2025-6251

Basso, L. S., Marani, L., Gatti, L. V., Miller, J. B., Gloor, M., Melack, J., ... Neves, R. A. L. (2021). Amazon methane budget derived from multi-year airborne observations highlights regional variations in emissions. *Communications Earth & Environment*, *2*(1), 246. doi: 10.1038/s43247-021-00314-4

Beck, V., Chen, H., Gerbig, C., Bergamaschi, P., Bruhwiler, L., Houweling, S., ... Wofsy, S. C. (2012). Methane airborne measurements and comparison to global models during barca. *Journal of Geophysical Research: Atmospheres*, *117*(D15). Retrieved from `https://agupubs.onlinelibrary.wiley.com/doi/abs/10.1029/2011JD017345` doi: https://doi.org/10.1029/2011JD017345

Bergamaschi, P., Houweling, S., Segers, A., Krol, M., Frankenberg, C., Scheepmaker, R. A., ... Gerbig, C. (2013). Atmospheric ch4 in the first decade of the 21st century: Inverse modeling analysis using sciamachy satellite retrievals and noaa surface measurements. *Journal of Geophysical Research: Atmospheres*, *118*(13), 7350-7369. Retrieved from `https://agupubs.onlinelibrary.wiley.com/doi/abs/10.1002/jgrd.50480` doi: https://doi.org/10.1002/jgrd.50480

Bey, I., Jacob, D. J., Yantosca, R. M., Logan, J. A., Field, B. D., Fiore, A. M., ... Schultz, M. G. (2001). Global modeling of tropospheric chemistry with assimilated meteorology: Model description and evaluation. *Journal of Geophysical Research: Atmospheres*, *106*(D19), 23073-23095. Retrieved from https://agupubs.onlinelibrary.wiley.com/doi/abs/10.1029/2001JD000807 doi: https://doi.org/10.1029/2001JD000807

Bloom, A. A., Bowman, K. W., Lee, M., Turner, A. J., Schroeder, R., Worden, J. R., ... Jacob, D. J. (2017). A global wetland methane emissions and uncertainty dataset for atmospheric chemical transport models (wetcharts version 1.0). *Geoscientific Model Development*, *10*(6), 2141–2156. Retrieved from https://gmd.copernicus.org/articles/10/2141/2017/ doi: 10.5194/gmd-10-2141-2017

Bloom, A. A., Bowman, K. W., Lee, M., Turner, A. J., Schroeder, R., Worden, J. R., ... Jacob, D. J. (2024). *CMS: Global 0.5-deg Wetland Methane Emissions and Uncertainty (WetCHARTs v1.3.3).* ORNL Distributed Active Archive Center. Retrieved from https://doi.org/10.3334/ORNLDAAC/2346 (Accessed: 2026-01-07) doi: 10.3334/ORNLDAAC/2346

Caldas, B., Thieme, M. L., Shahbol, N., Coelho, M. E., Grill, G., Van Damme, P. A., ... de Brito Ribeiro, M. C. L. (2023). Identifying the current and future status of freshwater connectivity corridors in the amazon basin. *Conservation Science and Practice*, *5*(1), e12853. Retrieved from https://conbio.onlinelibrary.wiley.com/doi/abs/10.1111/csp2.12853 doi: https://doi.org/10.1111/csp2.12853

Chen, S., Yuan, K., Li, F., Zhu, Q., & Zhuang, Q. (2025). Hysteretic temperature sensitivity in wetland ch4 emission modeling. *Agricultural and Forest Meteorology*, *372*, 110704. Retrieved from https://www.sciencedirect.com/science/article/pii/S0168192325003247 doi: https://doi.org/10.1016/j.agrformet.2025.110704

Chen, Y., Su, Z., Woolway, R. I., Wanders, N., Wu, S., Huang, Z., & Luo, M. (2026). Persistent river heatwaves are emerging worldwide under climate change. *Nature Communications*, *17*(1), 94. Retrieved from https://doi.org/10.1038/s41467-025-66868-5 doi: 10.1038/s41467-025-66868-5

Copernicus Atmosphere Monitoring Service. (2020). *Cams global inversion-optimised greenhouse gas fluxes and concentrations.* Copernicus Atmosphere Monitoring Service (CAMS) Atmosphere Data Store. Retrieved from https://doi.org/10.24381/ed2851d2 (Accessed on 07-03-2025) doi: 10.24381/ed2851d2

Curtius, J., Heinritzi, M., Beck, L. J., Poehlker, M. L., Tripathi, N., Krumm, B. E., ... Lelieveld, J. (2025, 2025 APR 1). Isoprene nitrates drive new particle formation in amazon's upper troposphere (vol 636, 124, 2024) [Correction; Early Access]. *NATURE*. doi: 10.1038/s41586-025-08906-2

Cusworth, D. H., Thorpe, A. K., Ayasse, A. K., Stepp, D., Heckler, J., Asner, G. P., ... Duren, R. M. (2022). Strong methane point sources contribute a disproportionate fraction of total emissions across multiple basins in the united states. *Proceedings of the National Academy of Sciences*, *119*(38), e2202338119. Retrieved from https://www.pnas.org/doi/abs/10.1073/pnas.2202338119 doi: 10.1073/pnas.2202338119

Dadheech, N., He, T.-L., & Turner, A. J. (2025). High-resolution greenhouse gas flux inversions using a machine learning surrogate model for atmospheric transport. *Atmospheric Chemistry and Physics*, *25*(10), 5159–5174. Retrieved from https://acp.copernicus.org/articles/25/5159/2025/ doi: 10.5194/acp-25-5159-2025

Delwiche, K. B., Harrison, J. A., Maasakkers, J. D., Sulprizio, M. P., Worden, J., Jacob, D. J., & Sunderland, E. M. (2022). Estimating drivers and pathways for hydroelectric reservoir methane emissions using a new mechanistic model. *Journal of Geophysical Research: Biogeosciences*, *127*(8), e2022JG006908.

Retrieved from https://agupubs.onlinelibrary.wiley.com/doi/abs/10.1029/2022JG006908 (e2022JG006908 2022JG006908) doi: https://doi.org/10.1029/2022JG006908

Delwiche, K. B., Knox, S. H., Malhotra, A., Fluet-Chouinard, E., McNicol, G., Feron, S., ... Jackson, R. B. (2021). Fluxnet-ch_4: a global, multi-ecosystem dataset and analysis of methane seasonality from freshwater wetlands. *Earth System Science Data*, *13*(7), 3607–3689. Retrieved from https://essd.copernicus.org/articles/13/3607/2021/ doi: 10.5194/essd-13-3607-2021

Dhakal, S., Minx, J. C., Toth, F. L., Abdel-Aziz, A., Figueroa Meza, M. J., Hubacek, K., ... Wiedmann, T. (2022). Emissions trends and drivers. In P. R. Shukla et al. (Eds.), *Climate change 2022: Mitigation of climate change.* Cambridge University Press. doi: 10.1017/9781009157926.004

DLR. (2023). *Halo data, base, cafe brazil [data set].* German Aerospace Center (DLR). Retrieved from https://halo-db.pa.op.dlr.de/mission/135 (last access: 18 June 2024)

Dutaur, L., & Verchot, L. V. (2007). A global inventory of the soil ch4 sink. *Global Biogeochemical Cycles*, *21*(4). Retrieved from https://agupubs.onlinelibrary.wiley.com/doi/abs/10.1029/2006GB002734 doi: https://doi.org/10.1029/2006GB002734

Flecker, A. S., Shi, Q., Almeida, R. M., Angarita, H., Gomes-Selman, J. M., García-Villacorta, R., ... Gomes, C. P. (2022). Reducing adverse impacts of amazon hydropower expansion. *Science*, *375*(6582), 753-760. Retrieved from https://www.science.org/doi/abs/10.1126/science.abj4017 doi: 10.1126/science.abj4017

France, J. L., Lunt, M. F., Andrade, M., Moreno, I., Ganesan, A. L., Lachlan-Cope, T., ... Jones, A. E. (2022). Very large fluxes of methane measured above bolivian seasonal wetlands. *Proceedings of the National Academy of Sciences*, *119*(32), e2206345119. Retrieved from https://www.pnas.org/doi/abs/10.1073/pnas.2206345119 doi: 10.1073/pnas.2206345119

Franco, M. A., Rizzo, L. V., Teixeira, M. J., Artaxo, P., Azevedo, T., Lelieveld, J., ... Machado, L. A. T. (2025). How climate change and deforestation interact in the transformation of the amazon rainforest. *Nature Communications*, *16*(1), 7944. Retrieved from https://doi.org/10.1038/s41467-025-63156-0 doi: 10.1038/s41467-025-63156-0

Frankenberg, C., Thorpe, A. K., Thompson, D. R., Hulley, G., Kort, E. A., Vance, N., ... Green, R. O. (2016). Airborne methane remote measurements reveal heavy-tail flux distribution in four corners region. *Proceedings of the National Academy of Sciences*, *113*(35), 9734-9739. Retrieved from https://www.pnas.org/doi/abs/10.1073/pnas.1605617113 doi: 10.1073/pnas.1605617113

Girkin, N. T., Cooper, H. V., Ledger, M. J., O'Reilly, P., Thornton, S. A., Åkesson, C. M., ... Roucoux, K. H. (2022). Tropical peatlands in the anthropocene: The present and the future. *Anthropocene*, *40*, 100354. Retrieved from https://www.sciencedirect.com/science/article/pii/S2213305422000352 doi: https://doi.org/10.1016/j.ancene.2022.100354

Hancock, S. E., Jacob, D. J., Chen, Z., Nesser, H., Davitt, A., Varon, D. J., ... Maasakkers, J. D. (2025). Satellite quantification of methane emissions from south american countries: a high-resolution inversion of tropomi and gosat observations. *Atmospheric Chemistry and Physics*, *25*(2), 797–817. Retrieved from https://acp.copernicus.org/articles/25/797/2025/ doi: 10.5194/acp-25-797-2025

He, Z., Gao, L., Liang, M., & Zeng, Z.-C. (2024). A survey of methane point source emissions from coal mines in shanxi province of china using ahsi on board gaofen-5b. *Atmospheric Measurement Techniques*, *17*(9), 2937–2956. Re-

trieved from https://amt.copernicus.org/articles/17/2937/2024/ doi: 10.5194/amt-17-2937-2024

Henze, D. K., Hakami, A., & Seinfeld, J. H. (2007). Development of the adjoint of geos-chem. *Atmospheric Chemistry and Physics*, *7*(9), 2413–2433. Retrieved from https://acp.copernicus.org/articles/7/2413/2007/ doi: 10.5194/acp-7-2413-2007

Hutchinson, M. (1989). A stochastic estimator of the trace of the influence matrix for laplacian smoothing splines. *Communications in Statistics - Simulation and Computation*, *18*(3), 1059–1076. Retrieved from https://doi.org/10.1080/03610918908812806 doi: 10.1080/03610918908812806

Jackson, R. B., Saunois, M., Bousquet, P., Canadell, J. G., Poulter, B., Stavert, A. R., ... Tsuruta, A. (2020, jul). Increasing anthropogenic methane emissions arise equally from agricultural and fossil fuel sources. *Environmental Research Letters*, *15*(7), 071002. Retrieved from https://dx.doi.org/10.1088/1748-9326/ab9ed2 doi: 10.1088/1748-9326/ab9ed2

Jacob, D. J., Varon, D. J., Cusworth, D. H., Dennison, P. E., Frankenberg, C., Gautam, R., ... Duren, R. M. (2022). Quantifying methane emissions from the global scale down to point sources using satellite observations of atmospheric methane. *Atmospheric Chemistry and Physics*, *22*(14), 9617–9646. Retrieved from https://acp.copernicus.org/articles/22/9617/2022/ doi: 10.5194/acp-22-9617-2022

Karandashev, K., Xu, Z.-H., Meuwly, M., Vaníček, J., & Richardson, J. O. (2017, 12). Kinetic isotope effects and how to describe them. *Structural Dynamics*, *4*(6), 061501. Retrieved from https://doi.org/10.1063/1.4996339 doi: 10.1063/1.4996339

Knox, S. H., Jackson, R. B., Poulter, B., McNicol, G., Fluet-Chouinard, E., Zhang, Z., ... Zona, D. (2019). Fluxnet-ch4 synthesis activity: Objectives, observations, and future directions. *Bulletin of the American Meteorological Society*, *100*(12), 2607 - 2632. Retrieved from https://journals.ametsoc.org/view/journals/bams/100/12/bams-d-18-0268.1.xml doi: 10.1175/BAMS-D-18-0268.1

Konopka, P., Ploeger, F., D'Amato, F., Campos, T., von Hobe, M., Honomichl, S. B., ... Hegglin, M. I. (2025). Isentropic mixing vs. convection in clams-3.0/messy: evaluation using satellite climatologies and in situ carbon monoxide observations. *Atmospheric Chemistry and Physics*, *25*(23), 17973–17996. Retrieved from https://acp.copernicus.org/articles/25/17973/2025/ doi: 10.5194/acp-25-17973-2025

Lan, X., Thoning, K., & Dlugokencky, E. (2025). *Trends in globally-averaged ch4, n2o, and sf6 determined from noaa global monitoring laboratory measurements.* Version 2025-03. doi: 10.15138/P8XG-AA10

Lehner, B., Anand, M., Fluet-Chouinard, E., Tan, F., Aires, F., Allen, G. H., ... Thieme, M. (2025a, 5). Global Lakes and Wetlands Database (GLWD) version 2.0. Retrieved from https://figshare.com/articles/dataset/Global_Lakes_and_Wetlands_Database_GLWD_version_2_0/28519994 doi: 10.6084/m9.figshare.28519994.v1

Lehner, B., Anand, M., Fluet-Chouinard, E., Tan, F., Aires, F., Allen, G. H., ... Thieme, M. (2025b). Mapping the world's inland surface waters: an upgrade to the global lakes and wetlands database (glwd v2). *Earth System Science Data*, *17*(6), 2277–2329. Retrieved from https://essd.copernicus.org/articles/17/2277/2025/ doi: 10.5194/essd-17-2277-2025

Lehner, B., & Döll, P. (2004). Development and validation of a global database of lakes, reservoirs and wetlands. *Journal of Hydrology*, *296*(1), 1-22. Retrieved from https://www.sciencedirect.com/science/article/pii/S0022169404001404 doi: https://doi.org/10.1016/j.jhydrol.2004.03.028

Lelieveld, J., Gromov, S., Pozzer, A., & Taraborrelli, D. (2016). Global tropospheric

hydroxyl distribution, budget and reactivity. *Atmospheric Chemistry and Physics*, *16*(19), 12477–12493. Retrieved from https://doi.org/10.5194/acp-16-12477-2016 doi: 10.5194/acp-16-12477-2016

Lin, J. C., Gerbig, C., Wofsy, S. C., Andrews, A. E., Daube, B. C., Davis, K. J., & Grainger, C. A. (2003). A near-field tool for simulating the upstream influence of atmospheric observations: The stochastic time-inverted lagrangian transport (stilt) model. *Journal of Geophysical Research: Atmospheres*, *108*(D16). Retrieved from https://agupubs.onlinelibrary.wiley.com/doi/abs/10.1029/2002JD003161 doi: https://doi.org/10.1029/2002JD003161

Lu, X., Jacob, D. J., Zhang, Y., Maasakkers, J. D., Sulprizio, M. P., Shen, L., ... Ma, S. (2021). Global methane budget and trend, 2010–2017: complementarity of inverse analyses using in situ (globalviewplus ch_4 obspack) and satellite (gosat) observations. *Atmospheric Chemistry and Physics*, *21*(6), 4637–4657. Retrieved from https://acp.copernicus.org/articles/21/4637/2021/ doi: 10.5194/acp-21-4637-2021

Maasakkers, J. D., Jacob, D. J., Sulprizio, M. P., Scarpelli, T. R., Nesser, H., Sheng, J.-X., ... Parker, R. J. (2019). Global distribution of methane emissions, emission trends, and oh concentrations and trends inferred from an inversion of gosat satellite data for 2010–2015. *Atmospheric Chemistry and Physics*, *19*(11), 7859–7881. Retrieved from https://acp.copernicus.org/articles/19/7859/2019/ doi: 10.5194/acp-19-7859-2019

Malley, C. S., Borgford-Parnell, N., Haeussling, S., Howard, I. C., Lefèvre, E. N., & Kuylenstierna, J. C. I. (2023, feb). A roadmap to achieve the global methane pledge. *Environmental Research: Climate*, *2*(1), 011003. Retrieved from https://doi.org/10.1088/2752-5295/acb4b4 doi: 10.1088/2752-5295/acb4b4

McKenna, D. S., Grooß, J.-U., Günther, G., Konopka, P., Müller, R., Carver, G., & Sasano, Y. (2002). A new chemical lagrangian model of the stratosphere (clams) 2. formulation of chemistry scheme and initialization. *Journal of Geophysical Research: Atmospheres*, *107*(D15), ACH 4-1-ACH 4-14. Retrieved from https://agupubs.onlinelibrary.wiley.com/doi/abs/10.1029/2000JD000113 doi: https://doi.org/10.1029/2000JD000113

McKenna, D. S., Konopka, P., Grooß, J.-U., Günther, G., Müller, R., Spang, R., ... Orsolini, Y. (2002). A new chemical lagrangian model of the stratosphere (clams) 1. formulation of advection and mixing. *Journal of Geophysical Research: Atmospheres*, *107*(D16), ACH 15-1-ACH 15-15. Retrieved from https://agupubs.onlinelibrary.wiley.com/doi/abs/10.1029/2000JD000114 doi: https://doi.org/10.1029/2000JD000114

Michael Keller, R. F. S. (1994). Methane emission by bubbling from gatun lake, panama. *Journal of Geophysical Research: Atmospheres*, *99*(D4), 8307-8319. Retrieved from https://agupubs.onlinelibrary.wiley.com/doi/abs/10.1029/92JD02170 doi: https://doi.org/10.1029/92JD02170

Murguia-Flores, F., Arndt, S., Ganesan, A. L., Murray-Tortarolo, G., & Hornibrook, E. R. C. (2018). Soil methanotrophy model (memo v1.0): a process-based model to quantify global uptake of atmospheric methane by soil. *Geoscientific Model Development*, *11*(6), 2009–2032. Retrieved from https://gmd.copernicus.org/articles/11/2009/2018/ doi: 10.5194/gmd-11-2009-2018

Nisbet, E. G., Manning, M. R., Dlugokencky, E. J., Fisher, R. E., Lowry, D., Michel, S. E., ... White, J. W. C. (2019). Very strong atmospheric methane growth in the 4 years 2014–2017: Implications for the paris agreement. *Global Biogeochemical Cycles*, *33*(3), 318-342. Retrieved from https://agupubs.onlinelibrary.wiley.com/doi/abs/10.1029/2018GB006009 doi: https://doi.org/10.1029/2018GB006009

Niwa, Y., Tohjima, Y., Terao, Y., Saeki, T., Ito, A., Umezawa, T., ... Sferlazzo,

D. (2025). Multi-observational estimation of regional and sectoral emission contributions to the persistent high growth rate of atmospheric ch_4 for 2020–2022. *Atmospheric Chemistry and Physics*, *25*(13), 6757–6785. Retrieved from https://acp.copernicus.org/articles/25/6757/2025/ doi: 10.5194/acp-25-6757-2025

Nussbaumer, C. M., Kohl, M., Pozzer, A., Tadic, I., Rohloff, R., Marno, D., ... Fischer, H. (2024). Ozone formation sensitivity to precursors and lightning in the tropical troposphere based on airborne observations. *Journal of Geophysical Research: Atmospheres*, *129*(14), e2024JD041168. Retrieved from https://agupubs.onlinelibrary.wiley.com/doi/abs/10.1029/2024JD041168 (e2024JD041168 2024JD041168) doi: https://doi.org/10.1029/2024JD041168

Ort, L., Dadheech, N., Yoon, J., Turner, A., Bloom, A. A., Lachnitt, H.-C., ... Fischer, H. (2026, February). *Supporting data for: Airborne observations reveal underestimated riverine methane emissions across the amazon.* Zenodo. Retrieved from https://doi.org/10.5281/zenodo.18504592 doi: 10.5281/zenodo.18504592

Ort, L., Röder, L. L., Parchatka, U., Königstedt, R., Crowley, D., Kunz, F., ... Fischer, H. (2024). In-flight characterization of a compact airborne quantum cascade laser absorption spectrometer. *Atmospheric Measurement Techniques*, *17*(11), 3553–3565. doi: 10.5194/amt-17-3553-2024

Pangala, S. R., Enrich-Prast, A., Basso, L. S., Peixoto, R. B., Bastviken, D., Hornibrook, E. R. C., ... Gauci, V. (2017). Large emissions from floodplain trees close the amazon methane budget. *Nature*, *552*(7684), 230–234. Retrieved from https://doi.org/10.1038/nature24639 doi: 10.1038/nature24639

Pérez-Domínguez, I., Del Prado, A., Mittenzwei, K., Hristov, J., Frank, S., Tabeau, A., ... others (2021). Short-and long-term warming effects of methane may affect the cost-effectiveness of mitigation policies and benefits of low-meat diets. *Nature Food*, *2*(12), 970–980. doi: https://doi.org/10.1038/s43016-021-00385-8

Prather, M. J., Holmes, C. D., & Hsu, J. (2012). Reactive greenhouse gas scenarios: Systematic exploration of uncertainties and the role of atmospheric chemistry. *Geophysical Research Letters*, *39*(9). Retrieved from https://agupubs.onlinelibrary.wiley.com/doi/abs/10.1029/2012GL051440 doi: https://doi.org/10.1029/2012GL051440

Predybaylo, E., Lelieveld, J., Pozzer, A., Gromov, S., Zimmermann, P., Osipov, S., ... McCabe, M. (2025). Surface temperature and ozone responses to the 2030 global methane pledge. *Climatic Change*, *178*(4), 78. Retrieved from https://doi.org/10.1007/s10584-025-03908-5 doi: 10.1007/s10584-025-03908-5

Prein, A. F., Langhans, W., Fosser, G., Ferrone, A., Ban, N., Goergen, K., ... Leung, R. (2015). A review on regional convection-permitting climate modeling: Demonstrations, prospects, and challenges. *Reviews of Geophysics*, *53*(2), 323–361. doi: 10.1002/2014RG000475

Rigby, M., Montzka, S. A., Prinn, R. G., White, J. W. C., Young, D., O'Doherty, S., ... Park, S. (2017). Role of atmospheric oxidation in recent methane growth. *Proceedings of the National Academy of Sciences*, *114*(21), 5373-5377. Retrieved from https://www.pnas.org/doi/abs/10.1073/pnas.1616426114 doi: 10.1073/pnas.1616426114

Rodgers, C. D. (1990). Characterization and error analysis of profiles retrieved from remote sounding measurements. *Journal of Geophysical Research: Atmospheres*, *95*(D5), 5587-5595. Retrieved from https://agupubs.onlinelibrary.wiley.com/doi/abs/10.1029/JD095iD05p05587 doi: https://doi.org/10.1029/JD095iD05p05587

Rodgers, C. D. (2000). *Inverse methods for atmospheric sounding: theory and practice* (Vol. 2). World scientific. (ISBN: 981-02-2740-X)

Saunois, M., Martinez, A., Poulter, B., Zhang, Z., Raymond, P., Regnier, P., ... Zhuang, Q. (2024). Global methane budget 2000–2020. *Earth System Science Data Discussions*, *2024*, 1–147. Retrieved from https://essd.copernicus.org/preprints/essd-2024-115/ doi: 10.5194/essd-2024-115

Saunois, M., Martinez, A., Poulter, B., Zhang, Z., Raymond, P. A., Regnier, P., ... Zhuang, Q. (2025). Global methane budget 2000–2020. *Earth System Science Data*, *17*(5), 1873–1958. Retrieved from https://essd.copernicus.org/articles/17/1873/2025/ doi: 10.5194/essd-17-1873-2025

Saunois, M., Stavert, A. R., Poulter, B., Bousquet, P., Canadell, J. G., Jackson, R. B., ... Zhuang, Q. (2020). The global methane budget 2000–2017. *Earth System Science Data*, *12*(3), 1561–1623. Retrieved from https://essd.copernicus.org/articles/12/1561/2020/ doi: 10.5194/essd-12-1561-2020

Scheuer, E. M., & Stoller, D. S. (1962). On the generation of normal random vectors. *Technometrics*, *4*(2), 278–281. Retrieved from https://www.tandfonline.com/doi/abs/10.1080/00401706.1962.10490011 doi: 10.1080/00401706.1962.10490011

Shindell, D., Kuylenstierna, J. C. I., Vignati, E., van Dingenen, R., Amann, M., Klimont, Z., ... Fowler, D. (2012). Simultaneously mitigating near-term climate change and improving human health and food security. *Science*, *335*(6065), 183-189. Retrieved from https://www.science.org/doi/abs/10.1126/science.1210026 doi: 10.1126/science.1210026

Silva Junior, C. H. L., Pessôa, A. C. M., Carvalho, N. S., Reis, J. B. C., Anderson, L. O., & Aragão, L. E. O. C. (2021). The brazilian amazon deforestation rate in 2020 is the greatest of the decade. *Nature Ecology & Evolution*, *5*(2), 144–145. Retrieved from https://doi.org/10.1038/s41559-020-01368-x doi: 10.1038/s41559-020-01368-x

Stanley, E. H., Casson, N. J., Christel, S. T., Crawford, J. T., Loken, L. C., & Oliver, S. K. (2016). The ecology of methane in streams and rivers: patterns, controls, and global significance. *Ecological Monographs*, *86*(2), 146-171. Retrieved from https://esajournals.onlinelibrary.wiley.com/doi/abs/10.1890/15-1027 doi: https://doi.org/10.1890/15-1027

Szopa, S., Naik, V., Adhikary, B., Artaxo, P., Berntsen, T., Collins, W. D., ... Zanis, P. (2021). Short-lived climate forcers (chapter 6). In V. Masson-Delmotte et al. (Eds.), *Ipcc 2021: Climate change 2021: The physical science basis. contribution of working group i to the sixth assessment report of the intergovernmental panel on climate change* (pp. 817–922). Cambridge, United Kingdom and New York, NY, USA: Cambridge University Press. Retrieved from https://www.ipcc.ch/report/ar6/wg1/ doi: 10.1017/9781009157896.008

Tarantola, A. (2005). *Inverse problem theory and methods for model parameter estimation*. Philadelphia, PA: Society for Industrial and Applied Mathematics (SIAM). (Completely rewritten edition of the 1987 volume)

Turner, A. J., Frankenberg, C., & Kort, E. A. (2019). Interpreting contemporary trends in atmospheric methane. *Proceedings of the National Academy of Sciences*, *116*(8), 2805-2813. Retrieved from https://www.pnas.org/doi/abs/10.1073/pnas.1814297116 doi: 10.1073/pnas.1814297116

Turner, A. J., Frankenberg, C., Wennberg, P. O., & Jacob, D. J. (2017). Ambiguity in the causes for decadal trends in atmospheric methane and hydroxyl. *Proceedings of the National Academy of Sciences*, *114*(21), 5367-5372. Retrieved from https://www.pnas.org/doi/abs/10.1073/pnas.1616020114 doi: 10.1073/pnas.1616020114

Turner, A. J., Jacob, D. J., Benmergui, J., Brandman, J., White, L., & Randles, C. A. (2018). Assessing the capability of different satellite observing configurations to resolve the distribution of methane emissions at kilometer scales. *Atmospheric Chemistry and Physics*,

18(11), 8265–8278. Retrieved from https://acp.copernicus.org/articles/18/8265/2018/ doi: 10.5194/acp-18-8265-2018

Turner, A. J., Kim, J., Fitzmaurice, H., Newman, C., Worthington, K., Chan, K., ... Cohen, R. C. (2020). Observed impacts of covid-19 on urban co2 emissions. *Geophysical Research Letters*, *47*(22), e2020GL090037. Retrieved from https://agupubs.onlinelibrary.wiley.com/doi/abs/10.1029/2020GL090037 (e2020GL090037 10.1029/2020GL090037) doi: https://doi.org/10.1029/2020GL090037

Uluocak, I. (2025). Hybrid deep learning models for predicting atmospheric methane concentrations: A comparative analysis through 2050. *Science China Earth Sciences*, 1–11. doi: https://doi.org/10.1007/s11430-024-1569-9

Yvon-Durocher, G., Allen, A. P., Bastviken, D., Conrad, R., Gudasz, C., St-Pierre, A., ... del Giorgio, P. A. (2014). Methane fluxes show consistent temperature dependence across microbial to ecosystem scales. *Nature*, *507*(7493), 488–491. doi: 10.1038/nature13164

Zhang, Z., Zimmermann, N. E., Stenke, A., Li, X., Hodson, E. L., Zhu, G., ... Poulter, B. (2017). Emerging role of wetland methane emissions in driving 21st century climate change. *Proceedings of the National Academy of Sciences*, *114*(36), 9647-9652. Retrieved from https://www.pnas.org/doi/abs/10.1073/pnas.1618765114 doi: 10.1073/pnas.1618765114

Zhu, Q., Jacob, D. J., Yuan, K., Li, F., Runkle, B. R. K., Chen, M., ... Halabisky, M. (2025, feb). Advancements and opportunities to improve bottom–up estimates of global wetland methane emissions. *Environmental Research Letters*, *20*(2), 023001. Retrieved from https://dx.doi.org/10.1088/1748-9326/adad02 doi: 10.1088/1748-9326/adad02

3.6 Supplement of "Airborne observations reveal underestimated riverine methane emissions across the Amazon"

Supporting Information for "Airborne observations reveal underestimated riverine methane emissions across the Amazon"

Linda Ort[1], Christian Frankenberg[2,3], Nikhil Dadheech[4], James (Young Suk) Yoon[4], Alexander J. Turner[4], A. Anthony Bloom[3], Paul Konopka[5], Hans-Christoph Lachnitt[6], Peter Hoor[6], Jos Lelieveld[1,7], Eric A. Kort[1,8], Horst Fischer[1]

[1]Atmospheric Chemistry Department, Max Planck Institute for Chemistry, Mainz, 55128, Germany

[2]Division of Geological and Planetary Sciences, California Institute of Technology, Pasadena, CA, 91125, USA

[3]Jet Propulsion Laboratory, California Institute of Technology, Pasadena, California, 91109, USA.

[4]Department of Atmospheric and Climate Science, University of Washington, Seattle, Washington, 98195, USA

[5]Institute of Climate and Energy Systems, Stratosphere (ICE-4), Forschungszentrum Jülich, 52428, Germany

[6]Institute for Atmospheric Physics, Johannes Gutenberg University, Mainz, 55128, Germany

[7]Climate and Atmosphere Research Center, The Cyprus Institute, Nicosia, 1645, Cyprus

[8]Climate and Space Sciences and Engineering, University of Michigan, Ann Arbor, 48109, USA

Contents of this file

3. Table S1

Introduction The supporting information presents further information on the methods used in this study, including more details on the observations and instrument (S1, S1.1, S1.2), model-observation comparison (S2), transport modeling (S3), Bayesian inversion and prior mean and covariance construction (S4, S4.1). Additionally, we provide overviews-plots of analysis using different prior inventories, altitude separations of observations, annual variability, and supporting results for the main study.

Text S1: Additional Information for Observations

Observations of CH_4 have been collected via infrared laser absorption spectroscopy (QLAS) above the Amazon basin from December 2022 though the end of January 2023 in the scope of the airborne campaign CAFE Brazil (Chemistry of the Atmosphere Field Experiment in Brazil, (Nussbaumer et al., 2024; Curtius et al., 2025)). Based in Manaus (Brazil), 16 local research flights were carried out with the High Altitude and LOng range research aircraft (HALO, (DLR, 2025)) to achieve spatial and vertical (up to 14.5 km) information from trace gas emissions, atmospheric chemistry, and new particle formation. The CH_4 observations were conducted with the Airborne Tropospheric Tracer In-situ Laser Absorption spectrometer (ATTILA, (Ort et al., 2024)), with 4.2% precision and a total measurement uncertainty of 17.5% on 1-second data. During strong ascents and descents, etalon structures of the multipass cell (astigmatic Herriott cell, (Herriott & Schulte, 1965)) are a limiting factor of instrumental precision. Frequent in-flight calibrations were conducted against a secondary standard (CH_4 = 1990 ppb), which was

quantified against a primary standard before and after the campaign. Linear alignment in between frequent in-flight calibrations (approx. every 20 minutes) has been carried out in the post-processing of the data, to assure alignment to environmental changes.

For reduction in noise, we used 60 s-averages for this study. The the standard deviation after linear correction over all in-flight calibrations (1σ =67.69 ppb) is used in the main study as measurement uncertainty over the whole campaign. The standard deviation before linear correction over all in-flight calibrations (1σ =315.35 ppb) is used for observations during altitude changes larger than 5 m between 60 s data time steps, assuming the highest possible uncertainty here. This conservative uncertainty approach assures observational reliability, covering the main limitations of this data set, which are non-linear and overlapping etalon structures, especially during rapid ascents and descents. A detailed characterization of the instrument has been done in the scope of a test-flight shown in Ort et al. (2024).

The regional background CH_4 mixing ratios are estimated to be the free tropospheric mean value of the observations (above 6 km, BG=1907 ppb). With this assumption we assume a well mixed free and upper troposphere, mostly conditioned with air from the East-to-North-Atlantic transported towards Brazil, which is typical for this time of year (Andreae et al., 2015). Monthly global averages are at 1921.96 ± 1.24 ppb in December 2022 and 1919.92 ± 1.37 ppb in January 2023, according to the NOAA surface stations (Lan & Dlugokencky, 2025). The closest (in time and space) NOAA station during the CAFE Brazil campaign is placed on Ascension Island (ASC; 7.9333°S, 14.3667°W) in the Atlantic with CH_4 =1882.23 ppb, measured on the 16^{th} of November 2022. In com-

parison to those ground based measurements, we report slightly higher values than the maritime ASC station, and lower mean values than the global averages in the free troposphere above the Amazon region ($6-12\,\mathrm{km}$ mean $\pm$ sdev: $1931.68 \pm 245.50\,\mathrm{ppb}$ in December 2022; $1894.69 \pm 196.78\,\mathrm{ppb}$ in January 2023). The average over both months is at $1907.47 \pm 215.54\,\mathrm{ppb}$, which we also used as the background value for the flux inversion. Within the PBL, large CH_4 mixing ratios of up to 2700 ppb can not only be found in the vicinity of river sides and wetlands (see 60 s data resolution in Figure S10).

Text S1.1: The ATTILA Instrument

The Airborne Tropospheric Tracer In-situ Laser Absorption spectrometer, short ATTILA, is a self-designed and self-constructed absorption spectrometer by the Max Planck Institute for Chemistry in 2019, specifically designed for airborne measurements. A harsh and confined observational platform like an aircraft often requires restrictions in size, weight and complexity of instrumentation, besides the highly demanding changes of the environment (altitude, pressure, temperature, yaw, pitch and roll angles). The ATTILA instrument was built to fulfill the requirements and for increasing the efficiency of measurements by the most simple design possible. The spectrometer contains two optical frames, each including a multi-pass cell (astigmatic Herriott cell (Herriott & Schulte, 1965), path-length of 32 m), a room-temperate quantum cascade laser, a mid-infrared detector, as well as only two lenses and four mirrors, each, directing the beams into the cells. The first cell measures CO (2190.0175 cm^{-1}; Li et al. (2015)) and N_2O (2190.3498 cm^{-1}; Toth (2004)) and the second cell measures CH_4 (1256.6 cm^{-1}; Ba et al. (2013)) and N_2O

(1255.42 cm^{-1}; Toth (2004). Both cells are flushed by the sampling air with an airflow of 0.1 L min^{-1} each, controlled by two compound mass flow controllers (Bronkhorst, IQ-FLOW), and therefore can measure two different absorption spectra simultaneously. The cells are pressurized to 50 hPa, controlled by a pump connected to the exhaust to ensure a natural inflow into the instrument from outside the aircraft, even at high altitudes. During operation, every 20 minutes for 60 seconds, a third mass flow controller leads calibration gas from a secondary standard gas bottle into both cells for the in-flight calibrations. In between those calibrations linear correction is applied in the post-processing of the data, after calibrations are synchronized. This ensures that the instrument is stabilized for the current environmental conditions throughout the flight and data can be compared (Röder et al., 2024). The calibrations prior and post linear correction is shown in Figure S2. The final 60 s-resolved CH_4 data, separated into four altitude ranges can be found in Figure S3. More information to the setup and characterization of the instrument can be found in Ort et al. (2024), where a test flight was dedicated to measure only calibration gas with constant mixing ratios, to identify instrumental artifacts during flight and operation.

Text S1.2: Water Dilution Correction

The gas was measured in ambient air; therefore, the effect of water density must be considered (Haracono et al., 2015). After performing a usual correction with the water vapor mixing ratio (χ_{H_2O}) via Equation S1, we found a remaining underestimation, on average, of up to 1.5 % onto the N_2O signal in the lower altitudes above the Amazon

basin (up to approx. 6 km), compared to the N_2O mixing ratio in the free and upper troposphere. This underestimation is highly suspicious, as there is no known sink of N_2O close to the surface, which could cause such a reduction. We have seen such effect after dry-correction only in measurements performed in the tropics. The H_2O measurements were conducted by the SHARC (Sophisticated Hygrometer for Atmospheric ResearCh) instrument, a tunable diode laser hygrometer developed at DLR Flight Experiments, which provides a total uncertainty (TU) of 5 % and a $\pm$ 1 ppm absolute offset uncertainty (Kaufmann et al., 2018). Tropical surface air usually contains 20000-25000 ppm (Kindel et al., 2015), which agrees well with the range of H_2O measurements during the CAFE Brazil campaign above the Amazon rainforest. However, the uncertainty of 5 % provides a ranging H_2O from 1000-1250 ppm, which is not enough to explain the underestimation of N_2O of 1.5 %. Therefore, we think this effect is more likely an artifact of condensation within the instruments, when humid ambient air enters the cooled multi-pass cells of the ATTILA instrument. As the air is not dried within our measurement setup, humidity can be traped to some extend. Therefore, we used a different water dilution correction method for the CH_4 data. As N_2O was measured simultaneously to CH_4 with the TRISTAR instrument ((Wienhold et al., 1998; Röder et al., 2024; Ort et al., 2024), TU = 3 %), we used the percentage difference of the medians of a 1 km resolved N_2O profile above the Amazon to align it with the median of the upper tropospheric N_2O values (from 7-13 km, $\sigma = 0.530$ ppb), assuming inertness of N_2O in the troposphere. The similar technical setup, as well as nearly similar CO measurements from both instruments (Ort et al., 2024; Röder et al., 2024), assure that we can use TRISTAR N_2O for the correction. Furthermore, from

O_3 measurements, which maximum mixing ratio achieved approx. 80 ppb at the highest altitude measured (14.5 km), we are confident, that there was no significant stratospheric influence, which would effect the measurements below 13 km. We apply the correction with the correction term *corr* to the CH_4 1 s-data ambient data (χ_{wet}) via Equation S2, only below 7 km, and N_2O data smaller than the reference N_2O value from the upper troposphere. Note, that with this alternative correction we neglect any possible source of N_2O at the tropical surface. The exact values for the correction and the N_2O 1 km-medians before and after the correction can be found in Table S1.

$$\chi_{dry} = \frac{\chi_{wet}}{1 - \chi_{H_2O}} \tag{S1}$$

$$\chi_{dry} = \chi_{wet} \cdot (1 + corr) \tag{S2}$$

However, the vertical profile of wet CH_4 already showed an increase towards the surface over the Amazon with a mean mixing ratio of 1967 ppb below 1 km. After a typical dry correction with water vapor this enhancement nearly doubled with a mean mixing ratio of 2015 ppb. The different correction method using the N_2O profile resulted in a mean mixing ratio of methane lower than 1 km of 2024 ppb. To prove consistency, we have performed an inversion with the dry-corrected CH_4 using the typical water vapor correction (Eq. S1), and achieve similar results, just with slightly smaller absolute numbers in fluxes (posterior maximum flux: 218 $g\,m^{-2}\,yr^{-1}$).

Text S2: Model-Observation Comparisons

Three atmospheric transport models are considered in this study: CAMS, GEOS-Chem,

and CLaMS. While all three models simulate atmospheric methane at global to regional scales, they differ substantially in their numerical framework, treatment of transport, and representation of surface methane emissions.

CAMS (Copernicus Atmosphere Monitoring Service) provides global CH_4 fields within an operational Earth system modeling framework. CH_4 simulations are constrained by data assimilation of satellite observations, leading to temporally consistent large-scale CH_4 distributions. Surface methane emissions in CAMS are prescribed using a combination of anthropogenic inventories (e.g., EDGAR) and climatological natural sources, including wetland methane emissions estimated using simulations with the Lund-Potsdam-Jena Earth Observation SIMulator model, providing monthly averaged data from 1990-2023 (LPJ-EOSIM version V001, Colligan, Poulter, and Quinn (2024)). However, these inversion-based emissions define wetlands as land areas that are either permanently or seasonally saturated, excluding small ponds, lakes, and coastal wetlands on a spatial grid resolution of $0.5°\times0.5°$ resolution, re-gridded onto $1°\times1°$, which can limit the representation of fine-scale emission heterogeneity in regions such as the Amazon Basin (Bergamaschi et al., 2013). Data products were accessed on the official Copernicus website (release: v23r1, source: TM5-MP 4D-Var, Copernicus Atmosphere Monitoring Service (2020); Bergamaschi et al. (2013)). A bilinear interpolation between surrounding model grid points was used to extract CAMS CH_4 mixing ratios for the comparison with the observations.

GEOS-Chem is a global three-dimensional chemical transport model driven by assimilated meteorological fields. It provides a flexible framework for testing different methane

emission inventories and wetland parameterizations. Anthropogenic emissions are commonly taken from inventories such as EDGAR (version 8), while natural emissions, particularly wetlands, are represented using process-based models (e.g., WetCHARTs) or climatological datasets. As a result, simulated Amazonian CH_4 concentrations in GEOS-Chem are strongly influenced by assumptions about wetland extent, inundation dynamics, and temperature sensitivity, as well as the quality of the underlying meteorology (Bey et al., 2001; Maasakkers et al., 2019; Delwiche et al., 2022).

The global methane simulation (v.14.5.2) used in this study was run at $2.0° \times 2.5°$ spatial resolution with 72 vertical levels between 2022-01-01 to 2023-02-01, which contains the entire observational period. MERRA-2 reanalysis was used for meteorological data; GFEIv2 for oil, gas, and coal; EDGARv8 for other anthropogenic methane emissions; WetCHARTsv1 for wetland emissions; Fung et al. (1991) for soil absorption and termites; the Delwiche et al. (2022) inventory for reservoir emissions; and GFED4 for biomass burning emissions. This simulation did not have interactive OH chemistry and instead uses global OH fields from the GEOS-Chem full chemistry model. We note that many of these inventories had not been updated for 2022 or 2023, and thus the exact model output is not a perfect representation of the observational time period but rather illustrates the general methane emission fluxes for previous years. The plane flight diagnostic was used to match the gridded output to the aircraft observations, with the latitudes/longitudes of the aircraft observations rounded to the nearest hundredth.

CLaMS-v3.0 (Chemical Lagrangian Model of the Stratosphere; Konopka et al. (2025) and references therein) employs a Lagrangian transport approach, explicitly following air

parcels and parameterizing mixing between them. This framework allows for a detailed representation of transport and mixing and is particularly suited for studies of transport pathways and source attribution. In contrast to Eulerian chemistry–transport models such as CAMS, CLaMS does not include an internal emission module. Instead, lower boundary conditions for methane are prescribed from gridded satellite observations. In particular, CH_4 fields derived from the Atmospheric Infrared Sounder (AIRS) are mapped onto a latitude–longitude–time grid with a resolution of typically $2° \times 6°$ and 5 days, respectively, and applied at a hybrid potential temperature coordinate $\zeta = 200\,\mathrm{K}$ (approximately 500–700 hPa) (Pommrich et al., 2014). These satellite-derived fields capture the large-scale spatial and temporal variability of methane, with the highest observational sensitivity in the middle troposphere. As a result, methane distributions in CLaMS are primarily constrained by transport and the prescribed satellite-derived lower boundary condition, while methane sources within the planetary boundary layer are not explicitly represented. Consequently, small-scale or short-lived emission enhancements, such as regional methane sources over the Amazon, may not be fully resolved due to the coarse spatial and temporal resolution and observational sensitivity of the satellite-derived boundary fields. For this study, CLaMS-v3.0 simulations were performed for the campaign period using ERA5 meteorological fields. The modeled methane fields were linearly interpolated in space and time along the flight tracks to enable direct comparison with the in situ observations.

Meteorological information was used from ERA5 reanalysis data, which was calculated using the European Center for Medium-Range Weather Forecasts (ECMWF) to generate a detailed record of the global atmosphere (Hersbach et al., 2020). ERA5 reanalysis data

has a temporal resolution of six hours and and a horizontal grid spacing of 1°. For the comparison with the CAFE Brazil campaign data, parameters were linearly interpolated along the flight path over time and space.

Overall, differences in simulated CH_4 over the Amazon arise from both transport formulation and prior emission assumptions. While CAMS benefits from observational constraints at large scales, GEOS-Chem and CLaMS provide greater flexibility for testing and optimizing emission inventories, at the expense of increased sensitivity to prior emission uncertainties.

Text S3: STILT Calculations

The STILT simulation was run for 7620 receptor positions within a spatial grid ranging from 80°W – 35°W, and 15°S – 10°N and a resolution of 0.1°×0.1°. From each receptor position, back-trajectories are calculated hourly resolved 120 hours backwards in time, using meteorological data from the GFS (Global Forecast System) provided in an hourly resolution. This neglects small-scale dynamical processes, like short-term convection, and causes that the majority of observational influence is coming from measurements below 6 km (see Fig. S10). Whenever a back-trajectory enters the PBL within the defined domain for at least on time step, the fraction of particles is providing the information, how sensitive the observation at receptor position n is to the mth surface grid cell and its potential surface flux. Hence, one can relate the ith observation (y_i) to the m surface

fluxes relative to the background concentration b_i using the associated footprint:

$$y_i = \mathbf{h}_i \mathbf{x} + b_i, \tag{S3}$$

where $\mathbf{h}_i$ is the $1 \times m$ footprint matrix, which describes the sensitivity of observation y_i to m surface fluxes with units similar to ppm $(\mu\text{mol}\,\text{m}^{-2}\,\text{s}^{-1})^{-1}$ (Rodgers, 2000). That surface sensitivity is subsequently time-integrated using temporally exponential decaying weights (Dadheech et al., 2025). Furthermore, not every receptor position results in a footprint within the given domain. Some trajectories are not reaching the PBL within five days or have left the spatial domain beforehand. This simulation exceeds footprints of $n = 5451$ receptor positions, resulting in a maximum count of endpoints per grid cell up to almost 700 counts (Figure S4). Those sensitivities for all trajectories of a single receptor position five-days backward in time were time-integrated, and smoothing at their edges was applied in the aggregation. We observed that using the default smoothing factor of 1 introduces artifacts through the smoothing function of STILT for high-altitude receptors. To remove these smoothing artifacts, we reduced the smoothing factor to 0.3.

Text S4: Bayesian inversion

The goal of this study is to infer CH_4 fluxes from the atmospheric observations. For this, we use a linear Bayesian approach to estimate greenhouse gas fluxes using atmospheric observations as done before in, e.g., Dadheech et al. (2025); Turner et al. (2018). The Bayesian inference relates the probability density function (PDF) of the posterior ($P(x|\mathbf{y})$)

to the observation likelihood PDF ($P(\mathbf{y}|\mathbf{x})$) and prior PDF ($P(\mathbf{x})$) as follows:

$$P(x|\mathbf{y}) \propto P(\mathbf{y}|\mathbf{x})P(\mathbf{x}). \tag{S4}$$

To estimate posterior surface fluxes, we applied an analytical Bayesian inversion using a linear forward model of the form

$$\mathbf{y} = \mathbf{H}\mathbf{x} + \mathbf{b}, \tag{S5}$$

where $\mathbf{y}$ is the vector of n observations (enhancement towards the background), $\mathbf{H}$ the sensitivity (Jacobian) matrix ($n \times m$), $\mathbf{x}$ a state vector of surface fluxes ($m \times 1$), and $\mathbf{b}$ representing an observational background value as defined in Text S1. Hence, for $\mathbf{H}$ we combined all footprints to a single matrix by first flatten each two-dimensional footprint matrix, and then, aggregating them to one matrix of the shape of $n \times m$. Here, the unknown vector is $\mathbf{x}$, which we further define as posterior state vector $\hat{\mathbf{x}}$. The footprint matrix contained 12,501 out of 111,801 cells with zero sensitivity tracked from the trajectory analysis within the domain. The remaining cells (89%) contain at least one endpoint of a trajectory with a certain fraction of particles arriving there. Reliability of observations is defined, when the highest 60^{th} percentiles of endpoints and particle fraction are found in a grid cell, which is defined in the main study as the 40% highest observational sensitivity area. This ensures consistency across data observed at different points in time and reduces measurement uncertainty.

Estimating the posterior requires the prior state to constrain the PDF, establishing a reference state that guides the least-squares optimization. The prior state vector $\mathbf{x}_p$ is assumed to follow a Gaussian distribution with covariance matrix $\mathbf{B}$ of shape ($m \times m$). Due to the fact that our spatial domain exceeds a prior covariance matrices size in the

order of 10^{10} $(m \times m)$ the inversion was calculated without forming large dense matrices, mainly by using matrix-free operations, and a sparse prior covariance matrix, constructed as explained below. The observational error covariance matrix $\mathbf{R}$ was chosen to be a diagonal matrix, as cross-observational error dependencies are unlikely. The estimate of posterior methane fluxes ($\hat{\mathbf{x}}$) is given by using the standard Gaussian update formulation (Eq. 1). To obtain the posterior flux uncertainty $\mathbf{P}$, we computed the posterior covariance as

$$\mathbf{P} = \mathbf{B} - \mathbf{B}\mathbf{H}^T(\mathbf{H}\mathbf{B}\mathbf{H}^T + \mathbf{R})^{-1}\mathbf{H}\mathbf{B}. \tag{S6}$$

The random probe Hutchinson estimator was used to approximate its diagonal elements, taking 100 samples to provide a grid-level posterior standard deviations ($\hat{\sigma}_{i,i} \approx \sqrt{\mathbf{P}_{i,i}}$), shown in Fig S7e and S7f.

Text S4.1: Prior mean and covariance matrix

WetCHARTs bottom-up estimates CH_4 fluxes from wetlands using empirical biogeochemical modeling with remote sensed inundation, model–driven relative humidity fluxes and a temperature sensitivity factor for a high spatial resolution ($0.5° \times 0.5°$) (Bloom et al., 2017; Zhu et al., 2025). The mean emission field corresponds to an ensemble average of various configurations, including wetland extent parameterizations, terrestrial biosphere models of heterotrophic respiration, and temperature parameterization. The variance of the ensemble members is the uncertainty of the mean emission field, sharing a similar magnitude to its mean estimate, with highest uncertainties evolving from the wetland

extent (Bloom et al., 2017). WetCHARTs CH_4 emissions do not only cover wetland emissions, they also include flooding from other natural or anthropogenic freshwater surfaces (e.g., reservoirs, rivers, lakes, seasonal flooded forests) due to their input parameterizations. Those different land cover types are shown in Figure S5, taken from the Global Lakes and Wetlands Database (GLWD) version 2, and also used for some ensemble simulations of WetCHARTs. Other emissions, such as from livestock, biomass burning, other anthropogenic sources, termites, etc., are not included. For the period of data coverage of this study biomass burning emissions can be neglected, while livestock emissions are underrepresented by the prior.

To overcome the spatial resolution differences of the WetCHARTs mean and uncertainties compared to the footprints, we have downsized the grid resolution of the prior from $0.5°\times0.5°$ to $0.1°\times0.1°$ grid, by splitting one coarse cell into 25 fine cells. The mean prior state vector was replicated for the finer grid resolution, while the covariance matrix was scaled according to the finer resolution and correlated (p =0.95) within one coarse cell, existing of $N = 5 \times 5 = 25$ fine grid cells. The variance σ^2_{fine} was then calculated as follows:

$$\sigma^2_{fine} = \sigma^2_{coarse} \frac{N}{1 + (N-1)p}. \tag{S7}$$

The prior error covariance matrix $\mathbf{B}$ describes uncertainties in the prior methane fluxes and their spatial correlations. Diagonal elements of $\mathbf{B}$ are constructed from grid-cell–specific prior uncertainty estimates using the ensemble variance of WetCHARTs, while off-diagonal elements are prescribed using spatial correlation that decays exponentially with distance. This formulation accounts for regional correlations between fluxes, particularly across grid

cells sharing similar land-cover types, following land cover types defined by GLWD (see Figure S5). Hence, the spatial covariance is expressed as the product of variance and correlation components,

$$\mathbf{B} = \sqrt{f_\sigma}\mathbf{V}^{1/2}\mathbf{M}\,\mathbf{V}^{1/2}, \tag{S8}$$

where $\mathbf{B} \in \Re^{m\times m}$ is the prior error covariance matrix, $\mathbf{V}$ is a diagonal matrix containing grid-cell–specific prior variances, and $\mathbf{M}$ is a spatial correlation matrix with correlations restricted to nearby grid cells and preferentially applied between cells sharing the same land-cover classification, resulting in a sparse structure. The scalar factor $f_\sigma = 0.95$ scales the overall magnitude of prior uncertainties and is chosen such that prior flux uncertainties and trajectory endpoint sensitivities represented in the observation operator $\mathbf{H}$ are regionally correlated over their nearest neighboring grid cells. Spatial correlations in $\mathbf{M}$ are defined using an exponential decay function

$$M_{ij} = \exp\left(-\frac{d_{ij}}{\tau_s}\right), \tag{S9}$$

where d_{ij} is the distance between grid-cell centers i and j, and τ_s (25 km) is the prescribed correlation length scale; correlations are set to zero beyond a cutoff distance to maintain sparsity. An example of the prior covariance matrix spatial structure for just one single grid cell is shown in Figure S6. The diagonal spatial structure of $\mathbf{B}$, so only ensemble variances, is shown in Figure S7c and S7d, as the square-root of $\mathbf{B}$.

The choice of the prior state vector highly impacts the inversion and therefore the solution found for the posterior. We have carefully tested the grade of influence on the results with various emission inventories, regarding different emission sources, spatial and

temporal resolutions, inter-annual variability, and number of observations, of which we have summarized the most important for this study in the Figures S8, S9, and S10.

The posterior solutions were consistent by using different prior wetland inventories, as shown in Figure S9. Here, we tested besides WetCHARTs also a simplified inversion including WetCHIMP, GCP, or a flat prior (mean value of WetCHARTs over the whole domain for every grid cell) as prior state vectors, and their ensemble variances (and mean) as prior covariance matrices. More information regarding the bottom-up estimates WetCHIMP and GCP can be found in Zhu et al. (2025). Particularly for the flat prior simulation, no spatial orientation was provided, hence, spatial variability in the posterior is only caused by the observations. However, all inversions show a similar spatial pattern, they do show different absolute numbers of posterior–prior differences. This, most likely, is due to the difference in absolute values in the prior state vectors, and therefore is providing a different base value of emissions the inversion tries to solve.

During the tests using different altitude ranges of the observations (see Fig S10), the posterior showed that most of the observational information is attributable to measurements below 6 km, and insensitive to either exclude or include measurements during altitude changes of larger than 5 m between the 60 s time steps, which contain higher uncertainties. The fact, that nearly no observational information is coming from observations above 6 km, is due to the transport model and the resolution of the meteorological data set, which was used (1 h). Therefore, short-term convection can not be resolved, resulting in less footprints for observations higher than 6 km.

References

Andreae, M. O., Acevedo, O. C., Araùjo, A., Artaxo, P., Barbosa, C. G. G., Barbosa, H. M. J., ... Yáñez Serrano, A. M. (2015). The amazon tall tower observatory (atto): overview of pilot measurements on ecosystem ecology, meteorology, trace gases, and aerosols. *Atmospheric Chemistry and Physics*, *15*(18), 10723–10776. Retrieved from https://acp.copernicus.org/articles/15/10723/2015/ doi: 10.5194/acp-15-10723-2015

Ba, Y. A., Wenger, C., Surleau, R., Boudon, V., Rotger, M., Daumont, L., ... Dubernet, M.-L. (2013). Mecasda and ecasda: Methane and ethene calculated spectroscopic databases for the virtual atomic and molecular data centre. *Journal of Quantitative Spectroscopy and Radiative Transfer*, *130*, 62-68. Retrieved from https://www.sciencedirect.com/science/article/pii/S0022407313001933 (HITRAN2012 special issue) doi: https://doi.org/10.1016/j.jqsrt.2013.05.001

Bergamaschi, P., Houweling, S., Segers, A., Krol, M., Frankenberg, C., Scheepmaker, R. A., ... Gerbig, C. (2013). Atmospheric ch4 in the first decade of the 21st century: Inverse modeling analysis using sciamachy satellite retrievals and noaa surface measurements. *Journal of Geophysical Research: Atmospheres*, *118*(13), 7350-7369. Retrieved from https://agupubs.onlinelibrary.wiley.com/doi/abs/10.1002/jgrd.50480 doi: https://doi.org/10.1002/jgrd.50480

Bey, I., Jacob, D. J., Yantosca, R. M., Logan, J. A., Field, B. D., Fiore, A. M., ...

Schultz, M. G. (2001). Global modeling of tropospheric chemistry with assimilated meteorology: Model description and evaluation. *Journal of Geophysical Research: Atmospheres*, *106*(D19), 23073-23095. Retrieved from https://agupubs.onlinelibrary.wiley.com/doi/abs/10.1029/2001JD000807 doi: https://doi.org/10.1029/2001JD000807

Bloom, A. A., Bowman, K. W., Lee, M., Turner, A. J., Schroeder, R., Worden, J. R., ... Jacob, D. J. (2017). A global wetland methane emissions and uncertainty dataset for atmospheric chemical transport models (wetcharts version 1.0). *Geoscientific Model Development*, *10*(6), 2141–2156. Retrieved from https://gmd.copernicus.org/articles/10/2141/2017/ doi: 10.5194/gmd-10-2141-2017

Colligan, T., Poulter, B., & Quinn, C. (2024). *LPJ-EOSIM L2 Global Simulated Daily Wetland Methane Flux V001.* NASA Land Processes Distributed Active Archive Center. (Data set, accessed 2026-02-18) doi: 10.5067/COMMUNITY/LPJ-EOSIM/LPJ_EOSIM_L2_DCH4E.001

Copernicus Atmosphere Monitoring Service. (2020). *Cams global inversion-optimised greenhouse gas fluxes and concentrations.* Copernicus Atmosphere Monitoring Service (CAMS) Atmosphere Data Store. Retrieved from https://doi.org/10.24381/ed2851d2 (Accessed on 07-03-2025) doi: 10.24381/ed2851d2

Curtius, J., Heinritzi, M., Beck, L. J., Poehlker, M. L., Tripathi, N., Krumm, B. E., ... Lelieveld, J. (2025, 2025 APR 1). Isoprene nitrates drive new particle formation in amazon's upper troposphere (vol 636, 124, 2024) [Correction; Early Access]. *NATURE*. doi: 10.1038/s41586-025-08906-2

Dadheech, N., He, T.-L., & Turner, A. J. (2025). High-resolution greenhouse gas flux inversions using a machine learning surrogate model for atmospheric transport. *Atmospheric Chemistry and Physics*, *25*(10), 5159–5174. Retrieved from https://acp.copernicus.org/articles/25/5159/2025/ doi: 10.5194/acp-25-5159-2025

Delwiche, K. B., Harrison, J. A., Maasakkers, J. D., Sulprizio, M. P., Worden, J., Jacob, D. J., & Sunderland, E. M. (2022). Estimating drivers and pathways for hydroelectric reservoir methane emissions using a new mechanistic model. *Journal of Geophysical Research: Biogeosciences*, *127*(8), e2022JG006908. Retrieved from https://agupubs.onlinelibrary.wiley.com/doi/abs/10.1029/2022JG006908 (e2022JG006908 2022JG006908) doi: https://doi.org/10.1029/2022JG006908

DLR. (2025). *Halo.* German Aerospace Center (DLR). Retrieved from https://www.dlr.de/en/research-and-transfer/projects-and-missions/halo-high-altitude-and-long-range-research-aircraft (last access: 11 April 2025)

Fung, I., John, J., Lerner, J., Matthews, E., Prather, M., Steele, L. P., & Fraser, P. J. (1991). Three-dimensional model synthesis of the global methane cycle. *Journal of Geophysical Research: Atmospheres*, *96*(D7), 13033-13065. Retrieved from https://agupubs.onlinelibrary.wiley.com/doi/abs/10.1029/91JD01247 doi: https://doi.org/10.1029/91JD01247

Haracono, Y., Iwata, H., Sakabe, A., Ueyama, M., Takahashi, K., Nagano, H., ... Kosugi, Y. (2015). Effects of water vapor dilution on trace gas flux, and practical correction

methods. *Journal of Agricultural Meteorology*, *71*(2), 65-76. doi: 10.2480/agrmet.D-14-00003

Herriott, D. R., & Schulte, H. J. (1965, Aug). Folded optical delay lines. *Appl. Opt.*, *4*(8), 883–889. Retrieved from https://opg.optica.org/ao/abstract.cfm?URI=ao-4-8-883 doi: 10.1364/AO.4.000883

Hersbach, H., Bell, B., Berrisford, P., Hirahara, S., Horányi, A., Muñoz-Sabater, J., ... others (2020). The era5 global reanalysis. *Quarterly Journal of the Royal Meteorological Society*, *146*(730), 1999–2049.

Kaufmann, S., Voigt, C., Heller, R., Jurkat-Witschas, T., Krämer, M., Rolf, C., ... Schumann, U. (2018). Intercomparison of midlatitude tropospheric and lower-stratospheric water vapor measurements and comparison to ecmwf humidity data. *Atmospheric Chemistry and Physics*, *18*(22), 16729–16745. Retrieved from https://acp.copernicus.org/articles/18/16729/2018/ doi: 10.5194/acp-18-16729-2018

Kindel, B., Pilewskie, P., Schmidt, K., Thornberry, T., Rollins, A., & Bui, T. (2015, 03). Upper-troposphere and lower-stratosphere water vapor retrievals from the 1400 and 1900 nm water vapor bands. *Atmospheric Measurement Techniques*, *8*, 1147-1156. doi: 10.5194/amt-8-1147-2015

Konopka, P., Ploeger, F., D'Amato, F., Campos, T., von Hobe, M., Honomichl, S. B., ... Hegglin, M. I. (2025). Isentropic mixing vs. convection in clams-3.0/messy: evaluation using satellite climatologies and in situ carbon monoxide observations. *Atmospheric Chemistry and Physics*, *25*(23), 17973–17996. Retrieved from https://acp

.copernicus.org/articles/25/17973/2025/ doi: 10.5194/acp-25-17973-2025

Lan, K. T., X., & Dlugokencky, E. (2025). *Trends in globally-averaged ch4, n2o, and sf6 determined from noaa global monitoring laboratory measurements.* Retrieved from https://doi.org/10.15138/P8XG-AA10 (last access: 24 February 2025)

Lehner, B., Anand, M., Fluet-Chouinard, E., Tan, F., Aires, F., Allen, G. H., ... Thieme, M. (2025a, 5). Global Lakes and Wetlands Database (GLWD) version 2.0. Retrieved from https://figshare.com/articles/dataset/Global_Lakes_and_Wetlands_Database_GLWD_version_2_0/28519994 doi: 10.6084/m9.figshare.28519994.v1

Lehner, B., Anand, M., Fluet-Chouinard, E., Tan, F., Aires, F., Allen, G. H., ... Thieme, M. (2025b). Mapping the world's inland surface waters: an upgrade to the global lakes and wetlands database (glwd v2). *Earth System Science Data*, *17*(6), 2277–2329. Retrieved from https://essd.copernicus.org/articles/17/2277/2025/ doi: 10.5194/essd-17-2277-2025

Lehner, B., & Döll, P. (2004). Development and validation of a global database of lakes, reservoirs and wetlands. *Journal of Hydrology*, *296*(1), 1-22. Retrieved from https://www.sciencedirect.com/science/article/pii/S0022169404001404 doi: https://doi.org/10.1016/j.jhydrol.2004.03.028

Li, G., Gordon, I. E., Rothman, L. S., Tan, Y., Hu, S.-M., Kassi, S., ... Medvedev, E. S. (2015). Rovibrational line lists for nine isotopologues of the co molecule in the x1σ+ ground electronic state. *The Astrophysical Journal Supplement Series*, *216*(1), 15. doi: 10.1088/0067-0049/216/1/15

Maasakkers, J. D., Jacob, D. J., Sulprizio, M. P., Scarpelli, T. R., Nesser, H., Sheng, J.-X., ... Parker, R. J. (2019). Global distribution of methane emissions, emission trends, and oh concentrations and trends inferred from an inversion of gosat satellite data for 2010–2015. *Atmospheric Chemistry and Physics*, *19*(11), 7859–7881. Retrieved from https://acp.copernicus.org/articles/19/7859/2019/ doi: 10.5194/acp-19-7859-2019

Messager, M. L., Lehner, B., Grill, G., Nedeva, I., & Schmitt, O. (2016). Estimating the volume and age of water stored in global lakes using a geo-statistical approach. *Nature Communications*, *7*(1), 13603. Retrieved from https://doi.org/10.1038/ncomms13603 doi: 10.1038/ncomms13603

Nussbaumer, C. M., Kohl, M., Pozzer, A., Tadic, I., Rohloff, R., Marno, D., ... Fischer, H. (2024). Ozone formation sensitivity to precursors and lightning in the tropical troposphere based on airborne observations. *Journal of Geophysical Research: Atmospheres*, *129*(14), e2024JD041168. Retrieved from https://agupubs.onlinelibrary.wiley.com/doi/abs/10.1029/2024JD041168 (e2024JD041168 2024JD041168) doi: https://doi.org/10.1029/2024JD041168

Ort, L., Röder, L. L., Parchatka, U., Königstedt, R., Crowley, D., Kunz, F., ... Fischer, H. (2024). In-flight characterization of a compact airborne quantum cascade laser absorption spectrometer. *Atmospheric Measurement Techniques*, *17*(11), 3553–3565. doi: 10.5194/amt-17-3553-2024

Pommrich, R., Müller, R., Grooß, J.-U., Konopka, P., Ploeger, F., Vogel, B., ... Riese, M. (2014). Tropical troposphere to stratosphere transport of carbon monoxide and

long-lived trace species in the chemical lagrangian model of the stratosphere (clams). *Geoscientific Model Development*, *7*(6), 2895–2916. Retrieved from https://gmd.copernicus.org/articles/7/2895/2014/ doi: 10.5194/gmd-7-2895-2014

Röder, L. L., Ort, L., Lelieveld, J., & Fischer, H. (2024). Quantitative analysis of temporal stability and instrument performance during field experiments of an airborne qclas via allan–werle-plots. *Applied Physics B*, *130*(7), 118. doi: 10.1007/s00340-024-08254-5

Rodgers, C. D. (2000). *Inverse methods for atmospheric sounding: theory and practice* (Vol. 2). World scientific. (ISBN: 981-02-2740-X)

Tomsche, L., Pozzer, A., Ojha, N., Parchatka, U., Lelieveld, J., & Fischer, H. (2019). Upper tropospheric ch 4 and co affected by the south asian summer monsoon during the oxidation mechanism observations mission. *Atmospheric Chemistry and Physics*, *19*(3), 1915–1939. doi: 10.5194/acp-19-1915-2019

Toth, R. (2004). Linelist of n2o parameters from 500 to 7500 cm-1. *JPL online*.

Turner, A. J., Jacob, D. J., Benmergui, J., Brandman, J., White, L., & Randles, C. A. (2018). Assessing the capability of different satellite observing configurations to resolve the distribution of methane emissions at kilometer scales. *Atmospheric Chemistry and Physics*, *18*(11), 8265–8278. Retrieved from https://acp.copernicus.org/articles/18/8265/2018/ doi: 10.5194/acp-18-8265-2018

Wienhold, F., Fischer, H., Hoor, P., Wagner, V., Königstedt, R., Harris, G., ... Schilling, T. (1998). Tristar-a tracer in-situ tdlas for atmospheric research. *Applied Physics*

B, *67*, 411–417. doi: 10.1007/s003400050524

Zhu, Q., Jacob, D. J., Yuan, K., Li, F., Runkle, B. R. K., Chen, M., ... Halabisky, M. (2025, feb). Advancements and opportunities to improve bottom–up estimates of global wetland methane emissions. *Environmental Research Letters*, *20*(2), 023001. Retrieved from https://dx.doi.org/10.1088/1748-9326/adad02 doi: 10.1088/1748-9326/adad02

Table S1. Dry correction values derived from the N_2O[a]vertical profile above the Amazon basin, defined from 15°S to 5°N and 75°W to 45°W. The correction term (corr) was applied to the 1-second CH_4 data for only N_2O 1-s-values lower than the reference value (median from 7-13 km).

altitude bins [km]	corr [%]	$N_2O_{ambient}$ [ppb]	N_2O_{corr} [ppb]
0-1	3.4056	326.404	338.914
1-2	2.7095	328.616	338.914
2-3	1.8762	331.304	338.914
3-4	1.3462	333.037	338.914
4-5	0.6234	335.429	338.914
5-6	0.3091	336.480	338.914
6-7	0.0565	337.330	338.913
7-8	0	338.173	338.173
8-9	0	338.944	338.944
9-10	0	339.599	339.599
10-11	0	339.504	338.504
11-12	0	338.686	338.686
12-13	0	338.883	338.884
13-14	0	339.252	339.252
14-15	0	337.785	337.785

[a] Measured by TRISTAR (Wienhold et al., 1998; Tomsche et al., 2019).

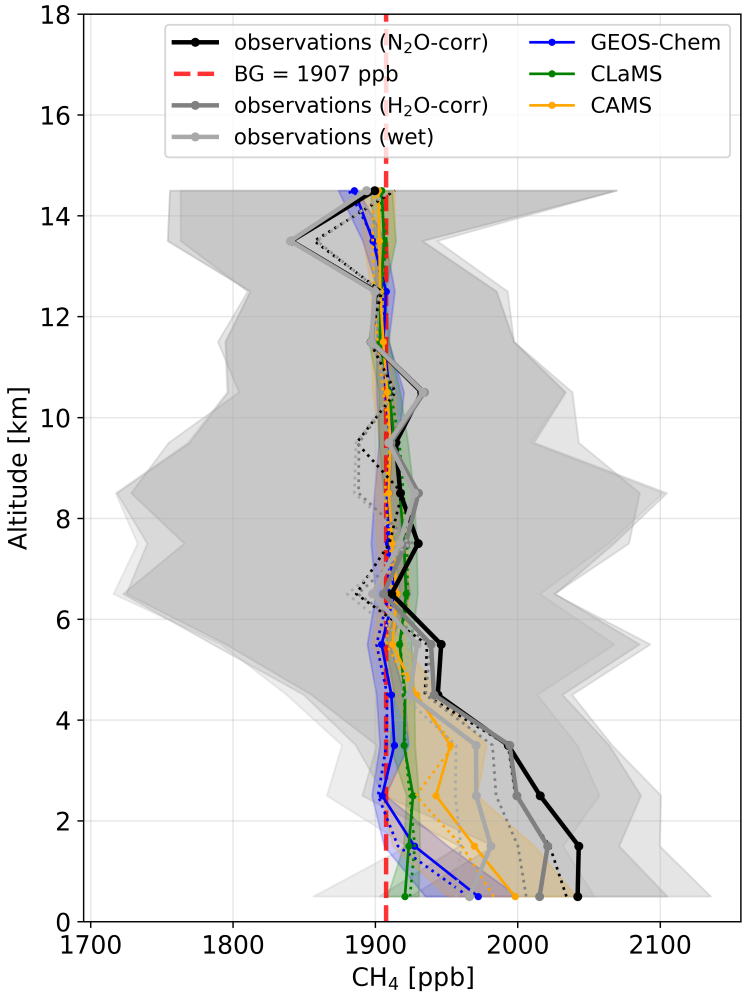

Figure S1. Vertical profile of methane measured and modeled above the Amazon region. The vertical profile is identical to Figure 1a in the main study, but additionally shows CH_4 ambient mixing ratios before water dilution correction (wet), and observations using only the H_2O correction via Equation S1 (H_2O-corr). The dry-corrected CH_4 profile already shows an enhancement towards the surface. However, the N_2O profile showed that this H_2O correction was not physically consistent (see Table S1). Therefore, we used an alternative correction via the N_2O profile (N_2O-corr) for the final data, as explained in the Text S1.2.

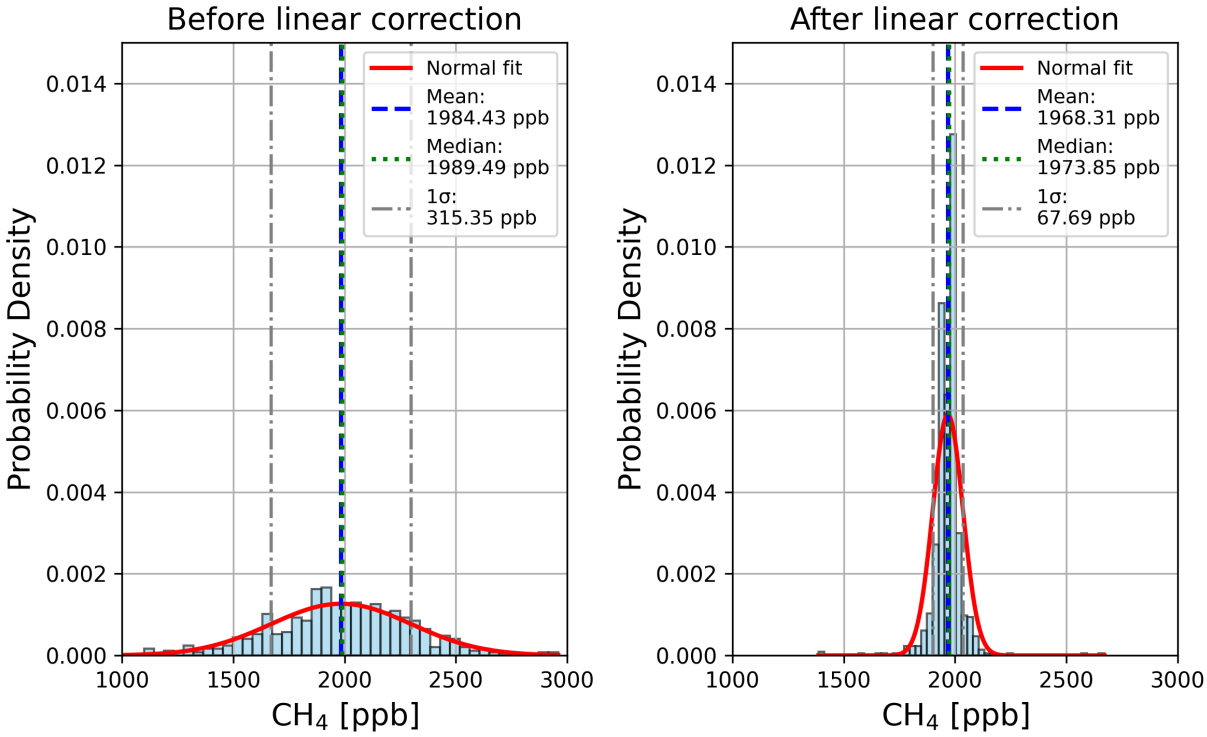

Figure S2. Normal distributions of all in-flight calibrations during the CAFE Brazil campaign. The left plot shows the calibrations before linear correction, the right plot after linear correction was performed. The reduction in the standard deviation applying linear correction is by a factor of approximately 4.5. The calibration frequency during each flight was at least every 20 minutes for 60 s, or whenever a new flight altitude was approached. The observational data in-between calibrations was corrected according to their surrounding calibrations. With this method, most of the instrumental drift error can be eliminated. Test flights were conducted to assure that this method can be applied (Röder et al., 2024; Ort et al., 2024).

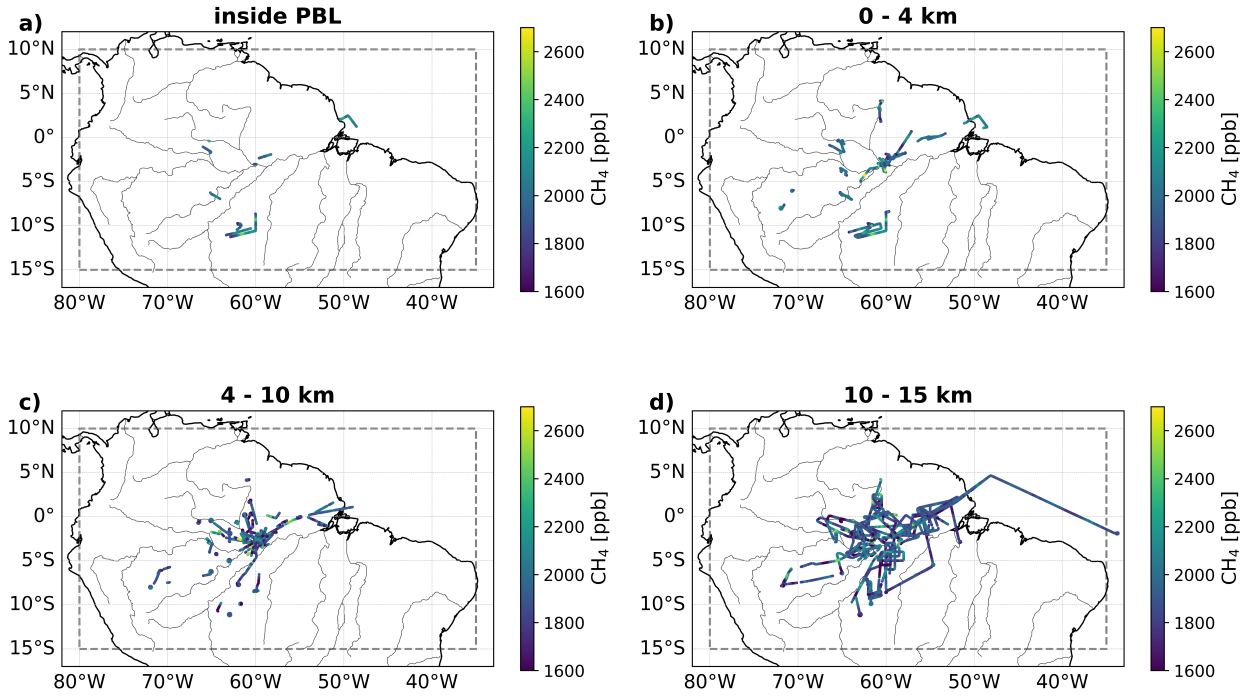

Figure S3. CH_4 observations in 60 s resolution separated into altitude ranges (a: inside PBL, below boundary layer height, BLH; b: 0 - 4 km, c: 4 - 10 km, d: 10 - 15 km). All those data points were used as input for the inversion, calculating the posterior flux inside the gray gridded box. The BLH was calculated based on ERA5 data.

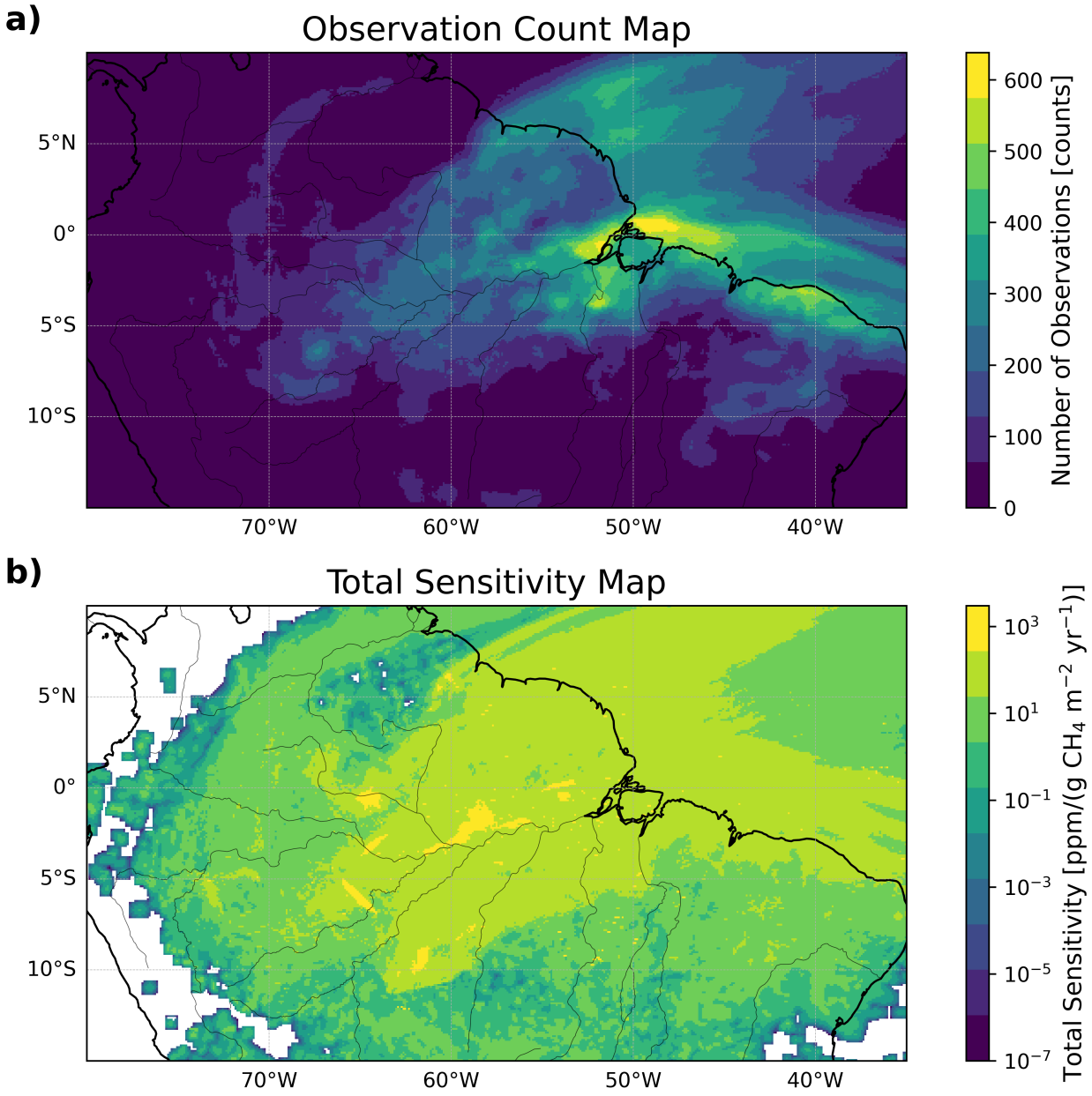

Figure S4. Counts of all trajectory endpoints per grid cell (a) and total particle dispersion fraction per cell (b) of the footprint matrix **H**, resulting from the simulation via STILT.

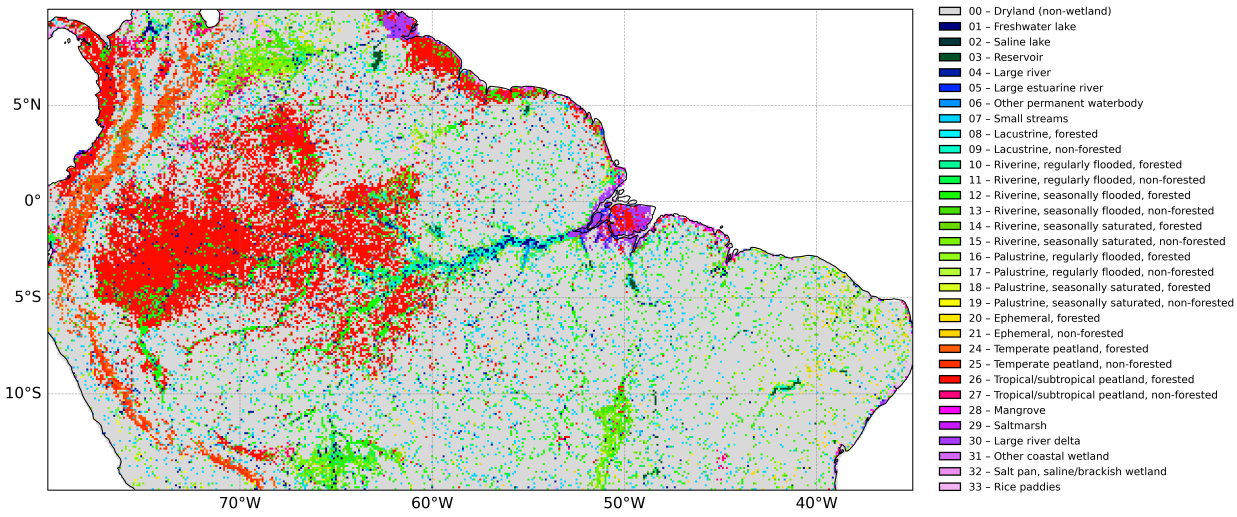

Figure S5. Land-cover type classifications by GLWD (Lehner et al., 2025b; Lehner & Döll, 2004), averaged for the grid resolution and domain of this study. Each grid cell has a original resolution of approximately 500 m at the equator. The original 500 m GLWD raster, taken from Lehner et al. (2025a), was read in geographic coordinates, wrapped to longitudes in the range -180° to 180°, and re-gridded to the 0.1°×0.1° grid using nearest-neighbor interpolation to retain discrete land-cover classes. Nearest-neighbor re-gridding was chosen because GLWD is a categorical land-cover product and the analysis requires a dominant class per model grid cell rather than sub-grid fractional coverage.

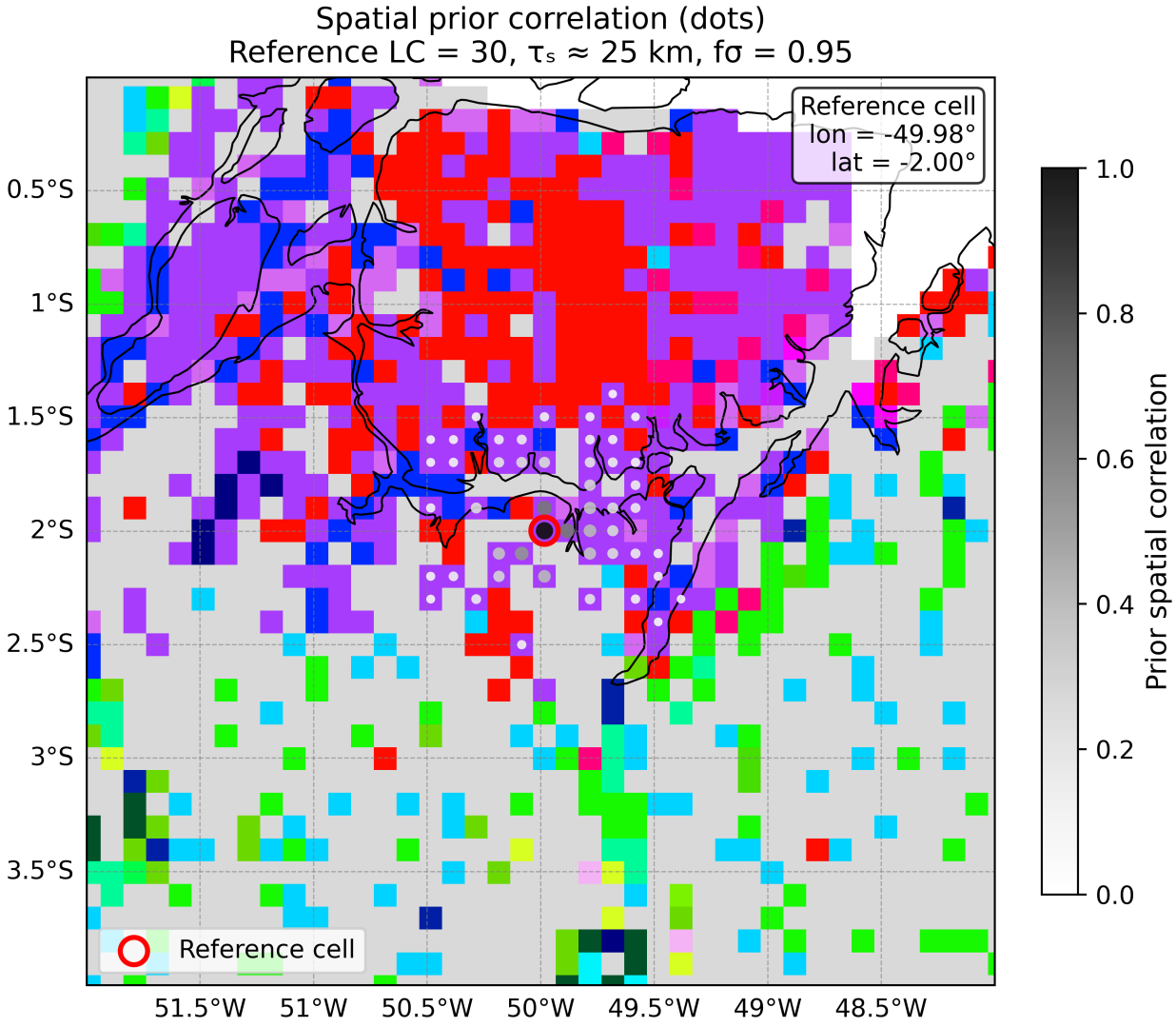

Figure S6. Spatial correlation across similar land-cover types shown for one example grid cell at 49.98°W and 2°S. The land-cover class "30" stands for "large river delta". Correlation is shown as gray dots within the grid cells, which are color-coded similar to the land-cover types shown in Figure S5. Spatial correlation is shown for $\tau_s = 25\,\text{km}$ and $f_\sigma = 0.95$. Full prior spatial correlation is at the starting grid cell (1), decaying exponential in space until it exceeds zero correlation within the distance limitation, or the lack of similar land-cover types.

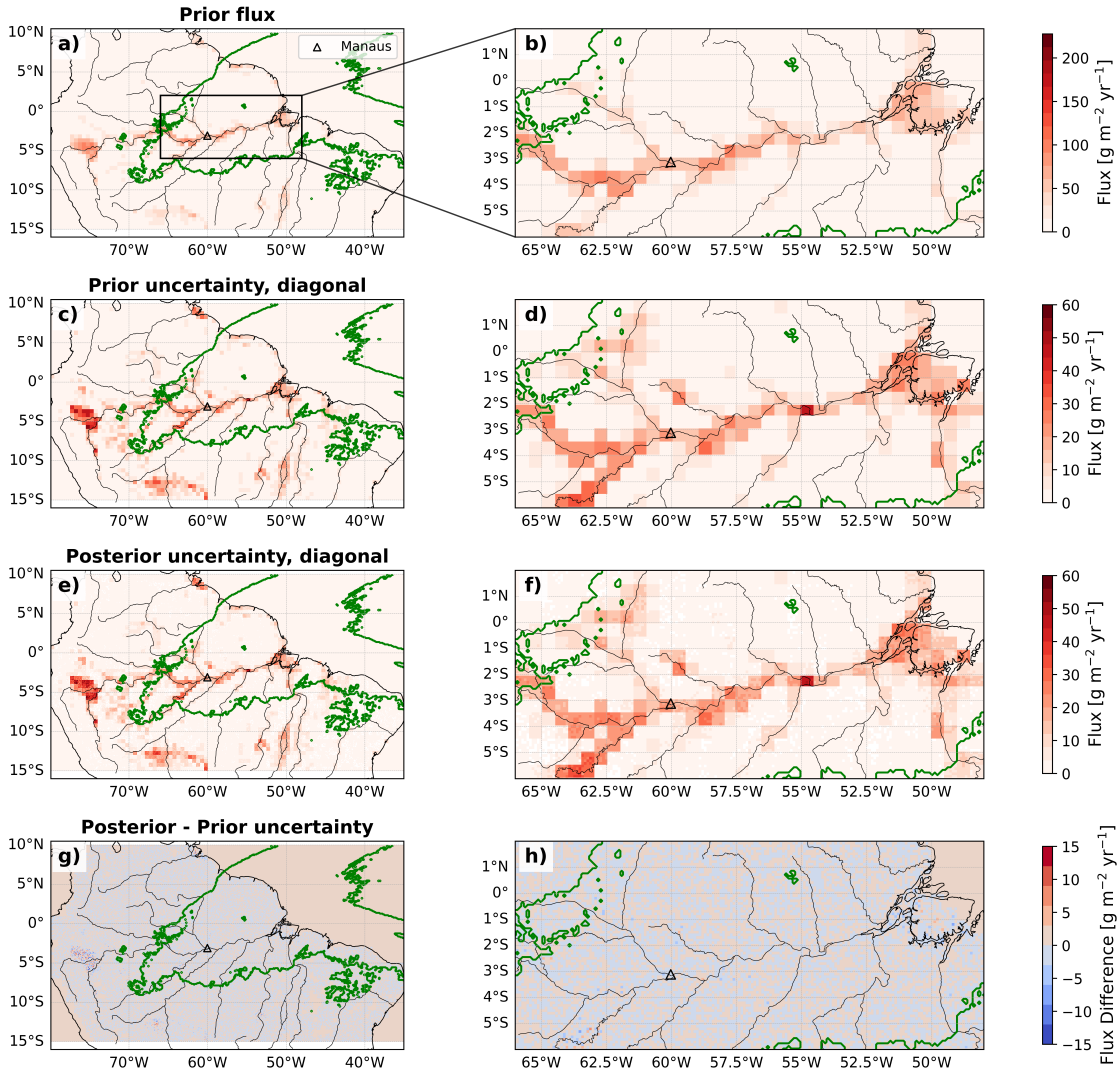

Figure S7. Prior flux (a, b), prior uncertainty (c, d), posterior uncertainty (e, f), and the uncertainty difference (g, h) shown in the same layout than Figure 2, with the full spatial domain in the left panel and the spatial extent in the right panel. The uncertainties are shown as standard deviations, resulting from the square-root of the diagonal variances of the prior and posterior uncertainty matrices $\mathbf{B}$ and $\mathbf{P}$, respectively, and their difference calculated as $\Delta\sigma = \sqrt{\sigma^2_{\mathbf{P}}} - \sqrt{\sigma^2_{\mathbf{B}}}$. The green contour lines show the area of 40% highest observational influence, and the triangles mark the location of the city of Manaus.

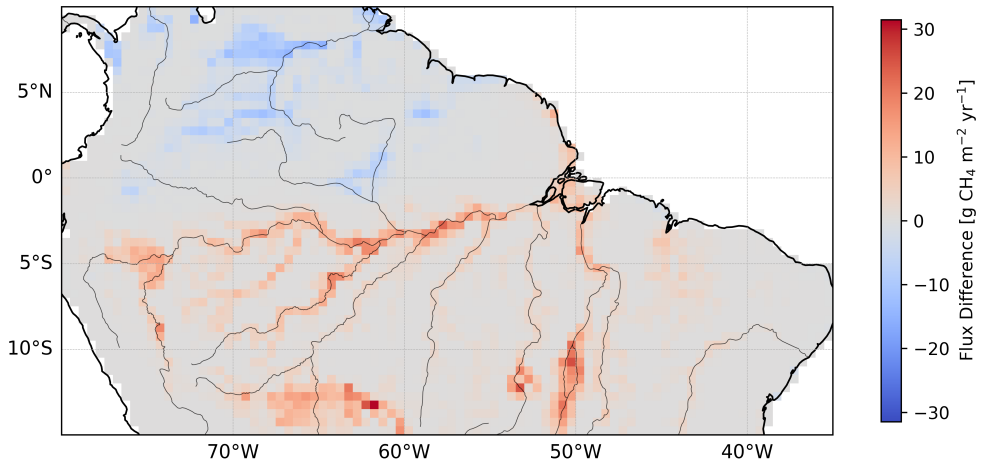

Figure S8. Flux difference using WetCHARTs monthly means of January and December vs an annual average over all months. Positive values indicate that December and January show higher emissions, negative fluxes vice versa.

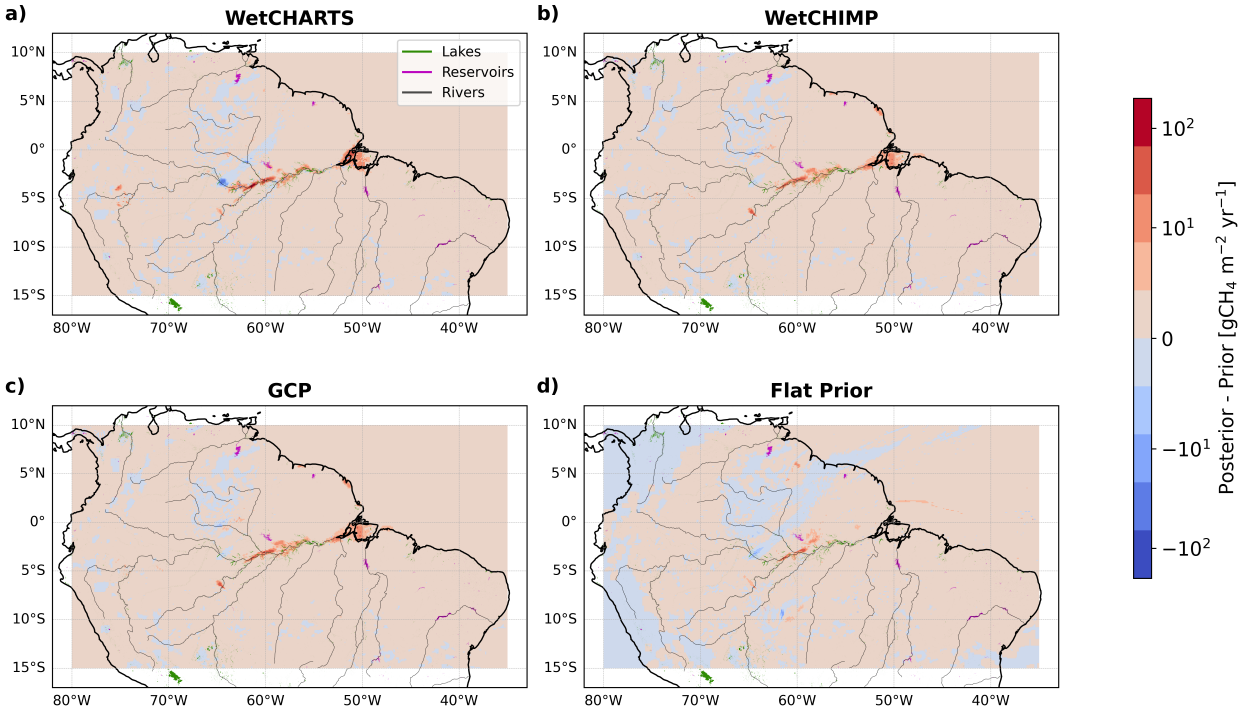

Figure S9. Posterior minus prior differences of four different priors (a: WetCHARTs, b: WetCHIMP, c: GCP, d: flat prior). The flat prior was chosen to match the magnitude of the other priors with a continuous flux throughout the whole domain of $10\,\mathrm{g\,m^{-2}\,yr^{-1}}$ and an uncertainty of $15\,\mathrm{g\,m^{-2}\,yr^{-1}}$ for every grid cell. Purple areas indicate reservoir positions, and green areas show the position of larger lakes in the domain (water surface data taken from the HydroLakes data base (Messager et al., 2016).) Those inversions were done using a simplified prior covariance matrix without spatial correlation and correlation factors by downsizing of f_σ =1. Despite the small difference in values by taking different priors, the spatial distribution of underestimated regions are nearly similar. Strongest difference shows the flat prior, which relies completely on the observational data and their footprints regarding spatial distribution of emissions.

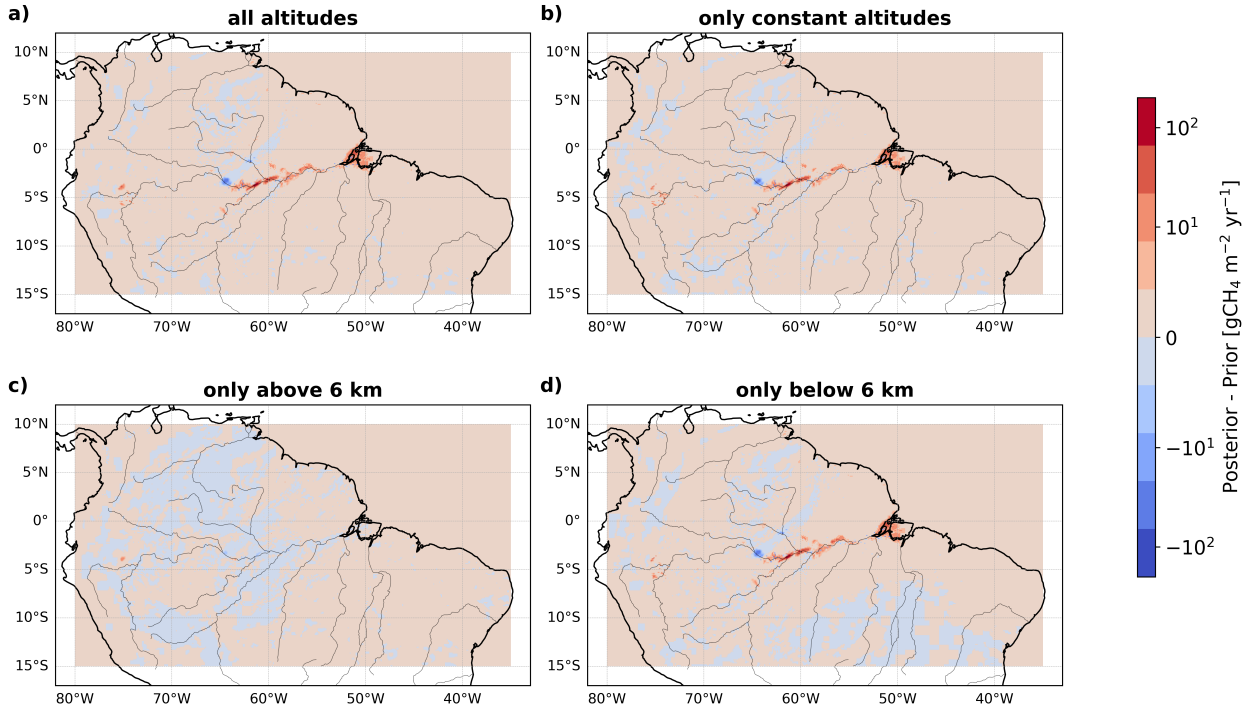

Figure S10. Posterior minus prior differences of four different observational inputs, separated by altitudes and using WetCHARTs as prior. Those inversions were done using a simplified prior covariance matrix without spatial correlation and correlation factors by downsizing of f_σ =1. All altitudes included in the inversion is shown in a); using only data along constant altitude flights excluding altitude changes larger than 5 m is shown in b); using observations at altitudes only above 6 km is shown in c); and using observations at altitudes only below 6 km is shown in d). By comparing the outcome of altitude separation, it can be said, that most of the posterior information relies on the observational data below 6 km. Furthermore, by separating the observational data by constant flight altitudes, hence excluding observational data with larger uncertainties, there is no significant change noticeable in the posterior fluxes.

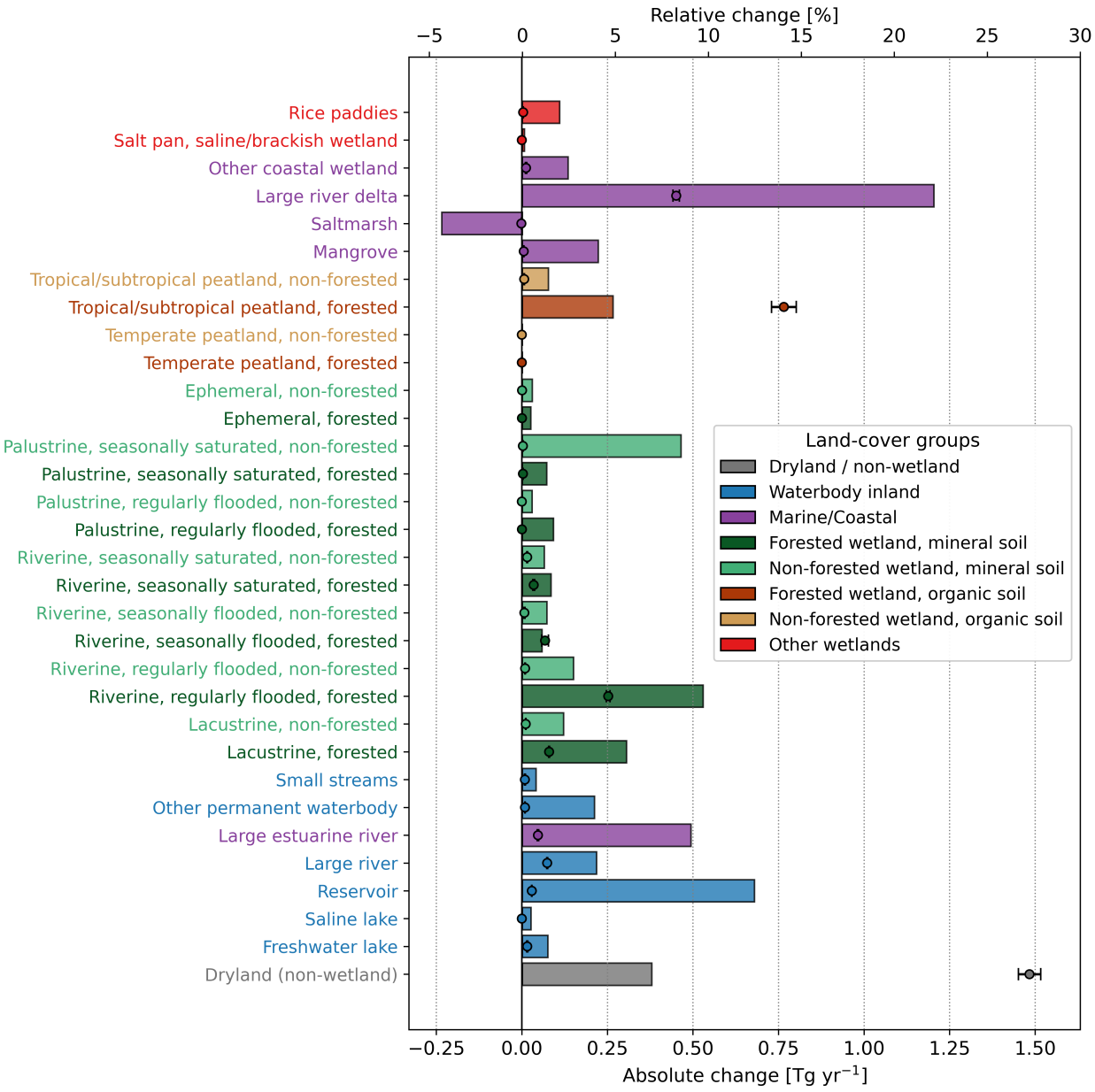

Figure S11. Same as Figure 3 in the main text, just for the whole Amazonian domain which is defined from 80°W – 35°W, and 15°S – 10°N.

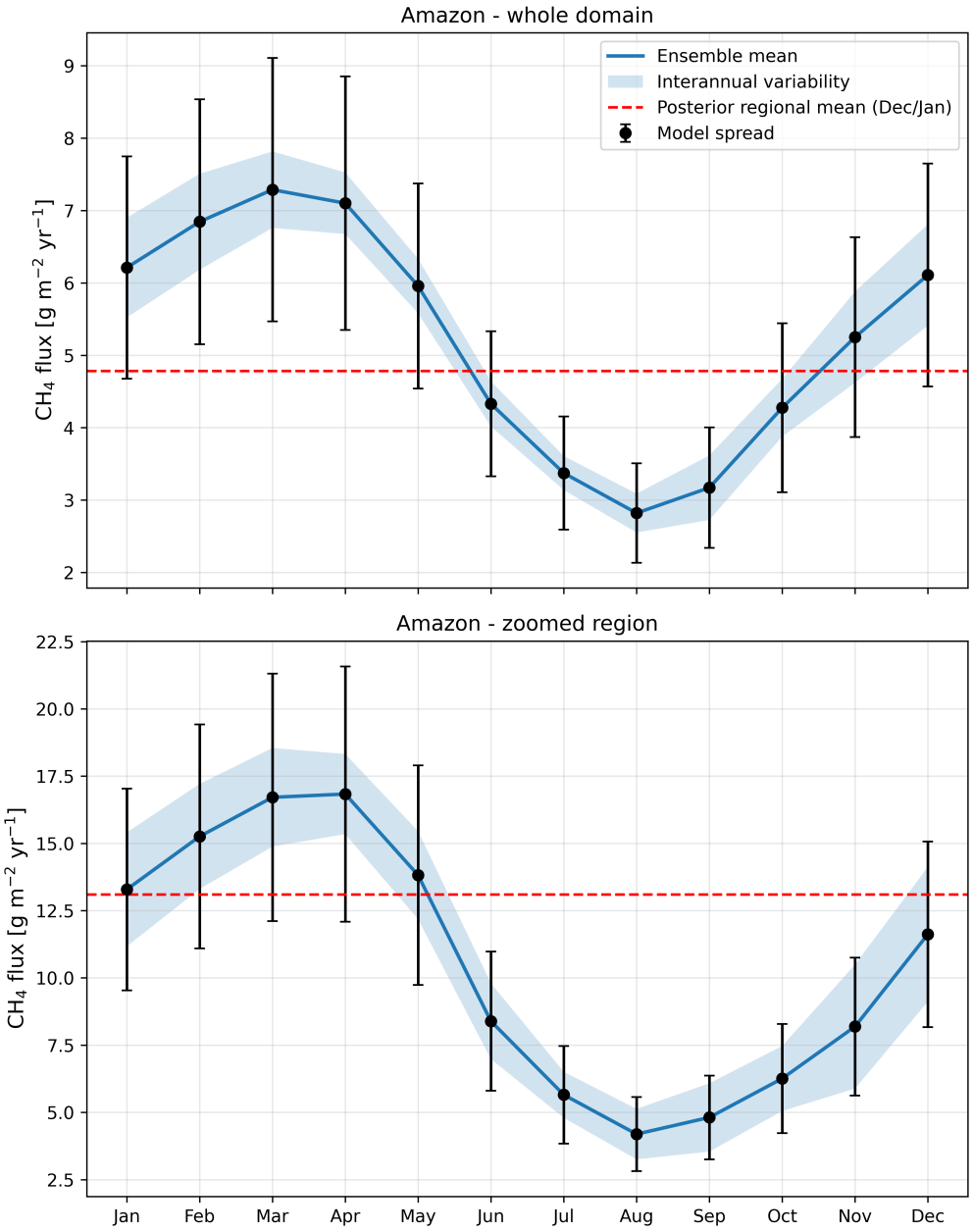

Figure S12. Seasonal cycle of WetCHARTs CH_4 fluxes over the Amazon for the full domain (top) and the zoomed subregion, same as used for the right panels in Fig2, and S7 (bottom). Solid lines show the 22-year (2001–2022) monthly climatology of the multi-model ensemble mean. Black error bars indicate the ensemble spread ($\pm 1\sigma$ across models), while light shading represents interannual variability ($\pm 1\sigma$ across years). The red dashed line denotes the posterior January–December mean flux derived from the inversion. Fluxes are shown in $\mathrm{g\,m^{-2}\,yr^{-1}}$.

Part III

The Role of Transport and Chemistry

3.7 Enhancement of O_3 – CO ratios at tropospheric subtropical latitudes: Photochemistry and stratospheric influence

This chapter presents an analysis about the role of photochemistry in comparison to dynamical transport processes within the troposphere onto trace gas distributions. This study uses airborne observations of O_3 and CO from twelve different airborne campaigns around the globe between 2012–2024, together with model simulations and a sensitivity study by the ECHAM5/Messy Atmospheric Chemistry (EMAC) model, to investigate the importance of lightning NO_x onto tropospheric O_3 and CO mixing ratios, in comparison with stratosphere-troposphere exchange processes.

I am the first author of this study, which was published in *Atmospheric Chemistry and Physics* in November 2025 as a research article. I participated in the CAFE Brazil campaign, the CAFE Pacific campaign, and in the PHILEAS campaign, being responsible for, among others, the CO measurements. I processed the CAFE Pacific and CAFE Brazil data, combined all airborne data sets, and analyzed them. Prof. Dr. Andrea Pozzer provided me with the EMAC simulations, which I used for the results presented. Together with Dr. Horst Fischer and Prof. Dr. Peter Hoor, I designed the study. I wrote the manuscript with proof-readings of all co-authors. All other co-authors were participants in other campaigns used for this study and provided me with insights of their publicly available data sets. More detailed author contributions can be found in the paper under *Author contributions*. All data used in this study can be found on the HALO database ((DLR), 2017), the NASA website (Wofsy et al., 2018), or on Zenodo (Ort and Pozzer, 2025; Obersteiner, 2024).

This work shows the importance of tropospheric photochemistry onto the global trace gas distribution, with a particular focus on the northern subtropics. Here, stratosphere-troposphere exchange (STE) processes and the downward branch of the Hadley cell merge, which both hold similar O_3 – CO ratios, but from two different mechanism; one purely dynamically mixing stratospheric air masses into the troposphere, and the other one, photochemically produced driven by lightning emissions, together with tropospheric transport. Latter mechanism showed a strong impact on the O_3 – CO ratio in the subtropics, equally important than STE for the trace gas distribution on a climatological average.

The supplementary material of this publication can be found in Section 3.8.

Atmos. Chem. Phys., 25, 14987–15007, 2025
https://doi.org/10.5194/acp-25-14987-2025

Atmospheric Chemistry and Physics
Open Access
EGU

Enhancement of O_3–CO ratios at tropospheric subtropical latitudes: Photochemistry and stratospheric influence

Linda Ort[1], Andrea Pozzer[1,10], Peter Hoor[2], Florian Obersteiner[3], Andreas Zahn[3], Thomas B. Ryerson[4], Chelsea R. Thompson[4], Jeff Peischl[5,6], Róisín Commane[7], Bruce Daube[8], Ilann Bourgeois[9], Jos Lelieveld[1,10], and Horst Fischer[1]

[1]Atmospheric Chemistry Department, Max Planck Institute for Chemistry, 55128 Mainz, Germany
[2]Institute for Atmospheric Physics, Johannes Gutenberg University, 55128 Mainz, Germany
[3]Institute of Meteorology and Climate Research – Atmospheric Trace Gases and Remote Sensing (IMK-ASF), Karlsruhe Institute of Technology, 76021 Karlsruhe, Germany
[4]NOAA Chemical Science Laboratory, Boulder, Colorado, 80301, USA
[5]Cooperative Institute for Research in Environmental Sciences, University of Colorado Boulder, Boulder, Colorado, 80309, USA
[6]NOAA Global Monitoring Laboratory, Boulder, Colorado, 80305, USA
[7]Department of Earth and Environmental Sciences, Lamont-Doherty Earth Observatory, Columbia University, Palisades, New York, 10964, USA
[8]Department of Earth and Planetary Sciences, Harvard University, Cambridge, Massachusetts, 02138, USA
[9]Université Savoie Mont Blanc, INRAE, CARRTEL, Thonon-Les-Bains 74200, France
[10]Climate and Atmosphere Research Center, The Cyprus Institute, Nicosia, 1645, Cyprus

Correspondence: Linda Ort (linda.ort@mpic.de)

Received: 27 March 2025 – Discussion started: 24 April 2025
Revised: 18 September 2025 – Accepted: 29 September 2025 – Published: 6 November 2025

Abstract. The subtropics are influenced by stratosphere-troposphere exchange processes through the subtropical jet streams and tropopause folding events, which are commonly identified by the opposing gradients of ozone (O_3) and carbon monoxide (CO) and thus their ratio. Here, we used airborne observations of CO and O_3, as well as the global three-dimensional ECHAM5/MESSy Atmospheric Chemistry (EMAC) model, to investigate whether there is another important mechanism that conditions the subtropics. We show that high O_3–CO ratios extend deeply into the troposphere in the subtropics, which is evident in both in situ observations and model results. Tropospheric photochemistry leads to similar O_3–CO ratios as those for stratospheric air diluted into the troposphere. In the upper tropical troposphere, frequent deep convective events produce lightning that leads to high concentrations of nitrogen oxides ($NO_x \equiv NO + NO_2$), which drive O_3 production and which further catalyze the recycling of hydroxyl (OH) radicals, which reduces CO. These lightning-affected air masses can be transported from the tropics into the subtropics via the Hadley circulation. We have excluded NO production through lightning in a sensitivity run of the EMAC model and see an annual relative reduction of the O_3–CO ratio of up to almost 50 % in the tropics and up to 40 % in the northern subtropics, with even larger seasonal variability and major effects on the vertical profiles of O_3 and CO. We therefore show that photochemistry is an additional key factor alongside stratosphere-troposphere mixing in determining O_3-rich and CO-poor air masses in the troposphere.

Published by Copernicus Publications on behalf of the European Geosciences Union.

1 Introduction

Transport processes in the subtropical troposphere are dominated by the Hadley circulation and stratosphere–troposphere exchange processes (STE). These processes shape the chemistry of the subtropics. Moist tropical air masses are lifted through deep convection within the intertropical convergence zone (ITCZ), distributed polewards in the upper troposphere. During the poleward transport the air cools and sinks at approximately 30° N and S, in the subtropical high-pressure belts. This thermally driven circulation which connects the tropics and the subtropics is known as the Hadley circulation (Seinfeld and Pandis, 2016).

Rapid chemical mixing in the upper troposphere and lower stratosphere (UTLS) occurs mainly through tropopause folding (Danielsen, 1968; Holton et al., 1995; Hoor et al., 2002), adiabatic mixing along isentropes, and up- and downdrafts of convective overshoots (Frey et al., 2015). Tropopause faults mostly occur in association with Rossby wave breaking or by the zonal shift of the subtropical jet streams at 30° N and S, resulting in bending of the tropopause (Postel and Hitchman, 2001). The transport of tropical air masses into the subtropics along the Hadley circulations is thought to take around 10 to 50 d (Seinfeld and Pandis, 2016), while mixing within the tropospheric hemispheres takes 1–2 months (Singh, 1995), and between the troposphere and stratosphere up to 0.8–2 years. Overall, the subtropical troposphere plays a critical role in the Earth's climate and atmospheric chemistry due to its unique position as a transition zone between the tropics and mid-latitudes as well as between the stratosphere and troposphere.

Ozone (O_3) and carbon monoxide (CO) are key trace gases in the troposphere and lower stratosphere. Ozone influences air quality, climate, and UV protection, while CO is an important combustion pollutant and regulates the atmosphere's oxidative capacity. The interactions and distributions of these two trace gases are critical for understanding air quality, atmospheric chemistry, and climate dynamics. Tropospheric O_3 originates naturally from the stratosphere (Danielsen, 1968) or through photodissociation of nitrogen oxides NO_x ($NO_x \equiv NO + NO_2$) in the presence of UV and visible light:

$$NO_2 + h\nu \rightarrow NO + O, \quad \text{(R1)}$$

$$O + O_2 + M \rightarrow O_3 + M, \quad \text{(R2)}$$

where M indicates a third molecule which stabilizes the O_3 formed as it absorbs the excess vibrational energy from the reaction (Seinfeld and Pandis, 2016). NO_x is produced by anthropogenic burning processes such as pollution emissions through aircraft, and industry, but also from natural sources, like biomass burning, soil emissions, and through lightning. Lightning NO_x (LNO_x) has been found to dominate O_3 chemistry in the upper troposphere (Nussbaumer et al., 2023a), particularly in the tropics, where 77 % of the world's lightning occurs. LNO_x in the upper troposphere has an approximated lifetime of 4–7 d (Schumann and Huntrieser, 2007).

In the presence of H_2O, and therefore mostly in the lower troposphere, ozone can be destroyed by photodissociation to form $O(^1D)$ and reaction with H_2O to form hydroxyl (OH) radicals through Reactions (R3) and (R4):

$$O_3 + h\nu \rightarrow O(^1D) + O_2, \quad \text{(R3)}$$

$$O(^1D) + H_2O \rightarrow 2OH. \quad \text{(R4)}$$

These reactions are the primary source of highly reactive OH radicals, which play a crucial role in removing most natural and anthropogenic gases from the atmosphere (Lelieveld et al., 2016). They can react within 1–2 s with CH_4, nonmethane volatile organic compounds (VOCs), and CO to form peroxy radicals ($HO_2 + RO_2$). In the free troposphere, the most important sink of OH radicals is through the reaction with CO (Lelieveld et al., 2016; Seinfeld and Pandis, 2016):

$$CO + OH \xrightarrow{O_2} HO_2 + CO_2. \quad \text{(R5)}$$

HO_2 radicals can further combine to form peroxides. Further propagation of the formed peroxides leads to higher-generation products, and reaction with NO for OH recycling, a secondary source of OH radicals. Different OH recycling mechanisms exist (e.g., O_x recycling, OVOC recycling, NO_x recycling), with NO_x recycling (Reaction R6) being the most prominent in highly NO_x-polluted regions and in the upper troposphere (Lelieveld et al., 2018):

$$HO_2 + NO \rightarrow NO_2 + OH. \quad \text{(R6)}$$

In the tropics, CO emissions are mostly derived from biomass burning and anthropogenic emissions (Crutzen and Andreae, 1990). In the free and upper troposphere, CO can further be produced through oxidation of CH_4 or other hydrocarbons (Strode et al., 2018). At the same time, high concentrations of OH through primary production on the surface, and secondary production in the upper troposphere, provide a strong sink for CO in the tropics. Overall, this shortens the lifetime of CO in the tropics to about one month, while its global lifetime is approximately three months in the troposphere (Lelieveld et al., 2016).

The subtropical troposphere is known to be mainly influenced by STE. The purpose of this study is to investigate the effect of transport and distribution of photochemistry via the Hadley circulation in the upper troposphere of the tropics into the subtropics. To study the relevance of that mechanism, we first present the zonal distribution of CO, O_3, and the O_3–CO ratio derived from airborne observations and further simulated by the dynamic EMAC chemistry model. Furthermore, we show with a sensitivity study of the model that internal tropospheric mixing processes along with chemical reactions make a higher-than-expected contribution to the tropospheric subtropical air masses.

2 Observations and model simulations

This study uses airborne in situ measurements of CO and O_3 from 12 different aircraft research campaigns as well as numerical results of the ECHAM5/MESSy EMAC model.

2.1 Airborne observations

The observations used in this work are from a combined data set of 12 different aircraft research missions, carried out from 2012 to 2024, covering all seasons (Table 1). Each campaign focused on investigations of dynamic and/or chemical processes of the troposphere and lower stratosphere based each in a different location around the world. The flight tracks of each campaign are shown in Fig. 1 and provide zonal and meridional coverage of the Earth, except for large parts of Asia. However, due to the long lifetimes of CO and O_3 in the troposphere, the Asian emissions are covered by long-distance transport processes, which also have been among the research goals of some of the campaigns (e.g., the Asian Summer Monsoon by OMO, WISE, PHILEAS). Specific research goals, and accordingly the flight planning, have been selected with consideration of specific weather or extreme events (e.g., deep convection, biomass burning events) and therefore can be biased to some extent. To minimize these biases, the medians of the averaged distributions are used in this study. Furthermore, the statistical representativeness of the selected observations has been tested with a model comparison of a full climatology and data just along the flight tracks. This comparison can be found in the Supplement. In particular, the modeled O_3–CO ratios along the flight tracks in the northern hemisphere and tropics have been found to agree well with the model climatology.

Two aircrafts were used throughout these campaigns: the High Altitude LOng-range (HALO) Gulfstream G550 research aircraft, run by the German Aerospace Center (DLR) and the NASA DC-8 aircraft, owned by the NASA Armstrong (Dryden) Flight Research Center. For CO measurements, four different instruments (UMAQS, QCLS, TRISTAR, ATTILA) and for O_3, two different instruments (FAIRO (Obersteiner, 2024), NO_yO_3) collected the data sets used in the scope of this work. The total measurement uncertainties for CO vary in a range of 0.94–1.8 ppbv and for O_3 from 2 % to 2.5 %. More detailed information on the uncertainties and equipment used during the campaigns can be found in Table 2 and in the Supplement. The measurement techniques for each tracer were similar. CO was measured by infrared absorption spectroscopy (Fried and Richter, 2006) with quantum cascade lasers (QCLS) (Faist et al., 1994; Pal and Pradhan, 2021) and multipass circulations of the types of White and Herriott (White, 1957; Herriott and Schulte, 1965; McManus et al., 1995; Wienhold et al., 1998) throughout all campaigns. The O_3 measurements were taken using UV absorption and chemiluminescence (CL) techniques (e.g., Toby, 1984; Ridley et al., 1992; Zahn et al., 2012). Frequent calibrations against primary and secondary standards during the research flights ensured comparability of the CO observations. For O_3, simultaneous UV absorption measurements alongside CL detection provide high accuracy and continuous in-flight calibrations.

From 2012 to 2024 there was no significant trend in the global average atmospheric mixing ratios of CO and O_3 in remote regions according to the measurements from the Carbon Cycle Cooperative Air Sampling Network (Laboratories, 1988) and the TOAR network data sets (Tarasick et al., 2019). Nevertheless, studies have shown annual variations, especially in more polluted and more densely populated regions. Field et al. (2016) has shown that in 2015 strong open biomass burning events caused by the global climate phenomenon El Niño resulted in the peaking of CO emissions in Indonesia which then spread into the upper troposphere over East Africa to the western Pacific Ocean. Furthermore, continuous control measures targeting industrial and transportation emissions in developed countries are leading to a moderate reduction of pollutants. For example, in China, from 2010 to 2017, a 16 % decrease in CO emissions could be achieved by replacing pollutant fuels (e.g., biofuel, coal) with cleaner fuels (e.g., natural gas, electricity) (Li et al., 2024).

Besides annual trends, there are seasonal and local variations in source regions (Hoor et al., 2002; Li et al., 2024). Emission rates in general depend on the amount of biomass burning and anthropocentric activity (e.g., heating, combustion), which are strongly season-dependent. In the tropics, the strongest seasonal differences are due to shifts of the zonal positioning of the ITCZ (Waliser and Somerville, 1994), in particular above land surface. The CAFE Brazil and CAFE Pacific campaigns collected a larger data set for continental areas in the tropics; these were run from December 2022 to January 2023 above the Amazon rainforest, and January to February 2024 above Australia, respectively. During CAFE Brazil, the seasonal shift of the ITCZ influences the contribution of air masses from the southern or northern hemispheres, affecting the Amazon basin. In January, the ITCZ is slightly south of the Amazon region, which leads to a stronger influence of air masses originating from the northern hemisphere in this region. The seasonal variation slightly shifts the deep convection activity zonally, and hence results in a broadening strong uptake of surface emissions in the vertical profile of the tropics. Note that meridional variations will also be averaged for this study.

However, zonal and annual averages, and the long lifetimes of O_3 and CO which ensure globally well transported and mixed distributions, tend to weaken the effects of those local and temporal emission variations. Nevertheless, these will be taken into account and further discussed in Sect. 3.

Overall, the twelve campaigns listed in Table 2 provide a good global coverage of in situ measurements from the boundary layer up to the lower stratosphere. In particular, good coverage can be found in the northern hemisphere, especially in the northern subtropical region. As the data sets

Table 1. Overview of aircraft campaigns used for this study. Most of the campaigns have been carried out with the HALO aircraft of the DLR (German Aerospace Center, Oberpfaffenhofen, Germany). The ATom campaigns have been carried out with the NASA DC-8 aircraft (Wofsy et al., 2018).

CAMPAIGN	START	END	AIRCRAFT
ESMVal (Earth System Model Validation)	10 Sep 2012	23 Sep 2012	HALO
OMO (Oxidation Mechanism Observations)	16 Jul 2015	25 Aug 2015	HALO
ATom 1 (Atmospheric Tomography Mission)	29 Jul 2016	23 Aug 2016	NASA DC-8
ATom 2 (Atmospheric Tomography Mission)	26 Jan 2017	21 Feb 2017	NASA DC-8
WISE (Wave-driven ISentropic Exchange)	31 Aug 2017	21 Oct 2017	HALO
ATom 3 (Atmospheric Tomography Mission)	28 Sep 2017	28 Oct 2017	NASA DC-8
ATom 4 (Atmospheric Tomography Mission)	24 Apr 2018	21 May 2018	NASA DC-8
CAFE Africa (The Chemistry of the Atmosphere Field Experiment in Africa)	7 Aug 2018	8 Sep 2018	HALO
SouthTRAC (Transport and Composition of the Southern Hemisphere UTLS)	19 Aug 2019	16 Nov 2019	HALO
CAFE Brazil (The Chemistry of the Atmosphere Field Experiment in Brazil)	30 Nov 2022	29 Jan 2023	HALO
PHILEAS (Probing High Latitude Export of air from the Asian Summer Monsoon)	6 Aug 2023	27 Sep 2023	HALO
CAFE Pacific (The Chemistry of the Atmosphere Field Experiment in the Pacific)	9 Jan 2024	1 Mar 2024	HALO

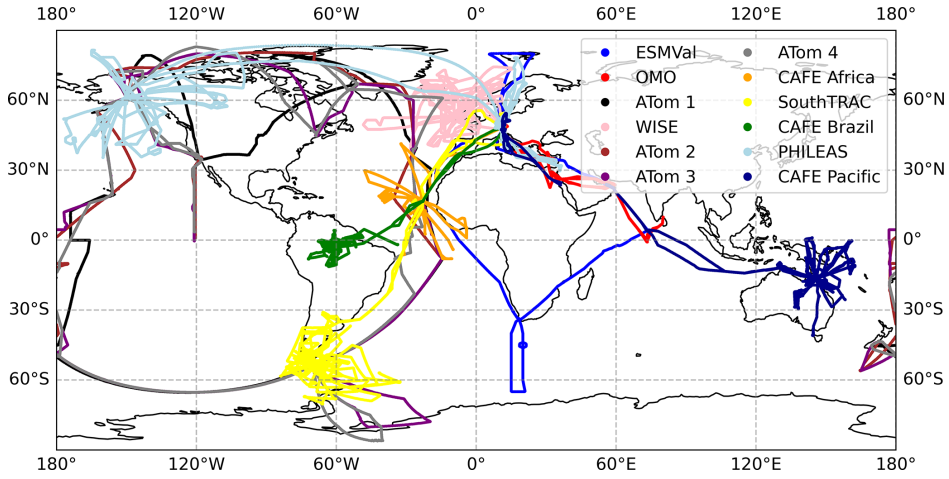

Figure 1. Overview of the flight tracks of the aircraft campaigns used in this study.

have been measured using various time resolutions, all sets were averaged to 60 s before they were combined. Furthermore, the measurements were transferred into the same grid resolution as the modeled data. More statistical information can be found in the Supplement.

2.2 EMAC model

The numerical results used for this study were simulated with the ECHAM5/MESSy Atmospheric Chemistry (EMAC) model (Jöckel et al., 2006, 2016 and publications therein). EMAC is a three-dimensional numerical chemistry and climate model which includes several sub-models describing lower and middle atmospheric processes and their interactions with the ocean, land, biosphere, human factors, and many other parameters. The simulation of atmospheric dynamics and transport processes is based on the fifth-generation of the European Centre Hamburg general circulation model (version 2.54.0; ECHAM5; Roeckner et al., 2006). Fully coupled chemistry and miscellaneous processes are provided by a set of submodels controlled by the second-generation Modular Earth Submodel System (version 2.54.0; MESSy; Jöckel et al., 2005, 2010).

Numerous experimental evaluations of the EMAC model have revealed it to be reliable (e.g., Jöckel et al., 2016; Tomsche et al., 2019; Lelieveld et al., 2018; Tadic et al., 2021; Nussbaumer et al., 2023b, 2024). In Lelieveld et al. (2018) a variety of atmospheric gases measured during the OMO aircraft campaign have been compared to the EMAC model, revealing a slight overestimation of tropospheric column O_3, and CO. O_3 overestimation by the model is attributed to an overestimation of transport from the stratosphere, related to the limited horizontal grid resolution of the model (1.875° × 1.875°) (Lelieveld et al., 2018). However, by reducing LNO_x emissions associated with deep convection, photochemical O_3 production declines in the upper tro-

Table 2. Information on the instrumentation, total measurement uncertainties (TMU), precision, data accuracy, time resolutions, and references for each campaign used in the scope of this work.

CAMPAIGN	INSTRUMENTATION	SPECIES	UNCERTAINTIES				REFERENCES
			TMU	precision	accuracy	time resolution	
ESMVal	TRISTAR	CO	1.8 ppbv			8 s	Schiller et al. (2008) Müller et al. (2016)
	FAIRO	O_3	2.5 %			12.5 Hz	Zahn et al. (2012) Rolf et al. (2015) Müller et al. (2016)
OMO	TRISTAR	CO	1.46 ppbv			8 s	Tadic et al. (2017) Tomsche et al. (2019)
	FAIRO	O_3	10 %			12.5 Hz	Zahn et al. (2012)
ATom 1[a], 2, 3, 4	QCLS	CO		0.15 ppbv	3.5 ppbv	1 Hz	Santoni et al. (2014) Strode et al. (2018)
	NO_yO_3 CL	O_3	2 %	15 pptv		1 Hz	Bourgeois et al. (2020, 2021)
WISE[b]	UMAQS FAIRO	CO O_3	0.94 ppbv 2.5 %			1 Hz 12.5 Hz	Kunkel et al. (2019) Zahn et al. (2012)
	NO_yO_3 CL	O_3	2 %	15 pptv		1 Hz	Bourgeois et al. (2020, 2021)
CAFE Africa	TRISTAR FAIRO	CO O_3	4.3 % 2.5 %			1 Hz 12.5 Hz	Tadic et al. (2017) Obersteiner (2024)
SouthTRAC	UMAQS FAIRO	CO O_3	1.4 ppbv 2.5 %	0.68 ppbv	1.22 ppbv	1 Hz 12.5 Hz	Müller et al. (2015) Obersteiner (2024)
CAFE Brazil	TRISTAR	CO	3.5 %	0.3 %	0.3 %	1 Hz	Schiller et al. (2008) Ort et al. (2024) Röder et al. (2024)
	FAIRO	O_3	2.5 %			12.5 Hz	Obersteiner (2024)
PHILEAS	UMAQS FAIRO	CO O_3	0.32 ppbv 2.5 %		0.64 ppbv	1 Hz 12.5 Hz	Riese et al. (2025) Obersteiner (2024)
CAFE Pacific	TRISTAR + ATTILA	CO	5.3 %	0.3 %	0.3 %	1 Hz	Ort et al. (2024) Nussbaumer et al. (2025)
	FAIRO	O_3	2.5 %			12.5 Hz	Obersteiner (2024)

[a] Thompson et al. (2022), [b] Riese and Hoor (2017).

posphere. Difficulties in representing the intermittent nature of convection and lightning has been shown in the study of Lelieveld et al. (2018) and are generally known to be a challenge for climate models. Comparisons of the CAFE Africa campaign measurements with the EMAC model show a weak correlation between measured and modeled NO in the upper troposphere (Nussbaumer et al., 2024). Nevertheless, this seems to be a regional issue, as, in general, measured NO_x, O_3, and HO_2 values are found to correlate well with the EMAC model (correlation coefficients of 0.5 and larger) in the OMO, CAFE Africa, CAFE Brazil, and ATom campaigns (Nussbaumer et al., 2024). More details on the EMAC model and its evaluation with measurements can be found in Righi et al. (2015) and Jöckel et al. (2016) and citations within.

The model resolution is T63L47MA, i.e., with a quadratic Gaussian grid resolution of $1.875° \times 1.875°$ and a vertical resolution up to 0.1 Pa, so as to include the stratosphere. The model has been weakly nudged by Jeuken et al. (1996) towards the European Center for Medium-Range Weather Forecasts (ECMWF) ERA5-interim data (Hersbach et al., 2020). The simulations cover a period of 20 years (i.e., 2000–2019). In this work, the hybrid pressure coordinates of the numerical simulations have been interpolated to an altitude of 1 km vertically; additionally, only monthly climatology of the data set has been used. In addition to the reference numerical simulation, a sensitivity numerical integration has been performed, binary identical to the reference simulation but with the lightning emissions of NO_x deactivated. In the following, we will refer to those two simulations as "REF" to

the standard simulation and "without LNO_x" to the sensitivity run excluding LNO_x emissions globally. Other sources of NO_x in the troposphere, such as surface and aviation emissions and mixing from the stratosphere, are included in both simulations. These simulations have been used before in Nussbaumer et al. (2023a) to investigate O_3 production from LNO_x in the upper tropical troposphere. In that study, the authors concluded that the only source of NO_x in the upper tropical troposphere is lightning, which is hence crucial for ozone production in that region.

A comparison along the flight tracks with the observations has shown good agreement of the climatology with the single point data (Supplement). Therefore, the full model is used for the investigation of the importance of LNO_x for the northern subtropics.

3 Results and discussion

3.1 Trace gas distributions based on observations

Figure 2a and b show the annual median zonal distributions of CO and O_3 mixing ratios, respectively, derived from all airborne in situ observations listed in Table 1. The data points are averaged over 1 km of altitude, 1.875° of latitude and over all longitudes. Their scales have been adjusted to emphasize tropospheric values. The black lines represent the lines of constant potential temperatures (Θ), which are calculated via Eq. (1), including the measured air temperature T and static pressure p, the surface pressure $p_0 = 1000$ hPa, and $\kappa = 0.286$.

$$\Theta = T\left(\frac{p_0}{p}\right)^{\kappa} \quad (1)$$

The grid cell has been hatched with white "xxx" if two conditions are met: (1) at least ten counts per grid cell (counts ≥ 10) and (2) good to moderate precision of the mean (standard error of the mean relative to the mean in percent: RSEM $\leq 15\,\%$). Note that each point is already an average to 60 s depending on each time resolution of the individual measurements, and that the precision includes seasonal and atmospheric variability. More details and the zonal distributions of the grid cell counts and the RSEM for each tracer individually can be found in the Supplement.

Both zonal distributions show a good coverage of the troposphere, despite some data gaps in the polar high latitudes, especially in the southern hemisphere. The observations made in the northern hemisphere are, with a few exceptions, contained within the confidence intervals previously defined (i.e., counts ≥ 10; RSEM $\leq 15\,\%$). Conversely, the southern hemisphere exhibits lower coverage within these conditions, particularly in the subtropics and polar latitudes.

The observations show the highest CO mixing ratios near the surface in the tropics and northern mid- to high latitudes, peaking with median mixing ratios of 120–140 ppbv, due to the close proximity to combustion sources (anthropogenic or natural). In the tropics, large amounts of CO can be released from biomass burning events mainly during the dry seasons (Galanter et al., 2000), and in the northern mid- to high latitudes, industrial combustion and other anthropogenic emissions are the main sources of CO (Tomsche et al., 2019). Highest CO is found at approx. 7.5° S and 2.5 km, a biomass burning plume originating from Africa captured along a single latitude transect during the CAFE Africa campaign (Crowley et al., 2025). The tropospheric background value of CO is approximately 60 ppbv in the southern hemisphere and 70–100 ppbv in the northern hemisphere, generally decreasing with increasing altitude. In the vicinity of deep convection or warm conveyor belts, close to a source region, CO shows instead a C-shaped vertical profile, which can be observed especially in the tropics in the ITCZ and the northern extra tropics. In the ITCZ, the level of main convective outflow is 10–12 km (potential temperature of 350–360 K), where the CO mixing ratio nearly achieves boundary layer mixing ratios. In the northern hemisphere, a local minimum of tropospheric CO mixing ratios can be identified in the subtropics. This minimum has been already observed during previous aircraft measurements, e.g., in 1997 and 1998, where surface CO mixing ratios in the northern subtropics varied from 60 to 140 ppbv and from 80 to 200 ppbv in the northern extra tropics (Hoor et al., 2002). With the increasing distance from the source regions towards higher altitudes, CO decreases to values below 40 ppbv. In the polar UTLS region, we record CO values of below 20 ppbv, which is due to the downward transport of stratospheric low-CO air. Close to the isentropic surfaces of 360 K, the tropopause can be expected in the tropics (Holton et al., 1995), while towards higher latitudes cross-tropopause exchange can happen at lower isentropic lines of 300–330 K (Sprenger and Wernli, 2003).

The O_3 zonal distribution in Fig. 2b, shows similar but inverted behavior compared to the CO zonal distribution. Low O_3 mixing ratios in the boundary layer are linked to dry deposition (Wesely and Hicks, 2000; Sumner et al., 2001), photodissociation (Reactions R3 and R4), and NO titration. These losses outweigh O_3 production through NO_2 photolysis (Reactions R1 and R2) especially in areas of low combustion NO_x emissions, e.g., remote places, forests, oceans. In the vicinity of strong NO_x combustion sources (biomass burning or industrial emissions), O_3 can be produced also at the surface. Nevertheless, low ozone values are prominent close to the surface, with minimum values in the tropics, where the median surface mixing ratios are lower than 20 ppbv. In the free troposphere, O_3 gradually increases with slightly higher values in the northern compared to southern hemisphere up to the O_3-rich stratosphere. In the ITCZ, through deep convection, low surface O_3 can be vertically mixed towards higher altitudes. Together with strong uptake, convective activity is a source of lightning, which produces O_3 via LNO_x, particularly in the convective outflow region in the ITCZ (Nussbaumer et al., 2023a). In contrast to the O_3 values in the tropics, a slight increase in O_3 mixing ratios

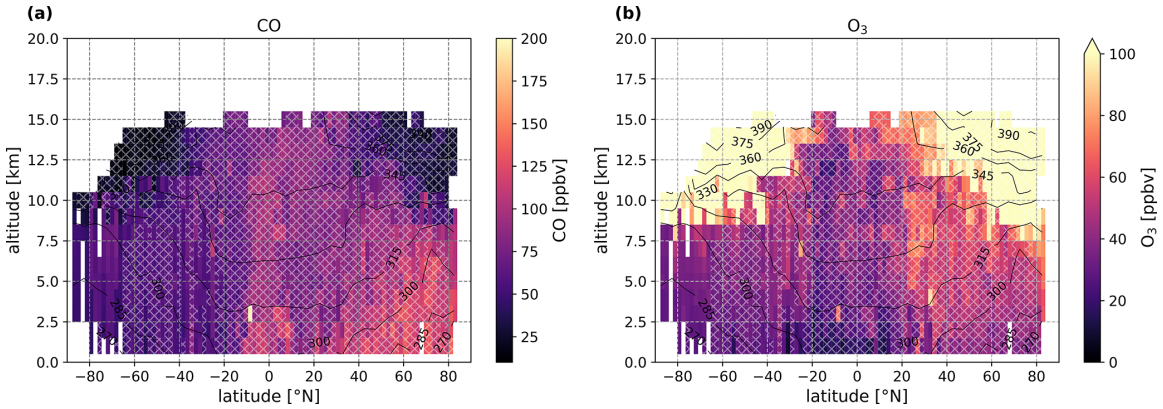

Figure 2. Zonal median distribution of CO **(a)** and O_3 **(b)** from the campaigns listed in Table 1. All airborne measurements have been averaged over 1 km of altitude, and 1.875° of latitude. The scale has been adjusted for O_3 to focus on tropospheric values. Black lines indicate layers of constant potential temperature, calculated using Eq. (1), and averaged over 5° and 1 km. Grid boxes, which represent averages with good to moderate standard error relative to the mean ($\leq 15\,\%$), and at least ten points per grid cell, are hatched with white "xxx". Note that each count represents an average of 60 s, depending on the time resolution of the measurements.

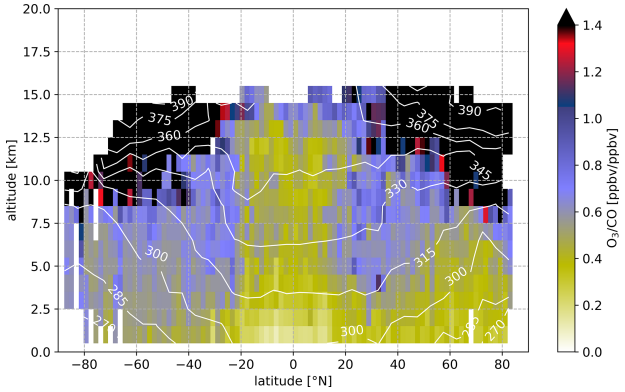

Figure 3. Same as Fig. 2, for the O_3–CO ratio, but without hatching and Θ shown as white lines.

can be noted in the vertical column of the northern subtropics around 30° N. While O_3 mixing ratios range from a few ppbv up to ~ 100 ppbv (Prather et al., 2011) in the troposphere, in the stratosphere, O_3 increases dramatically up to several thousands of ppmv due to photochemical production through higher energetic UV radiation and oxygen photolysis with a typical residence time of 1–2 years. In the stratospheric mid-latitudes and polar regions, the downward motion of the Brewer–Dobson circulation (Brewer, 1949; Dobson, 1956) transports stratospheric O_3-rich air closer to the tropopause. Here, ppbv values in the low hundreds have already been observed.

The ratio of O_3 to CO is shown in Fig. 3. In the absence of strong vertical transport, O_3 shows an increasing gradient towards higher altitudes, while CO decreases with altitude. This would result in low O_3–CO ratios near the surface and increasing ratios with altitude. This behavior is particularly observed in the southern extra tropics. Low O_3–CO ratios (< 0.6 ppbv ppbv^{-1}) up to 12.5 km in the ITCZ and up to 7.5 km in the northern mid-latitudes indicate transport of surface air masses with high CO and low O_3 mixing ratios. Higher O_3–CO ratios (> 0.6 ppbv ppbv^{-1}) represent air masses with lower CO and higher O_3, which can be observed closer to the stratosphere but also in the subtropics, which we will further define from 23.3–40°. This O_3–CO ratio enhancement is more pronounced in the northern compared to southern hemispheric subtropics in the observations. Although values are similar in the southern subtropics, the zonal gradient to higher latitudes is less pronounced than in the northern hemisphere, probably due to less data coverage, flight tracks that mostly traverse the ocean, and in general a lower CO background (no significant CO source in the southern high latitudes). In the following, we will focus on the northern subtropical region.

3.1.1 Observed northern hemispheric gradient

In the zonal distribution in Fig. 3, an increase in the O_3–CO ratio was observed in the northern subtropics around 23.3–40° N. For further analysis, we have calculated the zonal 10°, 2 km altitude-binned medians of the airborne measurements for CO, O_3, and their ratio for the northern hemisphere and shown in Fig. 4a, b, and c, respectively. The global gradients for the zonal medians, including the southern hemisphere, can be found in the Supplement. Only tropospheric values have been used based on O_3 mixing ratios lower than 100 ppbv, according to Prather et al. (2011).

The subtropics are dominated by relatively low CO and high O_3 mixing ratios, resulting in a median O_3–CO ratio of 0.7 ppbv ppbv^{-1} in the upper troposphere. Towards the tropics and the mid- to high latitudes, the O_3–CO ratios decrease

to 0.4–0.45 and 0.55–0.6 ppbv ppbv^{-1}, respectively, in the upper troposphere. This tendency is evident throughout all altitudes from 0 to 12 km. From the boundary layer to the upper troposphere, in the northern subtropics, CO mixing ratios range from 120 to 80 ppbv, and O_3 mixing ratios range from 35 to 65 ppbv, resulting in ratios of 0.35–0.7 ppbv ppbv^{-1}. Closer to the pole, we observe an enhancement of O_3 at higher altitudes (above 6 km), which could be due to the proximity of the tropopause and exchange processes with stratospheric O_3-rich air (Hoor et al., 2002, 2004).

Assuming that cross-tropopause exchange takes place mostly in the vicinity of the subtropical and polar jet streams and along isentropic layers, as has been shown in numerous studies (e.g., Lelieveld et al., 1997; Fischer et al., 2000; Krasauskas et al., 2021), enhanced O_3–CO ratios are expected in the subtropics and at the poles. Finding a negative correlation between O_3 and CO, several studies have identified air masses to originate from either the stratosphere or troposphere (Fischer et al., 2000; Hoor et al., 2002, 2004; Joppe et al., 2024). Here, we observe enhanced O_3–CO ratios covering the whole tropospheric column down to the boundary layer in the subtropics. This deep intrusion raises the question of whether cross-tropopause exchange, which transports high O_3 and low CO downward from the stratosphere into the troposphere, is the predominant mechanism affecting the troposphere subtropical column. To address this question, we investigated another possible mechanism that can lead to similar changes in the O_3–CO ratios in the subtropics. In the upper tropical troposphere, LNO_x emissions can lead to significant O_3 production, and simultaneously, catalyze OH recycling, which decreases CO in the atmosphere. Those emissions can be distributed via the Hadley circulation from the tropics into the subtropics. In the following, this hypothesis will be investigated using sensitivity simulations with the EMAC model (Sect. 2.2).

3.2 EMAC model simulations

To investigate whether a chemical mechanism contributes to the O_3 enhancement and CO decline in the subtropical troposphere, we use the three-dimensional chemistry and dynamic EMAC model. The model results cover 20 years of simulation (2000–2019) with monthly values and a spacial resolution of 1.875° × 1.875° × 1 km. This climatology has proven to be comparable to empirical observations (see Supplement). In the following, we test, whether the model reproduces the same subtropical O_3–CO ratio enhancement in its standard simulation (REF) which could be identified in the observations. As for the empirical observations, an annual zonal distribution of the modeled O_3–CO ratio has been calculated from this data set, shown in Fig. 5. An overview of the monthly zonal distributions can be found in the Supplement.

The ratio plotted in Fig. 5 shows similar features as identified in the zonal distribution of the airborne observations (Figs. 2 and 3). Low O_3–CO ratios are generally found in the lower troposphere and extend into higher altitudes in the mid- and high latitudes and in the tropics. Closer to the tropopause, O_3–CO ratios increase. Here, the model shows a slight overestimation of O_3 and CO, and hence of the O_3–CO ratio in the upper troposphere. A further difference can be noted in the tropical troposphere. The tropical "belt" of low O_3–CO ratio representing the ITCZ with strong uptake of surface mixing ratios through frequent convection seems to be less pronounced in the model than in the observations. This difference remains when looking at the model data extracted from the flight track (not shown here), which means that the representation of convection in the model is likely to cause this difference (Lelieveld et al., 2018; Nussbaumer et al., 2024).

The model shows a strong enhancement in both hemispheres, while the observations could not capture such ratios in the southern hemisphere, most likely due to the lack of observational data, especially towards the southern high-latitudes. In the model, relatively high O_3 and low CO values, indicated by high O_3–CO ratios, are found immediately above the boundary layer in both subtropical regions, compared to the values towards the tropics and mid-latitudes. However, background O_3 and CO ratios differ strongly between both hemispheres, mostly caused by the difference in land cover (natural) and anthropogenic emissions. This results in slightly lower O_3–CO ratios in the northern compared to the southern hemisphere, ranging from 0.4–1.1 and 0.45–1.4 ppbv ppbv^{-1}, respectively. Focusing on the northern hemisphere, the model captures well the features of observed zonal O_3–CO ratios.

3.2.1 Modeled northern hemispheric gradient

For a better comparison with the observations, we will focus on the northern hemispheric gradients in the following; however, we present the global zonal gradients, including the southern hemisphere, in the Supplement. In Fig. 6 the northern hemispheric gradients of the modeled CO, O_3, and the O_3–CO ratio for different altitude ranges are shown in (a), (b), and (c), respectively. Similar to the observations, the modeled data was averaged over 2 km and 10° of latitude over all longitudes for tropospheric values only, excluding data points with O_3 values higher than 100 ppbv, according to Prather et al. (2011).

In comparison to the observations, the modeled gradients for CO and O_3 mixing ratios are slightly higher except for the CO mixing ratios in the tropics, where the observations show higher CO mixing ratios throughout all altitudes. Furthermore, the decrease of CO in the northern subtropics is much more pronounced in the observations than in the model. Nevertheless, the difference between the model and the observations lies mostly within the range of the 25th and 75th percentiles and the gradients show a similar pattern: a higher O_3–CO ratio in the subtropics compared to the northern extra

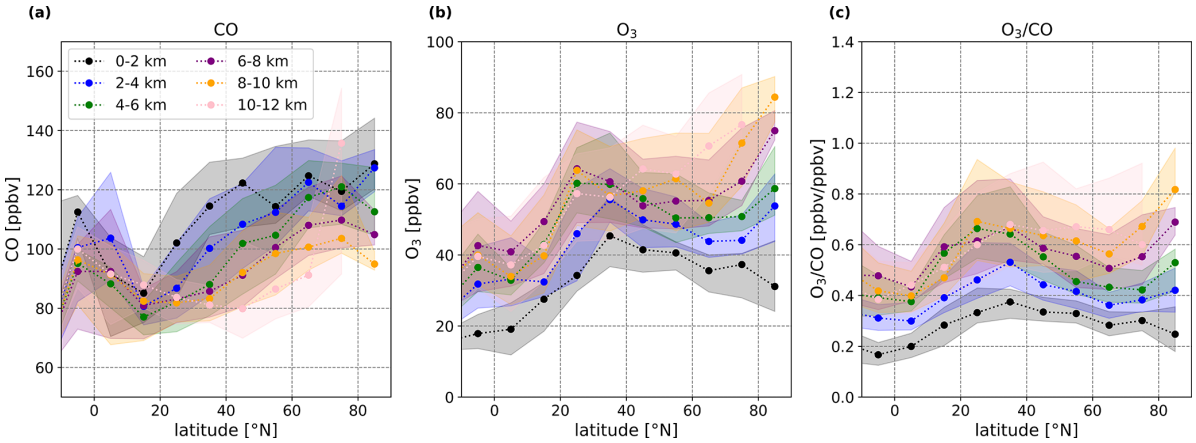

Figure 4. Northern hemispheric zonal gradients of CO **(a)**, O_3 **(b)**, and their ratio **(c)** based on all aircraft measurements, which are listed in Table 1, averaged over 10° of latitude, and 2 km of altitude. Displayed are the medians as dots and the 25th and 75th percentiles as shaded areas. Before the calculations, stratospheric values have been filtered out through excluding all measurements with O_3 values lower than 100 ppbv, according to the chemical troposphere definition of Prather et al. (2011).

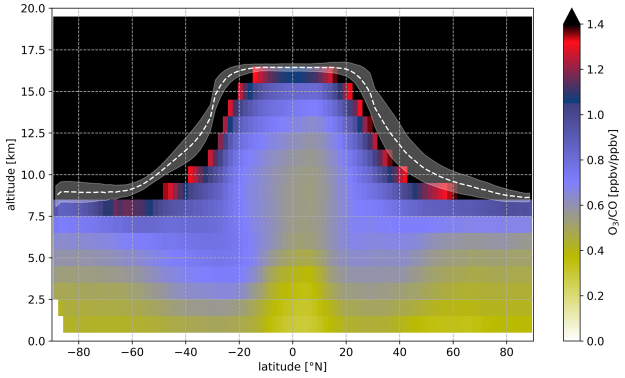

Figure 5. The median annual zonal distribution of the O_3–CO ratio calculated from the EMAC model data (REF). All data points are averaged over 1 km of altitude and 1.875° of latitude. The scale has been adjusted to display tropospheric values. The white dashed lines indicate the tropopause layer height with its standard deviation shaded in white.

tropics and tropics, particularly at lower altitudes. The underestimation of CO in the tropics results from applying global climatology, which results in the smoothing of emission regions with more remote regions. The flight track extraction tends to overestimate surface CO mixing ratios in the tropics, due to the complexity of modeling occasional biomass burning events and their exact emission rates.

Overall, the gradients of the O_3–CO ratio in Fig. 6c show a similar enhancement in the subtropics as has been observed (Fig. 4c), with modeled O_3–CO ratios ranging from 0.45 to 0.8 ppbv ppbv^{-1} in the northern subtropics with highest values close to the tropopause. The slight overestimation of the modeled median mixing ratios of CO and O_3 leads to $\sim$ 0.1 ppbv ppbv^{-1} higher O_3–CO ratios than in the observations. Nevertheless, the decreasing gradients towards the tropics and mid- to high latitudes are reproduced by the model.

3.3 Modeled sensitivity study: without LNO_x

The measured and modeled zonal distributions of the O_3–CO ratio, shown in Figs. 3 and 5, as well as the northern hemispheric gradients in Figs. 4 and 6, all indicate a strong enhancement in the O_3–CO ratio in the northern subtropics. It is to be expected that STE at the subtropical jet has a pronounced effect on the composition of the subtropical troposphere. This results in high O_3 and low CO mixing ratios in the troposphere of the subtropics. This process might be responsible for the O_3–CO ratio enhancement identified in the in situ observations and the model results. However, chemical processes in the upper troposphere driven by LNO_x emissions lead in principle to similar conditions, according to Reactions (R1), (R2), (R5), and (R6). Tropical convection associated with the ITCZ transports surface emissions into the upper troposphere. Lightning associated with deep convection produces significant amounts of NO, which catalyze a series of chemical reactions that yield O_3. In addition, NO is an important secondary OH source via recycling of peroxy radicals, leading to higher OH concentrations in the convective outflow (Lelieveld et al., 2018). This potentially shortens the lifetime of CO and other hydrocarbons (Lelieveld et al., 2016). The secondary production of highly reactive OH radicals results in reduced CO levels in the tropics. Overall, lightning is expected to yield enhanced O_3 and low CO mixing ratios. These air masses are transported within the troposphere following the Hadley circulation that transports tropical air masses into the subtropics. Thus, we hypothesise that high

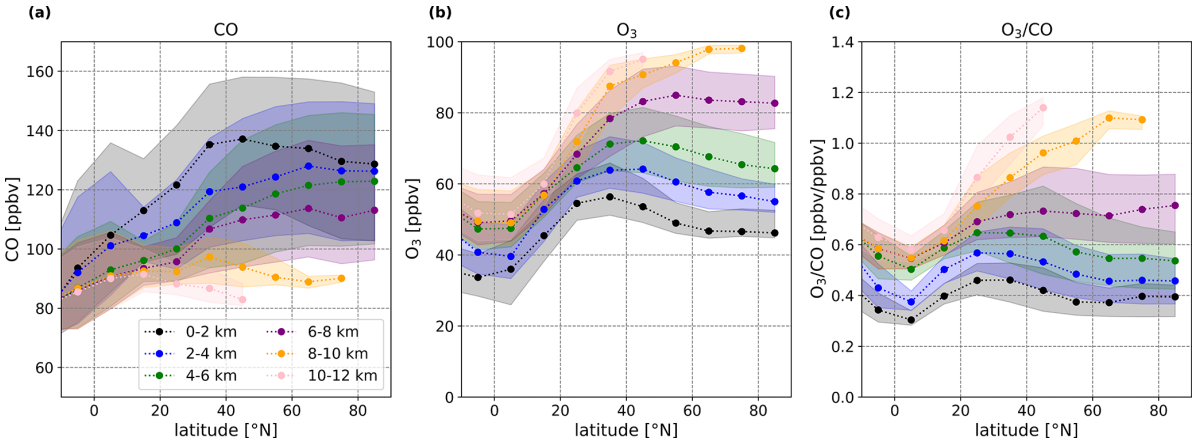

Figure 6. Northern hemispheric zonal gradients of CO **(a)**, O_3 **(b)**, and the O_3–CO ratio **(c)** from the EMAC model data (REF), averaged over 10° of latitude and 2 km of altitude. Dots represent medians and shaded areas denote the 25th and 75th percentiles. Before the calculations, only tropospheric data was selected based on the chemical definition of the tropopause by Prather et al. (2011) at 100 ppbv of O_3.

O_3–CO ratios in the subtropical troposphere are not only due to exchange processes with the stratosphere but result also through photochemistry within the troposphere. To test this hypothesis, we used a model sensitivity study without lightning NO_x production. By excluding LNO_x, the effect of high O_3 production and, indirectly, the loss of CO in the upper troposphere is excluded from the simulations, while all other mechanisms are kept as usual. Note that other reactions linked to NO_x chemistry, like the depletion of CH_4 and other hydrocarbons through OH, are also affected by the absence of LNO_x. However, dynamic processes, like STE, transport through tropospheric mesoscale circulations, surface emissions, and other chemical reactions which are not effected by LNO_x are unchanged. The difference between the "REF" and the "without LNO_x" simulations of the EMAC model can thus be interpreted as the effect of LNO_x on tropospheric chemistry (including, e.g., Reactions R1, R2, R5, R6). This effect we study on the basis of the absolute and relative differences of the zonal distribution, the change of the northern hemispheric gradients, and the vertical profile of the northern subtropics in the following sections. A zonal distribution of the annual average O_3–CO ratio from the sensitivity simulation can be found in the Supplement.

3.3.1 Relative and absolute differences due to LNO_x emissions

In Fig. 7 the absolute and relative differences for CO (a, b), O_3 (c, d), and OH (e, f) between the standard model run and the sensitivity run without lightning emissions are shown for the annual average, respectively. The absolute difference (D_{absolute}), calculated in Eq. (2), represents the total change of mixing ratios (MR) caused by LNO_x, and the relative difference (D_{relative}, Eq. 3) represents changes relative to the local mixing ratios provided by the standard simulation (REF) in percent.

$$D_{\text{absolute}} = \text{MR}_{\text{without LNO}_x} - \text{MR}_{\text{REF}} \quad (2)$$

$$D_{\text{relative}} = \frac{\text{MR}_{\text{without LNO}_x} - \text{MR}_{\text{REF}}}{\text{MR}_{\text{REF}}} \times 100 \quad (3)$$

As expected, by excluding LNO_x from the EMAC model simulations, generally, OH radicals are decreasing, CO is increasing and O_3 is decreasing. The largest impact is found in the tropics in the upper troposphere where the largest emissions of LNO_x are found (Schumann and Huntrieser, 2007; Nussbaumer et al., 2023b). The absence of NO reduces the secondary production of OH radicals by a factor of two to three (Reaction R6), according to Lelieveld et al. (2016), and are highly reactive with CO in the upper troposphere. Here, OH is reduced by a factor of 2.4, which increases absolute CO mixing ratios by 15–25 ppbv south and north of the ITCZ. This is a difference of over 30 % compared to values measured for CO in the upper tropical troposphere by excluding LNO_x.

Simultaneously, O_3 is reduced in the upper tropical troposphere by up to 40 % by excluding LNO_x. Average O_3 mixing ratios in the tropical upper troposphere are in the range of 50 ppbv. Inhibiting production through LNO_x decreases O_3 by 15–20 ppbv in that region. Especially in the upper tropical troposphere, LNO_x is expected to be the predominant driver of photochemically formed O_3, which we confirm with these results.

Overall, the sensitivity run indicates that without LNO_x, O_3 and OH production decreases. This yields lower O_3 and higher CO mixing ratios in the upper tropical troposphere. Subsequent transport in the Hadley circulation results in similar changes for O_3 and CO in the subtropics. Note that switching off LNO_x also affects the mixing ratios of CO and O_3 in the lowermost stratosphere, although to a lesser extent, compared to typical CO and O_3 values in the stratosphere.

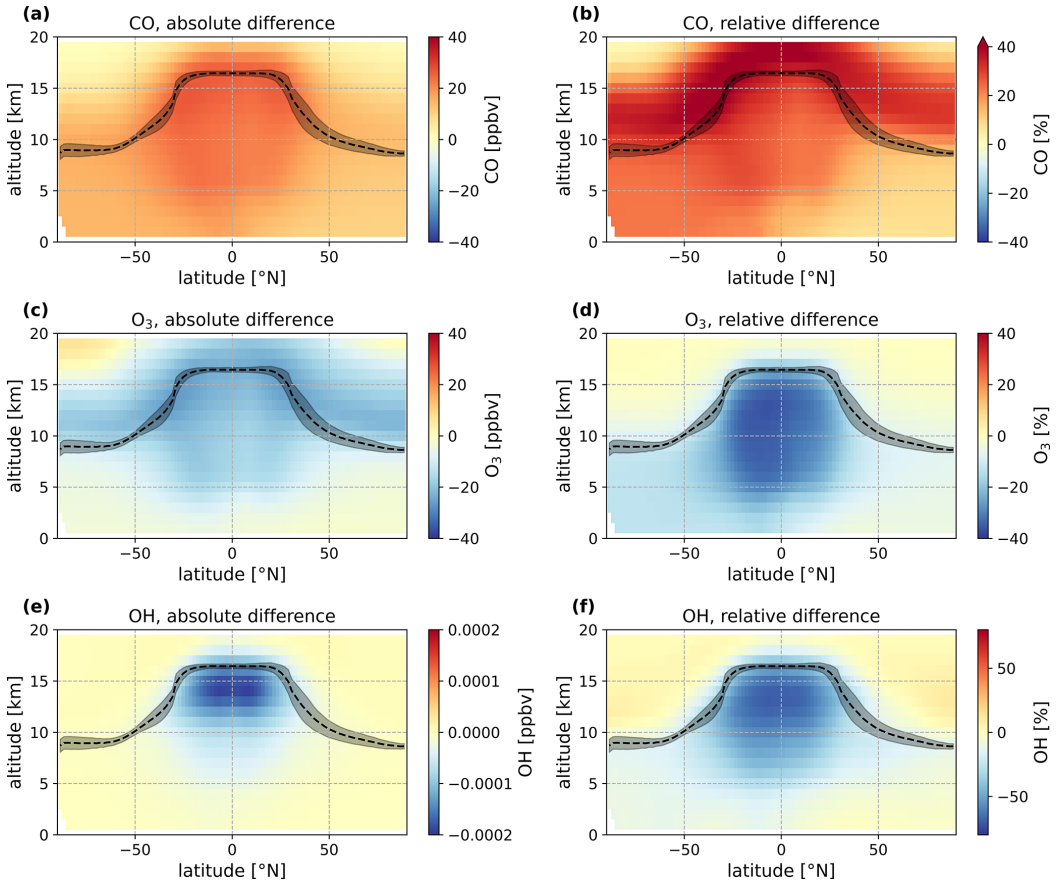

Figure 7. Relative and absolute differences of CO **(a, b)**, O_3 **(c, d)**, and OH **(e, f)** caused by excluding LNO_x emissions in the global 3D model EMAC, shown on annual averaged zonal mean distributions. On the left side **(a, c, e)** the absolute differences (Eq. 2) of the gas concentration are shown and on the right side **(b, d, f)** the relative differences (Eq. 3) in percentages normalized to the background concentrations. Note the scales for OH differ from CO and O_3. The black dashed lines and shaded area indicate the mean height of the tropopause layer and its standard deviation, respectively, by taking the zonal and annual average.

Nevertheless, these changes in the lowermost stratosphere are expected to be mainly caused by upwelling air transported through the tropical tropopause layer (TTL) into the stratosphere and distributed in the lowermost stratosphere.

The chemical lifetime of CO can be estimated with OH concentrations, assuming only its major atmospheric sink through OH in the upper troposphere and standard pressure and temperature conditions (200 hPa, 250 K) and a reactivity rate of $k = 1.57 \times 10^{-13}$ cm^3 molecules^{-1} s^{-1} according to McCabe et al. (2001). Using this approximation and only focusing on the absence of NO recycling the OH increases CO lifetimes in the upper tropical troposphere from approximately two months (67 d) up to five months (161 d). In comparison, Lelieveld et al. (2016) achieved a CO lifetime of 38 d for the upper tropical troposphere. Furthermore, we noticed a relative change in OH radicals also towards higher latitudes, which suggests OH recycling through transported NO, which lifetime is at $\sim$ 4–7 d (Schumann and Huntrieser, 2007). Transport through the Hadley circulation into the subtropics takes 10 to 50 d according to Seinfeld and Pandis (2016). Therefore, the photochemistry that results in higher O_3 and reduced CO is expected to continue during transport from the tropics to the subtropics. By calculating the change of chemical lifetimes of CO for the northern subtropics, we achieve a change from 56 d to approx. 70 d, over the whole tropospheric column. This is an increase of CO lifetimes by a factor of 1.24. Note that the production of CO by CH_4 oxidation is also altered by the absence of LNO_x emissions. While OH acts as an important sink for CH_4 as well (Lelieveld et al., 2016), longer lifetimes and thus higher levels of CH_4 are also expected as a consequence of excluding LNO_x emissions. Through the increase in CH_4 mixing ratios, more CO can be produced by its oxidation. However, CH_4 is quite stable with a lifetime of approximately 9 years (Szopa et al., 2021) and with mixing ratios an order of magnitude higher than CO (approx. 1770–1870 ppbv in the annual global mean at ma-

rine surfaces in the years from 2000 to 2019 according to the NOAA background stations network, Lan and Dlugokencky, 2025). Therefore, we expect the contribution to the increase of CO resulting from enhanced CH_4 to be rather small.

Overall, upper tropical LNO_x emissions can exert a profound influence all the way down to the lower troposphere of the subtropics (approximately 3 km). Therefore, the resulting changes in the subtropics are linked directly to LNO_x production in the upper tropical troposphere affecting the chemistry there, and along the path ways of the Hadley circulation.

3.3.2 Modeled northern hemispheric gradient without LNO_x

In Fig. 8, the modeled annual zonal northern hemispheric gradients of the CO (a), O_3 (b), and O_3–CO ratio (c) are shown for the "without LNO_x" simulation. The corresponding gradients for all latitudes can be found in the Supplement.

There are three main differences to the standard simulation, in addition to the above-mentioned generally higher CO and lower O_3 mixing ratios: lower O_3–CO ratios over the whole northern hemisphere; less vertical variation in the tropics and subtropics; and, a partially smaller meridional variability indicated by the 25th and 75th percentiles.

First, we focus on the generally lower O_3–CO ratios. Excluding LNO_x emissions causes an increase in tropospheric CO and a reduction in tropospheric O_3, as shown before, resulting in a smaller ratio. This reduction is most pronounced in the upper troposphere and continues into the free troposphere and lower troposphere with decreasing influence. Hence, the annual average of the O_3–CO ratio is nearly constant at 0.4 ppbv ppbv^{-1} throughout the whole subtropical troposphere and is even lower in the tropics at 0.3 ppbv ppbv^{-1}. Nevertheless, the local high of the O_3–CO ratio in the subtropics is still present, albeit weaker.

Secondly, vertical changes of the mixing ratios seem to be smaller, yielding similar O_3–CO ratios from the boundary to the upper troposphere. Only towards the pole, where the tropopause is much lower and the influence from the tropics much weaker, the vertical gradient is still visible.

Finally, the percentiles provide an indication of meridional variations over the zonal-vertical averages, showing reduced variability for the sensitivity run without lightning relative to the base run. This indicates enhanced homogeneity not only vertically but also meridionally.

The absolute and relative differences between the base run and the sensitivity run for the northern hemispheric gradients of the O_3–CO ratios are shown in Fig. 9a and b, respectively. Again, the corresponding gradients for the global distribution can be found in the Supplement.

Focusing on the absolute differences (Fig. 9a), calculated in Eq. (2), we find the largest change in the upper troposphere in the subtropics with O_3–CO ratios smaller by -0.4 ppbv ppbv^{-1} than for "REF". The least impact is found at the lowest altitude range (0–2 km) and towards the higher latitudes.

The relative differences, which are calculated with Eq. (3), show the normalized influences, which are strongest in the tropics slightly south of the equator extending into the subtropics. The relative effect is smallest again towards higher latitudes and lower altitudes but results in a change in the O_3–CO ratio of 50 % in the tropical upper troposphere and over 40 % in the subtropics.

3.3.3 Vertical distribution of the northern subtropics

The vertical distribution of the mean relative differences between the base run and the sensitivity run without LNO_x of CO, O_3 and the O_3–CO ratio for the northern subtropics, ranging from 23.3–40° N, are shown in Fig. 10. The main effect of switching off LNO_x is found in the upper troposphere, mainly around 12 km.

We can assume that deep convection, and hence local LNO_x emissions, are rare in the subtropical regions due to a general downward motion via the Hadley circulation. Nussbaumer et al. (2023a), who used a similar simulation with EMAC, concluded that lightning occurs and is observed mainly over land in the upper tropical troposphere.

As has already been seen in the zonal gradients, LNO_x emissions cause a strong impact on the subtropical mixing ratios of O_3 and CO, yielding enhanced O_3 and diminished CO. For zonal and annual averages, excluding LNO_x emissions increase CO by ~ 30 % and decrease O_3 by ~ 20 % in the upper subtropical troposphere (orange and blue bars in Fig. 10). This results in a change of the subtropical ratio of these two gases by over 30 % in the mean value of the upper subtropical troposphere. In general, the effect of LNO_x on O_3, CO, and the O_3–CO ratio decreases towards the surface in the subtropics. Nevertheless, there are still changes in the O_3–CO ratio of over 10 % attributable to the effect of LNO_x in altitudes lower than 1 km. Overall, the LNO_x effect on CO removal by OH recycling is one-third of the northern subtropical CO mixing ratio. Taking into account that seasonality and spatial differences have been averaged, the impact of tropical LNO_x on the subtropics is not expected to be equally distributed, and therefore stronger and lesser for each region and time.

3.3.4 Seasonal variability

The annual zonal distributions, shown and discussed in the previous sections, provided an average over all seasons. Therefore, seasonal variability has been smoothed out. To show the effect of excluding global LNO_x emissions on the seasonality, we first show zonal distributions of the O_3–CO ratio of both simulations for the two most contrasting months, January and July, in Fig. 11. Later in this section in Fig. 12, all monthly medians are shown for CO, O_3, and their ratio separately, as well as the fraction of different mecha-

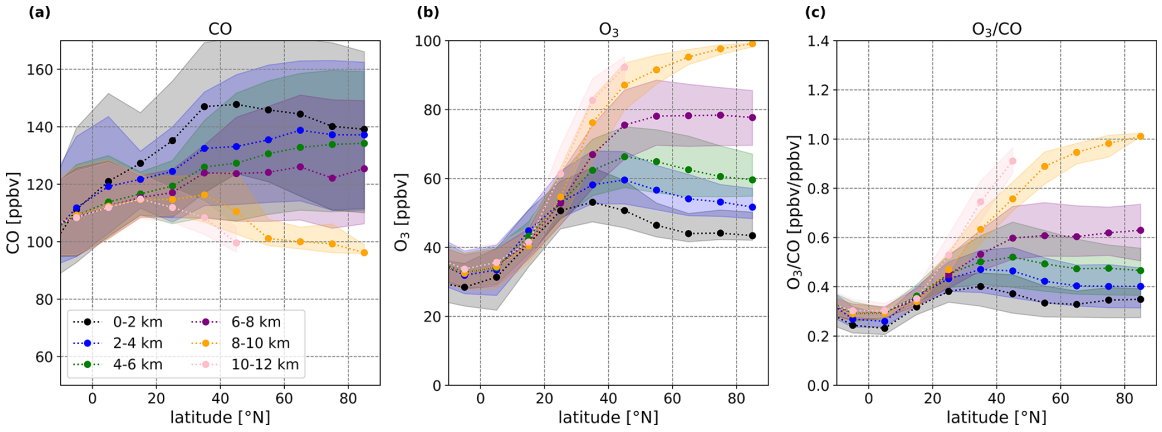

Figure 8. Same as Fig. 6, for the model simulation without LNO_x.

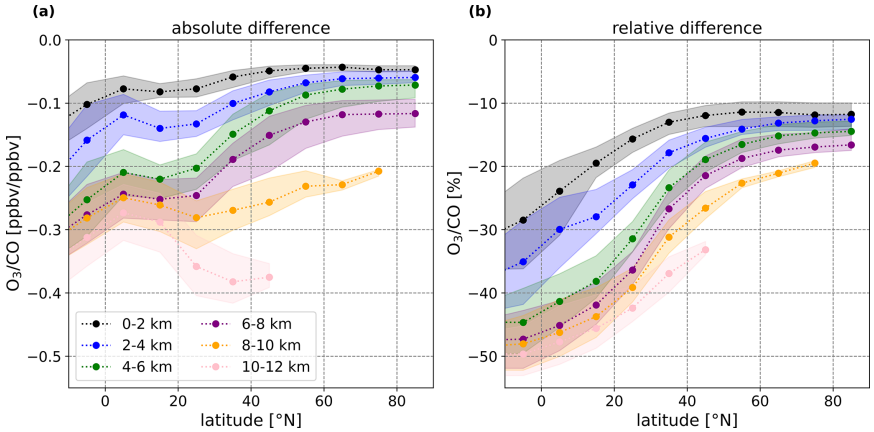

Figure 9. Same as Fig. 6, but for the absolute differences **(a)** and relative differences **(b)** of the O_3–CO ratio between the base run and the sensitivity run without LNO_x.

nisms of O_3 generation contributing to the northern subtropical troposphere. A selection of all monthly means of CO, O_3, and their ratio of the standard and the sensitivity run of the model can be found in the Supplement.

The strongest seasonal difference can be perceived in the standard run in the northern subtropics reaching a ratio difference of 0.5 ppbv ppbv^{-1} (Fig. 11a, c). Generally, the tropospherical O_3–CO ratio is strongest in the subtropics in summer in both hemispheres, and weakest in winter. By excluding LNO_x emissions in (b) and (d), the seasonal difference becomes even more pronounced, as the O_3–CO ratio is nearly constant throughout the whole troposphere in the northern subtropics in January (Fig. 11b). In the southern hemisphere the seasonality is much weaker, but the O_3–CO ratio is still shifted towards lower values by excluding LNO_x. Many studies have linked this hemispheric difference to tropopause height changes resulting in net mass transfer between the stratosphere and troposphere (Staley, 1962; Robinson, 1980; Murgatroyd et al., 1980; Sprenger and Wernli, 2003), with a more pronounced seasonal cycle in the northern than southern hemisphere (Appenzeller et al., 1996), also coupled to the amount of land cover. However, as the sensitivity run still shows strong seasonality, LNO_x is not expected to be the mechanism controlling the seasonal variation.

NO_x emissions from lightning have distinct spatial and temporal variations in the extra tropics, being highest in summer and lowest in winter, and pronounced in the northern hemisphere due to the larger land cover (Collier and Hughes, 2011b). Yet, 77 % of the world's lightning activity occurs in the tropics, between 30° S and 30° N (Schumann and Huntrieser, 2007), and mainly over land (Ricciardulli and Sardeshmukh, 2002; Williams and Stanfill, 2002). The occurrence of lightning in the tropics is to be expected to show no significant seasonal variation, as it moves along the ITCZ, even though lightning activity is highly complex and depends on thunderstorm activity and the properties of the aerosols, which have stronger spatial variations than temporal ones (Williams, 1985; Rycroft et al., 2000; Williams et al.,

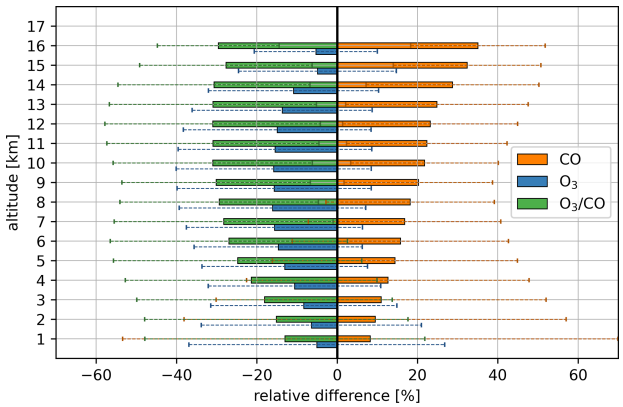

Figure 10. The mean relative differences in O_3 (blue bars), CO (orange bars), and their ratio (green bars) averaged over all longitudes, the northern subtropics ranging from 23.3–40° N, and for each kilometer, with exclusion of stratospheric values selected by O_3 values higher than 100 ppbv. This mean includes an average over all months. The error bars show the standard deviation and represent the meridional variability of the relative differences. Calculated using Eq. (3).

2002; Zipser et al., 2006; Collier and Hughes, 2011b, a). Tropical LNO_x, and its distribution of chemical successors seem to have a global impact over all seasons, as can be seen in the comparison of the standard and sensitivity simulation in Fig. 11. This is consistent with the findings of Mickley et al. (2001), who modeled an overestimation of 50 % of preindustrial O_3 during winter in the northern mid-latitudes compared to measurements and linked it to tropical LNO_x emissions.

When excluding LNO_x from the model simulations, seasonality is still strong. The remaining effects controlling O_3 production and CO loss are therefore expected to depend on another mechanism, like stratosphere–troposphere exchange, other NO_x sources, and changing background emissions.

In Fig. 12a, the monthly medians of CO, O_3, and their ratio are shown, averaged over the whole troposphere in the northern subtropics, from 23.3–40° N. Anthropogenic emissions peak during the winter and spring, especially in the northern hemisphere, with the background CO mixing ratios increasing up to 125 ppbv in the zonal median. Biomass burning also contributes to the background CO but is more common in the tropics, and at higher latitudes. O_3 is at a maximum in May at approximately 80 ppbv, with a gradually decreasing gradient up until winter. In winter, photolysis rates are lowest, hence the O_3 lifetime is longer and more O_3 accumulates (Mickley et al., 2001). During the summer, O_3 depletion is strongest due to higher photochemical activity.

For a clearer identification of seasonality in the model simulation we introduce the O_3S tracer, provided by the model, which identifies all O_3 originating from the stratosphere and propagating into the troposphere. With this tracer and the sensitivity run, by excluding the chemical production of O_3 by lightning emissions, we can identify different O_3 origins that contribute to the O_3–CO ratio. These are shown in Fig. 12b.

First, the O_3S tracer reveals the amount of O_3 coming from the stratosphere, which can be linked directly to STE. O_3S changes marginally between the two model simulations (not shown here). Therefore, we conclude that O_3 produced in the tropics and distributed from the TTL through the stratosphere seems to have a minor influence on O_3 transported into subtropical regions. The contribution of STE to the total tropospheric column O_3 budget in the northern subtropics comes to about 25 %–50 %, peaking in February and has a minimum in August. The STE influence is strongest close to the tropopause and diminishes towards the surface. Previous analyses showed that storm tracks and mountain chains in the subtropics are preferred regions for STE (Škerlak et al., 2014), being strongest in late spring–early summer, particularly over continents (Sprenger and Wernli, 2003). STE is strongly affected by the intensity of the jet streams, due to their role in the formation of tropopause folds, and the height of the tropopause. The location and strength of jet streams are strongly influenced by temperature differences between high and low latitudes. Jing and Banerjee (2018) found that anticyclonic wave-breaking events become more frequent in summer, and can be associated with stronger isentropic STE. Overall, STE seems to have a strong impact on the mixing ratios in the UTLS region; however, averaging over the whole troposphere, STE is found to have a minor effect on the seasonality driving the O_3–CO ratio in the northern subtropics. Škerlak et al. (2014) showed that STE influence on O_3 can be found all the way down to the planetary boundary layer throughout all seasons with global hot spots along mountain chains mainly in the subtropical summer. However, they identified an accumulation of O_3 below the tropopause, rather than originating directly from the stratosphere. Similar seasonality can be found in the southern hemisphere (not shown here).

The contribution of O_3 produced by LNO_x has been calculated by subtracting total O_3 from the "without LNO_x" run from total O_3 from the "REF" simulation of the model (tr. LNO_x, Fig. 12b). As most LNO_x is expected to be in the tropics (Schumann and Huntrieser, 2007), we conclude that this O_3 is mostly produced by tropical LNO_x emissions, transported via the Hadley circulation into the subtropics. The median contribution of photochemically produced O_3 to the northern subtropical tropospheric column varies between 5 % and 15 % throughout the year, with slightly higher contributions in summer than in winter. This modest seasonality indicates a minor contribution of local induced LNO_x emissions in summer and autumn.

Strong convective activity transports surface emissions upward, with impacts depending heavily on the inflow region. In highly polluted regions with strong NO_x emissions (e.g., anthropogenic, biomass burning), enhanced O_3–CO ratios

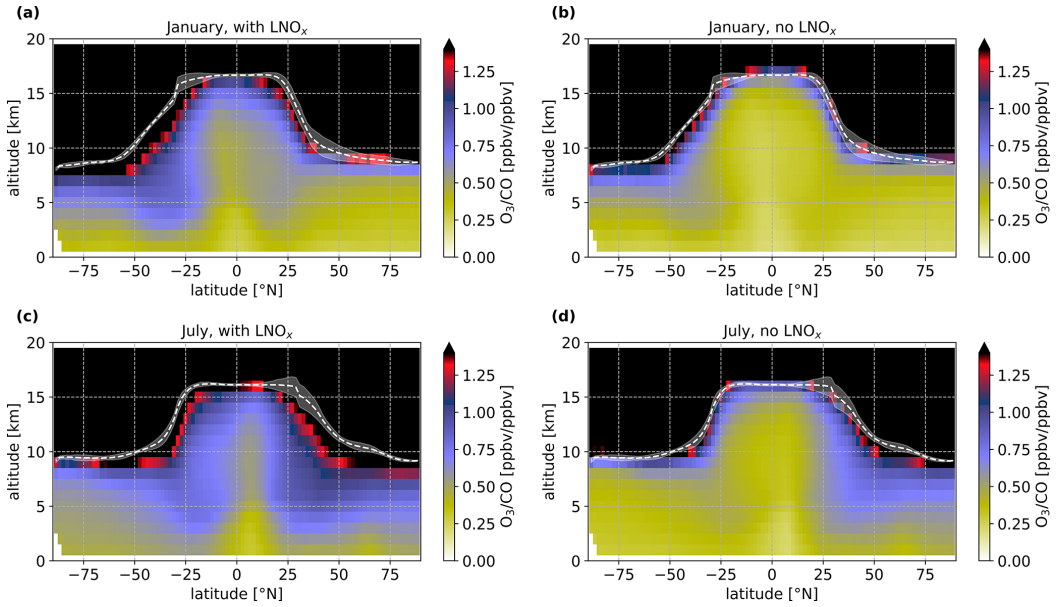

Figure 11. Monthly medians of the zonal distribution of the modeled O_3–CO ratio from January **(a, b)** and July **(c, d)**, with **(a, c)** and without **(b, d)** LNO_x. All monthly medians can be found in the Supplement.

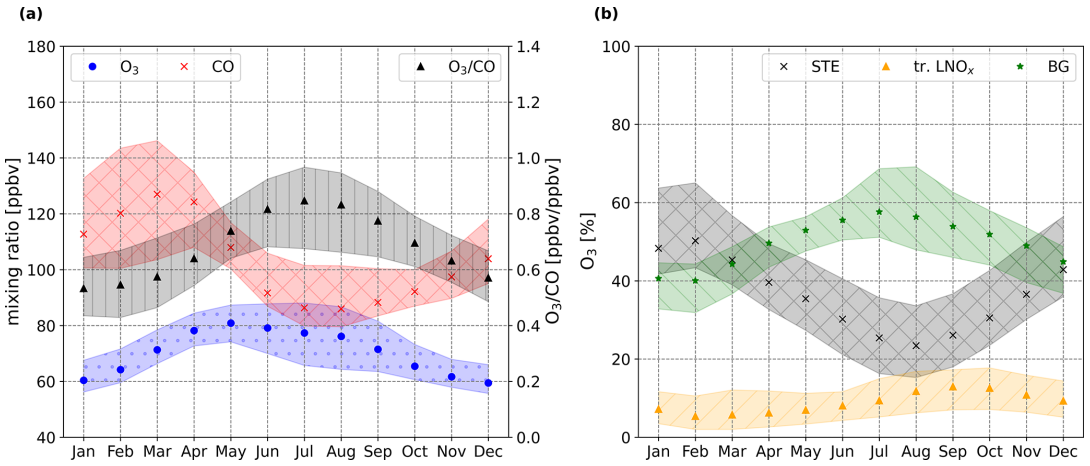

Figure 12. Monthly medians of CO, O_3, and the O_3–CO ratio in **(a)**, and different O_3 sources in **(b)** averaged over the whole troposphere of the northern subtropics, defined from 23.3–40° N. The shaded areas display the 25th and 75th percentiles. The different O_3 sources are defined by calculations of O_3 from the two model runs and the O_3S tracer of the model, which is the O_3 originating from the stratosphere only (STE, black crosses). The background O_3 mixing ratios of the northern subtropics are derived from the difference of all O_3 minus O_3S from the "without LNO_x" run (BG, green stars), and O_3 produced and transported from tropical LNO_x (tr. LNO_x, triangles) is calculated from the difference of total O_3 minus the O_3S tracer of "REF" minus the background mixing ratios. Adding all three O_3 origins in **(b)** results in the O_3 mixing ratios shown in **(a)**, being 100 %. Only tropospheric values have been taken for the calculations, by excluding O_3 higher than 100 ppbv according to Prather et al. (2011).

can be transported upwards by convection (e.g., Asian Summer Monsoon, see Mickley et al., 2001). While in remote areas, especially over the oceans and in the tropics, low O_3 is common at the surface through the strong sink of photodissociation and the reaction of $O(^1D)$ with water vapor, which leads to rather low O_3–CO ratios. Therefore, seasonal convective activity supports higher O_3–CO ratios in the tropospheric column, notably in summer (also noticed as a slight increase of O_3 from LNO_x during summer in Fig. 12b). Furthermore, deep convection is also linked to stratospheric–tropospheric mixing through overshoots and corresponding

downdrafts (Frey et al., 2015), additionally mixing high O_3 and low CO air masses into the upper troposphere.

Extracting O_3S from the total O_3 from the sensitivity run excluding LNO_x results in the background O_3 mixing ratio, defining O_3 which is neither coming from the stratosphere nor from tropical photochemistry including lightning NO_x. This remaining O_3 mixing ratio (BG, Fig. 12b) shows a strong seasonality, peaking in summer and having its minimum in winter. It contributes approximately 40 %–60 % to the total O_3 column of the northern subtropics, and mainly drives its seasonality. The seasonal variation of the background O_3 could be linked to other NO_x sources like soil, anthropogenic emissions, or biomass burning emissions (Škerlak et al., 2014), but these possibilities have not been further investigated in this study. Possible transport of PAN via the Ferrell circulation from the mid-latitudes into the subtropics and its thermal depletion in the downward branch is another potential source of NO_x.

In conclusion, STE seems to have a minor role in controlling the seasonality. Tropical LNO_x meridionally transported via the Hadley circulation influences the O_3 mixing ratio in the northern subtropics, and possible also the depletion of CO, throughout the year. The strongest effects on seasonality are exerted by the remaining factors defining the background mixing ratios.

4 Conclusions

Tropospheric chemistry and transport processes, within the troposphere as well as STE processes are important in conditioning the background mixing ratios of greenhouse gases and other trace gases in the troposphere. This study used in situ observations from 12 aircraft campaigns, from 2012–2024, to investigate the tropospherical zonal distribution of O_3 and CO and their ratio. Particularly in the northern subtropics, a strong enhancement in the O_3–CO ratio almost down to the boundary layer could be identified, which is usually expected to be caused by STE processes in the vicinity of the subtropical jet stream, bringing high-O_3 and low-CO air from the stratosphere into the troposphere. In this study, we have investigated another possible mechanism contributing to the chemical composition of the tropospherical subtropics, which had not yet been considered. High O_3–CO ratios can also be produced through photochemistry and transport within the troposphere. In the upper tropical troposphere, substantial emissions of LNO_x, especially in the ITCZ, are a major source of O_3, and, simultaneously, catalyze the recycling of OH radicals in the upper troposphere. Those highly reactive radicals are the main sink of CO in the free and upper troposphere, shortening the lifetime of CO. Thus, through the presence of LNO_x, high O_3–CO ratios can also be photochemically generated and distributed by the Hadley circulation into the subtropics. To test this hypothesis, we have used the general circulation and chemistry model EMAC and run a sensitivity study on the effect of LNO_x on the troposphere O_3–CO ratio. First, we show that the modeled zonal distributions give the same enhancement of O_3–CO ratio in the subtropics than the observations. Second, we identified a strong effect of LNO_x, which is mainly produced in the tropical troposphere, on the chemical composition of the subtropics outside the convective regions in the down-welling branch of the Hadley circulation. Photochemistry contributes by 40 % to the O_3–CO ratio in the upper troposphere of the northern subtropics. These air masses propagate through the whole vertical column of the northern subtropics, supported by the Hadley circulation. The effect of LNO_x on O_3 and CO in the southern subtropics, tropics, extra tropics, as well as in the UTLS region were also noticed, but were not in the focus of this work. We conclude that tropical LNO_x emissions are crucial for O_3 production and subsequently for CO loss through the secondary production of OH radicals, which can be distributed in significant amounts throughout the whole troposphere. Furthermore, we see a strong inter-annual variability, mainly influenced by a complex interaction of STE and background concentrations. The highest O_3–CO ratios have been identified in summer in the northern subtropics, corresponding with low CO and high O_3 mixing ratios. Besides contributing to the seasonality of background concentrations, STE is weakest in summer, which is in contrast to the enhancement of the O_3–CO ratios in summer. However, more frequent Rossby wave occurrences in summer are expected to contribute to stronger mixing throughout the troposphere. Furthermore, other tropospheric sources of NO_x seem to play an important role in conditioning the troposphere as well, which needs further investigation.

Meridional variations have been briefly discussed in this study. More detailed investigations could verify the impact of tropopheric photochemistry on the background concentrations of specific regions. Furthermore, LNO_x emissions are dependent on the frequency of deep convective systems as well as many other factors (e.g., ice-nucleating particles, emissions, turbulence, cloud top height), which can be hard to model. There are still major uncertainties in understanding the varying manifestations of these emissions over continental and maritime surfaces. However, we showed that lightning emissions have a strong effect on tropospheric photochemistry and global distributions of the O_3–CO ratio. This effect along tropospherical transport plays a key role in conditioning the troposphere and needs to be considered in future studies.

Code and data availability. The data measured during the campaigns ESMVal https://halo-db.pa.op.dlr.de/mission/14, OMO https://halo-db.pa.op.dlr.de/mission/0, WISE https://halo-db.pa.op.dlr.de/mission/96, CAFE Africa https://halo-db.pa.op.dlr.de/mission/98, South-TRAC https://halo-db.pa.op.dlr.de/mission/116, CAFE Brazil https://halo-db.pa.op.dlr.de/mission/135, PHILEAS

https://halo-db.pa.op.dlr.de/mission/138 and CAFE Pacific https://halo-db.pa.op.dlr.de/mission/140 are available on the HALO database platform via Deutsches Zentrum für Luft- und Raumfahrt (DLR) (2012); DLRDeutsches Zentrum für Luft- und Raumfahrt (DLR) (2015); Deutsches Zentrum für Luft- und Raumfahrt (DLR) (2017, 2018, 2019, 2023a, b, 2024), respectively. Specifically, data and code of FAIRO O_3 data processing can be accessed via https://doi.org/10.5281/zenodo.11275355 (Obersteiner, 2024). The ATom missions data sets can be accessed through the NASA website (Wofsy et al., 2018). EMAC model simulations can be accessed at https://doi.org/10.5281/zenodo.17476643 (Ort and Pozzer, 2025).

Supplement. The supplement related to this article is available online at https://doi.org/10.5194/acp-25-14987-2025-supplement.

Author contributions. LO, AP and HF designed the study; LO, HF, FO, AZ provided the HALO campaign data sets; TR, JP, IB, CT, BD provided the ATom data sets; AP provided the modeling data; LO analyzed and processed the data and wrote the paper; All others proofread and edited the paper.

Competing interests. At least one of the (co-)authors is a member of the editorial board of *Atmospheric Chemistry and Physics*. The peer-review process was guided by an independent editor, and the authors also have no other competing interests to declare.

Disclaimer. Publisher's note: Copernicus Publications remains neutral with regard to jurisdictional claims made in the text, published maps, institutional affiliations, or any other geographical representation in this paper. While Copernicus Publications makes every effort to include appropriate place names, the final responsibility lies with the authors. Views expressed in the text are those of the authors and do not necessarily reflect the views of the publisher.

Special issue statement. This article is part of the special issue "The Modular Earth Submodel System (MESSy) (ACP/GMD interjournal SI)". It is not associated with a conference.

Acknowledgements. The authors gratefully acknowledge the whole HALO and NASA DC-8 team, which were present for and contributed to all campaigns used for this study. Additionally, all institutes which took place in those campaigns are hereby acknowledged, including the Max Planck Institute of Chemistry, the atmospheric department of the University of Frankfurt, Karlsruhe Institute of Technology, the institute of physics at the University of Mainz, the NASA Armstrong (Dryden) Flight Research Center, the NOAA Earth System Research Laboratories, the University of Havard, and the Deutsches Zentrum für Luft- und Raumfahrt (DLR) in Oberpfaffenhofen. Acknowledgment is also given to ChatGPT (open AI), who helped out by coding problems now and then.

Financial support. This research has been supported by the Max-Planck-Institut für Chemie. Jeff Peischl, Ilann Bourgeois, and Chelsea R. Thompson were supported in part by NOAA cooperative agreement NA17OAR4320101.

The article processing charges for this open-access publication were covered by the Max Planck Society.

Review statement. This paper was edited by Frank Dentener and reviewed by two anonymous referees.

References

Appenzeller, C., Holton, J. R., and Rosenlof, K. H.: Seasonal variation of mass transport across the tropopause, Journal of Geophysical Research: Atmospheres, 101, 15071–15078, https://doi.org/10.1029/96JD00821, 1996.

Bourgeois, I., Peischl, J., Thompson, C. R., Aikin, K. C., Campos, T., Clark, H., Commane, R., Daube, B., Diskin, G. W., Elkins, J. W., Gao, R.-S., Gaudel, A., Hintsa, E. J., Johnson, B. J., Kivi, R., McKain, K., Moore, F. L., Parrish, D. D., Querel, R., Ray, E., Sánchez, R., Sweeney, C., Tarasick, D. W., Thompson, A. M., Thouret, V., Witte, J. C., Wofsy, S. C., and Ryerson, T. B.: Global-scale distribution of ozone in the remote troposphere from the ATom and HIPPO airborne field missions, Atmos. Chem. Phys., 20, 10611–10635, https://doi.org/10.5194/acp-20-10611-2020, 2020.

Bourgeois, I., Peischl, J., Neuman, J. A., Brown, S. S., Thompson, C. R., Aikin, K. C., Allen, H. M., Angot, H., Apel, E. C., Baublitz, C. B., Breweri, J. F., Campuzano-Josta, P., Commane, R., Crounse, J. D., Daube, B. C., DiGangi, J. P., Diskin, G. S., Emmons, L. K., Fiore, A. M., Gkatzelis, G. I., Hills, A., Hornbrook, R. S., Huey, L. G., Jimenez, J. L., Kim, M., Lacey, F., McKain, K., Murray, L. T., Nault, B. A., Parrish, D. D., Ray, E., Sweeney, Colmand Tanner, D., Wofsy, S. C., and Ryerson, T. B.: Large contribution of biomass burning emissions to ozone throughout the global remote troposphere, P. Natl. Acad. Sci. USA, 118, e2109628118, https://doi.org/10.1073/pnas.2109628118, 2021.

Brewer, A. W.: Evidence for a world circulation provided by the measurements of helium and water vapour distribution in the stratosphere, Quarterly Journal of the Royal Meteorological Society, 75, 351–363, https://doi.org/10.1002/qj.49707532603, 1949.

Collier, A. B. and Hughes, A. R.: Lightning and the African ITCZ, Journal of Atmospheric and Solar-Terrestrial Physics, 73, 2392–2398, https://doi.org/10.1016/j.jastp.2011.08.010, 2011a.

Collier, A. B. and Hughes, A. R. W.: A harmonic model for the temporal variation of lightning activity over Africa, Journal of Geophysical Research: Atmospheres, 116, https://doi.org/10.1029/2010JD014455, 2011b.

Crowley, J. N., Dörich, R., Eger, P., Helleis, F., Tadic, I., Fischer, H., Williams, J., Edtbauer, A., Wang, N., Holanda, B. A., Pöhlker, M., Pöschl, U., Pozzer, A., and Lelieveld, J.: Peroxy acetyl nitric anhydride (PAN) and peroxy acetic acid (PAA) over the Atlantic west of Africa during CAFE-Africa and the influence of

biomass-burning, Environmental Science: Atmospheres, 5, 620–635, https://doi.org/10.1039/d5ea00006h, 2025.

Crutzen, P. J. and Andreae, M. O.: Biomass Burning in the Tropics: Impact on Atmospheric Chemistry and Biogeochemical Cycles, Science, 250, 1669–1678, https://doi.org/10.1126/science.250.4988.1669, 1990.

Danielsen, E. F.: Stratospheric-Tropospheric Exchange Based on Radioactivity, Ozone and Potential Vorticity, Journal of Atmospheric Sciences, 25, 502–518, https://doi.org/10.1175/1520-0469(1968)025<0502:STEBOR>2.0.CO;2, 1968.

Deutsches Zentrum für Luft- und Raumfahrt (DLR): Mission: ESMVal, HALO database [data set], https://halo-db.pa.op.dlr.de/mission/14 (last access: 18 June 2024), 2012.

Deutsches Zentrum für Luft- und Raumfahrt (DLR): Mission: OMO, HALO database [data set], https://halo-db.pa.op.dlr.de/mission/0 (last access: 18 June 2024), 2015.

Deutsches Zentrum für Luft- und Raumfahrt (DLR): Mission: WISE, HALO database [data set], https://halo-db.pa.op.dlr.de/mission/96 (last access: 18 June 2024), 2017.

Deutsches Zentrum für Luft- und Raumfahrt (DLR): Mission: CAFE Africa, HALO database [data set], https://halo-db.pa.op.dlr.de/mission/98 (last access: 18 June 2024), 2018.

Deutsches Zentrum für Luft- und Raumfahrt (DLR): Mission: SouthTRAC, HALO database [data set], https://halo-db.pa.op.dlr.de/mission/116 (last access: 18 June 2024), 2019.

Deutsches Zentrum für Luft- und Raumfahrt (DLR): Mission: CAFE Brazil, HALO database [data set], https://halo-db.pa.op.dlr.de/mission/135 (last access: 18 June 2024), 2023a.

Deutsches Zentrum für Luft- und Raumfahrt (DLR): Mission: PHILEAS, HALO database [data set], https://halo-db.pa.op.dlr.de/mission/138 (last access: 18 June 2024), 2023b.

Deutsches Zentrum für Luft- und Raumfahrt (DLR): Mission: CAFE Pacific, HALO database [data set], https://halo-db.pa.op.dlr.de/mission/140 (last access: 23 December 2024), 2024.

Dobson, G. M. B.: Origin and distribution of the polyatomic molecules in the atmosphere, Proceedings of the Royal Society of London. Series A. Mathematical and Physical Sciences, 236, 187–193, https://doi.org/10.1098/rspa.1956.0127, 1956.

Faist, J., Capasso, F., Sivco, D. L., Sirtori, C., Hutchinson, A. L., and Cho, A. Y.: Quantum cascade laser, Science, 264, 553–556, https://doi.org/10.1126/science.264.5158.553, 1994.

Field, R. D., van der Werf, G. R., Fanin, T., Fetzer, E. J., Fuller, R., Jethva, H., Levy, R., Livesey, N. J., Luo, M., Torres, O., and Worden, H. M.: Indonesian fire activity and smoke pollution in 2015 show persistent nonlinear sensitivity to El Nino-induced drought, Proceedings of the National Academy of SCiences of the United States of America, 113, 9204–9209, https://doi.org/10.1073/pnas.1524888113, 2016.

Fischer, H., Wienhold, F., Hoor, P., Bujok, O., Schiller, C., Siegmund, P., Ambaum, M., Scheeren, H., and Lelieveld, J.: Tracer correlations in the northern high latitude lowermost stratosphere: Influence of cross-tropopause mass exchange, Geophysical Research Letters, 27, 97–100, https://doi.org/10.1029/1999GL010879, 2000.

Frey, W., Schofield, R., Hoor, P., Kunkel, D., Ravegnani, F., Ulanovsky, A., Viciani, S., D'Amato, F., and Lane, T. P.: The impact of overshooting deep convection on local transport and mixing in the tropical upper troposphere/lower stratosphere (UTLS), Atmos. Chem. Phys., 15, 6467–6486, https://doi.org/10.5194/acp-15-6467-2015, 2015.

Fried, A. and Richter, D.: Infrared Absorption Spectroscopy, in: Analytical Techniques for Atmospheric Measurement, edited by: Heard, D. E., Wiley Online Library, Chichester, UK, 72–146, https://doi.org/10.1002/9780470988510.ch2, 2006.

Galanter, M., Levy II, H., and Carmichael, G. R.: Impacts of biomass burning on tropospheric CO, NO, and O_3, Journal of Geophysical Research: Atmospheres, 105, 6633–6653, https://doi.org/10.1029/1999JD901113, 2000.

Herriott, D. R. and Schulte, H. J.: Folded Optical Delay Lines, Appl. Opt., 4, 883–889, https://doi.org/10.1364/AO.4.000883, 1965.

Hersbach, H., Bell, B., Berrisford, P., Hirahara, S., Horanyi, A., Munoz-Sabater, J., Nicolas, J., Peubey, C., Radu, R., Schepers, D., Simmons, A., Soci, C., Abdalla, S., Abellan, X., Balsamo, G., Bechtold, P., Biavati, G., Bidlot, J., Bonavita, M., De Chiara, G., Dahlgren, P., Dee, D., Diamantakis, M., Dragani, R., Flemming, J., Forbes, R., Fuentes, M., Geer, A., Haimberger, L., Healy, S., Hogan, R. J., Holm, E., Janiskova, M., Keeley, S., Laloyaux, P., Lopez, P., Lupu, C., Radnoti, G., de Rosnay, P., Rozum, I., Vamborg, F., Villaume, S., and Thepaut, J.-N.: The ERA5 global reanalysis, Q. J. Roy. Meteor. Soc., 146, 1999–2049, 2020.

Holton, J. R., Haynes, P. H., McIntyre, M. E., Douglass, A. R., Rood, R. B., and Pfister, L.: Stratosphere-troposphere exchange, Reviews of Geophysics, 33, 403–439, https://doi.org/10.1029/95RG02097, 1995.

Hoor, P., Fischer, H., Lange, L., Lelieveld, J., and Brunner, D.: Seasonal variations of a mixing layer in the lowermost stratosphere as identified by the CO-O_3 correlation from in situ measurements, Journal of Geophysical Research: Atmospheres, 107, ACL–1, https://doi.org/10.1029/2000JD000289, 2002.

Hoor, P., Gurk, C., Brunner, D., Hegglin, M. I., Wernli, H., and Fischer, H.: Seasonality and extent of extratropical TST derived from in-situ CO measurements during SPURT, Atmos. Chem. Phys., 4, 1427–1442, https://doi.org/10.5194/acp-4-1427-2004, 2004.

Jeuken, A., Siegmund, P., Heijboer, L., Feichter, J., and Bengtsson, L.: On the potential of assimilating meteorological analyses in a global climate model for the purpose of model validation, Journal of Geophysical Research: Atmospheres, 101, 16939–16950, https://doi.org/10.1029/96JD01218, 1996.

Jing, P. and Banerjee, S.: Rossby Wave Breaking and Isentropic Stratosphere-Troposphere Exchange During 1981–2015 in the Northern Hemisphere, Journal of Geophysical Research: Atmospheres, 123, 9011–9025, https://doi.org/10.1029/2018JD028997, 2018.

Jöckel, P., Sander, R., Kerkweg, A., Tost, H., and Lelieveld, J.: Technical Note: The Modular Earth Submodel System (MESSy) – a new approach towards Earth System Modeling, Atmos. Chem. Phys., 5, 433–444, https://doi.org/10.5194/acp-5-433-2005, 2005.

Jöckel, P., Tost, H., Pozzer, A., Brühl, C., Buchholz, J., Ganzeveld, L., Hoor, P., Kerkweg, A., Lawrence, M. G., Sander, R., Steil, B., Stiller, G., Tanarhte, M., Taraborrelli, D., van Aardenne, J., and Lelieveld, J.: The atmospheric chemistry general circulation model ECHAM5/MESSy1: consistent simulation of ozone from the surface to the mesosphere, Atmos. Chem. Phys., 6, 5067–5104, https://doi.org/10.5194/acp-6-5067-2006, 2006.

Jöckel, P., Kerkweg, A., Pozzer, A., Sander, R., Tost, H., Riede, H., Baumgaertner, A., Gromov, S., and Kern, B.: Development cycle 2 of the Modular Earth Submodel System (MESSy2), Geosci. Model Dev., 3, 717–752, https://doi.org/10.5194/gmd-3-717-2010, 2010.

Jöckel, P., Tost, H., Pozzer, A., Kunze, M., Kirner, O., Brenninkmeijer, C. A. M., Brinkop, S., Cai, D. S., Dyroff, C., Eckstein, J., Frank, F., Garny, H., Gottschaldt, K.-D., Graf, P., Grewe, V., Kerkweg, A., Kern, B., Matthes, S., Mertens, M., Meul, S., Neumaier, M., Nützel, M., Oberländer-Hayn, S., Ruhnke, R., Runde, T., Sander, R., Scharffe, D., and Zahn, A.: Earth System Chemistry integrated Modelling (ESCiMo) with the Modular Earth Submodel System (MESSy) version 2.51, Geosci. Model Dev., 9, 1153–1200, https://doi.org/10.5194/gmd-9-1153-2016, 2016.

Joppe, P., Schneider, J., Kaiser, K., Fischer, H., Hoor, P., Kunkel, D., Lachnitt, H.-C., Marsing, A., Röder, L., Schlager, H., Tomsche, L., Voigt, C., Zahn, A., and Borrmann, S.: The influence of extratropical cross-tropopause mixing on the correlation between ozone and sulfate aerosol in the lowermost stratosphere, Atmos. Chem. Phys., 24, 7499–7522, https://doi.org/10.5194/acp-24-7499-2024, 2024.

Krasauskas, L., Ungermann, J., Preusse, P., Friedl-Vallon, F., Zahn, A., Ziereis, H., Rolf, C., Plöger, F., Konopka, P., Vogel, B., and Riese, M.: 3-D tomographic observations of Rossby wave breaking over the North Atlantic during the WISE aircraft campaign in 2017, Atmos. Chem. Phys., 21, 10249–10272, https://doi.org/10.5194/acp-21-10249-2021, 2021.

Kunkel, D., Hoor, P., Kaluza, T., Ungermann, J., Kluschat, B., Giez, A., Lachnitt, H.-C., Kaufmann, M., and Riese, M.: Evidence of small-scale quasi-isentropic mixing in ridges of extratropical baroclinic waves, Atmos. Chem. Phys., 19, 12607–12630, https://doi.org/10.5194/acp-19-12607-2019, 2019.

Laboratories, N. G. M. L. E. S. R.: Carbon Cycle Greenhouse Gases - GGGRN Data – CO – Cooperative Air Sampling Network, https://gml.noaa.gov/ccgg/data/co.html (last access: 12 July 2024), 1988.

Lan, X., K. T. and Dlugokencky, E.: Trends in globally-averaged CH_4, N_2O, and SF_6 determined from NOAA Global Monitoring Laboratory measurements, NOAA Global Monitoring Laboratory, https://doi.org/10.15138/P8XG-AA10, 2025.

Lelieveld, J., Bregman, B., Arnold, F., Bürger, V., Crutzen, P. J., Fischer, H., Waibel, A., Siegmund, P., and van Velthoven, P. F. J.: Chemical perturbation of the lowermost stratosphere through exchange with the troposphere, Geophysical Research Letters, 24, 603–606, https://doi.org/10.1029/97GL00255, 1997.

Lelieveld, J., Gromov, S., Pozzer, A., and Taraborrelli, D.: Global tropospheric hydroxyl distribution, budget and reactivity, Atmos. Chem. Phys., 16, 12477–12493, https://doi.org/10.5194/acp-16-12477-2016, 2016.

Lelieveld, J., Bourtsoukidis, E., Brühl, C., Fischer, H., Fuchs, H., Harder, H., Hofzumahaus, A., Holland, F., Marno, D., Neumaier, M., Pozzer, A., Schlager, H., Williams, J., Zahn, A., and Ziereis, H.: The South Asian monsoon – pollution pump and purifier, Science, 361, 270–273, https://doi.org/10.1126/science.aar2501, 2018.

Li, M., Kurokawa, J., Zhang, Q., Woo, J.-H., Morikawa, T., Chatani, S., Lu, Z., Song, Y., Geng, G., Hu, H., Kim, J., Cooper, O. R., and McDonald, B. C.: MIXv2: a long-term mosaic emission inventory for Asia (2010–2017), Atmos. Chem. Phys., 24, 3925–3952, https://doi.org/10.5194/acp-24-3925-2024, 2024.

McCabe, D. L., Trevino, L. K., and Butterfield, K. D.: Cheating in Academic Institutions: A Decade of Research, Ethics & Behavior, 11, 219–232, https://doi.org/10.1207/S15327019EB1103_2, 2001.

McManus, J. B., Kebabian, P. L., and Zahniser, M. S.: Astigmatic mirror multipass absorption cells for long-path-length spectroscopy, Appl. Opt., 34, 3336–3348, https://doi.org/10.1364/AO.34.003336, 1995.

Mickley, L. J., Jacob, D. J., and Rind, D.: Uncertainty in preindustrial abundance of tropospheric ozone: Implications for radiative forcing calculations, Journal of Geophysical Research: Atmospheres, 106, 3389–3399, https://doi.org/10.1029/2000JD900594, 2001.

Müller, S., Hoor, P., Berkes, F., Bozem, H., Klingebiel, M., Reutter, P., Smit, H., Wendisch, M., Spichtinger, P., and Borrmann, S.: In situ detection of stratosphere-troposphere exchange of cirrus particles in the midlatitudes, Geophysical Research Letters, 42, 949–955, https://doi.org/10.1002/2014GL062556, 2015.

Müller, S., Hoor, P., Bozem, H., Gute, E., Vogel, B., Zahn, A., Bönisch, H., Keber, T., Krämer, M., Rolf, C., Riese, M., Schlager, H., and Engel, A.: Impact of the Asian monsoon on the extratropical lower stratosphere: trace gas observations during TACTS over Europe 2012, Atmos. Chem. Phys., 16, 10573–10589, https://doi.org/10.5194/acp-16-10573-2016, 2016.

Murgatroyd, R. J., O'Neill, A., Massey, H. S. W., Beynon, W. J. G., Houghton, J. T., and Thomas, L.: Interaction between the troposphere and stratosphere, Philosophical Transactions of the Royal Society of London. Series A, Mathematical and Physical Sciences, 296, 87–102, https://doi.org/10.1098/rsta.1980.0158, 1980.

Nussbaumer, C. M., Fischer, H., Lelieveld, J., and Pozzer, A.: What controls ozone sensitivity in the upper tropical troposphere?, Atmos. Chem. Phys., 23, 12651–12669, https://doi.org/10.5194/acp-23-12651-2023, 2023a.

Nussbaumer, C. M., Place, B. K., Zhu, Q., Pfannerstill, E. Y., Wooldridge, P., Schulze, B. C., Arata, C., Ward, R., Bucholtz, A., Seinfeld, J. H., Goldstein, A. H., and Cohen, R. C.: Measurement report: Airborne measurements of NO_x fluxes over Los Angeles during the RECAP-CA 2021 campaign, Atmos. Chem. Phys., 23, 13015–13028, https://doi.org/10.5194/acp-23-13015-2023, 2023b.

Nussbaumer, C. M., Kohl, M., Pozzer, A., Tadic, I., Rohloff, R., Marno, D., Harder, H., Ziereis, H., Zahn, A., Obersteiner, F., Hofzumahaus, A., Fuchs, H., Künstler, C., Brune, W. H., Ryerson, T. B., Peischl, J., Thompson, C. R., Bourgeois, I., Lelieveld, J., and Fischer, H.: Ozone Formation Sensitivity to Precursors and Lightning in the Tropical Troposphere Based on Airborne Observations, Journal of Geophysical Research: Atmospheres, 129, e2024JD041168, https://doi.org/10.1029/2024JD041168, 2024.

Nussbaumer, C. M., Pozzer, A., Hewson, M., Ort, L., Krumm, B., Byron, J., Williams, J., Joppe, P., Obersteiner, F., Zahn, A., Lelieveld, J., and Fischer, H.: Low tropospheric ozone over the Indo-Pacific warm pool related to non-electrified convection, Geophysical Research Letters, 52, https://doi.org/10.1029/2024GL112788, 2025.

Obersteiner, F.: FAIROmeta, version: v0.1.9, Zenodo [data set/-code], https://doi.org/10.5281/zenodo.11275355, 2024.

Ort, L. and Pozzer, A.: Supporting data for: Enhancement of O3 – CO ratios at tropospheric subtropical latitudes: Photochemistry and stratospheric influence, Version 1.0, Zenodo [data set], https://doi.org/10.5281/zenodo.17476643, 2025.

Ort, L., Röder, L. L., Parchatka, U., Königstedt, R., Crowley, D., Kunz, F., Wittkowski, R., Lelieveld, J., and Fischer, H.: In-flight characterization of a compact airborne quantum cascade laser absorption spectrometer, Atmos. Meas. Tech., 17, 3553–3565, https://doi.org/10.5194/amt-17-3553-2024, 2024.

Pal, M. and Pradhan, M.: Quantum Cascade Laser Spectroscopy, Modern Techniques of Spectroscopy: Basics, Instrumentation, and Applications, 363–387 pp., https://doi.org/10.1007/978-981-33-6084-6_14, 2021.

Postel, G. A. and Hitchman, M. H.: A Case Study of Rossby Wave Breaking along the Subtropical Tropopause, Monthly Weather Review, 129, 2555–2569, https://doi.org/10.1175/1520-0493(2001)129<2555:ACSORW>2.0.CO;2, 2001.

Prather, M. J., Zhu, X., Tang, Q., Hsu, J., and Neu, J. L.: An atmospheric chemist in search of the tropopause, Journal of Geophysical Research: Atmospheres, 116, https://doi.org/10.1029/2010JD014939, 2011.

Ricciardulli, L. and Sardeshmukh, P. D.: Local Time- and Space Scales of Organized Tropical Deep Convection, Journal of Climate, 15, 2775–2790, https://doi.org/10.1175/1520-0442(2002)015<2775:LTASSO>2.0.CO;2, 2002.

Ridley, B., Grahek, F., and Walega, J.: A small high-sensitivity, medium-response ozone detector suitable for measurements from light aircraft, Journal of Atmospheric and Oceanic Technology, 9, 142–148, https://doi.org/10.1175/1520-0426(1992)009<0142:ASHSMR>2.0.CO;2, 1992.

Riese, M., K. M. and Hoor, P.: WISE: project description, https://www.halo.dlr.de/science/missions/wise/wise.html (last access: 15 July 2024), 2017.

Riese, M., Hoor, P., Rolf, C., et al.: Long-range transport of polluted Asian summer monsoon air to high latitudes during the PHILEAS campaign in the boreal summer 2023, Bulletin of the American Meteorological Society, BAMS–D–24–0232.1, https://doi.org/10.1175/BAMS-D-24-0232.1, 2025.

Righi, M., Eyring, V., Gottschaldt, K.-D., Klinger, C., Frank, F., Jöckel, P., and Cionni, I.: Quantitative evaluation of ozone and selected climate parameters in a set of EMAC simulations, Geosci. Model Dev., 8, 733–768, https://doi.org/10.5194/gmd-8-733-2015, 2015.

Robinson, G. D.: The transport of minor atmospheric constituents between troposphere and stratosphere, Quarterly Journal of the Royal Meteorological Society, 106, 227–253, https://doi.org/10.1002/qj.49710644802, 1980.

Röder, L. L., Ort, L., Lelieveld, J., and Fischer, H.: Quantitative analysis of temporal stability and instrument performance during field experiments of an airborne QCLAS via Allan–Werle-plots, Applied Physics B, 130, 118, https://doi.org/10.1007/s00340-024-08254-5, 2024.

Roeckner, E., Brokopf, R., Esch, M., Giorgetta, M., Hagemann, S., Kornblueh, L., Manzini, E., Schlese, U., and Schulzweida, U.: Sensitivity of simulated climate to horizontal and vertical resolution in the ECHAM5 atmosphere model, Journal of Climate, 19, 3771–3791, https://doi.org/10.1175/JCLI3824.1, 2006.

Rolf, C., Afchine, A., Bozem, H., Buchholz, B., Ebert, V., Guggenmoser, T., Hoor, P., Konopka, P., Kretschmer, E., Müller, S., Schlager, H., Spelten, N., Sumińska-Ebersoldt, O., Ungermann, J., Zahn, A., and Krämer, M.: Transport of Antarctic stratospheric strongly dehydrated air into the troposphere observed during the HALO-ESMVal campaign 2012, Atmos. Chem. Phys., 15, 9143–9158, https://doi.org/10.5194/acp-15-9143-2015, 2015.

Rycroft, M., Israelsson, S., and Price, C.: The global atmospheric electric circuit, solar activity and climate change, Journal of Atmospheric and Solar-Terrestrial Physics, 62, 1563–1576, https://doi.org/10.1016/S1364-6826(00)00112-7, 2000.

Santoni, G. W., Daube, B. C., Kort, E. A., Jiménez, R., Park, S., Pittman, J. V., Gottlieb, E., Xiang, B., Zahniser, M. S., Nelson, D. D., McManus, J. B., Peischl, J., Ryerson, T. B., Holloway, J. S., Andrews, A. E., Sweeney, C., Hall, B., Hintsa, E. J., Moore, F. L., Elkins, J. W., Hurst, D. F., Stephens, B. B., Bent, J., and Wofsy, S. C.: Evaluation of the airborne quantum cascade laser spectrometer (QCLS) measurements of the carbon and greenhouse gas suite – CO_2, CH_4, N_2O, and CO – during the CalNex and HIPPO campaigns, Atmos. Meas. Tech., 7, 1509–1526, https://doi.org/10.5194/amt-7-1509-2014, 2014.

Schiller, C., Bozem, H., Gurk, C., Parchatka, U., Königstedt, R., Harris, G., Lelieveld, J., and Fischer, H.: Applications of quantum cascade lasers for sensitive trace gas measurements of CO, CH_4, N_2O and HCHO, Applied Physics B, 92, 419–430, https://doi.org/10.1007/s00340-008-3125-0, 2008.

Schumann, U. and Huntrieser, H.: The global lightning-induced nitrogen oxides source, Atmos. Chem. Phys., 7, 3823–3907, https://doi.org/10.5194/acp-7-3823-2007, 2007.

Seinfeld, J. H. and Pandis, S. N.: Atmospheric chemistry and physics: from air pollution to climate change, John Wiley & Sons, 3rd edn., ISBN: 978-1-118-94740-1, 2016.

Singh, H. B.: Composition, chemistry, and climate of the atmosphere, Van Nostrand Reinhold New York, ISBN 0-442-01264-0, 1995.

Sprenger, M. and Wernli, H.: A northern hemispheric climatology of cross-tropopause exchange for the ERA15 time period (1979–1993), Journal of Geophysical Research: Atmospheres, 108, https://doi.org/10.1029/2002JD002636, 2003.

Staley, D. O.: On the Mechanism of Mass and Radioactivity Transport from Stratosphere to Troposphere, Journal of Atmospheric Sciences, 19, 450–467, https://doi.org/10.1175/1520-0469(1962)019<0450:OTMOMA>2.0.CO;2, 1962.

Strode, S. A., Liu, J., Lait, L., Commane, R., Daube, B., Wofsy, S., Conaty, A., Newman, P., and Prather, M.: Forecasting carbon monoxide on a global scale for the ATom-1 aircraft mission: insights from airborne and satellite observations and modeling, Atmos. Chem. Phys., 18, 10955–10971, https://doi.org/10.5194/acp-18-10955-2018, 2018.

Sumner, A. L., Shepson, P. B., Couch, T. L., Thornberry, T., Carroll, M. A., Sillman, S., Pippin, M., Bertman, S., Tan, D., Faloona, I., Brune, W., Young, V., Cooper, O., Moody, J., and Stockwell, W.: A study of formaldehyde chemistry above a forest canopy, Journal of Geophysical Research: Atmospheres, 106, 24387–24405, https://doi.org/10.1029/2000JD900761, 2001.

Szopa, S., Naik, V., Adhikary, B., Artaxo, P., Berntsen, T., Collins, W. D., Fuzzi, S., Gallardo, L., Kiendler-Scharr, A., Klimont, Z., Liao, H., Unger, N., and Zanis, P.: Short-Lived Climate

Forcers (Chapter 6), in: IPCC 2021: Climate Change 2021: The Physical Science Basis. Contribution of Working Group I to the Sixth Assessment Report of the Intergovernmental Panel on Climate Change, edited by: Masson-Delmotte, V., Zhai, P., Pirani, A., Connors, S., Péan, C., Berger, S., Caud, N., Chen, Y., Goldfarb, L., Gomis, M., Huang, M., Leitzell, K., Lonnoy, E., Matthews, J., Maycock, T., Waterfield, T., Yelekçi, K., Yu, R., and Zhu, B., 817–922 pp., Cambridge University Press, Cambridge, United Kingdom and New York, NY, USA, https://doi.org/10.1017/9781009157896.008, 2021.

Tadic, I., Parchatka, U., Königstedt, R., and Fischer, H.: In-flight stability of quantum cascade laser-based infrared absorption spectroscopy measurements of atmospheric carbon monoxide, Applied Physics B, 123, 1–9, https://doi.org/10.1007/s00340-017-6721-z, 2017.

Tadic, I., Nussbaumer, C. M., Bohn, B., Harder, H., Marno, D., Martinez, M., Obersteiner, F., Parchatka, U., Pozzer, A., Rohloff, R., Zöger, M., Lelieveld, J., and Fischer, H.: Central role of nitric oxide in ozone production in the upper tropical troposphere over the Atlantic Ocean and western Africa, Atmos. Chem. Phys., 21, 8195–8211, https://doi.org/10.5194/acp-21-8195-2021, 2021.

Tarasick, D., Galbally, I. E., Cooper, O. R., Schultz, M. G., Ancellet, G., Leblanc, T., Wallington, T. J., Ziemke, J., Liu, X., Steinbacher, M., Staehelin, J., Vigouroux, C., Hannigan, J. W., García, O., Foret, G., Zanis, P., Weatherhead, E., Petropavlovskikh, I., Worden, H., Osman, M., Liu, J., Chang, K.-L., Gaudel, A., Lin, M., Granados-Muñoz, M., Thompson, A. M., Oltmans, S. J., Cuesta, J., Dufour, G., Thouret, V., Hassler, B., Trickl, T., and Neu, J. L.: Tropospheric Ozone Assessment Report: Tropospheric ozone from 1877 to 2016, observed levels, trends and uncertainties, Elementa: Science of the Anthropocene, 7, 39, https://doi.org/10.1525/elementa.376, 2019.

Thompson, C. R., Wofsy, S. C., Prather, M. J., et al.: The NASA Atmospheric Tomography (ATom) mission: Imaging the chemistry of the global atmosphere, Bulletin of the American Meteorological Society, 103, E761–E790, https://doi.org/10.1175/BAMS-D-20-0315.1, 2022.

Toby, S.: Chemiluminescence in the reactions of ozone, Chemical Reviews, 84, 277–285, https://doi.org/10.1021/cr00061a003, 1984.

Tomsche, L., Pozzer, A., Ojha, N., Parchatka, U., Lelieveld, J., and Fischer, H.: Upper tropospheric CH_4 and CO affected by the South Asian summer monsoon during the Oxidation Mechanism Observations mission, Atmos. Chem. Phys., 19, 1915–1939, https://doi.org/10.5194/acp-19-1915-2019, 2019.

Škerlak, B., Sprenger, M., and Wernli, H.: A global climatology of stratosphere–troposphere exchange using the ERA-Interim data set from 1979 to 2011, Atmos. Chem. Phys., 14, 913–937, https://doi.org/10.5194/acp-14-913-2014, 2014.

Waliser, D. E. and Somerville, R. C.: Preferred latitudes of the intertropical convergence zone, Journal of Atmospheric Sciences, 51, 1619–1639, https://doi.org/10.1175/1520-0469(1994)051<1619:PLOTIC>2.0.CO;2, 1994.

Wesely, M. and Hicks, B.: A review of the current status of knowledge on dry deposition, Atmospheric Environment, 34, 2261–2282, https://doi.org/10.1016/S1352-2310(99)00467-7, 2000.

White, J. U.: Optical system providing a long optical path, uS Patent 2,779,230, https://patents.google.com/patent/US2779230A (last access: 24 June 2024), 1957.

Wienhold, F., Fischer, H., Hoor, P., Wagner, V., Königstedt, R., Harris, G., Anders, J., Grisar, R., Knothe, M., Riedel, W., Liibken, F.-J., and Schilling, T.: TRISTAR-A tracer in-situ TDLAS for atmospheric research, Applied Physics B, 67, 411–417, https://doi.org/10.1007/s003400050524, 1998.

Williams, E. and Stanfill, S.: The physical origin of the land–ocean contrast in lightning activity, Comptes Rendus Physique, 3, 1277–1292, https://doi.org/10.1016/S1631-0705(02)01407-X, 2002.

Williams, E., Rosenfeld, D., Madden, N., Gerlach, J., Gears, N., Atkinson, L., Dunnemann, N., Frostrom, G., Antonio, M., Biazon, B., Camargo, R., Franca, H., Gomes, A., Lima, M., Machado, R., Manhaes, S., Nachtigall, L., Piva, H., Quintiliano, W., Machado, L., Artaxo, P., Roberts, G., Renno, N., Blakeslee, R., Bailey, J., Boccippio, D., Betts, A., Wolff, D., Roy, B., Halverson, J., Rickenbach, T., Fuentes, J., and Avelino, E.: Contrasting convective regimes over the Amazon: Implications for cloud electrification, Journal of Geophysical Research: Atmospheres, 107, LBA 50-1–LBA 50-19, https://doi.org/10.1029/2001JD000380, 2002.

Williams, E. R.: Large-scale charge separation in thunderclouds, Journal of Geophysical Research: Atmospheres, 90, 6013–6025, https://doi.org/10.1029/JD090iD04p06013, 1985.

Wofsy, S. C., Afshar, S., Allen, H. M., Apel, E. C., Asher, E. C., Barletta, B., Bent, J., Bian, H., Biggs, B. C., Blake, D. R., Blake, N., Bourgeois, I., Brock, C. A., Brune, W. H., Budney, J. W., Bui, T. P., Butler, A., Campuzano-Jost, P., Chang, C. S., Chin, M., Commane, R., Correa, G., Crounse, J. D., Cullis, P. D., Daube, B. C., Day, D. A., Dean-Day, J. M., Dibb, J. E., DiGangi, J. P., Diskin, G. S., Dollner, M., Elkins, J. W., Erdesz, F., Fiore, A. M., Flynn, C. M., Froyd, K. D., Gesler, D. W., Hall, S. R., Hanisco, T. F., Hannun, R. A., Hills, A. J., Hintsa, E. J., Hoffman, A., Hornbrook, R. S., Huey, L. G., Hughes, S., Jimenez, J. L., Johnson, B. J., Katich, J. M., Keeling, R. F., Kim, M. J., Kupc, A., Lait, L. R., Lamarque, J.-F., Liu, J., McKain, K., McLaughlin, R. J., Meinardi, S., Miller, D. O., Montzka, S. A., Moore, F. L., Morgan, E. J., Murphy, D. M., Murray, L. T., Nault, B. A., Neuman, J. A., Newman, P. A., Nicely, J. M., Pan, X., Paplawsky, W., Peischl, J., Prather, M. J., Price, D. J., Ray, E., Reeves, J. M., Richardson, M., Rollins, A. W., Rosenlof, K. H., Ryerson, T. B., Scheuer, E., Schill, G. P., Schroder, J. C., Schwarz, J. P., St. Clair, J. M., Steenrod, S. D., Stephens, B. B., Strode, S. A., Sweeney, C., Tanner, D., Teng, A. P., Thames, A. B., Thompson, C. R., Ullmann, K., Veres, P. R., Vieznor, N., Wagner, N. L., Watt, A., Weber, R., Weinzierl, B., Wennberg, P. O., Williamson, C. J., Wilson, J. C., Wolfe, G. M., Woods, C. T., and Zeng, L. H.: ATom: Merged Atmospheric Chemistry, Trace Gases, and Aerosols, ORNL DAAC [data set], https://doi.org/10.3334/ORNLDAAC/1581, 2018.

Zahn, A., Weppner, J., Widmann, H., Schlote-Holubek, K., Burger, B., Kühner, T., and Franke, H.: A fast and precise chemiluminescence ozone detector for eddy flux and airborne application, Atmos. Meas. Tech., 5, 363–375, https://doi.org/10.5194/amt-5-363-2012, 2012.

Zipser, E. J., Cecil, D. J., Liu, C., Nesbitt, S. W., and Yorty, D. P.: WHERE ARE THE MOST INTENSE THUNDERSTORMS ON EARTH?, Bulletin of the American Meteorological Society, 87, 1057–1072, https://doi.org/10.1175/BAMS-87-8-1057, 2006.

3.8 Supplement of "Enhancement of O_3 – CO ratios at tropospheric subtropical latitudes: Photochemistry and stratospheric influence"

Supplement of Atmos. Chem. Phys., 25, 14987–15007, 2025
https://doi.org/10.5194/acp-25-14987-2025-supplement

Atmospheric Chemistry and Physics Open Access

Supplement of

Enhancement of O_3–CO ratios at tropospheric subtropical latitudes: Photochemistry and stratospheric influence

Linda Ort et al.

Correspondence to: Linda Ort (linda.ort@mpic.de)

S1 Aircraft observations

The aircraft observations were taken from 12 different missions (ESMVal, OMO, WISE, ATom 1, ATom 2, ATom 3, ATom 4, CAFE Africa, SouthTRAC, CAFE Brazil, PHILEAS, CAFE Pacific) from 2012 to 2024, taking place in different locations and months. Additional information for each campaign and supporting material are presented below.

S1.1 The ESMVal campaign

The EMSVal (Earth System Model Validation) research phase took place in September 2012 and was carried out using the HALO research aircraft starting from its base at the German Aerospace center (DLR) in Oberpfaffenhofen, Germany, before circling the African continent. The campaign aimed to investigate the global climate–chemical–aerosol–cloud system and to validate numerical models. During the mission, several vertical profiles and a coverage of almost all latitudes from 80°S to 80°N could be achieved with seven research flights around the African and Europe continents. The ESMVal data sets are available on the HALO data base (DLR, 2012).

The CO concentrations have been measured with the tracer in situ TDLAS for atmospheric research (TRISTAR) spectrometer. This infrared spectrometer has been originally designed by Wienhold et al. (1998) but has been modified throughout the numerous campaigns which it has been used (Schiller et al., 2008; Tadic et al., 2017; Tomsche et al., 2019; Röder et al., 2024). For ESMVal, TRISTAR measured with alternating three-channel QCLS in the infrared range the absorption of CO, N_2O, and CH_4 through a 64-m-path multipass double corner cube White cell (White (1957); Wienhold et al. (1998)) with liquid-nitrogen-cooled detectors and lasers. For CO concentrations, one quantum cascade laser emitted at 2158.30 cm^{-1} and had a time resolution of 8 s (Müller et al., 2016). The total uncertainty of the CO measurements relative to the working standard during the ESMVal mission, including the instrumental drift between the calibration cycle every 30 minutes and the 2σ precision, is 1.8 ppbv overall (Schiller et al., 2008; Müller et al., 2016).

O_3 measurements were carried out with a dual-channel system instrument named FAIRO. This instrument combines two techniques to measure O_3 and thereby ensuring a high accuracy and high measurement frequency. FAIRO measures O_3 with UV photometry using light absorption at wavelengths between 250 and 260 nm and chemiluminescence (CL) detection at 254 nm (Hartley-Bande) (Zahn et al., 2012; Chiu et al., 2024). Under laboratory conditions the measurement uncertainties are 2 % for the UV photometry and 0.5 % for the CL detection with a time resolution up to 12.5 Hz. Due to the fact that the CL detection measures relative to the UV photometry as a continuous calibration, the overall measurement uncertainty of the data is 2.5 % (Rolf et al. (2015); Müller et al. (2016)). Further information can be found in Zahn et al. (2012).

S1.2 The OMO campaign

In July to August 2015, the OMO (Oxidation Mechanism Observations) mission took place in the upper troposphere over the eastern Mediterranean and the Arabian Peninsula. Over 18 research flights with the HALO research aircraft, the outflow of the South Asian summer monsoon was sampled and the influence on the Asian monsoon anticyclone was investigated (e.g., Tomsche et al. (2019); Hottmann et al. (2020)). The data sets of the OMO mission are available on the HALO data base (DLR, 2015).

The CO observations of the OMO campaign were measured with the TRISTAR instrument, the same QCLS instrument as introduced in Section S1.1. The averaged measurement uncertainty for CO over all flights, including drift behavior and precision of the instrument, is 5.1 % according to a certified reference gas with CO concentrations of 121.44 ± 1.46 ppbv (Tomsche et al., 2019).

The O_3 measurements were carried out with the FAIRO instrument with the same measurement uncertainty as already described above in Section S1.1. Unfortunately, during this campaign, the measurement uncertainty was influenced by a leak in the system and hence comes to approximated 10 %.

S1.3 The WISE campaign

In September and October 2017, the aircraft mission WISE (Wave-driven ISentropic Exchange) studied horizontal transport and mixing in the northern extra-tropical region over Iceland and exchange processes of the upper troposphere and lower stratosphere (UTLS). Based out of Shannon, Ireland, 15 research flights with the HALO research aircraft were carried out to investigate stratosphere–troposphere exchange processes with a number of trace gases and their horizontal and vertical gradients in the extra-tropical UTLS region through, e.g., planetary wave, Rossby wave breaking events, and their impact on cirrus cloud formation and radiative forcing (Riese and Hoor, 2017; Kunkel et al., 2019; Krasauskas et al., 2020; Bartolome Garcia et al., 2021). The WISE data sets can be accessed on the HALO data base (DLR, 2017).

CO measurements of WISE have been provided by the University of Mainz Airborne Quantum Cascade Laser-spectrometer (UMAQS), which is based on an Aerodyne Quantum Cascade Laser Mini Monitor (Aerodyne Research Inc, MA, USA) using direct absorption spectroscopy in a 76-m astigmatic multipass cell (McManus et al., 2010) with a continuous-wave quantum cascade laser to measure CO and N_2O with a sweep rate of 2 kHz, resulting in a temporal resolution of 1 Hz (Müller et al., 2015). The CO concentration is measured at an absorption wavelength of 2203.16 cm^{-1}. Frequent in-flight calibrations with a secondary standard assure stability and drift corrections during the measurements. The measurement uncertainty for CO is determined to be 0.94 ppbv for CO (Kunkel et al., 2019).

The O_3 measurements have been carried out with the FAIRO instrument with the same measurement uncertainty as already described above in Section S1.1.

S1.4 The ATom campaign

The NASA Atmospheric Tomography (ATom) mission (https://espo.nasa.gov/atom/, last access: 26 June 2024), operated by the NASA Armstrong (Dryden) Flight Research Center, aimed to collect in situ measurements of chemical components of the atmosphere in remote places over all seasons with the NASA DC-8 aircraft. The four campaign missions (ATom-1, -2, -3, -4)took place from 2016 to 2018 mostly over the ocean with a total of 47 scientific flights including several vertical profiles from 0.15 to 13 km with one mission in each season. For this study, the data of all ATom missions are used, which include ATom-1 (July–August 2016) (Strode et al., 2018), ATom-2 (January–February 2017), ATom-3 (September–November 2017), and ATom-4 (April–May 2018). Each mission started in Palmdale, California, and traversed the remote Pacific and Atlantic oceans, collecting various chemical and gas properties of the lower atmosphere over a wide range of latitudes. More information can be found in the overview article of the ATom campaign by Thompson et al. (2022). The ATom data sets are available on the ATom website (Wofsy et al., 2018).

The CO measurements used for this study were carried out with the Harvard QCLS instrument (Santoni et al., 2014). This QCLS instrument measures the absorption of CO at 2160 cm^{-1} with a pulsed quantum cascade laser through a 76-m-long astigmatic multi-pass cell and a liquid-nitrogen-cooled HgCdTe detector. The ATom CO concentration accuracy and precision are 3.5 and 0.15 ppbv, respectively (Strode et al., 2018), and it has a time resolution of 1 Hz.

The O_3 observations were sampled by the National Oceanic and Atmospheric Administration (NOAA) nitrogen oxides and ozone (NO_yO_3) instrument (Ridley et al., 1992). Besides other channels, the O_3 channel of this instrument uses CL detection together with the addition of pure NO as a reagent gas to measure ambient O_3 concentrations. The CL detection is calibrated on the ground and frequently during the flights with an independent instrument using UV optical absorption at 254 nm (Bourgeois et al., 2021). The NO_yO_3 instrument provides a total precision of 0.015 ppbv and a measurement uncertainty of 2 % of the O_3 data with a time resolution of 1 Hz (Bourgeois et al., 2020, 2021).

S1.5 The CAFE campaigns

The CAFE Africa and CAFE Brazil missions are part of three Chemistry of the Atmosphere Aircraft Observation (CAFE) missions, which aimed to understand chemical and dynamical processes in the tropical troposphere in more detail based on in situ measurements by the HALO aircraft. CAFE Africa was the first mission in August and September 2018 based in Sal on Capo Verde and covered with 14 research flights the northern tropical to subtropical region west of Africa. More information can

be found in Tadic et al. (2021). From December 2022 to January 2023 the second CAFE mission took place over the Amazon rainforest region based in Manaus, Brazil, including 16 local research flights and 4 transfer flights through Sal, Capo Verde. Here, the focus was on surface emissions, their transport and chemistry, and role in new particle formation in the free and upper troposphere. From January until February 2024, the third mission, CAFE Pacific, based in Cairns, Australia, was carried out above the Pacific northeast of Australia, as well as above the Australian continent. The data sets of the CAFE Africa, Brazil, and Pacific campaigns are available on the HALO data base (DLR, 2018, 2023a, 2024).

CO measurements were carried out with a further improved version of the TRISTAR instrument, introduced in Section S1.1. Since CAFE Africa, TRISTAR has been running on room-temperature lasers and detectors, which are stabilized by a 40°C – heating plate and the scanning and processing of the spectra are controlled digitally and no longer using analog technology. For CAFE Brazil, the alternating three-laser-system has been reduced to a single-laser-system providing continuous measurements on a 1-Hz frequency to gain more duty time for the gas of interest. Over all CAFE campaigns, frequent in-flight calibrations have been made with compressed air conditioned by a primary standard bottle with the standard errors given by the manufacturer (Luxfer Gas Cylinders Ltd., Colwick, Nottingham, England) with 0.36 ppbv for CO. CO measurements are provided with a temporal resolution of 10 s. Furthermore, another QCLS spectrometer, named ATTILA, measured CO simultaneously during the CAFE Brazil and CAFE Pacific campaigns (Ort et al., 2024). For this study, CO observations were taken from TRISTAR with a total measurement uncertainty of 4.3 % and 3.5 % for CAFE Africa and CAFE Brazil for 1 Hz data, respectively (Schiller et al., 2008; Ort et al., 2024; Röder et al., 2024). For CAFE Pacific, a combination of CO data from ATTILA and TRISTAR has been taken to cover all research flights. The mean measurement uncertainty is 5.3 % for the combination of TRISTAR and ATTILA CO measurements.

The O_3 measurements were carried out with the FAIRO instrument with the same measurement uncertainty as already described above in Section S1.1.

S1.6 The SouthTRAC campaign

From August to November 2019, the Southern Hemisphere Transport, Dynamics, and Chemistry (SouthTRAC) campaign based in Rio Grande, Argentina, measured over the course of 23 scientific flights the dynamical and chemical composition aspects of the Antarctic upper troposphere and gravity waves up to the mesosphere (Rapp et al., 2021). The mission was flown with the HALO aircraft and included four transfer flights from Oberpfaffenhofen, Germany, with a large zonal coverage. Altitudes up to 14.5 km could be reached. More information can be found on the SouthTRAC website (Rapp et al., 2019). The SouthTRAC data sets are available on the HALO data base (DLR, 2019).

CO measurements of SouthTRAC were also measured by the UMAQS instrument, described in Section S1.3. The CO measurements of the SouthTRAC campaign have a precision of 0.68 ppbv (2σ) and an accuracy of 1.22 ppbv, which results in a total uncertainty (relative to the secondary standard) of 1.4 ppbv (Müller et al., 2015).

The O_3 measurements were carried out with the FAIRO instrument with the same measurement uncertainty as already described above in section S1.1.

S1.7 The PHILEAS campaign

Probing high latitude export of air from the Asian summer monsoon was the research perspective of the PHILEAS campaign in summer 2023. The campaign was divided into two phases–one measuring the inflow of the Asian Summer Monsoon over Europe with the aircraft based in Oberpfaffenhofen, Germany and the second one based in Anchorage, Alaska, USA, to measure the long-range transported outflow of the Asian summer monsoon. In total, there were 18 research flights including 2 transfer flights with a fuel stop in Iceland. The PHILEAS data sets are available on the HALO data base (DLR, 2023b).

CO observations were carried out with the UMAQS instrument, which has been described in Section S1.3. The measurements uncertainty of CO is 0.32 ppbv with an accuracy of 0.64 ppbv.

The O_3 measurements were carried out with the FAIRO instrument with the same measurement uncertainty as already de-

scribed above in Section S1.1.

S2 Measurement statistics

The left panel of Figure S1 (a, c, e) shows the number of data points used to calculate the concentration of CO, O_3, and their ratio for each grid box, available from the twelve campaign data sets used in this study. Note that before averaging, each data set had a different time resolution and therefore already represents an average of different time resolutions onto 60 s (see Table 2 in main study). On the right side of Figure S1 (b, d, f), the standard errors of the means relative to the mean (RSEM) in percent are displayed for CO, O_3 and their ratio, respectively. The RSEM is given by:

$$\text{RSEM} = \frac{\frac{\sigma}{\sqrt{N}}}{mean} \times 100, \tag{S1}$$

with the standard deviation σ, the number per grid cell N, and the $mean$ of each grid cell. The RSEM provides a variability of the averaged measurements relative to the mean value of each grid cell. Note that this also includes atmospheric and seasonal variability in averaging all campaigns. However, when RSEM is small (<5%), and counts are high (≥ 10), the observations show very good agreement throughout all data sets. This is the case, for example, in the tropical upper troposphere, where seasonal variability is small. For regions with stronger seasonal variability, e. g., at the tropopause, RSEM is higher ($\leq 15\%$), even if there is a high number of counts per grid cell. Conversely, small RSEM with small counts per grid cell, e. g., in the southern polar latitudes and southern subtropics, show regions with small variability, but averages from only a few flights through this area, which neglects annual variability. Therefore, we decided to categorize the data set using two conditions to show statistical relevant data, with a sufficient number of counts per grid cell ($N \geq 10$) and a reasonable variability of the mean values (RSEM $\leq 15\%$). This has been indicated using hatching in Figure 2 in the main study.

The highest RSEM and therefore the strongest variability between the campaign data sets is found in the vicinity to the tropopause, especially for O_3 (Fig. S1, d). We attribute this to the different altitudes of the tropopause throughout the years and the different campaigns. Especially close to the tropopause, the gradient of O_3 is very steep, with increasing O_3 towards the stratosphere, and therefore leads to such high variability. However, as we are focusing on the troposphere and filter out mixing ratios higher than 100 ppbv of O_3, following Prather et al. (2011)), these differences have a negligible effect on our results. In the RSEM of CO, only a few grid points show very large percentages above 15%. Those can be linked to extreme events (e. g., biomass burning), which were measured during single measurement campaigns and increase the standard deviation.

S3 Comparison of observations with model

To test the statistical representativeness of the observations, the model was compared with the observations (Figure S2). For this, the flight tracks were extracted on a 1-hour resolution from the monthly climatology of the model, following a nearest point algorithm. The extracted data has been binned with a zonal resolution of 10° and a vertical resolution of 2 km. This flight track extraction is an interpolation and should give worse results for comparison between the model and the observations. Taking this into account, there is good agreement between the model-generated climatological data and the flight track extracted data of the model across the troposphere. This confirms that there is sufficient observational data for our analysis, and the selected campaigns are considered statistically representative. In the southern hemisphere, however, the difference between "mod" and "ft mod" becomes larger from 6 km upwards, which shows that there is not enough observational data to represent the climatology of the southern hemisphere mid- to upper troposphere. However, this supports the focus on the northern hemisphere in the main study.

Comparing the full model and the observations in Figure S2, they are mostly in agreement in the lower troposphere and free troposphere. Towards the tropopause, there seems to be an increased overestimation of the model. Here, the model overestimates mainly O_3, as for CO the comparison looks better (not shown here). Nevertheless, as this comparison is following just a nearest point algorithm based on hourly data, a direct comparison should approximate the data. However, this comparison is

sufficient for the scope of this work and allows us to confidently use the whole model data for the $O_3 - CO$ ratio analysis of the northern subtropics, the sensitivity study, and representing the observations.

S4 Global zonal gradients

In Figure S3 the global 10° and 2 km averaged zonal gradients for CO, O_3, and their ratio are shown for the observations ((a), (b), (c)), the model ((d), (e), (f)) and the sensitivity model run ((g), (h), (i)). The smaller number of observations available for the southern hemisphere mean that this study was focused on the northern hemisphere. Nevertheless, the observations and the model show a good agreement in the CO values on the southern hemisphere, while O_3 seems to be overestimated by the model, mostly in the upper troposphere. This overestimation of O_3 could be identified also in the study of Jöckel et al. (2016). A subtropical enhancement of the $O_3 - CO$ ratio in the southern hemisphere can be seen by the model, but it is not as clear in the observations. Besides the lack of data for the southern hemisphere, this can be due to the difference in the chemical background concentrations prevailing in the southern mid- to high latitudes. As the Hadley circulation and its transport from the tropics into the subtropics is similar in both hemispheres, stratosphere–troposphere mixing processes might be different due to less land cover, stronger zonal winds, and less vertical exchange processes, as there are less obstacles. Therefore, mixing with the stratosphere is less pronounced as is the seasonal cycle of total stratospheric mass exchange (Appenzeller et al., 1996). The overestimation of O_3 in the upper troposphere in the model might be an indicator of an overestimation of STE in the model or the representation of the right tropopause height. Furthermore, the southern extra tropics contain the cleanest air on Earth, due to the lower population, cities, biomass burning, land cover, and ship traffic. CO background mixing ratios in the southern hemisphere is 60 ppbv and O_3 mixing ratios is 30 ppbv at the surface, both being lower than in the northern hemispheric extra tropics, where CO varies from 100 – 140 ppbv and O_3 from 30 – 45 ppbv (Fig. S3, (a), (b)). Especially for CO, there is no increase in surface emissions towards the southern higher latitudes. All those factors contribute to the less pronounced enhancement of the $O_3 - CO$ ratio in the southern subtropics, as we could identify in the northern subtropics.
The sensitivity run of the model excludes all lightning emissions from the simulation. As discussed in the main study, this results in generally higher CO, and lower O_3 mixing ratios globally as well as less variation in the tracers in the vertical column of the troposphere. This is also the case for the southern hemisphere, which can be seen in the lowest panel of Figure S3 and in the annual zonal distribution in Figure S4. Thus, in terms of $O_3 - CO$ ratios, the hemispheres are almost identical. In the northern hemisphere, there is generally more lightning than in the southern hemisphere due to the larger land cover (Schumann and Huntrieser, 2007). Nevertheless, in the southern hemisphere, the background values are much lower, and other causes of high $O_3 - CO$ ratios are much less important (i.e., stratosphere–troposphere mixing), hence the absolute and relative differences of excluding LNO_x are generally stronger in the southern hemisphere than in the northern. The absolute and relative difference in the $O_3 - CO$ ratio including and excluding LNO_x is by a factor of two larger in the southern hemisphere than in the northern hemisphere (Fig. S5).

S4.1 Seasonal variability

Figures S6, S7, S8, S9, S10, and S11 show monthly zonal distributions of CO, O_3, and $O_3 - CO$ ratios from the standard simulation and the sensitivity run excluding LNO_x from the EMAC model. A strong seasonality can be seen for both CO and O_3. Maximum CO emissions are modeled in the boreal winter, while O_3 mixing ratios are found in the boreal summer in the northern hemisphere. This influences also the $O_3 - CO$ ratio in the subtropics in both hemispheres, peaking in the summer months and being weakest during winter (Fig. S10). By excluding LNO_x emissions (Fig. S11) the $O_3 - CO$ ratios generally decline, resulting in a much more homogeneous troposphere than when lightning emissions are included. Nevertheless, the maximum increase in the subtropical $O_3 - CO$ ratio can still be noted in the summer, stronger in the northern than in the southern hemisphere, which makes other factors responsible for the strong seasonality.

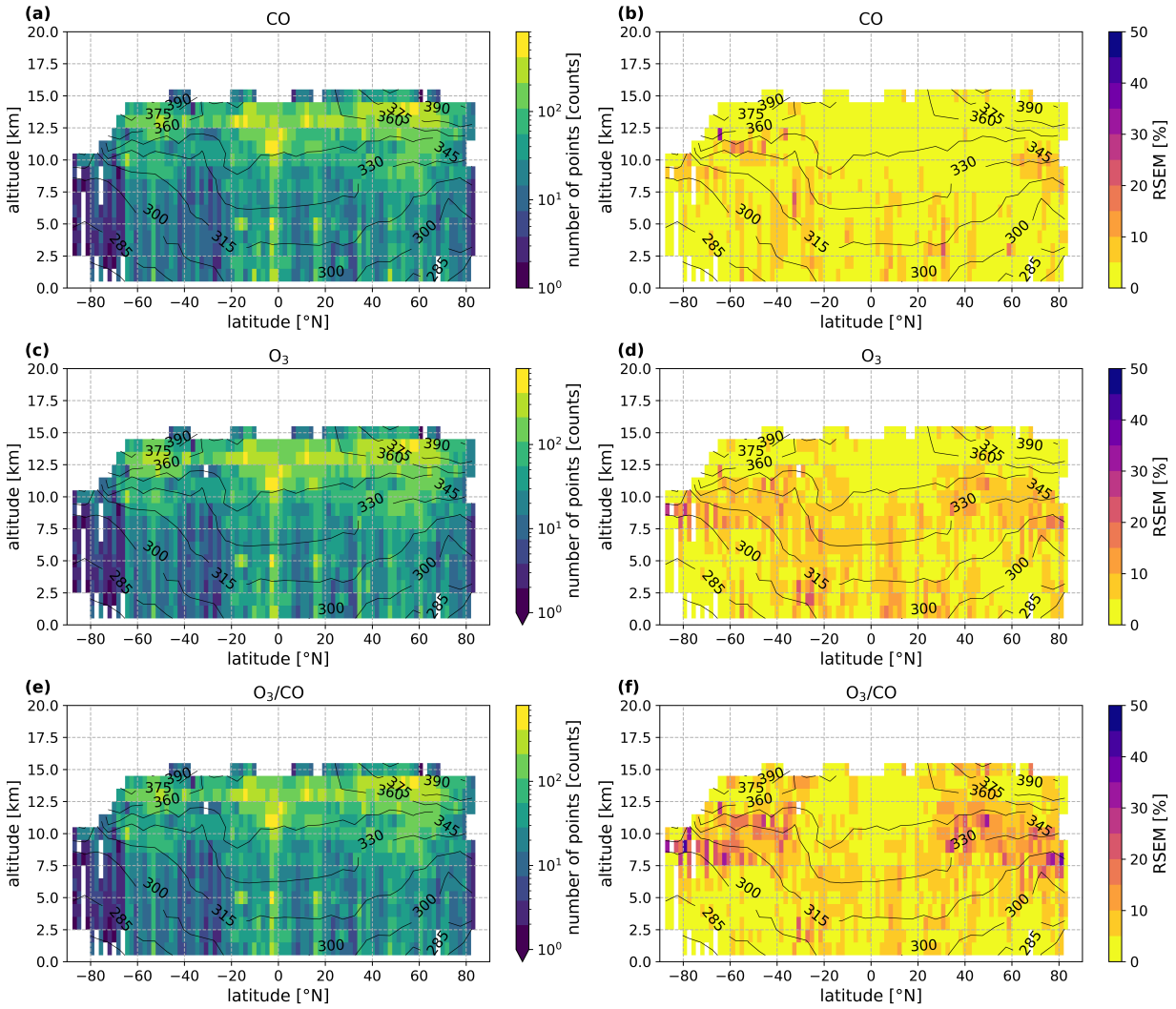

Figure S1. Zonal distribution of CO (a, b), O_3 (c, d), and their ratio (e, f) showing the number of data points per grid cell and the standard error of the mean relative to the mean (RSEM) in percent, calculated via Eq. 1, respectively. Black lines indicate layers of constant potential temperature, averaged over 5° and 1 km.

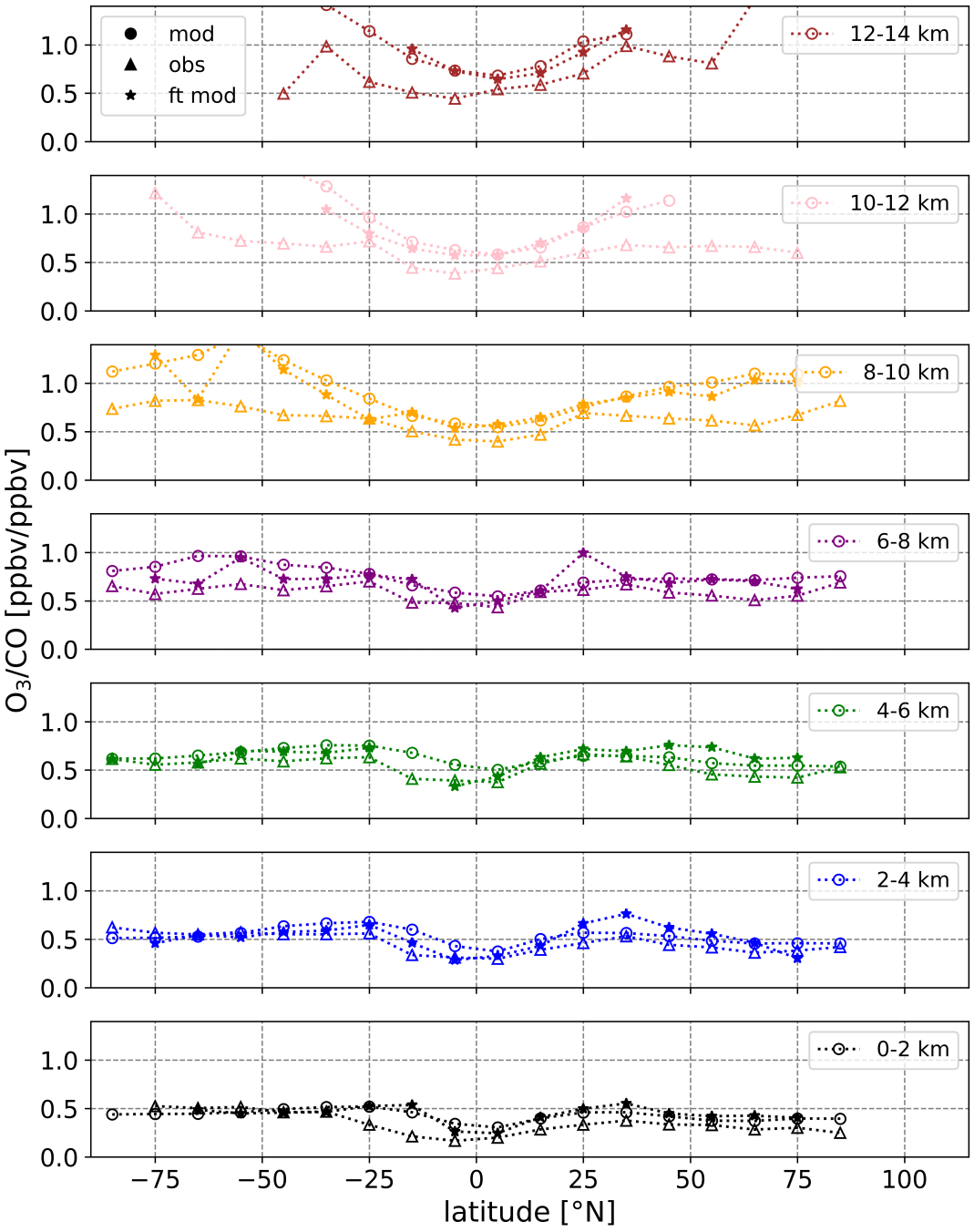

Figure S2. Comparison of the model climatology (mod, circles), observations (obs, triangles), and the model sampled along the flight tracks (ft mod, stars). Displayed are the zonal medians averaged over 10° and 2 km. Before the calculations, stratospheric values were filtered out by excluding all data points with O_3 mixing ratios higher than 100 ppbv, according to Prather et al. (2011).

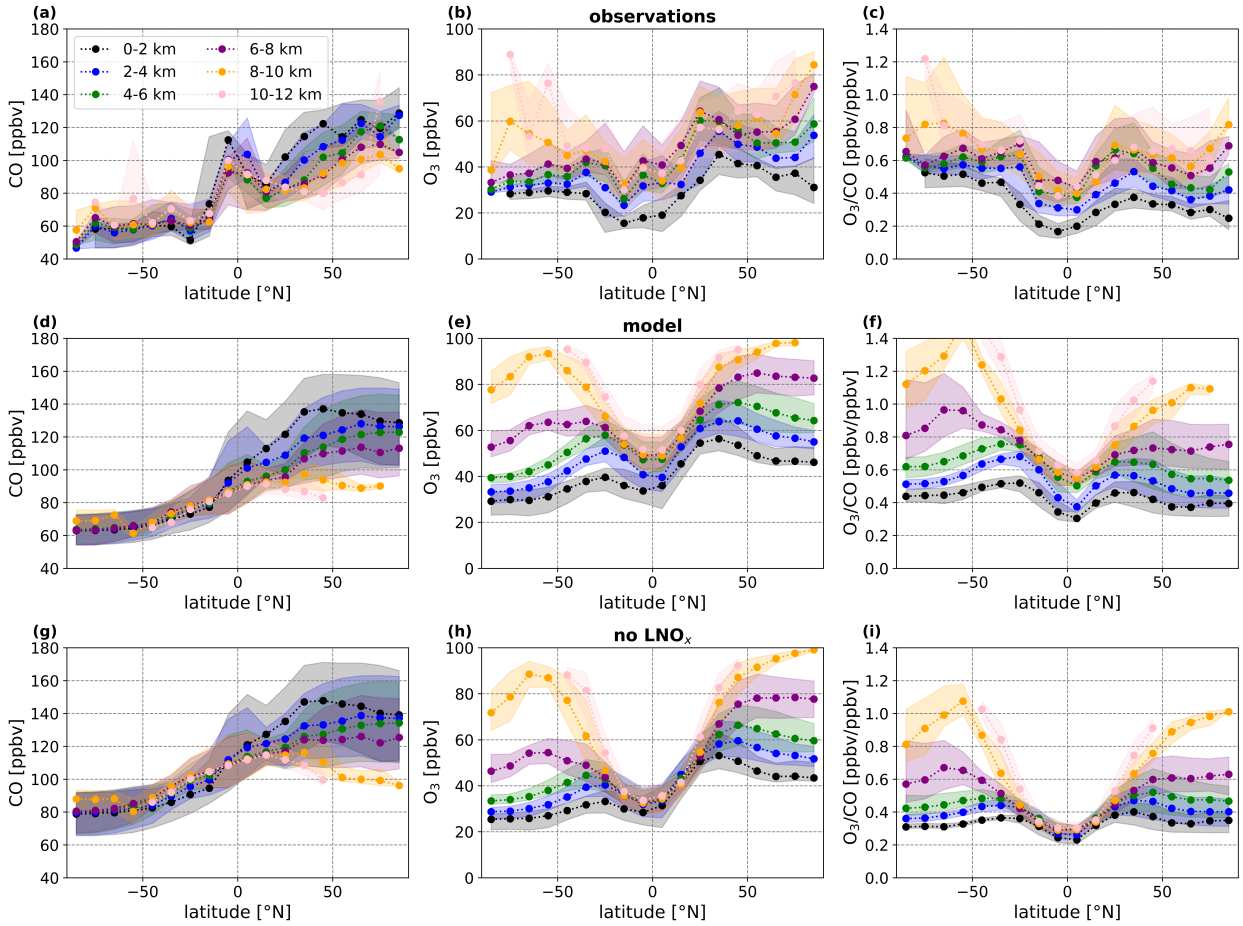

Figure S3. Global zonal gradients of the observations, the model, and the sensitivity run, excluding LNO_x for CO ((a), (d), (g)), O_3 ((b), (e), (h)), and their ratio ((c), (f), (i)), respectively. The gradients represent the zonal median values with the 25th and 75th percentiles as shaded areas from averages of 10° of latitude, and 2 km of altitude. Before the calculations, stratospheric values were filtered out by excluding all data points with O_3 mixing ratios higher than 100 ppbv, according to Prather et al. (2011).

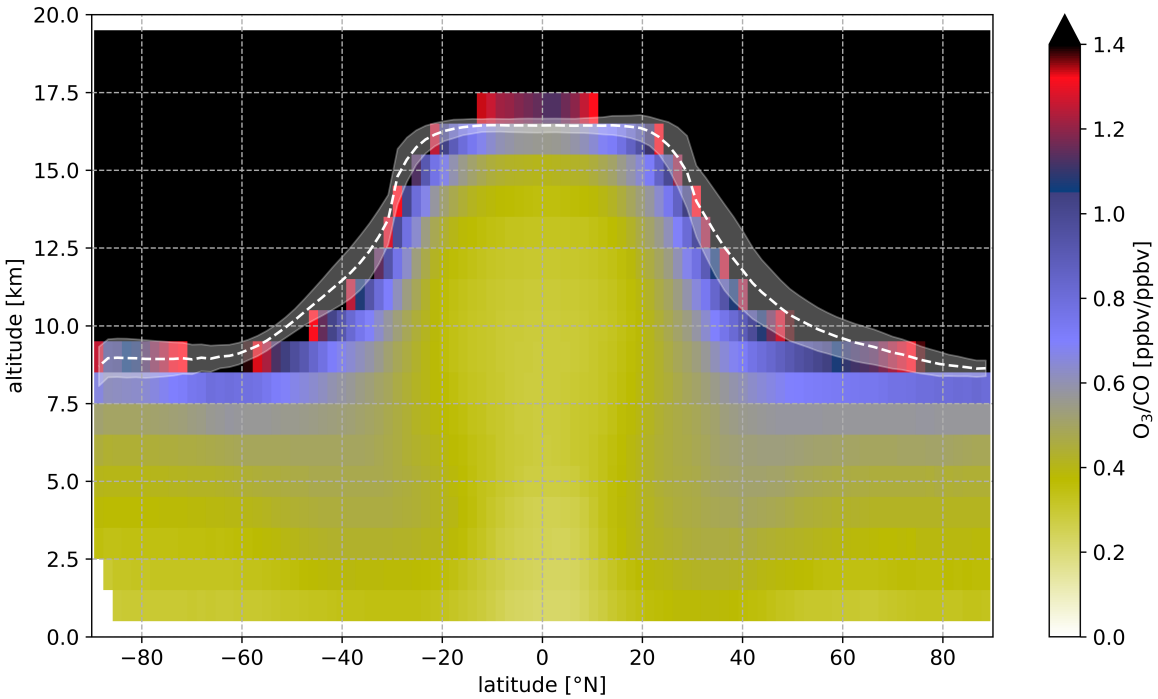

Figure S4. The median annual zonal distribution of the sensitivity simulation, excluding LNO_x for the ratio between O_3 and CO. All data points are averaged over 1 km altitude and 1.875° latitude. The scale has been adjusted to display tropospheric values. The white dashed line indicates the tropopause height and the standard deviation is shaded in white.

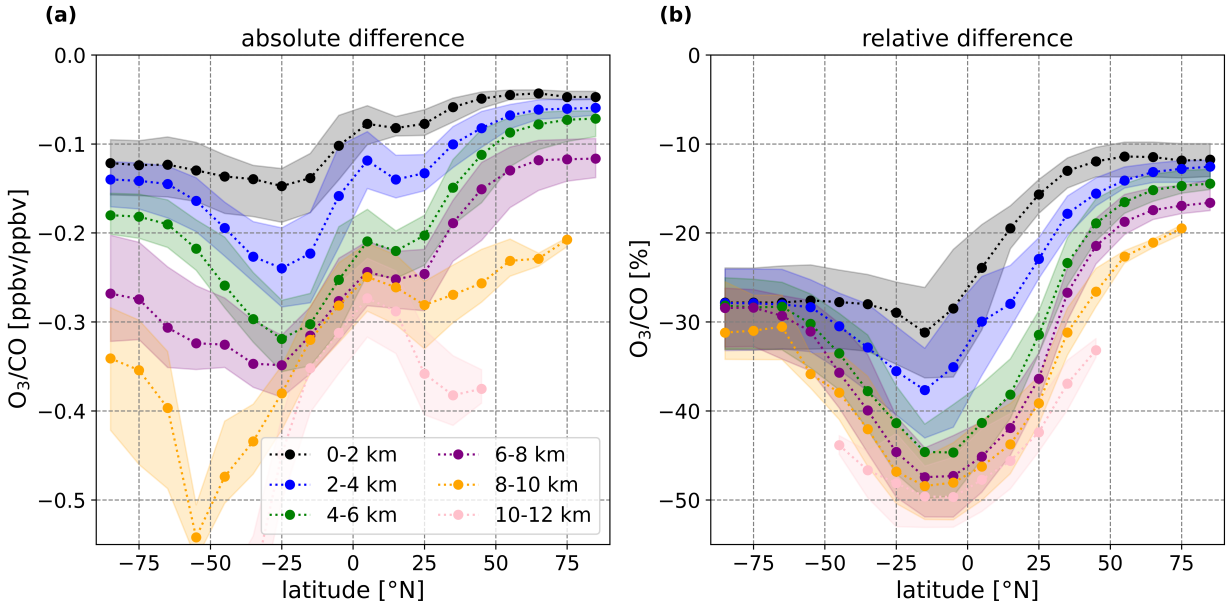

Figure S5. Modeled global zonal gradients of the absolute (a) and the relative (b) difference of the standard simulation and the sensitivity run excluding LNO_x, created by the EMAC model, averaged over all longitudes, 10° of latitude, and 2 km of altitude. Dots represent medians as dots and the 25th and 75th percentiles are represented as shaded areas. Before the calculations, stratospheric values were filtered out by excluding all data points above 100 ppbv of O_3, according to Prather et al. (2011). The calculation of the relative and absolute differences can be found in the main study.

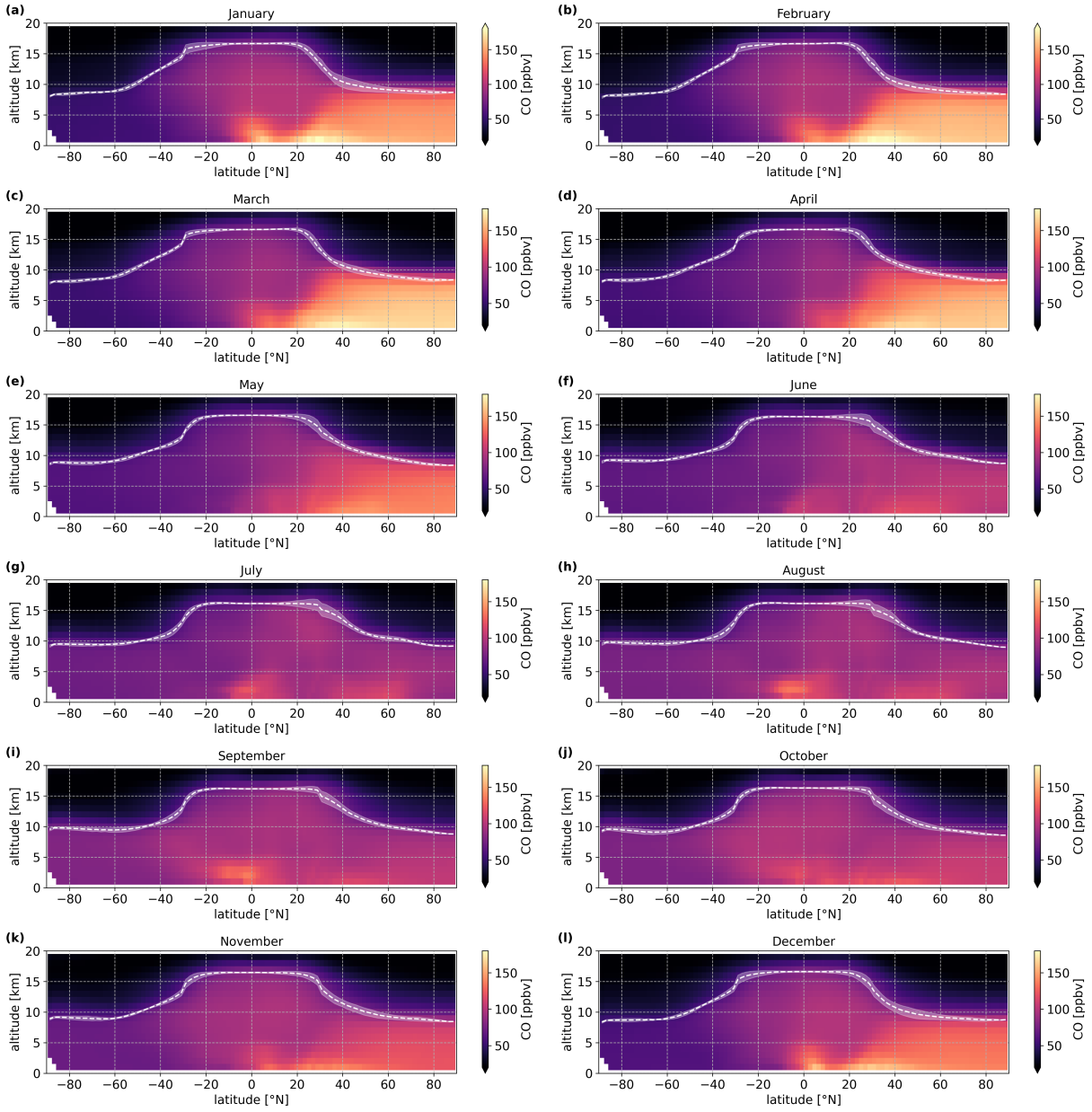

Figure S6. Modeled global zonal distributions of CO over all months including January (a), February (b), March (c), April (d), May (e), June (f), July (g), August (h), September (i), October (j), November (k), and December (l), created by the EMAC model data (standard simulation), averaged over all longitudes, 1 km of altitude, and 1.875° of latitude. Displayed are the mean values. The scale has been adjusted to represent tropospheric values. The white dotted line represents the height of the tropopause with standard deviation derived by averaging over the longitudes.

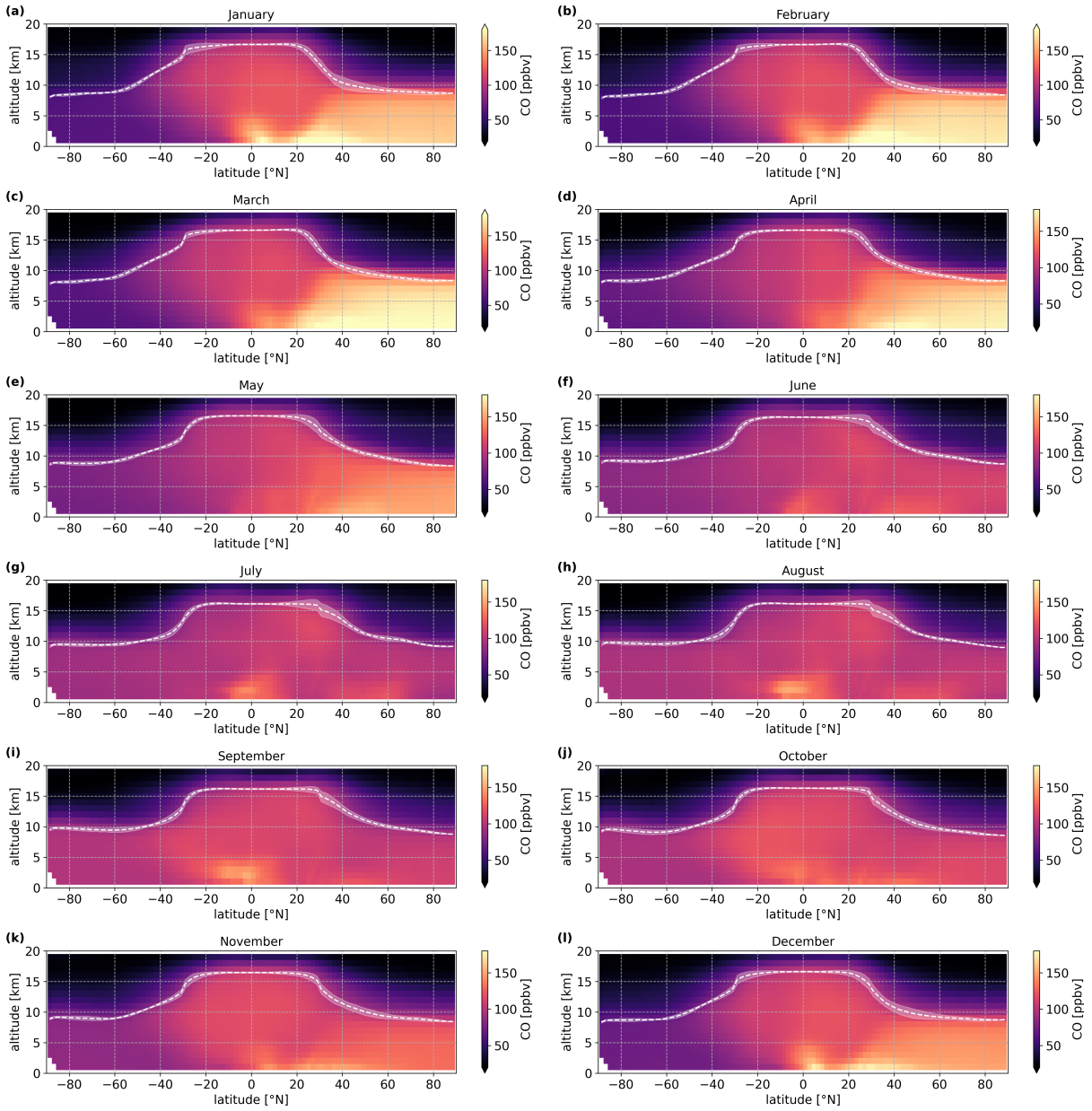

Figure S7. Same as Figure S6, for the sensitivity run excluding LNO_x.

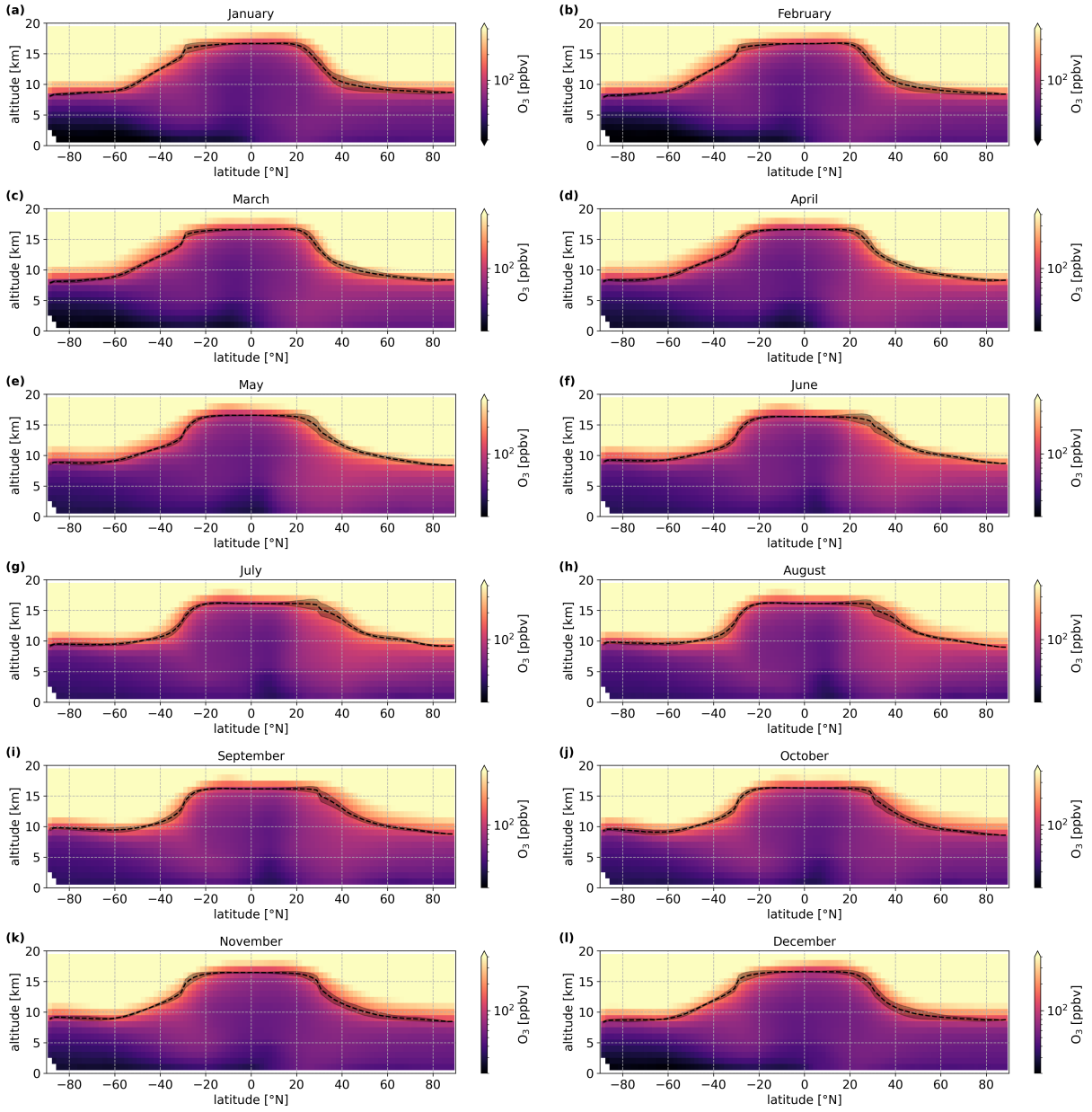

Figure S8. Modeled global zonal distributions of O_3 over all months including January (a), February (b), March (c), April (d), May (e), June (f), July (g), August (h), September (i), October (j), November (k), and December (l), created by the EMAC model data (standard simulation), averaged over all longitudes, 1 km of altitude, and 1.875° of latitude. Displayed are the mean values. The scale has been adjusted to represent tropospheric values. The black dotted line represents the height of the tropopause with standard deviation derived by averaging over the longitudes.

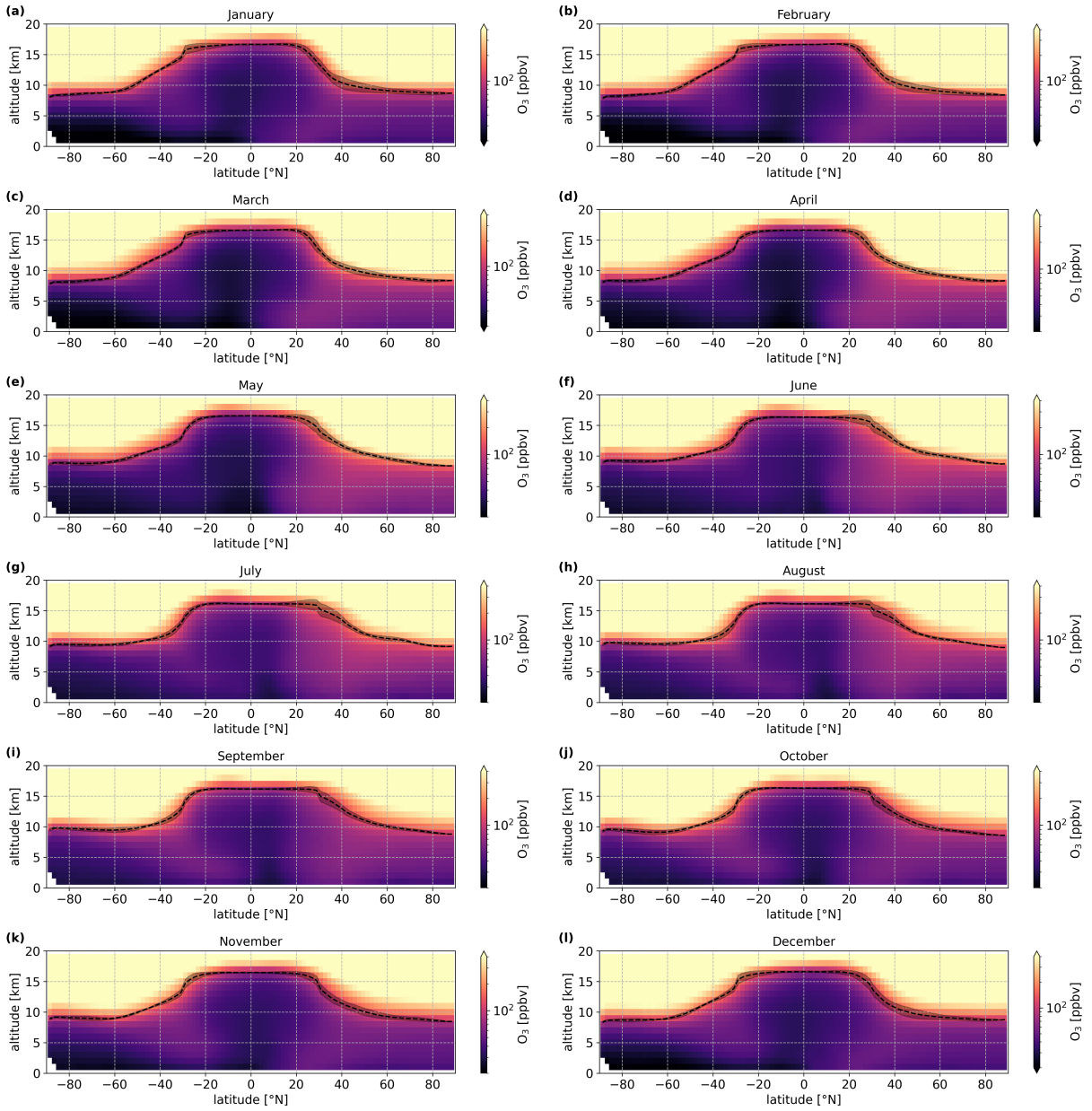

Figure S9. Same as Figure S8, for the sensitivity run excluding LNO_x.

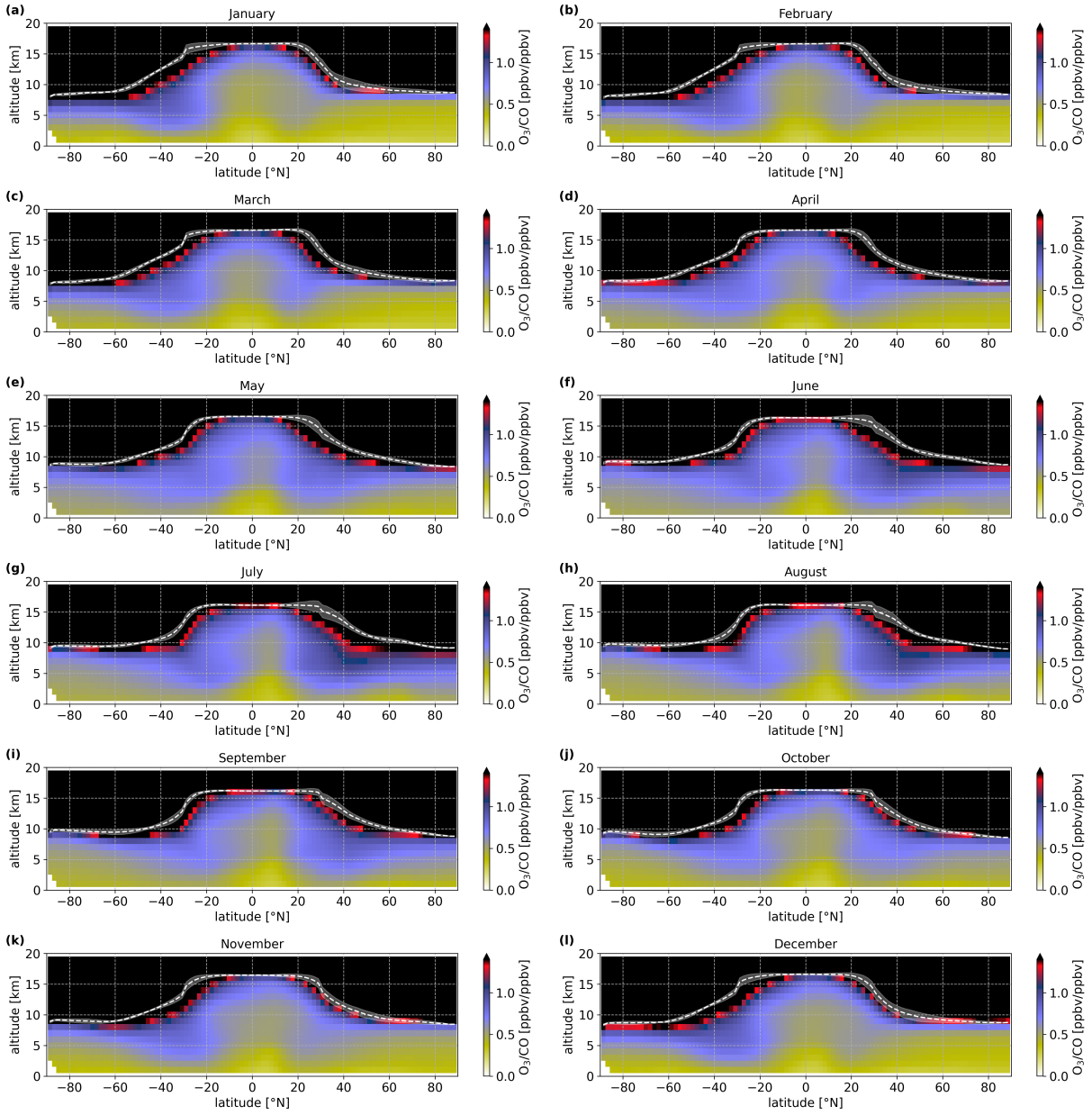

Figure S10. Modeled global zonal distributions of the $O_3 - CO$ ratio of the sensitivity run without LNO_x over all months including January (a), February (b), March (c), April (d), May (e), June (f), July (g), August (h), September (i), October (j), November (k), and December (l), created by the EMAC model data (standard simulation), averaged over all longitudes, 1 km of altitude, and 1.875° of latitude. Displayed are the mean values. The scale has been adjusted to represent tropospheric values. The white dotted line represents the height of the tropopause with standard deviation derived by averaging over the longitudes.

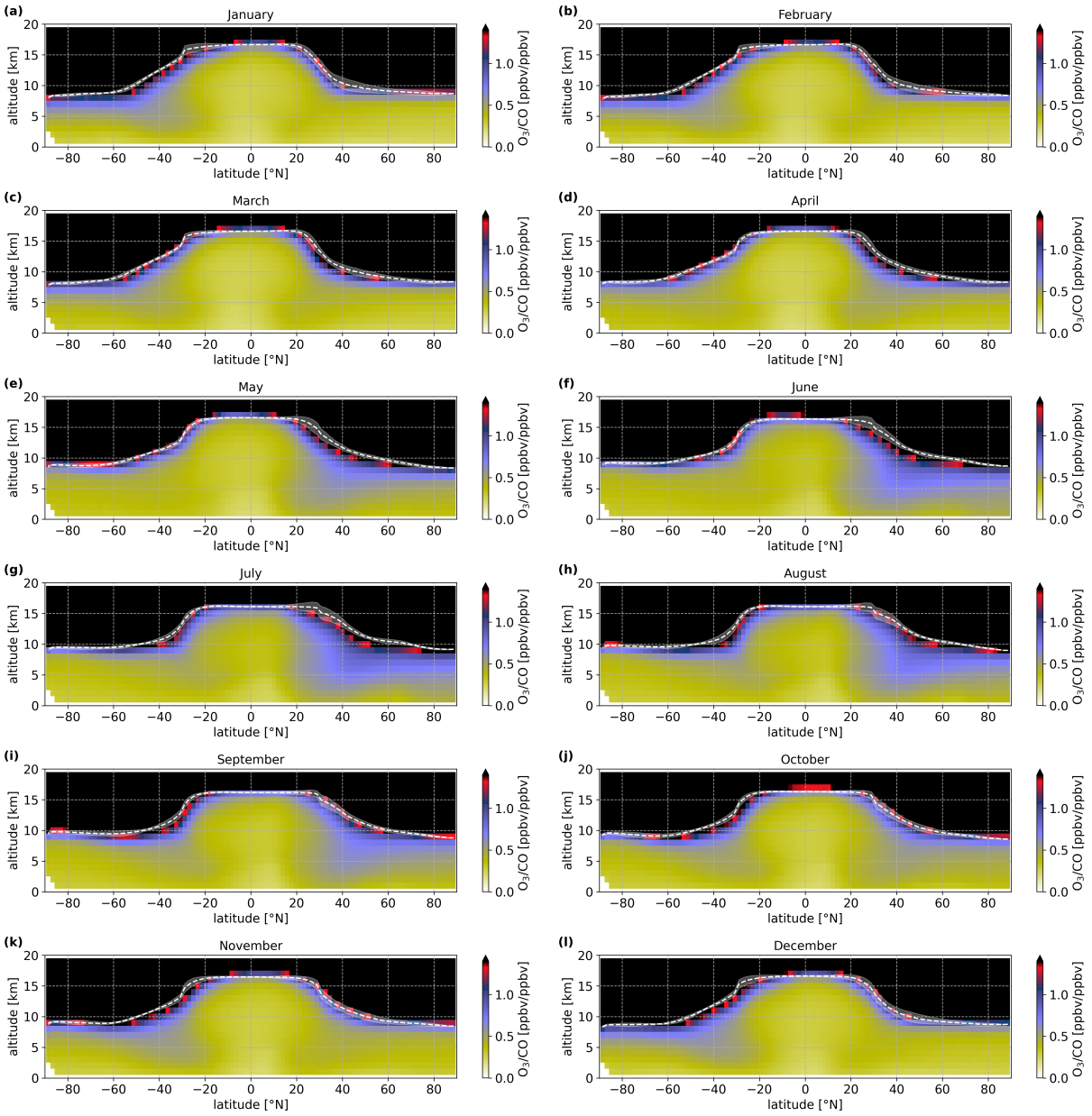

Figure S11. Same as Figure S10, for the sensitivity run excluding LNO_x.

References

Appenzeller, C., Holton, J. R., and Rosenlof, K. H.: Seasonal variation of mass transport across the tropopause, Journal of Geophysical Research: Atmospheres, 101, 15 071–15 078, https://doi.org/https://doi.org/10.1029/96JD00821, 1996.

Bartolome Garcia, I., Spang, R., Ungermann, J., Griessbach, S., Krämer, M., Höpfner, M., and Riese, M.: Observation of cirrus clouds with GLORIA during the WISE campaign: detection methods and cirrus characterization, Atmospheric Measurement Techniques, 14, 3153–3168, https://doi.org/10.5194/amt-14-3153-2021, 2021.

Bourgeois, I., Peischl, J., Thompson, C. R., Aikin, K. C., Campos, T., Clark, H., Commane, R., Daube, B., Diskin, G. W., Elkins, J. W., Gao, R.-S., Gaudel, A., Hintsa, E. J., Johnson, B. J., Kivi, R., McKain, K., Moore, F. L., Parrish, D. D., Querel, R., Ray, E., Sánchez, R., Sweeney, C., Tarasick, D. W., Thompson, A. M., Thouret, V., Witte, J. C., Wofsy, S. C., and Ryerson, T. B.: Global-scale distribution of ozone in the remote troposphere from the ATom and HIPPO airborne field missions, Atmospheric Chemistry and Physics, 20, 10 611–10 635, https://doi.org/10.5194/acp-20-10611-2020, 2020.

Bourgeois, I., Peischl, J., Neuman, J. A., Brown, S. S., Thompson, C. R., Aikin, K. C., Allen, H. M., Angot, H., Apel, E. C., Baublitz, C. B., Breweri, J. F., Campuzano-Josta, P., Commane, R., Crounse, J. D., Daube, B. C., DiGangi, J. P., Diskin, G. S., Emmons, L. K., Fiore, A. M., Gkatzelis, G. I., Hills, A., Hornbrook, R. S., Huey, L. G., Jimenez, J. L., Kim, M., Lacey, F., McKain, K., Murray, L. T., Nault, B. A., Parrish, D. D., Ray, E., Sweeney, Colmand Tanner, D., Wofsy, S. C., and Ryerson, T. B.: Large contribution of biomass burning emissions to ozone throughout the global remote troposphere, Proceedings of the National Academy of Sciences, 118, e2109628 118, https://doi.org/10.1073/pnas.2109628118, 2021.

Chiu, R., Obersteiner, F., Franchin, A., Campos, T., Bailey, A., Webster, C., Zahn, A., and Volkamer, R.: Intercomparison of fast airborne ozone instruments to measure eddy covariance fluxes: spatial variability in deposition at the ocean surface and evidence for cloud processing, Atmospheric Measurement Techniques, 17, 5731–5746, https://doi.org/10.5194/amt-17-5731-2024, 2024.

DLR: HALO data, base, ESMVal mission [data set], https://halo-db.pa.op.dlr.de/mission/14, last access: 18 June 2024, 2012.

DLR: HALO data base, OMO mission [data set], https://halo-db.pa.op.dlr.de/mission/0, last access: 18 June 2024, 2015.

DLR: HALO data, base, WISE mission [data set], https://halo-db.pa.op.dlr.de/mission/96, last access: 18 June 2024, 2017.

DLR: HALO data, base, CAFE Africa [data set], https://halo-db.pa.op.dlr.de/mission/98, last access: 18 June 2024, 2018.

DLR: HALO data, base, SouthTRAC mission [data set], https://halo-db.pa.op.dlr.de/mission/116, last access: 18 June 2024, 2019.

DLR: HALO data, base, CAFE Brazil [data set], https://halo-db.pa.op.dlr.de/mission/135, last access: 18 June 2024, 2023a.

DLR: HALO data, base, PHILEAS mission [data set], https://halo-db.pa.op.dlr.de/mission/138, last access: 18 June 2024, 2023b.

DLR: HALO data, base, CAFE Pacific [data set], https://halo-db.pa.op.dlr.de/mission/140, last access: 23 December 2024, 2024.

Hottmann, B., Hafermann, S., Tomsche, L., Marno, D., Martinez, M., Harder, H., Pozzer, A., Neumaier, M., Zahn, A., Bohn, B., et al.: Impact of the South Asian monsoon outflow on atmospheric hydroperoxides in the upper troposphere, Atmospheric chemistry and physics, 20, 12 655–12 673, https://doi.org/10.5194/acp-20-12655-2020, 2020.

Jöckel, P., Tost, H., Pozzer, A., Kunze, M., Kirner, O., Brenninkmeijer, C. A. M., Brinkop, S., Cai, D. S., Dyroff, C., Eckstein, J., Frank, F., Garny, H., Gottschaldt, K.-D., Graf, P., Grewe, V., Kerkweg, A., Kern, B., Matthes, S., Mertens, M., Meul, S., Neumaier, M., Nützel, M., Oberländer-Hayn, S., Ruhnke, R., Runde, T., Sander, R., Scharffe, D., and Zahn, A.: Earth system chemistry integrated modelling (ESCiMo) with the modular earth submodel system (MESSy) version 2.51, Geoscientific Model Development, 9, 1153–1200, https://doi.org/10.5194/gmd-9-1153-2016, 2016.

Krasauskas, L., Ungermann, J., Preusse, P., Friedl-Vallon, F., Zahn, A., Ziereis, H., Rolf, C., Ploeger, F., Konopka, P., Vogel, B., and Riese, M.: 3-D tomographic observations of Rossby wave breaking over the Northern Atlantic during the WISE aircraft campaign in 2017, Atmospheric Chemistry and Physics Discussions, 2020, 1–30, https://doi.org/10.5194/acp-21-10249-2021, 2020.

Kunkel, D., Hoor, P., Kaluza, T., Ungermann, J., Kluschat, B., Giez, A., Lachnitt, H.-C., Kaufmann, M., and Riese, M.: Evidence of small-scale quasi-isentropic mixing in ridges of extratropical baroclinic waves, Atmospheric Chemistry and Physics, 19, 12 607–12 630, https://doi.org/10.5194/acp-19-12607-2019, 2019.

McManus, J. B., Zahniser, M. S., Jr., D. D. N., Shorter, J. H., Herndon, S. C., Wood, E. C., and Wehr, R.: Application of quantum cascade lasers to high-precision atmospheric trace gas measurements, Optical Engineering, 49, 111 124, https://doi.org/10.1117/1.3498782, 2010.

Müller, S., Hoor, P., Berkes, F., Bozem, H., Klingebiel, M., Reutter, P., Smit, H., Wendisch, M., Spichtinger, P., and Borrmann, S.: In situ detection of stratosphere-troposphere exchange of cirrus particles in the midlatitudes, Geophysical research letters, 42, 949–955, https://doi.org/10.1002/2014GL062556, 2015.

Müller, S., Hoor, P., Bozem, H., Gute, E., Vogel, B., Zahn, A., Bönisch, H., Keber, T., Krämer, M., Rolf, C., et al.: Impact of the Asian monsoon on the extratropical lower stratosphere: trace gas observations during TACTS over Europe 2012, Atmospheric chemistry and physics, 16, 10 573–10 589, https://doi.org/10.5194/acp-16-10573-2016, 2016.

Ort, L., Röder, L. L., Parchatka, U., Königstedt, R., Crowley, D., Kunz, F., Wittkowski, R., Lelieveld, J., and Fischer, H.: In-flight characterization of a compact airborne quantum cascade laser absorption spectrometer, Atmospheric Measurement Techniques, 17, 3553–3565, https://doi.org/10.5194/amt-17-3553-2024, 2024.

Prather, M. J., Zhu, X., Tang, Q., Hsu, J., and Neu, J. L.: An atmospheric chemist in search of the tropopause, Journal of Geophysical Research: Atmospheres, 116, https://doi.org/https://doi.org/10.1029/2010JD014939, 2011.

Rapp, M., Martin, R., Sinnhuber, B.-M., Hoor, P., and Engel, A.: SouthTRAC mission website, https://www.pa.op.dlr.de/southtrac/home/science/scientific-objectives/, last access: 13 June 2024, 2019.

Rapp, M., Kaifler, B., Dörnbrack, A., Gisinger, S., Mixa, T., Reichert, R., Kaifler, N., Knobloch, S., Eckert, R., Wildmann, N., Giez, A., Krasauskas, L., Preusse, P., Geldenhuys, M., Riese, M., Woiwode, W., Friedl-Vallon, F., Sinnhuber, B.-M., de la Torre, A., Alexander, P., Hormaechea, J. L., Janches, D., Garhammer, M., Chau, J. L., Conte, J. F., Hoor, P., and Engel, A.: SOUTHTRAC-GW: An airborne field campaign to explore gravity wave dynamics at the world's strongest hotspot, Bulletin of the American Meteorological Society, 102, E871–E893, https://doi.org/10.1175/BAMS-D-20-0034.1, 2021.

Ridley, B., Grahek, F., and Walega, J.: A small high-sensitivity, medium-response ozone detector suitable for measurements from light aircraft, Journal of Atmospheric and Oceanic Technology, 9, 142–148, https://doi.org/10.1175/1520-0426(1992)009<0142:ASHSMR>2.0.CO;2, 1992.

Riese, M., K. M. and Hoor, P.: WISE: project description, https://www.halo.dlr.de/science/missions/wise/wise.html, last access: 15 July 2024, 2017.

Röder, L. L., Ort, L., Lelieveld, J., and Fischer, H.: Quantitative analysis of temporal stability and instrument performance during field experiments of an airborne QCLAS via Allan–Werle-plots, Applied Physics B, 130, 118, https://doi.org/10.1007/s00340-024-08254-5, 2024.

Rolf, C., Afchine, A., Bozem, H., Buchholz, B., Ebert, V., Guggenmoser, T., Hoor, P., Konopka, P., Kretschmer, E., Müller, S., Schlager, H., Spelten, N., Suminska-Ebersoldt, O., Ungermann, J., Zahn, A., and Krämer, M.: Transport of Antarctic stratospheric strongly dehydrated air into the troposphere observed during the HALO-ESMVal campaign 2012, Atmospheric chemistry and physics, 15, 9143–9158, https://doi.org/10.5194/acp-15-9143-2015, 2015.

Santoni, G., Daube, B. C., Kort, E., Jiménez, R., Park, S., Pittman, J., Gottlieb, E., Xiang, B., Zahniser, M., Nelson, D., et al.: Evaluation of the airborne quantum cascade laser spectrometer (QCLS) measurements of the carbon and greenhouse gas suite–CO 2, CH 4, N 2 O, and CO–during the CalNex and HIPPO campaigns, Atmospheric Measurement Techniques, 7, 1509–1526, https://doi.org/10.5194/amt-7-1509-2014, 2014.

Schiller, C., Bozem, H., Gurk, C., Parchatka, U., Königstedt, R., Harris, G., Lelieveld, J., and Fischer, H.: Applications of quantum cascade lasers for sensitive trace gas measurements of CO, CH_4, N_2O and HCHO, Applied Physics B, 92, 419–430, https://doi.org/10.1007/s00340-008-3125-0, 2008.

Schumann, U. and Huntrieser, H.: The global lightning-induced nitrogen oxides source, Atmospheric Chemistry and Physics, 7, 3823–3907, https://doi.org/10.5194/acp-7-3823-2007, 2007.

Strode, S. A., Liu, J., Lait, L., Commane, R., Daube, B., Wofsy, S., Conaty, A., Newman, P., and Prather, M.: Forecasting carbon monoxide on a global scale for the ATom-1 aircraft mission: insights from airborne and satellite observations and modeling, Atmospheric Chemistry and Physics, 18, 10 955–10 971, https://doi.org/10.5194/acp-18-10955-2018, 2018.

Tadic, I., Parchatka, U., Königstedt, R., and Fischer, H.: In-flight stability of quantum cascade laser-based infrared absorption spectroscopy measurements of atmospheric carbon monoxide, Applied Physics B, 123, 1–9, https://doi.org/10.1007/s00340-017-6721-z, 2017.

Tadic, I., Nussbaumer, C. M., Bohn, B., Harder, H., Marno, D., Martinez, M., Obersteiner, F., Parchatka, U., Pozzer, A., Rohloff, R., et al.: Central role of nitric oxide in ozone production in the upper tropical troposphere over the Atlantic Ocean and western Africa, Atmospheric Chemistry and Physics, 21, 8195–8211, https://doi.org/10.5194/acp-21-8195-2021, 2021.

Thompson, C. R., Wofsy, S. C., Prather, M. J., Newman, P. A., Hanisco, T. F., Ryerson, T. B., Fahey, D. W., Apel, E. C., Brock, C. A., Brune, W. H., Froyd, K., Katich, J. M., Nicely, J. M., Peischl, J., Ray, E., Veres, P. R., Wang, S., Allen, H. M., Asher, E., Bian, H., Blake, D., Bourgeois, I., Budney, J., Bui, T. P., Butler, A., Campuzano-Jost, P., Chang, C., Chin, M., Commane, R., Correa, G., Crounse, J. D., Daube, B., Dibb, J. E., DiGangi, J. P., Diskin, G. S., Dollner, M., Elkins, J. W., Fiore, A. M., Flynn, C. M., Guo, H., Hall, S. R., Hannun, R. A., Hills, A., Hintsa, E. J., Hodzic, A., Hornbrook, R. S., Huey, L. G., Jimenez, J. L., Keeling, R. F., Kim, M. J., Kupc, A., Lacey, F., Lait, L. R., Lamarque, J.-F., Liu, J., McKain, K., Meinardi, S., Miller, D. O., Montzka, S. A., Moore, F. L., Morgan, E. J., Murphy, D. M., Murray, L. T., Nault, B. A., Neuman, J. A., Nguyen, L., Gonzalez, Y., Rollins, A., Rosenlof, K., Sargent, M., Schill, G., Schwarz, J. P., Clair, J. M. S., Steenrod, S. D., Stephens, B. B., Strahan, S. E., Strode, S. A., Sweeney, C., Thames, A. B., Ullmann, K., Wagner, N., Weber, R., Weinzierl, B., Wennberg, P. O., Williamson, Christina J. amd Wolfe, G. M., and Zeng, L.: The NASA Atmospheric Tomography (ATom) mission: Imaging the chemistry of the global atmosphere, Bulletin of the American Meteorological Society, 103, E761–E790, https://doi.org/10.1175/BAMS-D-20-0315.1, 2022.

Tomsche, L., Pozzer, A., Ojha, N., Parchatka, U., Lelieveld, J., and Fischer, H.: Upper tropospheric CH 4 and CO affected by the South Asian summer monsoon during the Oxidation Mechanism Observations mission, Atmospheric Chemistry and Physics, 19, 1915–1939, https://doi.org/10.5194/acp-19-1915-2019, 2019.

White, J. U.: Optical system providing a long optical path, last access: 24 June 2024, uS Patent 2,779,230, 1957.

Wienhold, F., Fischer, H., Hoor, P., Wagner, V., Königstedt, R., Harris, G., Anders, J., Grisar, R., Knothe, M., Riedel, W., Libken, F.-J., and Schilling, T.: TRISTAR-A tracer in-situ TDLAS for atmospheric research, Applied Physics B, 67, 411–417, https://doi.org/10.1007/s003400050524, 1998.

Wofsy, S., Afshar, S., Allen, H., Apel, E., Asher, E., Barletta, B., Bent, J., Bian, H., Biggs, B., Blake, D., et al.: ATom: Merged atmospheric chemistry, trace gases, and aerosols, ORNL DAAC, https://doi.org/10.3334/ORNLDAAC/1581, 2018.

Zahn, A., Weppner, J., Widmann, H., Schlote-Holubek, K., Burger, B., Kühner, T., and Franke, H.: A fast and precise chemiluminescence ozone detector for eddy flux and airborne application, Atmospheric Measurement Techniques, 5, 363–375, https://doi.org/https://doi.org/10.5194/amt-5-363-2012, 2012.

4 Conclusions & Outlook

This thesis presented a comprehensive investigation of atmospheric composition using airborne in-situ observations, addressing challenges that span instrument development, regional-scale surface emissions, and atmospheric transport and chemistry. By combining computational tools with in-situ observations and modeling, this work contributes to the improved understanding of trace gas emissions and transport and their chemical interactions, with a focus on the troposphere.

A newly developed infrared quantum cascade laser absorption spectrometer has been introduced and characterized in its airborne performance. During its first successful campaign, strong enhancements in lower altitudes of CH_4 mixing ratios above the Amazon were found. Those measurements were compared to model simulations, which could not represent the observed enhancement. Together with a transport model and an inversion approach, the measurements were linked to prior surface emissions, which then could be improved by the observations. The results showed strong underestimations of CH_4 emissions in the vicinity of large river beds, reservoirs, and extensive river deltas in the Amazon region. Finally, a combined data set of twelve aircraft missions revealed a strong enhancement in the O_3 – CO ratio in the northern subtropical troposphere. Comparisons with the EMAC model showed similar features in the O_3 – CO ratio. Therefore, the model was used to perform a sensitivity study excluding lightning NO_x emissions, which showed a strong influence on the global O_3 – CO ratio distribution, mainly transported from the upper tropical troposphere via the Hadley circulation into the subtropics.

Building on the results presented in this thesis, future research can further expand the capabilities of airborne in-situ observations to address remaining uncertainties in atmospheric composition, surface emissions, and tropospheric transport. High precision and high-resolution observations in remote regions are crucial to improve chemistry-transport models and emission inventories. Further enhancing the robustness and sensitivity of airborne infrared spectrometer under rapidly changing environmental conditions is key in providing valuable data. In particular, more airborne performance characterization, as shown in Ort et al., 2024, would further quantify systematic uncertainties on such extreme platforms and could facilitate harmonization in precision across the variety of absorption spectrometers.

Additionally, future work could move towards a stronger integrated observing–modeling system for the tropical troposphere. Coordinated airborne campaigns in conjunction with satellite observations (e.g., TROPOMI, or future satellite missions) would enable a multi-scale evaluation of not only methane emission hotspots. Improvements in the temporal and spatial resolution of satellite data, by stationary satellite missions, or higher spatial resolution able to capture small cloud-free regions in between deep-convective cells, could capture the variability of emissions in more detail. Achieving more data in high emission regions would be beneficial in exploring contributions of different soil and vegetation properties in the carbon budget, which could be embedded into global models. Particularly in tropical ecosystems, such as the Amazon or the Congo Basin, extension in surface networks are limited by the remoteness and political or institutional constraints. Therefore, sustained satellite and airborne monitoring could cover such regions to provide critical constraints on climate-biosphere feedbacks under ongoing land-use change and warming.
The inversion results presented in Section 3.5 also indicate land-cover-dependent adjustments of methane fluxes in the Amazon region, highlighting the importance of ecosystem-specific emission processes. Future studies should explore temporally resolved inversions to assess seasonal variability and extreme-event impacts (e.g., droughts, flooding, fire). Coupling the inversion framework with process-based wetland or biogeochemical models may help disentangle anthropogenic and natural contributions. Furthermore, extending the approach to multi-species inversions (e.g., CH_4-CO joint optimization) could reduce posterior uncertainties and strengthen constraints on emission sector attribution.
Moreover, tropospheric transport and mixing are crucial to trace gas distributions and chemical interactions. Ort et al., 2025 showed the importance of intertropospherical transport and photochemistry mainly influenced by lightning emissions, not only on the trace gas distribution of the troposphere, but also, to some extent, on the UTLS. In a changing climate, lightning activity is expected to increase (Schumann and Huntrieser, 2007), and so is stratosphere-troposphere exchange (STE) (Hegglin and Shepherd, 2009). Increasing lightning activity influences the oxidative capacity of the atmosphere, wildfire activity, and ozone production (e.g., Finney et al., 2018; Pérez-Invernón et al., 2023). Increasing stratosphere-troposphere exchange enhances the downward transport of ozone-rich, dry, high-PV air into the troposphere, thereby increasing upper tropospheric ozone concentrations, modifying oxidative capacity, influencing humidity and cloud formation, and potentially affecting surface air quality and climate forcing (Hegglin and Shepherd, 2009). Therefore, the changing effect and the contribution via those two different pathways studied in Ort et al., 2025 on trace- and greenhouse gases is important to investigate for future scenarios. Another major source of uncertainty in chemistry-

transport models arises from the representation of deep convection and vertical transport, particularly in tropical regions. Rapid convective uplift strongly affects the redistribution of trace gases and can introduce biases in modeled concentrations and inferred surface fluxes. Future work should therefore focus on improving convective parameterizations in chemistry–transport models, for example, through higher temporal and spatial resolution simulations and observational constraints from airborne vertical profiles. Moreover, the study Ort et al., 2025 has directed to another important source of NO_x, which contributes to STE and tropical photochemistry by conditioning the subtropics. High latitude wildfires produce large amounts of PAN, which could be another important source of NO_x in the subtropics, which future work could investigate.

In summary, this thesis combines instrumental characterization, emission inversion, and process-based analysis to provide a comprehensive perspective on the drivers of tropospheric composition. The careful evaluation of measurement performance establishes the reliability and precision required for airborne trace gas observations. Building upon this foundation, inverse modeling enables the quantification of regional emissions and highlights discrepancies in current inventories. Finally, the analysis of photochemical and dynamical conditioning demonstrates that trace gas distributions are not solely controlled by emissions, but emerge from the interplay between chemical transformation and atmospheric transport, particularly in dynamically active regions.
Altogether, these results underline that understanding atmospheric composition requires an integrated framework linking measurement accuracy, emission constraints, and dynamical-chemical coupling. With climate-driven changes in circulation and chemistry, process-based approaches are crucial for reliable interpretation and prediction of atmospheric composition.

Bibliography

(DLR), G. A. C. (2017). *HALO database [data set], last update: 1 October 2020*. last access: 18 June 2024. URL: https://doi.org/10.17616/R39Q0T.

Abdu, M. A., D. Pancheva, and A. Bhattacharyya (2011). **Aeronomy of the Earth's Atmosphere and Ionosphere**. Springer.

Adam, O., T. Bischoff, and T. Schneider (2016). **Seasonal and interannual variations of the energy flux equator and ITCZ. Part I: Zonally averaged ITCZ position**. *Journal of Climate* 29:9, 3219–3230. DOI: 10.1175/JCLI-D-15-0512.1.

Ainsworth, E. A., C. R. Yendrek, S. Sitch, W. J. Collins, and L. D. Emberson (2012). **The effects of tropospheric ozone on net primary productivity and implications for climate change**. *Annual review of plant biology* 63, 637–661. DOI: 10.1146/annurev-arplant-042110-103829.

Andreae, M. O., P. Artaxo, V. Beck, M. Bela, S. Freitas, C. Gerbig, K. Longo, J. W. Munger, K. T. Wiedemann, and S. C. Wofsy (2012). **Carbon monoxide and related trace gases and aerosols over the Amazon Basin during the wet and dry seasons**. *Atmospheric Chemistry and Physics* 12:13, 6041–6065. DOI: 10.5194/acp-12-6041-2012. URL: https://acp.copernicus.org/articles/12/6041/2012/.

Andrews, D. G. (2010). **An introduction to atmospheric physics**. Cambridge University Press.

Andrews, D. G., C. B. Leovy, and J. R. Holton (1987). **Middle atmosphere dynamics**. Vol. 40. Academic press.

Bacsik, Z., J. Mink, and G. Keresztury (2004). **FTIR Spectroscopy of the Atmosphere. I. Principles and Methods**. *Applied Spectroscopy Reviews* 39:3, 295–363. DOI: 10.1081/ASR-200030192. eprint: https://doi.org/10.1081/ASR-200030192. URL: https://doi.org/10.1081/ASR-200030192.

Balasus, N., D. J. Jacob, A. A. Bloom, J. D. East, L. A. Estrada, S. E. Hancock, M. He, T. A. Mooring, A. J. Turner, and J. R. Worden (2026). **2019–2024 trends in African livestock and wetland emissions as contributors to the global methane rise**. *EGUsphere* 2026. preprint, 1–30. DOI: 10.5194/egusphere-2025-6251. URL: https://egusphere.copernicus.org/preprints/2026/egusphere-2025-6251/.

Basso, L. S., L. Marani, L. V. Gatti, J. B. Miller, M. Gloor, J. Melack, H. L. Cassol, G. Tejada, L. G. Domingues, E. Arai, A. H. Sanchez, S. M. Corrêa, L. Anderson, L. E. O. C. Aragão, C. S. C. Correia, S. P. Crispim, and R. A. L. Neves (2021). **Amazon methane budget derived from multi-year airborne observations highlights regional variations in emissions**. *Communications Earth & Environment* 2:1, 246. DOI: 10.1038/s43247-021-00314-4.

Bauchinger, S., A. Engel, M. Jesswein, T. Keber, H. Bönisch, F. Obersteiner, A. Zahn, N. Emig, P. Hoor, H.-C. Lachnitt, F. Weyland, L. Ort, and T. J. Schuck (2025). **The extratropical tropopause – trace gas perspective on tropopause definition choice**. *Atmospheric Chemistry and Physics* 25:21, 14167–14186. DOI: 10.5194/acp-25-14167-2025. URL: https://acp.copernicus.org/articles/25/14167/2025/.

Belikov, D. A., N. Saitoh, and P. K. Patra (2022). **An Analysis of Interhemispheric Transport Pathways Based on Three-Dimensional Methane Data by GOSAT Observations and Model Simulations**. *Journal of Geophysical Research: Atmospheres* 127:14. e2021JD035688 2021JD035688, e2021JD035688. DOI: https://doi.org/10.1029/2021JD035688. eprint: https://agupubs.onlinelibrary.wiley.com/doi/pdf/10.1029/2021JD035688. URL: https://agupubs.onlinelibrary.wiley.com/doi/abs/10.1029/2021JD035688.

Berden, G. and R. Engeln (2009). **Cavity Ring-Down Spectroscopy: Techniques and Applications**. Wiley. ISBN: 9781444308242. URL: https://books.google.de/books?id=5jQM88VYwzQC.

Berden, G., R. Peeters, and G. Meijer (2000). **Cavity ring-down spectroscopy: Experimental schemes and applications**. *International Reviews in Physical Chemistry* 19:4, 565–607. DOI: 10.1080/014423500750040627. eprint: https://doi.org/10.1080/014423500750040627. URL: https://doi.org/10.1080/014423500750040627.

Bloom, A. A., K. W. Bowman, M. Lee, A. J. Turner, R. Schroeder, J. R. Worden, R. Weidner, K. C. McDonald, and D. J. Jacob (2017). **A global wetland methane emissions and uncertainty dataset for atmospheric chemical transport models (WetCHARTs version 1.0)**. *Geoscientific Model Development* 10:6, 2141–2156. DOI: 10.5194/gmd-10-2141-2017. URL: https://gmd.copernicus.org/articles/10/2141/2017/.

Boljka, L. and T. Birner (2020). **Tropopause-level planetary wave source and its role in two-way troposphere–stratosphere coupling**. *Weather and Climate Dynamics* 1:2, 555–575. DOI: 10.5194/wcd-1-555-2020. URL: https://wcd.copernicus.org/articles/1/555/2020/.

Bourgeois, I., J. Peischl, J. A. Neuman, S. S. Brown, C. R. Thompson, K. C. Aikin, H. M. Allen, H. Angot, E. C. Apel, C. B. Baublitz, J. F. Breweri, P. Campuzano-Josta, R. Commane, J. D. Crounse, B. C. Daube, J. P. DiGangi, G. S. Diskin, L. K. Emmons, A. M. Fiore, G. I. Gkatzelis, A. Hills, R. S. Hornbrook, L. G. Huey, J. L. Jimenez, M. Kim, F. Lacey, K. McKain, L. T. Murray, B. A. Nault, D. D. Parrish, E. Ray, D. Sweeney Colmand Tanner, S. C. Wofsy, and T. B. Ryerson (2021). **Large contribution of biomass burning emissions to ozone throughout the global remote troposphere**. *Proceedings of the National Academy of Sciences* 118:52, e2109628118. DOI: 10.1073/pnas.2109628118.

Brasseur, G. P., J. J. Orlando, and G. S. Tyndall (1999). **Atmospheric chemistry and global change**. Vol. 654. Oxford University Press New York.

Brewer, A. W. (1949). **Evidence for a world circulation provided by the measurements of helium and water vapour distribution in the stratosphere**. *Quarterly Journal of the Royal Meteorological Society* 75:326, 351–363. DOI: https://doi.org/10.1002/

qj.49707532603. eprint: https://rmets.onlinelibrary.wiley.com/doi/pdf/10.1002/qj.49707532603. URL: https://rmets.onlinelibrary.wiley.com/doi/abs/10.1002/qj.49707532603.

Caldwell, M. M., L. O. Björn, J. F. Bornman, S. D. Flint, G. Kulandaivelu, A. H. Teramura, and M. Tevini (1998). **Effects of increased solar ultraviolet radiation on terrestrial ecosystems**. *Journal of Photochemistry and Photobiology B: Biology* 46:1-3, 40–52. DOI: 10.1016/S1011-1344(98)00184-5. URL: https://doi.org/10.1016/S1011-1344(98)00184-5.

Chapman, S. (1930). **A theory of upper-atmospheric ozone**. *Mem. Roy. Meteor. Soc.* 3, 103–125.

Clerbaux, C., J. Hadji-Lazaro, S. Turquety, G. Mégie, and P.-F. Coheur (2003). **Trace gas measurements from infrared satellite for chemistry and climate applications**. *Atmospheric Chemistry and Physics* 3:5, 1495–1508. DOI: 10.5194/acp-3-1495-2003. URL: https://acp.copernicus.org/articles/3/1495/2003/.

Conrad, R. (1989). **Control of methane production in terrestrial ecosystems**. In: *Exchange of trace gases between terrestrial ecosystems and the atmosphere*. Ed. by M. Andreae and D. Schimel. Vol. 47. Life Science Research Report. Dahlem workshop on exchnage of trace gases between terrestrial ecosystems and the atmosphere, Berlin, Germany, FEB 19-24, 1989. Senate Berlin; Stiftverband Deut Wissensch; Deut Forschungsgemeinsch, 39–58. ISBN: 0-471-92551-9.

Crutzen, P. J. and D. H. Ehhalt (1977). **Effects of nitrogen fertilizers and combustion on the stratospheric ozone layer**. *Ambio*, 112–117. DOI: 4312257.

Crutzen, P. J. and M. O. Andreae (1990). **Biomass Burning in the Tropics: Impact on Atmospheric Chemistry and Biogeochemical Cycles**. *Science* 250:4988, 1669–1678. DOI: 10.1126/science.250.4988.1669. eprint: https://www.science.org/doi/pdf/10.1126/science.250.4988.1669. URL: https://www.science.org/doi/abs/10.1126/science.250.4988.1669.

D'Amato, F., M. Barucci, G. Bianchini, and S. Viciani (June 2025). **Quantum cascade laser (QCL) in airborne atmospheric measurements: a review (Invited)**. *Opt. Express* 33:11, 22745–22754. DOI: 10.1364/OE.558437. URL: https://opg.optica.org/oe/abstract.cfm?URI=oe-33-11-22745.

Danielsen, E. F. (1968). **Stratospheric-Tropospheric Exchange Based on Radioactivity, Ozone and Potential Vorticity**. *Journal of Atmospheric Sciences* 25:3, 502–518. DOI: 10.1175/1520-0469(1968)025<0502:STEBOR>2.0.CO;2. URL: https://journals.ametsoc.org/view/journals/atsc/25/3/1520-0469_1968_025_0502_stebor_2_0_co_2.xml.

Dean, J. F., J. J. Middelburg, T. Röckmann, R. Aerts, L. G. Blauw, M. Egger, M. S. M. Jetten, A. E. E. de Jong, O. H. Meisel, O. Rasigraf, C. P. Slomp, M. H. in't Zandt, and A. J. Dolman (2018). **Methane Feedbacks to the Global Climate System in a Warmer World**. *Reviews of Geophysics* 56:1, 207–250. DOI: https://doi.org/10.1002/2017RG000559. eprint: https://agupubs.onlinelibrary.wiley.com/doi/pdf/10.1002/2017RG000559. URL: https://agupubs.onlinelibrary.wiley.com/doi/abs/10.1002/2017RG000559.

Delmas, R., D. Serça, and C. Jambert (1997). **Global inventory of NOx sources**. *Nutrient Cycling in Agroecosystems* 48:1, 51–60. ISSN: 1573-0867. DOI: 10.1023/A:1009793806086. URL: https://doi.org/10.1023/A:1009793806086.

DLR (2023). *HALO data, base, CAFE Brazil [data set]*. last access: 18 June 2024. URL: https://halo-db.pa.op.dlr.de/mission/135.

Dobson, G. M. B. (1956). **Origin and distribution of the polyatomic molecules in the atmosphere**. *Proceedings of the Royal Society of London. Series A. Mathematical and Physical Sciences* 236:1205, 187–193. DOI: 10.1098/rspa.1956.0127.

Domeisen, D. I. V. and R. A. Plumb (2012). **Traveling planetary-scale Rossby waves in the winter stratosphere: The role of tropospheric baroclinic instability**. *Geophysical Research Letters* 39:20. DOI: https://doi.org/10.1029/2012GL053684. eprint: https://agupubs.onlinelibrary.wiley.com/doi/pdf/10.1029/2012GL053684. URL: https://agupubs.onlinelibrary.wiley.com/doi/abs/10.1029/2012GL053684.

Faist, J., F. Capasso, D. L. Sivco, C. Sirtori, A. L. Hutchinson, and A. Y. Cho (1994). **Quantum cascade laser**. *Science* 264:5158, 553–556. DOI: 10.1126/science.264.5158.553.

Finney, D. L., R. M. Doherty, O. Wild, D. S. Stevenson, I. A. MacKenzie, and A. M. Blyth (2018). **A projected decrease in lightning under climate change**. *Nature Climate Change* 8:3, 210–213. ISSN: 1758-6798. DOI: 10.1038/s41558-018-0072-6.

Fischer, H., F. Wienhold, P. Hoor, O. Bujok, C. Schiller, P. Siegmund, M. Ambaum, H. Scheeren, and J. Lelieveld (2000). **Tracer correlations in the northern high latitude lowermost stratosphere: Influence of cross-tropopause mass exchange**. *Geophysical Research Letters* 27:1, 97–100. DOI: 10.1029/1999GL010879.

Foias, C., O. Manley, R. Temam, and Y. Treve (1983). **Asymptotic analysis of the navier-stokes equations**. *Physica D: Nonlinear Phenomena* 9:1, 157–188. ISSN: 0167-2789. DOI: https://doi.org/10.1016/0167-2789(83)90297-X. URL: https://www.sciencedirect.com/science/article/pii/016727898390297X.

Franco, M. A., L. V. Rizzo, M. J. Teixeira, P. Artaxo, T. Azevedo, J. Lelieveld, C. A. Nobre, C. Pöhlker, U. Pöschl, J. Shimbo, X. Xu, and L. A. T. Machado (2025). **How climate change and deforestation interact in the transformation of the Amazon rainforest**. *Nature Communications* 16:1, 7944. ISSN: 2041-1723. DOI: 10.1038/s41467-025-63156-0. URL: https://doi.org/10.1038/s41467-025-63156-0.

Frey, W., R. Schofield, P. Hoor, D. Kunkel, F. Ravegnani, A. Ulanovsky, S. Viciani, F. D'Amato, and T. P. Lane (2015). **The impact of overshooting deep convection on local transport and mixing in the tropical upper troposphere/lower stratosphere (UTLS)**. *Atmospheric Chemistry and Physics* 15:11, 6467–6486. DOI: 10.5194/acp-15-6467-2015. URL: https://doi.org/10.5194/acp-15-6467-2015.

Fried, A., G. Diskin, P. Weibring, D. Richter, J. Walega, G. Sachse, T. Slate, M. Rana, and J. Podolske (2008). **Tunable infrared laser instruments for airborne atmospheric studies**. *Applied Physics B* 92, 409–417. DOI: 10.1007/s00340-008-3136-x.

Fried, A. and D. Richter (2006). **Infrared absorption spectroscopy**. *Analytical Techniques for Atmospheric Measurement*, 72–146. DOI: 10.1002/9780470988510.ch2.

Froidevaux, L., D. E. Kinnison, B. Gaubert, M. J. Schwartz, N. J. Livesey, W. G. Read, C. G. Bardeen, J. R. Ziemke, and R. A. Fuller (2025). **Tropical upper-tropospheric trends in ozone and carbon monoxide (2005–2020): observational and model results**. *Atmospheric Chemistry and Physics* 25:1, 597–624. DOI: 10.5194/acp-25-597-2025. URL: https://acp.copernicus.org/articles/25/597/2025/.

Fueglistaler, S., A. Dessler, T. Dunkerton, I. Folkins, Q. Fu, and P. W. Mote (2009). **Tropical tropopause layer**. *Reviews of Geophysics* 47:1, 8755–1209. DOI: 10.1029/2008RG000267.

Garfinkel, C. I., C. Schwartz, I. P. White, and J. Rao (2020). **Predictability of the Early Winter Arctic Oscillation from Autumn Eurasian Snowcover in Subseasonal Forecast Models**. *Climate Dynamics* 55:3, 961–974. ISSN: 1432-0894. DOI: 10.1007/s00382-020-05305-3. URL: https://doi.org/10.1007/s00382-020-05305-3.

Gettelman, A., P. Hoor, L. L. Pan, W. J. Randel, M. I. Hegglin, and T. Birner (2011). **THE EXTRATROPICAL UPPER TROPOSPHERE AND LOWER STRATOSPHERE**. *Reviews of Geophysics* 49:3. DOI: https://doi.org/10.1029/2011RG000355. eprint: https://agupubs.onlinelibrary.wiley.com/doi/pdf/10.1029/2011RG000355. URL: https://agupubs.onlinelibrary.wiley.com/doi/abs/10.1029/2011RG000355.

Gordon, I. E., L. S. Rothman, R. J. Hargreaves, R. Hashemi, E. V. Karlovets, F. M. Skinner, E. K. Conway, C. Hill, R. V. Kochanov, Y. Tan, P. Wcisło, A. A. Finenko, K. Nelson, P. F. Bernath, M. Birk, V. Boudon, A. Campargue, K. V. Chance, A. Coustenis, B. J. Drouin, J.-M. Flaud, R. R. Gamache, J. T. Hodges, D. Jacquemart, E. J. Mlawer, A. V. Nikitin, V. I. Perevalov, M. Rotger, J. Tennyson, G. C. Toon, H. Tran, V. G. Tyuterev, E. M. Adkins, A. Baker, A. Barbe, E. Canè, A. G. Császár, A. Dudaryonok, O. Egorov, A. J. Fleisher, H. Fleurbaey, A. Foltynowicz, T. Furtenbacher, J. J. Harrison, J.-M. Hartmann, V.-M. Horneman, X. Huang, T. Karman, J. Karns, S. Kassi, I. Kleiner, V. Kofman, F. Kwabia-Tchana, N. N. Lavrentieva, T. J. Lee, D. A. Long, A. A. Lukashevskaya, O. M. Lyulin, V. Y. Makhnev, W. Matt, S. T. Massie, M. Melosso, S. N. Mikhailenko, D. Mondelain, H. S. P. Müller, O. V. Naumenko, A. Perrin, O. L. Polyansky, E. Raddaoui, P. L. Raston, Z. D. Reed, M. Rey, C. Richard, R. Tóbiás, I. Sadiek, D. W. Schwenke, E. Starikova, K. Sung, F. Tamassia, S. A. Tashkun, J. Vander Auwera, I. A. Vasilenko, A. A. Vigasin, G. L. Villanueva, B. Vispoel, G. Wagner, A. Yachmenev, and S. N. Yurchenko (Jan. 2022). **The HITRAN2020 molecular spectroscopic database**. 277107949, 107949. DOI: 10.1016/j.jqsrt.2021.107949.

Hancock, S. E., D. J. Jacob, Z. Chen, H. Nesser, A. Davitt, D. J. Varon, M. P. Sulprizio, N. Balasus, L. A. Estrada, M. Cazorla, L. Dawidowski, S. Diez, J. D. East, E. Penn, C. A. Randles, J. Worden, I. Aben, R. J. Parker, and J. D. Maasakkers (2025). **Satellite quantification of methane emissions from South American countries: a high-resolution inversion of TROPOMI and GOSAT observations**. *Atmospheric Chemistry and Physics* 25:2, 797–817. DOI: 10.5194/acp-25-797-2025. URL: https://acp.copernicus.org/articles/25/797/2025/.

Hartmann, D. L. (1979). **Baroclinic Instability of Realistic Zonal-Mean States to Planetary Waves**. *Journal of Atmospheric Sciences* 36:12, 2336–2349. DOI: 10.1175/1520-0469(1979)036<2336:BIORZM>2.0.CO;2. URL: https://journals.ametsoc.org/view/journals/atsc/36/12/1520-0469_1979_036_2336_biorzm_2_0_co_2.xml.

Heard, D. E. (2006). **1**, 1–71. In: *Analytical Techniques for Atmospheric Measurement*. John Wiley Sons, Ltd. ISBN: 9780470988510. DOI: https://doi.org/10.1002/9780470988510.ch1. eprint: https://onlinelibrary.wiley.com/doi/pdf/10.1002/9780470988510.ch1. URL: https://onlinelibrary.wiley.com/doi/abs/10.1002/9780470988510.ch1.

Hegglin, M. I. and T. G. Shepherd (2009). **Large climate-induced changes in ultraviolet index and stratosphere-to-troposphere ozone flux**. *Nature Geoscience* 2:10, 687–691. ISSN: 1752-0908. DOI: 10.1038/ngeo604. URL: https://doi.org/10.1038/ngeo604.

Held, I. M., M. Ting, and H. Wang (2002). **Northern Winter Stationary Waves: Theory and Modeling**. *Journal of Climate* 15:16, 2125–2144. DOI: 10.1175/1520-0442(2002)015<2125:NWSWTA>2.0.CO;2. URL: https://journals.ametsoc.org/view/journals/clim/15/16/1520-0442_2002_015_2125_nwswta_2.0.co_2.xml.

Herman, R., C. Webster, R. May, D. Scott, H. Hu, E. Moyer, P. Wennberg, T. Hanisco, E. Lanzendorf, R. Salawitch, Y. Yung, J. Margitan, and T. Bui (1999). **Measurements of CO in the upper troposphere and lower stratosphere**. *Chemosphere - Global Change Science* 1:1, 173–183. ISSN: 1465-9972. DOI: https://doi.org/10.1016/S1465-9972(99)00008-2. URL: https://www.sciencedirect.com/science/article/pii/S1465997299000082.

Herriott, D. R. and H. J. Schulte (Aug. 1965). **Folded Optical Delay Lines**. *Appl. Opt.* 4:8, 883–889. DOI: 10.1364/AO.4.000883. URL: https://opg.optica.org/ao/abstract.cfm?URI=ao-4-8-883.

Heue, K.-P., T. Wagner, S. P. Broccardo, D. Walter, S. J. Piketh, K. E. Ross, S. Beirle, and U. Platt (2008). **Direct observation of two dimensional trace gas distributions with an airborne Imaging DOAS instrument**. *Atmospheric Chemistry and Physics* 8:22, 6707–6717. DOI: 10.5194/acp-8-6707-2008. URL: https://acp.copernicus.org/articles/8/6707/2008/.

Hoerling, M. P., T. K. Schaack, and A. J. Lenzen (1991). **Global Objective Tropopause Analysis**. *Monthly Weather Review* 119:8, 1816–1831. DOI: 10.1175/1520-0493(1991)119<1816:GOTA>2.0.CO;2. URL: https://journals.ametsoc.org/view/journals/mwre/119/8/1520-0493_1991_119_1816_gota_2_0_co_2.xml.

Holloway, J. S., R. O. Jakoubek, D. D. Parrish, C. Gerbig, A. Volz-Thomas, S. Schmitgen, A. Fried, B. Wert, B. Henry, and J. R. Drummond (2000). **Airborne intercomparison of vacuum ultraviolet fluorescence and tunable diode laser absorption measurements of tropospheric carbon monoxide**. *Journal of Geophysical Research: Atmospheres* 105:D19, 24251–24261. DOI: https://doi.org/10.1029/2000JD900237. eprint: https://agupubs.onlinelibrary.wiley.com/doi/pdf/10.1029/2000JD900237. URL: https://agupubs.onlinelibrary.wiley.com/doi/abs/10.1029/2000JD900237.

Holton, J. R., P. H. Haynes, M. E. McIntyre, A. R. Douglass, R. B. Rood, and L. Pfister (1995). **Stratosphere-troposphere exchange**. *Reviews of Geophysics* 33:4, 403–439. DOI: https://doi.org/10.1029/95RG02097. eprint: https://agupubs.onlinelibrary.wiley.com/doi/pdf/10.1029/95RG02097. URL: https://agupubs.onlinelibrary.wiley.com/doi/abs/10.1029/95RG02097.

Hoor, P., H. Fischer, L. Lange, J. Lelieveld, and D. Brunner (2002). **Seasonal variations of a mixing layer in the lowermost stratosphere as identified by the CO-O3 correlation from in situ measurements**. *Journal of Geophysical Research: Atmospheres* 107:D5, ACL–1. DOI: 10.1029/2000JD000289. URL: https://doi.org/10.1029/2000JD000289.

Hoskins, B. J., M. E. McIntyre, and A. W. Robertson (1985). **On the use and significance of isentropic potential vorticity maps**. *Quarterly Journal of the Royal Meteorological Society* 111:470, 877–946. DOI: https://doi.org/10.1002/qj.49711147002. eprint: https://rmets.onlinelibrary.wiley.com/doi/pdf/10.1002/qj.49711147002. URL: https://rmets.onlinelibrary.wiley.com/doi/abs/10.1002/qj.49711147002.

Jackson, R. B., M. Saunois, P. Bousquet, J. G. Canadell, B. Poulter, A. R. Stavert, P. Bergamaschi, Y. Niwa, A. Segers, and A. Tsuruta (July 2020). **Increasing anthropogenic methane emissions arise equally from agricultural and fossil fuel sources**. *Environmental Research Letters* 15:7, 071002. DOI: 10.1088/1748-9326/ab9ed2. URL: https://dx.doi.org/10.1088/1748-9326/ab9ed2.

Jacob, D. (2001). **The role of water vapour in the atmosphere. A short overview from a climate modeller's point of view**. *Physics and Chemistry of the Earth, Part A: Solid Earth and Geodesy* 26:6. Proceedings of the First COST Action 716 Workshop Towards Operational GPS Meteorology and the Second Network Workshop of the International GPS Service (IGS), 523–527. ISSN: 1464-1895. DOI: https://doi.org/10.1016/S1464-1895(01)00094-1. URL: https://www.sciencedirect.com/science/article/pii/S1464189501000941.

Jha, R. K. (2022). **Non-Dispersive Infrared Gas Sensing Technology: A Review**. *IEEE Sensors Journal* 22:1, 6–15. DOI: 10.1109/JSEN.2021.3130034.

Jing, P. and S. Banerjee (2018). **Rossby Wave Breaking and Isentropic Stratosphere-Troposphere Exchange During 1981–2015 in the Northern Hemisphere**. *Journal of Geophysical Research: Atmospheres* 123:17, 9011–9025. DOI: https://doi.org/10.1029/2018JD028997. eprint: https://agupubs.onlinelibrary.wiley.com/doi/pdf/10.1029/2018JD028997. URL: https://agupubs.onlinelibrary.wiley.com/doi/abs/10.1029/2018JD028997.

Johnston, H. S. (1975). **Global ozone balance in the natural stratosphere**. *Reviews of Geophysics* 13:5, 637–649. DOI: https://doi.org/10.1029/RG013i005p00637. eprint: https://agupubs.onlinelibrary.wiley.com/doi/pdf/10.1029/RG013i005p00637. URL: https://agupubs.onlinelibrary.wiley.com/doi/abs/10.1029/RG013i005p00637.

Joppe, P., J. Schneider, K. Kaiser, H. Fischer, P. Hoor, D. Kunkel, H.-C. Lachnitt, A. Marsing, L. Röder, H. Schlager, L. Tomsche, C. Voigt, A. Zahn, and S. Borrmann (2024). **The influence of extratropical cross-tropopause mixing on the correlation between ozone and sulfate aerosol in the lowermost stratosphere**. *Atmospheric Chemistry and Physics* 24:13, 7499–7522. DOI: 10.5194/acp-24-7499-2024. URL: https://acp.copernicus.org/articles/24/7499/2024/.

Krasauskas, L., J. Ungermann, P. Preusse, F. Friedl-Vallon, A. Zahn, H. Ziereis, C. Rolf, F. Ploeger, P. Konopka, B. Vogel, and M. Riese (2020). **3-D tomographic observations of Rossby wave breaking over the Northern Atlantic during the WISE aircraft**

campaign in 2017. *Atmospheric Chemistry and Physics Discussions* 2020, 1–30. DOI: 10.5194/acp-21-10249-2021.

Kunkel, D., P. Hoor, T. Kaluza, J. Ungermann, B. Kluschat, A. Giez, H.-C. Lachnitt, M. Kaufmann, and M. Riese (2019). **Evidence of small-scale quasi-isentropic mixing in ridges of extratropical baroclinic waves**. *Atmospheric Chemistry and Physics* 19:19, 12607–12630. DOI: 10.5194/acp-19-12607-2019.

Kunz, A., P. Konopka, R. Müller, and L. L. Pan (2011). **Dynamical tropopause based on isentropic potential vorticity gradients**. *Journal of Geophysical Research: Atmospheres* 116:D1. DOI: https://doi.org/10.1029/2010JD014343. eprint: https://agupubs.onlinelibrary.wiley.com/doi/pdf/10.1029/2010JD014343. URL: https://agupubs.onlinelibrary.wiley.com/doi/abs/10.1029/2010JD014343.

Lan, X., K. Thoning, and E. Dlugokencky (2025). *Trends in globally-averaged CH4, N2O, and SF6 determined from NOAA Global Monitoring Laboratory measurements*. DOI: 10.15138/P8XG-AA10.

Lashof, D. A. and D. R. Ahuja (Apr. 1990). **Relative contributions of greenhouse gas emissions to global warming**. *Nature* 344:6266, 529–531. ISSN: 1476-4687. DOI: 10.1038/344529a0. URL: https://doi.org/10.1038/344529a0.

Lelieveld, J., B. Bregman, F. Arnold, V. Bürger, P. J. Crutzen, H. Fischer, A. Waibel, P. Siegmund, and P. F. J. van Velthoven (1997). **Chemical perturbation of the lowermost stratosphere through exchange with the troposphere**. *Geophysical Research Letters* 24:5, 603–606. DOI: https://doi.org/10.1029/97GL00255. eprint: https://agupubs.onlinelibrary.wiley.com/doi/pdf/10.1029/97GL00255. URL: https://agupubs.onlinelibrary.wiley.com/doi/abs/10.1029/97GL00255.

Lelieveld, J., F. J. Dentener, W. Peters, and M. C. Krol (2004). **On the role of hydroxyl radicals in the self-cleansing capacity of the troposphere**. *Atmospheric Chemistry and Physics* 4:9/10, 2337–2344. DOI: 10.5194/acp-4-2337-2004. URL: https://acp.copernicus.org/articles/4/2337/2004/.

Lelieveld, J., E. Bourtsoukidis, C. Brühl, H. Fischer, H. Fuchs, H. Harder, A. Hofzumahaus, F. Holland, D. Marno, M. Neumaier, A. Pozzer, H. Schlager, J. Williams, A. Zahn, and H. Ziereis (2018). **The South Asian monsoon—pollution pump and purifier**. *Science* 361:6399, 270–273. DOI: 10.1126/science.aar2501.

Lelieveld, J. and R. van Dorland (1995). "Ozone chemistry changes in the troposphere and consequent radiative forcing of climate." In: *Atmospheric Ozone as a Climate Gas: General Circulation Model Simulations*. Springer, 227–258. DOI: 10.1007/978-3-642-79869-6_16.

Lelieveld, J., S. Gromov, A. Pozzer, and D. Taraborrelli (2016). **Global tropospheric hydroxyl distribution, budget and reactivity**. *Atmospheric Chemistry and Physics* 16:19, 12477–12493. DOI: 10.5194/acp-16-12477-2016. URL: https://doi.org/10.5194/acp-16-12477-2016.

Mayerhöfer, T. G., S. Pahlow, and J. Popp (2020). **The Bouguer-Beer-Lambert Law: Shining Light on the Obscure**. *ChemPhysChem* 21:18, 2029–2046. DOI: https://doi.org/10.1002/cphc.202000464. eprint: https://chemistry-europe.onlinelibrary.wiley.com/doi/

pdf/10.1002/cphc.202000464. URL: https://chemistry-europe.onlinelibrary.wiley.com/doi/abs/10.1002/cphc.202000464.

McManus, J. B., P. L. Kebabian, and M. S. Zahniser (June 1995). **Astigmatic mirror multipass absorption cells for long-path-length spectroscopy**. *Appl. Opt.* 34:18, 3336–3348. DOI: 10.1364/AO.34.003336. URL: https://opg.optica.org/ao/abstract.cfm?URI=ao-34-18-3336.

Müller, M., B. E. Anderson, A. J. Beyersdorf, J. H. Crawford, G. S. Diskin, P. Eichler, A. Fried, F. N. Keutsch, T. Mikoviny, K. L. Thornhill, J. G. Walega, A. J. Weinheimer, M. Yang, R. J. Yokelson, and A. Wisthaler (2016a). **In situ measurements and modeling of reactive trace gases in a small biomass burning plume**. *Atmospheric Chemistry and Physics* 16:6, 3813–3824. DOI: 10.5194/acp-16-3813-2016. URL: https://acp.copernicus.org/articles/16/3813/2016/.

Müller, S., P. Hoor, F. Berkes, H. Bozem, M. Klingebiel, P. Reutter, H. Smit, M. Wendisch, P. Spichtinger, and S. Borrmann (2015). **In situ detection of stratosphere-troposphere exchange of cirrus particles in the midlatitudes**. *Geophysical research letters* 42:3, 949–955. DOI: 10.1002/2014GL062556.

Müller, S., P. Hoor, H. Bozem, E. Gute, B. Vogel, A. Zahn, H. Bönisch, T. Keber, M. Krämer, C. Rolf, et al. (2016b). **Impact of the Asian monsoon on the extratropical lower stratosphere: trace gas observations during TACTS over Europe 2012**. *Atmospheric chemistry and physics* 16:16, 10573–10589. DOI: 10.5194/acp-16-10573-2016.

Murgatroyd, R. J., A. Oapos;Neill, H. S. W. Massey, W. J. G. Beynon, J. T. Houghton, and L. Thomas (1980). **Interaction between the troposphere and stratosphere**. *Philosophical Transactions of the Royal Society of London. Series A, Mathematical and Physical Sciences* 296:1418, 87–102. DOI: 10.1098/rsta.1980.0158. eprint: https://royalsocietypublishing.org/doi/pdf/10.1098/rsta.1980.0158. URL: https://royalsocietypublishing.org/doi/abs/10.1098/rsta.1980.0158.

Murguia-Flores, F., S. Arndt, A. L. Ganesan, G. Murray-Tortarolo, and E. R. C. Hornibrook (2018). **Soil Methanotrophy Model (MeMo v1.0): a process-based model to quantify global uptake of atmospheric methane by soil**. *Geoscientific Model Development* 11:6, 2009–2032. DOI: 10.5194/gmd-11-2009-2018. URL: https://gmd.copernicus.org/articles/11/2009/2018/.

Navier, C.-L. (1838). **Navier stokes equation**. *Chez Carilian-Goeury: Paris, France.*

Nisbet, E. G., M. R. Manning, E. J. Dlugokencky, R. E. Fisher, D. Lowry, S. E. Michel, C. L. Myhre, S. M. Platt, G. Allen, P. Bousquet, R. Brownlow, M. Cain, J. L. France, O. Hermansen, R. Hossaini, A. E. Jones, I. Levin, A. C. Manning, G. Myhre, J. A. Pyle, B. H. Vaughn, N. J. Warwick, and J. W. C. White (2019). **Very Strong Atmospheric Methane Growth in the 4 Years 2014–2017: Implications for the Paris Agreement**. *Global Biogeochemical Cycles* 33:3, 318–342. DOI: https://doi.org/10.1029/2018GB006009. eprint: https://agupubs.onlinelibrary.wiley.com/doi/pdf/10.1029/2018GB006009. URL: https://agupubs.onlinelibrary.wiley.com/doi/abs/10.1029/2018GB006009.

Niwa, Y., Y. Tohjima, Y. Terao, T. Saeki, A. Ito, T. Umezawa, K. Yamada, M. Sasakawa, T. Machida, S.-I. Nakaoka, H. Nara, H. Tanimoto, H. Mukai, Y. Yoshida, S. Morimoto, S. Takatsuji, K. Tsuboi, Y. Sawa, H. Matsueda, K. Ishijima, R. Fujita, D. Goto, X. Lan, K. Schuldt, M. Heliasz, T. Biermann, L. Chmura, J. Necki, I. Xueref-Remy, and D. Sferlazzo (2025). **Multi-observational estimation of regional and sectoral emission contributions to the persistent high growth rate of atmospheric CH_4 for 2020–2022**. *Atmospheric Chemistry and Physics* 25:13, 6757–6785. DOI: 10.5194/acp-25-6757-2025. URL: https://acp.copernicus.org/articles/25/6757/2025/.

Norval, M., R. Lucas, A. Cullen, F. De Gruijl, J. Longstreth, Y. Takizawa, and J. Van Der Leun (2011). **The human health effects of ozone depletion and interactions with climate change**. *Photochemical & Photobiological Sciences* 10:2, 199–225. DOI: 10.1039/C0PP90044C.

Nussbaumer, C. M., H. Fischer, J. Lelieveld, and A. Pozzer (2023). **What controls ozone sensitivity in the upper tropical troposphere?** *Atmospheric Chemistry and Physics* 23:19, 12651–12669. DOI: 10.5194/acp-23-12651-2023.

Nussbaumer, C. M., M. Kohl, A. Pozzer, I. Tadic, R. Rohloff, D. Marno, H. Harder, H. Ziereis, A. Zahn, F. Obersteiner, A. Hofzumahaus, H. Fuchs, C. Künstler, W. H. Brune, T. B. Ryerson, J. Peischl, C. R. Thompson, I. Bourgeois, J. Lelieveld, and H. Fischer (2024). **Ozone Formation Sensitivity to Precursors and Lightning in the Tropical Troposphere Based on Airborne Observations**. *Journal of Geophysical Research: Atmospheres* 129:14. e2024JD041168 2024JD041168, e2024JD041168. DOI: https://doi.org/10.1029/2024JD041168. eprint: https://agupubs.onlinelibrary.wiley.com/doi/pdf/10.1029/2024JD041168. URL: https://agupubs.onlinelibrary.wiley.com/doi/abs/10.1029/2024JD041168.

Nuvolone, D., D. Petri, and F. Voller (2018). **The effects of ozone on human health**. *Environmental Science and Pollution Research* 25, 8074–8088. DOI: 10.1007/s11356-017-9239-3.

Obersteiner, F. (May 2024). *FAIROmeta*. Version v0.1.9. Zenodo. DOI: 10.5281/zenodo.11275355. URL: https://doi.org/10.5281/zenodo.11275355.

Oceanic, N. and A. Administration (Aug. 2024). *Layers of the Atmosphere*. last access: 29.09.2025. URL: https://www.noaa.gov/jetstream/atmosphere/layers-of-atmosphere.

Ort, L., C. Frankenberg, N. Dadheech, J. Yoon, A. J. Turner, A. Bloom, P. Konopka, H. Lachnitt, P. Hoor, J. Lelieveld, E. A. Kort, and H. Fischer (2026a). **Airborne observations reveal underestimated riverine methane emissions across the Amazon**. *ESS Open Archive*. preprint, submitted to *Geophysical Research Letters* on 19 February 2026. DOI: 10.22541/essoar.177248180.00166712/v1.

Ort, L., A. Pozzer, P. Hoor, F. Obersteiner, A. Zahn, T. B. Ryerson, C. R. Thompson, J. Peischl, R. Commane, B. Daube, I. Bourgeois, J. Lelieveld, and H. Fischer (2025). **Enhancement of O_3–CO ratios at tropospheric subtropical latitudes: Photochemistry and stratospheric influence**. *Atmospheric Chemistry and Physics* 25:21, 14987–15007. DOI: 10.5194/acp-25-14987-2025. URL: https://acp.copernicus.org/articles/25/14987/2025/.

Ort, L., N. Dadheech, J. Yoon, A. Turner, A. A. Bloom, H.-C. Lachnitt, P. Konopka, and H. Fischer (Feb. 2026b). *Supporting data for: Airborne observations reveal underestimated riverine methane emissions across the Amazon*. Zenodo. DOI: 10.5281/zenodo.18504592. URL: https://doi.org/10.5281/zenodo.18504592.

Ort, L. and A. Pozzer (Oct. 2025). *Supporting data for: Enhancement of O3 – CO ratios at tropospheric subtropical latitudes: Photochemistry and stratospheric influence*. Version 1.0. Zenodo. DOI: 10.5281/zenodo.17476643. URL: https://doi.org/10.5281/zenodo.17476643.

Ort, L., L. L. Röder, U. Parchatka, R. Königstedt, D. Crowley, F. Kunz, R. Wittkowski, J. Lelieveld, and H. Fischer (2024). **In-flight characterization of a compact airborne quantum cascade laser absorption spectrometer**. *Atmospheric Measurement Techniques* 17:11, 3553–3565. DOI: 10.5194/amt-17-3553-2024.

Ortega, I., J. W. Hannigan, B. C. Baier, K. McKain, and D. Smale (2025). **Advancing CH_4 and N_2O retrieval strategies for NDACC/IRWG FTIR observations with the support of airborne in situ measurements**. *Atmospheric Measurement Techniques* 18:11, 2353–2371. DOI: 10.5194/amt-18-2353-2025. URL: https://amt.copernicus.org/articles/18/2353/2025/.

Pal, M. and M. Pradhan (2021). **Quantum Cascade Laser Spectroscopy**. *Modern Techniques of Spectroscopy: Basics, Instrumentation, and Applications*, 363–387. DOI: 10.1007/978-981-33-6084-6_14.

Peng, S., X. Lin, R. L. Thompson, Y. Xi, G. Liu, D. Hauglustaine, X. Lan, B. Poulter, M. Ramonet, M. Saunois, Y. Yin, Z. Zhang, B. Zheng, and P. Ciais (2022). **Wetland emission and atmospheric sink changes explain methane growth in 2020**. *Nature* 612:7940, 477–482. ISSN: 1476-4687. DOI: 10.1038/s41586-022-05447-w. URL: https://doi.org/10.1038/s41586-022-05447-w.

Pérez-Domínguez, I., A. Del Prado, K. Mittenzwei, J. Hristov, S. Frank, A. Tabeau, P. Witzke, P. Havlik, H. van Meijl, J. Lynch, et al. (2021). **Short-and long-term warming effects of methane may affect the cost-effectiveness of mitigation policies and benefits of low-meat diets**. *Nature Food* 2:12, 970–980. DOI: https://doi.org/10.1038/s43016-021-00385-8.

Pérez-Invernón, F. J., F. J. Gordillo-Vázquez, H. Huntrieser, and P. Jöckel (2023). **Variation of lightning-ignited wildfire patterns under climate change**. *Nature Communications* 14:1, 739. ISSN: 2041-1723. DOI: 10.1038/s41467-023-36500-5.

Plane, J. M. and A. Saiz-Lopez (2006). **3**, 147–188. In: *Analytical Techniques for Atmospheric Measurement*. John Wiley Sons, Ltd. ISBN: 9780470988510. DOI: https://doi.org/10.1002/9780470988510.ch3. eprint: https://onlinelibrary.wiley.com/doi/pdf/10.1002/9780470988510.ch3. URL: https://onlinelibrary.wiley.com/doi/abs/10.1002/9780470988510.ch3.

Postel, G. A. and M. H. Hitchman (1999). **A Climatology of Rossby Wave Breaking along the Subtropical Tropopause**. *Journal of the Atmospheric Sciences* 56:3, 359–373. DOI: 10.1175/1520-0469(1999)056<0359:ACORWB>2.0.CO;2. URL: https://journals.ametsoc.org/view/journals/atsc/56/3/1520-0469_1999_056_0359_acorwb_2.0.co_2.xml.

Postel, G. A. and M. H. Hitchman (2001). **A Case Study of Rossby Wave Breaking along the Subtropical Tropopause**. *Monthly Weather Review* 129:10, 2555–2569. DOI: 10.1175/1520-0493(2001)129<2555:ACSORW>2.0.CO;2. URL: https://journals.ametsoc.org/view/journals/mwre/129/10/1520-0493_2001_129_2555_acsorw_2.0.co_2.xml.

Prather, M., M. McElroy, S. Wofsy, G. Russell, and D. Rind (1987). **Chemistry of the global troposphere: Fluorocarbons as tracers of air motion**. *Journal of Geophysical Research: Atmospheres* 92:D6, 6579–6613. DOI: https://doi.org/10.1029/JD092iD06p06579. eprint: https://agupubs.onlinelibrary.wiley.com/doi/pdf/10.1029/JD092iD06p06579. URL: https://agupubs.onlinelibrary.wiley.com/doi/abs/10.1029/JD092iD06p06579.

Prather, M. J., X. Zhu, Q. Tang, J. Hsu, and J. L. Neu (2011). **An atmospheric chemist in search of the tropopause**. *Journal of Geophysical Research: Atmospheres* 116:D4. DOI: https://doi.org/10.1029/2010JD014939. eprint: https://agupubs.onlinelibrary.wiley.com/doi/pdf/10.1029/2010JD014939. URL: https://agupubs.onlinelibrary.wiley.com/doi/abs/10.1029/2010JD014939.

Pressman, J. and P. Warneck (1970). **The Stratosphere as a Chemical Sink for Carbon Monoxide**. *Journal of Atmospheric Sciences* 27:1, 155–163. DOI: 10.1175/1520-0469(1970)027<0155:TSAACS>2.0.CO;2. URL: https://journals.ametsoc.org/view/journals/atsc/27/1/1520-0469_1970_027_0155_tsaacs_2_0_co_2.xml.

Ray, E. A., F. L. Moore, H. Garny, E. J. Hintsa, B. D. Hall, G. S. Dutton, D. Nance, J. W. Elkins, S. C. Wofsy, J. Pittman, B. Daube, B. C. Baier, J. Li, and C. Sweeney (2024). **Age of air from in situ trace gas measurements: insights from a new technique**. *Atmospheric Chemistry and Physics* 24:21, 12425–12445. DOI: 10.5194/acp-24-12425-2024. URL: https://acp.copernicus.org/articles/24/12425/2024/.

Reiche, J., R. Lucas, A. L. Mitchell, J. Verbesselt, D. H. Hoekman, J. Haarpaintner, J. M. Kellndorfer, A. Rosenqvist, E. A. Lehmann, C. E. Woodcock, et al. (2016). **Combining satellite data for better tropical forest monitoring**. *Nature Climate Change* 6:2, 120–122. DOI: 10.1038/nclimate2919.

Rella, C. W., J. Hoffnagle, Y. He, and S. Tajima (2015). **Local- and regional-scale measurements of CH_4, $^{13}CH_4$, and C_2H_6 in the Uintah Basin using a mobile stable isotope analyzer**. *Atmospheric Measurement Techniques* 8:10, 4539–4559. DOI: 10.5194/amt-8-4539-2015. URL: https://amt.copernicus.org/articles/8/4539/2015/.

Riese, M., P. Hoor, C. Rolf, D. Kunkel, B. Vogel, F. Köllner, M. Pöhlker, F. Ploeger, J. Ungermann, W. Woiwode, S. Johansson, R. Bauer, K. Barmpounis, S. Borrmann, P. Brauner, J. Clemens, A. Dragoneas, F. Ekinci, N. Emig, A. Engel, O. Eppers, S. Fadnavis, F. Friedl-Vallon, M. Geldenhuys, G. Günther, J. Grooß, M. Hegglin, M. Höpfner, M. Jesswein, P. Joppe, J. Kaumanns, O. Kachula, T. Keber, E. Kretschmer, H. C. Lachnitt, V. Lauther, P. Lloyd, S. Molleker, R. Müller, T. Neubert, L. Ort, U. Pöschl, C. Pöhlker, M. Rapp, M. Retzlaff, S. Rhode, J. Schneider, T. Schuck, B.-M. Sinnhuber, N. Spelten, J. Strobel, L. Tomsche, K. Turhal, R. van Luijt, S. Versick, C. Voigt, M. Volk, M. von Hobe, F. Weyland, A. Zahn, H. Ziereis, and L. Zlotos (2025). **Long-range transport of polluted Asian summer monsoon air to high latitudes during the PHILEAS campaign in the bo-**

real summer 2023. *Bulletin of the American Meteorological Society*, BAMS-D-24–0232.1. DOI: 10.1175/BAMS-D-24-0232.1. URL: https://journals.ametsoc.org/view/journals/bams/aop/BAMS-D-24-0232.1/BAMS-D-24-0232.1.xml.

Röder, L. L., L. Ort, J. Lelieveld, and H. Fischer (2024). **Quantitative analysis of temporal stability and instrument performance during field experiments of an airborne QCLAS via Allan–Werle-plots**. *Applied Physics B* 130:7, 118. DOI: 10.1007/s00340-024-08254-5.

Rodhe, H. (1992). "4 Modeling Biogeochemical Cycles." In: *Global Biogeochemical Cycles*. Ed. by S. S. Butcher, R. J. Charlson, G. H. Orians, and G. V. Wolfe. Vol. 50. International Geophysics. Academic Press, 55–72. DOI: https://doi.org/10.1016/S0074-6142(08)62687-X. URL: https://www.sciencedirect.com/science/article/pii/S007461420862687X.

Rowland, F. S. (1991). **Stratospheric ozone depletion**. *Annual Review of Physical Chemistry* 42:1, 731–768. URL: https://doi.org/10.1146/annurev.pc.42.100191.003503,%201991.

Saunois, M., P. Bousquet, B. Poulter, A. Peregon, P. Ciais, J. G. Canadell, E. J. Dlugokencky, G. Etiope, D. Bastviken, S. Houweling, G. Janssens-Maenhout, F. N. Tubiello, S. Castaldi, R. B. Jackson, M. Alexe, V. K. Arora, D. J. Beerling, P. Bergamaschi, D. R. Blake, G. Brailsford, V. Brovkin, L. Bruhwiler, C. Crevoisier, P. Crill, K. Covey, C. Curry, C. Frankenberg, N. Gedney, L. Höglund-Isaksson, M. Ishizawa, A. Ito, F. Joos, H.-S. Kim, T. Kleinen, P. Krummel, J.-F. Lamarque, R. Langenfelds, R. Locatelli, T. Machida, S. Maksyutov, K. C. McDonald, J. Marshall, J. R. Melton, I. Morino, V. Naik, S. O'Doherty, F.-J. W. Parmentier, P. K. Patra, C. Peng, S. Peng, G. P. Peters, I. Pison, C. Prigent, R. Prinn, M. Ramonet, W. J. Riley, M. Saito, M. Santini, R. Schroeder, I. J. Simpson, R. Spahni, P. Steele, A. Takizawa, B. F. Thornton, H. Tian, Y. Tohjima, N. Viovy, A. Voulgarakis, M. van Weele, G. R. van der Werf, R. Weiss, C. Wiedinmyer, D. J. Wilton, A. Wiltshire, D. Worthy, D. Wunch, X. Xu, Y. Yoshida, B. Zhang, Z. Zhang, and Q. Zhu (2016). **The global methane budget 2000–2012**. *Earth System Science Data* 8:2, 697–751. DOI: 10.5194/essd-8-697-2016. URL: https://essd.copernicus.org/articles/8/697/2016/.

Saunois, M., A. Martinez, B. Poulter, Z. Zhang, P. Raymond, P. Regnier, J. G. Canadell, R. B. Jackson, P. K. Patra, P. Bousquet, P. Ciais, E. J. Dlugokencky, X. Lan, G. H. Allen, D. Bastviken, D. J. Beerling, D. A. Belikov, D. R. Blake, S. Castaldi, M. Crippa, B. R. Deemer, F. Dennison, G. Etiope, N. Gedney, L. Höglund-Isaksson, M. A. Holgerson, P. O. Hopcroft, G. Hugelius, A. Ito, A. K. Jain, R. Janardanan, M. S. Johnson, T. Kleinen, P. Krummel, R. Lauerwald, T. Li, X. Liu, K. C. McDonald, J. R. Melton, J. Mühle, J. Müller, F. Murguia-Flores, Y. Niwa, S. Noce, S. Pan, R. J. Parker, C. Peng, M. Ramonet, W. J. Riley, G. Rocher-Ros, J. A. Rosentreter, M. Sasakawa, A. Segers, S. J. Smith, E. H. Stanley, J. Thanwerdas, H. Tian, A. Tsuruta, F. N. Tubiello, T. S. Weber, G. van der Werf, D. E. Worthy, Y. Xi, Y. Yoshida, W. Zhang, B. Zheng, Q. Zhu, Q. Zhu, and Q. Zhuang (2024). **Global Methane Budget 2000–2020**. *Earth System Science Data Discussions* 2024, 1–147. DOI: 10.5194/essd-2024-115. URL: https://essd.copernicus.org/preprints/essd-2024-115/.

Saunois, M., A. Martinez, B. Poulter, Z. Zhang, P. A. Raymond, P. Regnier, J. G. Canadell, R. B. Jackson, P. K. Patra, P. Bousquet, P. Ciais, E. J. Dlugokencky, X. Lan, G. H. Allen,

D. Bastviken, D. J. Beerling, D. A. Belikov, D. R. Blake, S. Castaldi, M. Crippa, B. R. Deemer, F. Dennison, G. Etiope, N. Gedney, L. Höglund-Isaksson, M. A. Holgerson, P. O. Hopcroft, G. Hugelius, A. Ito, A. K. Jain, R. Janardanan, M. S. Johnson, T. Kleinen, P. B. Krummel, R. Lauerwald, T. Li, X. Liu, K. C. McDonald, J. R. Melton, J. Mühle, J. Müller, F. Murguia-Flores, Y. Niwa, S. Noce, S. Pan, R. J. Parker, C. Peng, M. Ramonet, W. J. Riley, G. Rocher-Ros, J. A. Rosentreter, M. Sasakawa, A. Segers, S. J. Smith, E. H. Stanley, J. Thanwerdas, H. Tian, A. Tsuruta, F. N. Tubiello, T. S. Weber, G. R. van der Werf, D. E. J. Worthy, Y. Xi, Y. Yoshida, W. Zhang, B. Zheng, Q. Zhu, Q. Zhu, and Q. Zhuang (2025). **Global Methane Budget 2000–2020**. *Earth System Science Data* 17:5, 1873–1958. DOI: 10.5194/essd-17-1873-2025. URL: https://essd.copernicus.org/articles/17/1873/2025/.

Saunois, M., A. R. Stavert, B. Poulter, P. Bousquet, J. G. Canadell, R. B. Jackson, P. A. Raymond, E. J. Dlugokencky, S. Houweling, P. K. Patra, P. Ciais, V. K. Arora, D. Bastviken, P. Bergamaschi, D. R. Blake, G. Brailsford, L. Bruhwiler, K. M. Carlson, M. Carrol, S. Castaldi, N. Chandra, C. Crevoisier, P. M. Crill, K. Covey, C. L. Curry, G. Etiope, C. Frankenberg, N. Gedney, M. I. Hegglin, L. Höglund-Isaksson, G. Hugelius, M. Ishizawa, A. Ito, G. Janssens-Maenhout, K. M. Jensen, F. Joos, T. Kleinen, P. B. Krummel, R. L. Langenfelds, G. G. Laruelle, L. Liu, T. Machida, S. Maksyutov, K. C. McDonald, J. McNorton, P. A. Miller, J. R. Melton, I. Morino, J. Müller, F. Murguia-Flores, V. Naik, Y. Niwa, S. Noce, S. O'Doherty, R. J. Parker, C. Peng, S. Peng, G. P. Peters, C. Prigent, R. Prinn, M. Ramonet, P. Regnier, W. J. Riley, J. A. Rosentreter, A. Segers, I. J. Simpson, H. Shi, S. J. Smith, L. P. Steele, B. F. Thornton, H. Tian, Y. Tohjima, F. N. Tubiello, A. Tsuruta, N. Viovy, A. Voulgarakis, T. S. Weber, M. van Weele, G. R. van der Werf, R. F. Weiss, D. Worthy, D. Wunch, Y. Yin, Y. Yoshida, W. Zhang, Z. Zhang, Y. Zhao, B. Zheng, Q. Zhu, Q. Zhu, and Q. Zhuang (2020). **The Global Methane Budget 2000–2017**. *Earth System Science Data* 12:3, 1561–1623. DOI: 10.5194/essd-12-1561-2020. URL: https://essd.copernicus.org/articles/12/1561/2020/.

Schoeberl, M. R., R. Ueyama, and L. Pfister (2022). **A Lagrangian View of Seasonal Stratosphere-Troposphere Exchange**. *Journal of Geophysical Research: Atmospheres* 127:16. e2022JD036772 2022JD036772, e2022JD036772. DOI: https://doi.org/10.1029/2022JD036772. eprint: https://agupubs.onlinelibrary.wiley.com/doi/pdf/10.1029/2022JD036772. URL: https://agupubs.onlinelibrary.wiley.com/doi/abs/10.1029/2022JD036772.

Schuck, T. J., J. Degen, E. Hintsa, P. Hoor, M. Jesswein, T. Keber, D. Kunkel, F. Moore, F. Obersteiner, M. Rigby, T. Wagenhäuser, L. M. Western, A. Zahn, and A. Engel (2024). **The interhemispheric gradient of SF_6 in the upper troposphere**. *Atmospheric Chemistry and Physics* 24:1, 689–705. DOI: 10.5194/acp-24-689-2024. URL: https://acp.copernicus.org/articles/24/689/2024/.

Schumann, U. and H. Huntrieser (2007). **The global lightning-induced nitrogen oxides source**. *Atmospheric Chemistry and Physics* 7:14, 3823–3907. DOI: 10.5194/acp-7-3823-2007. URL: https://doi.org/10.5194/acp-7-3823-2007.

Seiler, W. (1974). **The cycle of atmospheric CO.** *Tellus* 26:1-2, 116–135. DOI: 10.3402/tellusa.v26i1-2.9743. eprint: https://doi.org/10.3402/tellusa.v26i1-2.9743. URL: https://doi.org/10.3402/tellusa.v26i1-2.9743.

Seinfeld, J. H. and S. N. Pandis (2016). **Atmospheric chemistry and physics: from air pollution to climate change**. John Wiley & Sons.

Shaw, J. T., G. Allen, P. Barker, J. R. Pitt, D. Pasternak, S. J.-B. Bauguitte, J. Lee, K. N. Bower, M. C. Daly, M. F. Lunt, A. L. Ganesan, A. R. Vaughan, F. Chibesakunda, M. Lambakasa, R. E. Fisher, J. L. France, D. Lowry, P. I. Palmer, S. Metzger, R. J. Parker, N. Gedney, P. Bateson, M. Cain, A. Lorente, T. Borsdorff, and E. G. Nisbet (2022). **Large Methane Emission Fluxes Observed From Tropical Wetlands in Zambia**. *Global Biogeochemical Cycles* 36:6. e2021GB007261 2021GB007261, e2021GB007261. DOI: https://doi.org/10.1029/2021GB007261. eprint: https://agupubs.onlinelibrary.wiley.com/doi/pdf/10.1029/2021GB007261. URL: https://agupubs.onlinelibrary.wiley.com/doi/abs/10.1029/2021GB007261.

Shepherd, T. G. (2003). **Large-Scale Atmospheric Dynamics for Atmospheric Chemists**. *Chemical Reviews* 103:12, 4509–4532. DOI: 10.1021/cr020511z.

Shindell, D., J. C. I. Kuylenstierna, E. Vignati, R. van Dingenen, M. Amann, Z. Klimont, S. C. Anenberg, N. Muller, G. Janssens-Maenhout, F. Raes, J. Schwartz, G. Faluvegi, L. Pozzoli, K. Kupiainen, L. Höglund-Isaksson, L. Emberson, D. Streets, V. Ramanathan, K. Hicks, N. T. K. Oanh, G. Milly, M. Williams, V. Demkine, and D. Fowler (2012). **Simultaneously Mitigating Near-Term Climate Change and Improving Human Health and Food Security**. *Science* 335:6065, 183–189. DOI: 10.1126/science.1210026. eprint: https://www.science.org/doi/pdf/10.1126/science.1210026. URL: https://www.science.org/doi/abs/10.1126/science.1210026.

Silveira Petruci, J. F. da, D. N. Barreto, M. A. Dias, E. P. Felix, and A. A. Cardoso (2022). **Analytical methods applied for ozone gas detection: A review**. *TrAC Trends in Analytical Chemistry* 149, 116552. ISSN: 0165-9936. DOI: https://doi.org/10.1016/j.trac.2022.116552. URL: https://www.sciencedirect.com/science/article/pii/S0165993622000358.

Singh, H. B. (1995). **Composition, chemistry, and climate of the atmosphere**. Van Nostrand Reinhold New York.

Škerlak, B., M. Sprenger, and H. Wernli (2014). **A global climatology of stratosphere–troposphere exchange using the ERA-Interim data set from 1979 to 2011**. *Atmospheric Chemistry and Physics* 14:2, 913–937. DOI: 10.5194/acp-14-913-2014. URL: https://acp.copernicus.org/articles/14/913/2014/.

Staehelin, J., N. R. Harris, C. Appenzeller, and J. Eberhard (2001). **Ozone trends: A review**. *Reviews of Geophysics* 39:2, 231–290. DOI: 10.1029/1999RG000059.

Stendel, M., J. Francis, R. White, P. D. Williams, and T. Woollings (2021). "Chapter 15 - The jet stream and climate change." In: *Climate Change (Third Edition)*. Ed. by T. M. Letcher. Third Edition. Elsevier, 327–357. ISBN: 978-0-12-821575-3. DOI: https://doi.org/10.1016/B978-0-12-821575-3.00015-3. URL: https://www.sciencedirect.com/science/article/pii/B9780128215753000153.

Stevenson, D. S., P. J. Young, V. Naik, J.-F. Lamarque, D. T. Shindell, A. Voulgarakis, R. B. Skeie, S. B. Dalsoren, G. Myhre, T. K. Berntsen, G. A. Folberth, S. T. Rumbold, W. J. Collins, I. A. MacKenzie, R. M. Doherty, G. Zeng, T. P. C. van Noije, A. Strunk, D. Bergmann, P. Cameron-Smith, D. A. Plummer, S. A. Strode, L. Horowitz, Y. H. Lee, S. Szopa, K. Sudo, T. Nagashima, B. Josse, I. Cionni, M. Righi, V. Eyring, A. Conley, K. W. Bowman, O. Wild, and A. Archibald (2013). **Tropospheric ozone changes, radiative forcing and attribution to emissions in the Atmospheric Chemistry and Climate Model Intercomparison Project (ACCMIP)**. *Atmospheric Chemistry and Physics* 13:6, 3063–3085. DOI: 10.5194/acp-13-3063-2013. URL: https://acp.copernicus.org/articles/13/3063/2013/.

Strode, S. A., J. Liu, L. Lait, R. Commane, B. Daube, S. Wofsy, A. Conaty, P. Newman, and M. Prather (2018). **Forecasting carbon monoxide on a global scale for the ATom-1 aircraft mission: insights from airborne and satellite observations and modeling**. *Atmospheric Chemistry and Physics* 18:15, 10955–10971. DOI: 10.5194/acp-18-10955-2018.

Swinehart, D. F. (1962). **The beer-lambert law**. *Journal of chemical education* 39:7, 333.

Szopa, S., V. Naik, B. Adhikary, P. Artaxo, T. Berntsen, W. D. Collins, S. Fuzzi, L. Gallardo, A. Kiendler-Scharr, Z. Klimont, H. Liao, N. Unger, and P. Zanis (2021). "Short-Lived Climate Forcers (Chapter 6)." In: *IPCC 2021: Climate Change 2021: The Physical Science Basis. Contribution of Working Group I to the Sixth Assessment Report of the Intergovernmental Panel on Climate Change*. Ed. by V. Masson-Delmotte, P. Zhai, A. Pirani, S. Connors, C. Péan, S. Berger, N. Caud, Y. Chen, L. Goldfarb, M. Gomis, M. Huang, K. Leitzell, E. Lonnoy, J. Matthews, T. Maycock, T. Waterfield, K. Yeleki, R. Yu, and B. Zhu. Cambridge, United Kingdom and New York, NY, USA: Cambridge University Press, 817–922. DOI: 10.1017/9781009157896.008. URL: https://www.ipcc.ch/report/ar6/wg1/.

Tang, X., S. Madronich, T. Wallington, and D. Calamari (1998). **Changes in tropospheric composition and air quality**. *Journal of Photochemistry and Photobiology B: Biology* 46:1-3, 83–95. DOI: 10.1016/S1011-1344(98)00187-0. URL: https://doi.org/10.1016/S1011-1344(98)00187-0.

Thompson, C. R., S. C. Wofsy, M. J. Prather, P. A. Newman, T. F. Hanisco, T. B. Ryerson, D. W. Fahey, E. C. Apel, C. A. Brock, W. H. Brune, K. Froyd, J. M. Katich, J. M. Nicely, J. Peischl, E. Ray, P. R. Veres, S. Wang, H. M. Allen, E. Asher, H. Bian, D. Blake, I. Bourgeois, J. Budney, T. P. Bui, A. Butler, P. Campuzano-Jost, C. Chang, M. Chin, R. Commane, G. Correa, J. D. Crounse, B. Daube, J. E. Dibb, J. P. DiGangi, G. S. Diskin, M. Dollner, J. W. Elkins, A. M. Fiore, C. M. Flynn, H. Guo, S. R. Hall, R. A. Hannun, A. Hills, E. J. Hintsa, A. Hodzic, R. S. Hornbrook, L. G. Huey, J. L. Jimenez, R. F. Keeling, M. J. Kim, A. Kupc, F. Lacey, L. R. Lait, J.-F. Lamarque, J. Liu, K. McKain, S. Meinardi, D. O. Miller, S. A. Montzka, F. L. Moore, E. J. Morgan, D. M. Murphy, L. T. Murray, B. A. Nault, J. A. Neuman, L. Nguyen, Y. Gonzalez, A. Rollins, K. Rosenlof, M. Sargent, G. Schill, J. P. Schwarz, J. M. S. Clair, S. D. Steenrod, B. B. Stephens, S. E. Strahan, S. A. Strode, C. Sweeney, A. B. Thames, K. Ullmann, N. Wagner, R. Weber, B. Weinzierl, P. O. Wennberg, G. M. Williamson Christina J. amd Wolfe, and L. Zeng (2022). **The NASA Atmospheric Tomography**

(ATom) mission: Imaging the chemistry of the global atmosphere. *Bulletin of the American Meteorological Society* 103:3, E761–E790. DOI: 10.1175/BAMS-D-20-0315.1.

Tiao, G. C., G. E. P. Box, and W. J. Hamming (1975). **Analysis of Los Angeles Photochemical Smog Data: A Statistical Overview**. *Journal of the Air Pollution Control Association* 25:3, 260–268. DOI: 10.1080/00022470.1975.10470082. eprint: https://doi.org/10.1080/00022470.1975.10470082. URL: https://doi.org/10.1080/00022470.1975.10470082.

Tittel, F. K., D. Richter, and A. Fried (2003), 458–529. In: *Solid-State Mid-Infrared Laser Sources*. Ed. by I. T. Sorokina and K. L. Vodopyanov. Berlin, Heidelberg: Springer Berlin Heidelberg. ISBN: 978-3-540-36491-7. DOI: 10.1007/3-540-36491-9_11. URL: https://doi.org/10.1007/3-540-36491-9_11.

Turner, A. J., D. J. Jacob, J. Benmergui, J. Brandman, L. White, and C. A. Randles (2018). **Assessing the capability of different satellite observing configurations to resolve the distribution of methane emissions at kilometer scales**. *Atmospheric Chemistry and Physics* 18:11, 8265–8278. DOI: 10.5194/acp-18-8265-2018. URL: https://acp.copernicus.org/articles/18/8265/2018/.

Turner, A. J., J. Kim, H. Fitzmaurice, C. Newman, K. Worthington, K. Chan, P. J. Wooldridge, P. Köehler, C. Frankenberg, and R. C. Cohen (2020). **Observed Impacts of COVID-19 on Urban CO2 Emissions**. *Geophysical Research Letters* 47:22. e2020GL090037 10.1029/2020GL090037, e2020GL090037. DOI: https://doi.org/10.1029/2020GL090037. eprint: https://agupubs.onlinelibrary.wiley.com/doi/pdf/10.1029/2020GL090037. URL: https://agupubs.onlinelibrary.wiley.com/doi/abs/10.1029/2020GL090037.

Uluocak, I. (2025). **Hybrid deep learning models for predicting atmospheric methane concentrations: A comparative analysis through 2050**. *Science China Earth Sciences*, 1–11. DOI: https://doi.org/10.1007/s11430-024-1569-9.

Wallace, J. M. and P. V. Hobbs (2006). **Atmospheric science: an introductory survey**. Vol. 92. Elsevier.

Weinheimer, A. J. (2006). 7, 311–360. In: *Analytical Techniques for Atmospheric Measurement*. John Wiley Sons, Ltd. ISBN: 9780470988510. DOI: https://doi.org/10.1002/9780470988510.ch7. eprint: https://onlinelibrary.wiley.com/doi/pdf/10.1002/9780470988510.ch7. URL: https://onlinelibrary.wiley.com/doi/abs/10.1002/9780470988510.ch7.

White, J. U. (Jan. 1957). *Optical system providing a long optical path, last access: 24 June 2024*. US Patent 2,779,230.

Wienhold, F., H. Fischer, P. Hoor, V. Wagner, R. Königstedt, G. Harris, J. Anders, R. Grisar, M. Knothe, W. Riedel, F.-J. Liibken, and T. Schilling (1998). **TRISTAR-A tracer in-situ TDLAS for atmospheric research**. *Applied Physics B* 67, 411–417. DOI: 10.1007/s003400050524.

Williams, J. (2006). 5, 229–264. In: *Analytical Techniques for Atmospheric Measurement*. John Wiley Sons, Ltd. ISBN: 9780470988510. DOI: https://doi.org/10.1002/9780470988510.ch5. eprint: https://onlinelibrary.wiley.com/doi/pdf/10.1002/9780470988510.ch5. URL: https://onlinelibrary.wiley.com/doi/abs/10.1002/9780470988510.ch5.

Wofsy, S., S. Afshar, H. Allen, E. Apel, E. Asher, B. Barletta, J. Bent, H. Bian, B. Biggs, D. Blake, et al. (2018). **ATom: Merged atmospheric chemistry, trace gases, and aerosols**. *ORNL DAAC*. DOI: 10.3334/ORNLDAAC/1581.

Zhang, Z., N. E. Zimmermann, A. Stenke, X. Li, E. L. Hodson, G. Zhu, C. Huang, and B. Poulter (2017). **Emerging role of wetland methane emissions in driving 21st century climate change**. *Proceedings of the National Academy of Sciences* 114:36, 9647–9652. DOI: 10.1073/pnas.1618765114. eprint: https://www.pnas.org/doi/pdf/10.1073/pnas.1618765114. URL: https://www.pnas.org/doi/abs/10.1073/pnas.1618765114.

Zhu, Q., D. J. Jacob, K. Yuan, F. Li, B. R. K. Runkle, M. Chen, A. A. Bloom, B. Poulter, J. D. East, W. J. Riley, G. McNicol, J. Worden, C. Frankenberg, and M. Halabisky (Feb. 2025). **Advancements and opportunities to improve bottom–up estimates of global wetland methane emissions**. *Environmental Research Letters* 20:2, 023001. DOI: 10.1088/1748-9326/adad02. URL: https://dx.doi.org/10.1088/1748-9326/adad02.

List of Publications

Publications in Peer Reviewed Journals - First Author

Ort, L., C. Frankenberg, N. Dadheech, J. Yoon, A. J. Turner, A. Bloom, P. Konopka, H. Lachnitt, P. Hoor, J. Lelieveld, E. A. Kort, and H. Fischer (2026). **Airborne observations reveal underestimated riverine methane emissions across the Amazon**. *ESS Open Archive*. preprint, submitted to *Geophysical Research Letters* on 19 February 2026. DOI: 10.22541/essoar.177248180.00166712/v1.

Ort, L., A. Pozzer, P. Hoor, F. Obersteiner, A. Zahn, T. B. Ryerson, C. R. Thompson, J. Peischl, R. Commane, B. Daube, I. Bourgeois, J. Lelieveld, and H. Fischer (2025). **Enhancement of O_3–CO ratios at tropospheric subtropical latitudes: Photochemistry and stratospheric influence**. *Atmospheric Chemistry and Physics* 25:21, 14987–15007. DOI: 10.5194/acp-25-14987-2025. URL: https://acp.copernicus.org/articles/25/14987/2025/.

Ort, L., L. L. Röder, U. Parchatka, R. Königstedt, D. Crowley, F. Kunz, R. Wittkowski, J. Lelieveld, and H. Fischer (2024). **In-flight characterization of a compact airborne quantum cascade laser absorption spectrometer**. *Atmospheric Measurement Techniques* 17:11, 3553–3565. DOI: 10.5194/amt-17-3553-2024.

Publications in Peer Reviewed Journals - Co-authorships

Bauchinger, S., A. Engel, M. Jesswein, T. Keber, H. Bönisch, F. Obersteiner, A. Zahn, N. Emig, P. Hoor, H.-C. Lachnitt, F. Weyland, **Ort, L.**, and T. J. Schuck (2025). **The extratropical tropopause – trace gas perspective on tropopause definition choice**. *Atmospheric Chemistry and Physics* 25:21,

14167–14186. DOI: 10.5194/acp-25-14167-2025. URL: https://acp.copernicus.org/articles/25/14167/2025/.

Curtius, J., M. Heinritzi, L. J. Beck, M. L. Poehlker, N. Tripathi, B. E. Krumm, P. Holzbeck, C. M. Nussbaumer, L. H. Pardo, T. Klimach, K. Barmpounis, S. T. Andersen, R. Bardakov, B. Bohn, M. A. Cecchini, J.-P. Chaboureau, T. Dauhut, D. Dienhart, R. Doerich, A. Edtbauer, A. Giez, A. Hartmann, B. A. Holanda, P. Joppe, K. Kaiser, T. Keber, H. Klebach, O. O. Krueger, A. Kuerten, C. Mallaun, D. Marno, M. Martinez, C. Monteiro, C. Nelson, **Ort, L.**, S. S. Raj, S. Richter, A. Ringsdorf, F. Rocha, M. Simon, S. Sreekumar, A. Tsokankunku, G. R. Unfer, I. D. Valenti, N. Wang, A. Zahn, M. Zauner-Wieczorek, R. I. Albrecht, M. O. Andreae, P. Artaxo, J. N. Crowley, H. Fischer, H. Harder, D. L. Herdies, L. A. T. Machado, C. Poehlker, U. Poeschl, A. Possner, A. Pozzer, J. Schneider, J. Williams, and J. Lelieveld (2025 APR 1 2025). **Isoprene nitrates drive new particle formation in Amazon's upper troposphere (vol 636, 124, 2024)**. English. *NATURE*. ISSN: 0028-0836. DOI: 10.1038/s41586-025-08906-2.

Ekinci, F., O. Eppers, O. Appel, F. Ploeger, A. Dragoneas, S. Molleker, P. Brauner, H.-C. Lachnitt, F. Weyland, **Ort, L.**, H.-C. Clemen, N. Emig, L. Tomsche, M. Ebert, P. Hoor, B. Vogel, Y. Cheng, J. Schneider, S. Borrmann, and F. Köllner (2026). **Enhancement of ammonium nitrate aerosol in the Northern Hemisphere lower stratosphere linked to Asian summer monsoon outflow**. *EGUsphere*. submitted on 21 February 2026.

Jesswein, M., V. Lauther, N. Emig, P. Hoor, T. Keber, H.-C. Lachnitt, **Ort, L.**, T. Schuck, J. Strobel, R. Van Luijt, C. M. Volk, F. Weyland, and A. Engel (2025). **Tracing elevated abundance of CH_2Cl_2 in the subarctic upper troposphere to the Asian Summer Monsoon**. *Atmospheric Chemistry and Physics* 25:14, 8107–8126. DOI: 10.5194/acp-25-8107-2025. URL: https://acp.copernicus.org/articles/25/8107/2025/.

Nussbaumer, C. M., A. Pozzer, M. Hewson, **Ort, L.**, B. Krumm, J. Byron, J. Williams, P. Joppe, F. Obersteiner, A. Zahn, J. Lelieveld, and H. Fischer (2025). **Low Tropospheric Ozone Over the Indo-Pacific Warm Pool Related to Non-Electrified Convection**. *Geophysical Research Letters* 52:5. e2024GL112788 2024GL112788, e2024GL112788. DOI: https://doi.org/10.1029/2024GL112788. eprint: https://agupubs.onlinelibrary.wiley.com/doi/pdf/10.

1029/2024GL112788. URL: https://agupubs.onlinelibrary.wiley.com/doi/abs/10.1029/2024GL112788.

Reppert, V., O. Eisen, H. Schmithüsen, S. Arndt, G. Ascenso, **Ort, L.**, and Z. Jurányi (2025). **Tracking In-Situ Snow Accumulation at Neumayer, Coastal Antarctica: Signs of Climatic Changes in the past 30 Years?** *EGUsphere* 2025, 1–32. DOI: 10.5194/egusphere-2025-5199. URL: https://egusphere.copernicus.org/preprints/2025/egusphere-2025-5199/.

Riese, M., P. Hoor, C. Rolf, D. Kunkel, B. Vogel, F. Köllner, M. Pöhlker, F. Ploeger, J. Ungermann, W. Woiwode, S. Johansson, R. Bauer, K. Barmpounis, S. Borrmann, P. Brauner, J. Clemens, A. Dragoneas, F. Ekinci, N. Emig, A. Engel, O. Eppers, S. Fadnavis, F. Friedl-Vallon, M. Geldenhuys, G. Günther, J. Grooß, M. Hegglin, M. Höpfner, M. Jesswein, P. Joppe, J. Kaumanns, O. Kachula, T. Keber, E. Kretschmer, H. C. Lachnitt, V. Lauther, P. Lloyd, S. Molleker, R. Müller, T. Neubert, **Ort, L.**, U. Pöschl, C. Pöhlker, M. Rapp, M. Retzlaff, S. Rhode, J. Schneider, T. Schuck, B.-M. Sinnhuber, N. Spelten, J. Strobel, L. Tomsche, K. Turhal, R. van Luijt, S. Versick, C. Voigt, M. Volk, M. von Hobe, F. Weyland, A. Zahn, H. Ziereis, and L. Zlotos (2025). **Long-range transport of polluted Asian summer monsoon air to high latitudes during the PHILEAS campaign in the boreal summer 2023**. *Bulletin of the American Meteorological Society*, BAMS-D-24–0232.1. DOI: 10.1175/BAMS-D-24-0232.1. URL: https://journals.ametsoc.org/view/journals/bams/aop/BAMS-D-24-0232.1/BAMS-D-24-0232.1.xml.

Röder, L. L., **Ort, L.**, J. Lelieveld, and H. Fischer (2024). **Quantitative analysis of temporal stability and instrument performance during field experiments of an airborne QCLAS via Allan–Werle-plots**. *Applied Physics B* 130:7, 118. DOI: 10.1007/s00340-024-08254-5.

Rojas Benavente, N., S. Botía, A. Henkes, A. Vara-Vela, A. C. Prudente Junior, B.-H. Martins Portella, C. Quaresma Dias Júnior, D. Ho, F. Santos da Silva, F. A. F. D'Oliveira, H. Van Asperen, H. Fischer, **Ort, L.**, L. Varanda Rizzo, M. Galkowski, P. Artaxo, T. Glauch, and L. A. T. Machado (2026). **Assessment of WRF-GHG model simulations during the CAFE-Brazil Experiment**. *Atmospheric Chemistry and Physics*. planned to be submitted to ACP.

Vogel, B., V. Lauther, F. Köllner, F. Ekinci, C. Rolf, J. Strobel, R. van Luijt, M. C. Volk, S. Borrmann, A. Dragoneas, O. Eppers, S. Molleker, P. Hoor, **Ort, L.**, F. Weyland, A. Zahn, J. Clemens, G. Günther, O. Kachula, R. Müller, F. Ploeger, and M. Riese (2025). **Continental and marine source regions contributing to the outflow of the Asian summer monsoon anticyclone during the PHILEAS campaign in summer 2023**. *EGUsphere* 2025, 1–49. DOI: 10.5194/egusphere-2025-5609. URL: https://egusphere.copernicus.org/preprints/2025/egusphere-2025-5609/.

Conference Oral Presentations

Ort, L., C. Frankenberg, N. Dadheech, J. Yoon, A. J. Turner, H.-C. Lachnitt, P. Hoor, J. Lelieveld, and H. Fischer (2025). **Large methane enhancements above the Amazon Basin**. *General Assembly of the American Geosciences Union*. 15-19 December 2025, New Orleans, LA, USA.

Ort, L., L. L. Röder, and H. Fischer (2023). **Analysis of QCL spectrometer via Allan-Werle-Plot techniques for increasing complexity from laboratory environments towards field and airborne deployments**. *FLAIR 2023 - Field Laser Applications in Industry and Research*. Assisi, Italy.

Conference Poster Presentations

Ort, L., C. Frankenberg, N. Dadheech, J. Yoon, A. J. Turner, H.-C. Lachnitt, P. Hoor, J. Lelieveld, and H. Fischer (2025). **Large Methane Fluxes above the Amazon Basin**. *2nd IGAC-iCACGP Early Career Researcher online Conference*. 25-26 September 2025, online.

Ort, L., L. L. Röder, P. Hoor, J. Lelieveld, and H. Fischer (2024). **Methane Enhancement Above the Amazon Rainforest**. *General Assembly of the European Geosciences Union*. 15-19 April 2024, Vienna, Austia.

Ort, L., L. L. Röder, P. Hoor, F. Obersteiner, A. Zahn, J. Lelieveld, and H. Fischer (2023). **Aircraft measurements of carbon monoxide and methane to characterize dynamical transport processes in the tropical upper troposphere**. *General Assembly of the European Geosciences Union.* 24-28 April 2023, Vienna, Austia.

Appendix

Table 4.1: Declaration of AI-use for this thesis.

AI-tool	Used for	Why?	Where?
DeepL Write	Improvement of my text formulations	To improve english phrasing	Section 2, 4
ChatGPT	Search for fitting literature	help to find relevant references	Section 2
	Text structure ideas	Improving paragraphs in their conceptual structures	Section 2
	Formatting help	Improve format	whole thesis